



UNIVERSIDADE DE BRASÍLIA - UNB
INSTITUTO DE GEOCIÊNCIAS - IG
PROGRAMA DE PÓS-GRADUAÇÃO EM GEOLOGIA

**DISTRIBUIÇÃO COMPOSICIONAL INTRAGRÃO E SEU
SIGNIFICADO PARA SULFETOS AURÍFEROS**

Wendell Fabricio-Silva

TESE DE DOUTORADO Nº 174

Orientadora: Profa. Dra. Maria Emilia Schutesky

Coorientador: Prof. Dr. Hartwig E. Frimmel (Würzburg Universität)

Coorientador: Prof. Dr. Carlos A. Rosière (UFMG)

BRASÍLIA, 2021

Ficha catalográfica elaborada automaticamente,
com os dados fornecidos pelo(a) autor(a)

Fd

Fabricio-Silva, Wendell
Distribuição composicional intragrão e seu significado
para sulfetos auríferos / Wendell Fabricio-Silva; orientador
Maria Emilia Schutesky; co-orientador Carlos Alberto
Rosière. -- Brasília, 2021.
280 p.

Tese (Doutorado - Doutorado em Geologia) -- Universidade
de Brasília, 2021.

1. Ouro. 2. Sulfetos. 3. Zonamento Composicional. 4.
Remobilização. 5. Idade de Mineralização. I. Schutesky, Maria
Emilia, orient. II. Rosière, Carlos Alberto, co-orient. III.
Título.

UNIVERSIDADE DE BRASÍLIA - UNB
INSTITUTO DE GEOCIÊNCIAS - IG
PÓS-GRADUAÇÃO EM GEOLOGIA

DISTRIBUIÇÃO COMPOSICIONAL INTRAGRÃO E SEU SIGNIFICADO PARA
SULFETOS AURÍFEROS

Tese de Doutorado

Wendell Fabricio-Silva

Área de Concentração: Prospecção e Geologia Econômica

Orientadora:

Profa. Dra. Maria Emília Schutesky

Co-orientadores:

Prof. Dr. Hartwig E. Frimmel (Würzburg Universität)

Prof. Dr. Carlos A. Rosière (UFMG)

Banca Examinadora:

Prof. Dr. Claudinei Gouvea de Oliveira (IG – UnB)

Prof. Dr. Luís Gustavo Ferreira Viegas (IG – UnB)

Prof. Dr. Steffen Hagemann (UWA – Australia)

Profa. Dra. Rosaline Cristina Figueiredo e Silva (UFMG)

Brasília-DF, abril de 2021.

“Deixe o mundo um pouco melhor que o encontrou.” Robert Baden-Powell

AGRADECIMENTOS

A vida é curta e, portanto, busco participar do maior número de experiências possível. E minha experiência acadêmica no período de doutoramento não me trouxe tão-somente um desenvolvimento intelectual basilar para o que quero de mim, mas a oportunidade de coexistir e trabalhar com muitas pessoas ferrenhas.

Minha família foi meu maior suporte. Minha esposa Flávia e minha filha Lis também lutaram comigo. Que sorte tenho por tê-las. Sem elas, certamente não teria conseguido. Aos meus pais, que não tiveram a chance de completar o 5º ano do ensino fundamental, mas que me deram todas as condições de ser um Ph.D.

Ao Prof. Bernhard Bühn, que me acolheu na Universidade de Brasília e foi meu primeiro orientador. O primário luto pela sua morte foi se transformando em combustível para que eu fosse mais além.

À minha orientadora, Maria Emilia, que foi minha amiga e tornou tudo mais fácil para mim. Sempre sorridente e paciente com meus aferros, que não foram poucos. Espero, e vou, continuar sempre muito próximo. É uma inspiração muito grande para mim como pesquisadora e pessoa.

Ao meu co-orientador e amigo de todas as horas, Carlos “Mestre” Rosière. Sempre solícito e honesto. Cientista por definição.

Ao meu orientador do período de cientista visitante na Uni Würzburg, Hartwig Frimmel, que me acompanhou e acompanha de muito perto. Me deu um suporte *in loco* impecável e dispendeu muita energia em minha pesquisa. Aos pesquisadores e professores da Uni Würzburg, especialmente Alex Kawohl, Volker von Seckendorff, Thomas Will, Enzio Garayp, Martin Okrusch e Steffan Höhn.

Aos amigos da UnB, parceiros de luta e pessoas de alto nível, como Italo, Gabi, Terras Raras, Alanielson, Moriá, Isabela, Bruno, Tassio, e tantos outros.

A todos os professores do IG-UnB que, mesmo extraoficialmente, contribuíram enormemente com minha tese, com destaque para Claudinei, Paola, Detlef, Catarina, Dermeval, Catarina, Nilson e Adalene.

Aos pesquisadores, que contribuíram com discussões ou análises laboratoriais, como Denis Fougerouse (Curtin University, Australia), Daniel Kontak (Laurentian University, Canadá), Nicholas Saintilan (University of Durham, Reino Unido), Phillip Gopon (University of Leoben, Áustria), Leonardo Lagoeiro (UFPR), Andy Tomkins (Monash University, Austrália), Alice Bosco (Unicamp) e Mariana Brando (UERJ).

Aos meus amigos de infância, sempre próximos e que ajudaram com revisões ou outros apoios: Daniel “Pias”, Raul “Mala”, Bruno “Banana” e João “Pancinha”.

Às companhias Jaguar Mining Inc, AngloGold Ashanti, Iamgold Corporation, que forneceram acesso e amostragem nas minas visitadas.

Este estudo foi financiado em parte pela Coordenação de Aperfeiçoamento de Pessoal de Nível Superior - Brasil (CAPES) – Código de Financiamento 001. Também agradeço à CAPES pelo financiamento do Programa de Doutorado Sanduíche no Exterior (PDSE; nº 88881.188398/2018-01), realizado na Alemanha nos anos de 2018 e 2019.

Seguirei adiante, buscando outras e novas experiências.

SUMÁRIO

AGRADECIMENTOS	IV
SUMÁRIO.....	VI
ÍNDICE DE FIGURAS.....	IX
ÍNDICE DE TABELAS.....	XVI
RESUMO	XVII
1. INTRODUÇÃO	19
1.1 ESCOPO DA TESE.....	19
1.2 JUSTIFICATIVA E IMPORTÂNCIA DO ESTUDO.....	22
1.3 OBJETIVO DA TESE.....	23
1.4 DEPÓSITOS DE OURO ESTUDADOS.....	24
1.5 PRODUÇÃO TÉCNICO-CIENTÍFICA ASSOCIADA	26
1.6 ABORDAGEM E MÉTODOS ANALÍTICOS.....	30
1.6.1 <i>Amostragem e geoquímica de rocha-total</i>	31
1.6.2 <i>Microssonda Eletrônica</i>	32
1.6.3 <i>EBSD</i>	32
1.6.4 <i>Mapas compostionais de cristais de sulfeto</i>	33
1.6.5 <i>Elementos-traço por LA-ICP-MS</i>	33
2. ZONAMENTO EM SULFETOS: PROCESSOS E CONDIÇÕES PARA DEPÓSITOS DE OURO.....	34
2.1 RESUMO	34
2.2 INTRODUÇÃO	35
2.3 TÉCNICAS ANALÍTICAS DE ALTA RESOLUÇÃO UTILIZADAS EM NANOGEOQUÍMICA	37
2.3.1 <i>NanoSIMS</i>	38
2.3.2 <i>TEM-EDS</i>	40
2.3.3 <i>Atom Probe Tomography</i>	41
2.4 A CRYSTALIZAÇÃO DE SULFETOS NA FORMAÇÃO DO ZONAMENTO.....	43
2.5 MECANISMOS DE REMOBILIZAÇÃO.....	47
2.6 RECENTES AVANÇOS EM REMOBILIZAÇÃO E SUAS APLICAÇÕES	53
2.7 DISCUSSÕES E CONCLUSÕES	55
2.8 AGRADECIMENTOS	56
2.9 REFERÊNCIAS	56
3. INTRAGRAN GOLD MOBILITY AND ITS SIGNIFICANCE FOR THE “TIMING OF MINERALIZATION”	71
3.1 ABSTRACT	71
3.2 INTRODUCTION.....	72

3.3	PRIMARY ZONING	74
3.4	CHANGES IN METAL CONTENT DURING REMOBILIZATION	75
3.5	THE AGE OF MINERALIZATION AND THE OTHER HALF OF THE HISTORY.....	78
3.6	CONSIDERATIONS ON THE USE OF GEOCHRONOLOGY	81
3.7	ACKNOWLEDGMENTS.....	83
3.8	REFERENCES.....	83
4.	TEMPERATURE-CONTROLLED ORE EVOLUTION IN OROGENIC-GOLD SYSTEMS RELATED TO SYNCHRONOUS GRANITIC MAGMATISM: AN EXAMPLE FROM THE IRON QUADRANGLE PROVINCE, BRAZIL..	89
4.1	ABSTRACT	89
4.2	INTRODUCTION.....	91
4.3	GEOLOGICAL SETTING	93
4.3.1	<i>Iron Quadrangle area</i>	93
4.3.2	<i>The age of the TTG-Pitangui greenstone belt terrane</i>	95
4.4	SAMPLING AND ANALYTICAL METHODS	97
4.5	RESULTS.....	100
4.5.1	<i>Geology of the Satinoco deposit</i>	100
4.5.2	<i>Hydrothermal alteration and mineralization styles.....</i>	105
4.5.3	<i>Garnet porphyroblasts: textures, generations, and compositions.....</i>	111
4.5.4	<i>The sulfide assemblages and gold mineralization</i>	115
4.5.5	<i>Compositional variation of gold-bearing sulfide assemblages</i>	119
4.5.6	<i>Geothermometry</i>	127
4.6	DISCUSSION	131
4.6.1	<i>Paragenetic sequence of the hydrothermal alteration minerals</i>	131
4.6.2	<i>The sulfide assemblages</i>	134
4.6.3	<i>Age of the TTG-greenstone terrane and timing of gold mineralization.....</i>	140
4.6.4	<i>Role of granite in the mineralization history</i>	141
4.6.5	<i>Metallogenetic classification</i>	147
4.7	CONCLUSIONS	148
4.8	ACKNOWLEDGMENTS.....	150
4.9	REFERENCES.....	150
5.	HOW DOES ARSENOPYRITE LOSE ITS PRIMARY GEOCHEMICAL SIGNATURE? A GLIMPSE FROM OROGENIC GOLD DEPOSITS IN BRAZIL	160
5.1	INTRODUCTION.....	160
5.2	GEOLOGICAL BACKGROUND.....	162
5.3	INDIVIDUAL AU DEPOSITS	165
5.4	METHODOLOGY.....	170
5.5	ARSENOPYRITE: TEXTURES AND ELEMENTAL COMPOSITION	173
5.5.1	<i>São Sebastião deposit</i>	177

5.5.2	<i>Turmalina deposit</i>	181
5.5.3	<i>Satinoco deposit</i>	183
5.5.4	<i>Composition of pyrite compared to arsenopyrite</i>	187
5.6	DISCUSSION	190
5.6.1	<i>Evolution of gold-bearing sulfides</i>	190
5.6.2	<i>The Ni concentration from ore-forming fluids</i>	193
5.6.3	<i>Discriminating arsenopyrite and pyrite compositions</i>	194
5.6.4	<i>Au remobilization processes</i>	197
5.6.5	<i>Relative chronology between the sulfide parageneses and gold mobility</i>	200
5.7	REFERENCES.....	202
6.	TEXTURA E ASSINATURA GEOQUÍMICA DE SULFETOS AURÍFEROS: CONJECTURAS SOBRE ALTERAÇÃO HIDROTERMAL, FONTE DOS METAIS E IDADE RELATIVA	213
6.1	Evolução tectono-termal e sua relação com as fases de mineralização aurífera no depósito Turmalina, Quadrilátero Ferrífero, Minas Gerais	215
6.2	TECTONOTHERMAL EVOLUTION AND MULIPHASE ORE-FORMING PROCESSES AT TURMALINA GOLD DEPOSIT, QUADRILÁTERO FERRÍFERO, BRAZIL	216
6.3	MULTIPLE MINERALIZATION STAGES AND RELATIVE TIMING OF GOLD DISTRIBUTION IN THE SATINOCO DEPOSIT, NW OF QUADRILÁTERO FERRÍFERO, BRAZIL.....	218
6.4	DEPÓSITOS DE OURO OROGÊNICO E O PAPEL DO MAGMATISMO GRANÍTICO SINCRÔNICO: CONTRIBUIÇÃO COM FLUIDO MINERALIZANTE OU APENAS MOTOR TERMODINÂMICO?	220
6.5	O PARADIGMA “IDADE DA MINERALIZAÇÃO”: PORQUE PRECISAMOS REVISITAR ESTE CONCEITO À LUZ DA NANOGEOQUÍMICA?.....	222
7.	CONCLUSÕES.....	224
8.	REFERÊNCIAS.....	229
ANEXO I: MAPAS DE EBSD E RESULTADOS DE LA-ICP-MS PARA OS DEPÓSITOS DE PILAR DE GOIÁS E CRIXÁS		
	244	
ANEXO II: FEIÇÕES PETROGRÁFICAS REPRESENTATIVAS DOS DEPÓSITOS SATINOCO E TURMALINA	249	
ANEXO III: RESULTADOS DE EPMA PARA GRANADA DE TRÊS GERAÇÕES DO GREENSTONE BELT PITANGUI .	251	
ANEXO IV: RESULTADOS DE EPMA REPRESENTATIVOS DE SULFETOS NOS DEPÓSITOS DE OURO SELECIONADOS	252	
ANEXO V: RESULTADOS DE LA-ICP-MS COM CONTEÚDOS DE ELEMENTOS MENORES E TRAÇOS EM SULFETOS DOS DEPÓSITOS TURMALINA, SATINOCO E SÃO SEBASTIÃO	266	
ANEXO VI: MAPAS COMPOSIÇÃO INTRACRISTALINOS SUPLEMENTARES DOS DEPÓSITOS ESTUDADOS .	268	
ANEXO VII: GEOQUÍMICA DE ROCHA TOTAL EM SATINOCO E TURMALINA: RESULTADOS E DISCUSSÕES	271	

ÍNDICE DE FIGURAS

Fig. 1-1. Fluxograma da amostragem, métodos analíticos e tipos de abordagem aplicados no estudo.	31
Fig. 2-1. Diagrama esquemático modificado de Pearce et al. (2018) com ênfase em técnicas analíticas mais utilizadas em nanogeоquímica. Mostra a resolução espacial mínima em função da maior extensão aérea prática de cada técnica (linhas espessas). As linhas com cores indicam as diferentes técnicas analíticas. As linhas tracejadas indicam as técnicas de altíssima resolução espacial. As figuras no entorno do diagrama representam exemplos de trabalhos com aplicação de técnicas utilizando sulfetos (pirita e arsenopirita) em depósitos de ouro (Ciobanu et al. 2012; Dubosq et al. 2018; Yan et al. 2018; Fabricio-Silva et al. 2019; Fougerouse et al. 2019; Fabricio-Silva et al. 2020; Gourcerol et al. 2020). Abreviações: pXRF – Fluorescência de raios-X picoescala; μ XRF – Micro fluorescência de raios-X; HRXCT - Tomografia computadorizada de raio-X de alta resolução CT; sXRF – Fluorescência de raio-X sincrotron; SIMS - espectrometria de massa de íons secundários; SEM – Microscopia eletrônica; WDS – espectroscopia de raios-X dispersiva de comprimento de onda; TEM – microscopia eletrônica de transmissão; TKD – Difração de transmissão de Kikuchi.	39
Fig. 2-2. Visão esquemática de um microscópio atômico (APT). O espécimen amostral é congelado ($T < -195$ °C), submetido a um campo de alta tensão (V_{DC}) e iluminado por pulsos de laser, desencadeando a evaporação do campo de íons, que voam através de um contra eletrodo e são coletados pelo detector sensível de posição. O detector também registra o tempo de voo, o que permite a identificação do elemento (Modificado e adaptado de Gault, 2016).....	42
Fig. 2-3. Diagrama esquemático mostrando o efeito da taxa de crescimento do cristal de arsenopirita (Apy) e sua resposta na distribuição de Au. Crescimento rápido resulta numa maior tendência de distribuição homogênea de ouro. Crescimento lento facilita a difusão de átomos em superfícies, resultando na formação de nanopartículas de ouro. Modificado e adaptado de (Fougerouse et al. 2016b).	45

Fig. 2- 4. Estágios do mecanismo de CDR para pirita (Py). Modificado e adaptado de Hastie et al. (2020) usando conceitos de reações de substituição mineral de Putnis (2009). A fase de Py1a é híbrida entre a pirita de primeira geração (Py₁) e a substituição da pirita de segunda geração (Py₂).52

Fig. 3-1. Diagram with the set of crystallization mechanisms and remobilization as processes of generation and enrichment of gold deposits associated with sulfides. Gold-bearing sulfides crystallize by intrinsic or extrinsic processes (often a combination of both). After crystallization, the gold present in the sulfides can be remobilized through liberation, transport, and deposition, in a cyclic and usually continuous process.79

Fig. 4-1. Regional geology schematic map of the southern region of the San Francisco Craton. (A) Schematic geological map of the Iron Quadrangle (Minas Gerais / Brazil) showing the Archean greenstone belts, as well as some of the major Archean gold deposits. Compiled and adapted after Dorr (1969) and Renger et al. (1994). (B) Map of the Pitangui geological region (modified and adapted after Fabricio-Silva, 2016; Brando Soares et al., 2017; Marinho et al., 2018).95

Fig. 4-2. (A) Stratigraphic column of the host rocks in the Satinoco deposit and their relation to the regional stratigraphic column of the Pitangui greenstone belt and Turmalina-A and Turmalina-B orebodies. (B) Horizontal drill hole FTS-1406 logging of the C-Central orebody with representatives macroscopic and microscopic photos. The left column represents photos of some selected samples. In the schematic drill hole, the color intensity is disproportionate with the amount of hydrothermal silica (grey: less silica; light blue: more silica). The other schematic local mineral enrichments are shown as: garnet, chlorite, sulfide (light grey layers and ellipses, representing brecciated and disseminated, respectively), quartz ± carbonate veins, and black shales bands. The two columns in the right side represent, respectively, estimated total sulfides (vol %) and the gold content (in ppm) based in whole-rock ICP-MS analyses.....102

Fig. 4-3. (A-E) Pictures illustrating underground representative granite apophysis and their structural relationship with the host rocks and orebodies. (F) Photomicrograph of metamafic host rock (garnet-biotite-chlorite-quartz schist) seen in B. Transmitted

light, parallel polarizers. (G) Photomicrograph of representative texture seen in the granite apophysis showed in B. Equigranular granite with quartz, k-feldspar (microcline), plagioclase (partially sericitized) and biotite. Transmitted light, crossed polarizers.....104

Fig. 4-4. Schematic cartoon illustrating the Neoarchean late-tectonic intrusive magmatism at the Pitangui greenstone belt and its relationship between the thrust/shear zones and gold mineralization. Note the spatial distribution of the contact metamorphism and the metamorphic facies. Modified after Brando Soares et al. (2020). See photomicrographs containing the alteration minerals for each metamorphic paragenesis in App. Fig. A1 – In Economic Geology).....105

Fig. 4-5. Vein systems at the Satinoco deposit. (A) V₁ vein showing milky quartz rimmed by recrystallized smoky quartz and sulfides. (B) Underground stope ceiling displaying pinch-and-swell structures in V₁ vein. Note deformed vein contains inclusion bands with preserved S₁ foliation (weakly developed) in metabasalt. (C) Drill core with quartz-carbonate V₂ vein crosscutting S₁, S₂, and granite apophysis. (D) Disseminated gold-bearing sulfide range parallel to V₁ vein. (E) Drill core showing granite apophysis with a xenolith of metabasalt. Note arsenopyrite grains in both granite and metabasalt. (F) Drill core showing aggregates of sulfides forming hydraulic breccias in V₁ vein, disseminated sulfide range, and V₂ veinlets with sulfide and carbonate. Apy – arsenopyrite; Cal – calcite; Po – pyrrhotite; Lö – löllingite....108

Fig. 4-6. Photomicrographs of representative garnet porphyroblasts from the two generations (Grt₁ and Grt₂). The compositional profiles are indicated by yellow squares (spot analysis location) and the garnet domains (core and rims) are highlighted in lines yellow and red (see legend).....112

Fig. 4-7. Chemical profiles of representative garnet porphyroblasts from the FTS-1406 drill hole. The pseudo sections and the spot analysis locations are shown in figure 6 and the chemical composition values can be found in Appendix Table A1.114

Fig. 4-8. Au-bearing sulfide stages and gold mineralization types at the Satinoco deposit. A) BSE image of sulfides from sulfide stage I and gold grains as inclusion I and free. B) BSE image of Apy₂ replacing löllingite and Apy₁ as inclusion in Grt₂. Note that the gold inclusions rims a löllingite crystal. C) Photomicrograph with reflected light showing Apy₁. D) BSE image of pyrite and fracture-controlled gold and gold inclusion II associated with sphalerite. E) Polished thin section showing pyrite crosscutting sulfides parallel to S₁ foliation (yellow lines). The white square indicates

the position of the (D). F) Polished thin section that shows deformed black shale and sulfides from assemblage I associated with foliation S ₁ . The white square indicates the position of the (G) and (H). G) Photomicrograph showing the detail of the V ₁ vein deformed by S ₂ crenulation cleavage (red lines). H) BSE image of (G) showing Apy ₁ and Lö related to the V ₁ vein. I) BSE image of Apy-Lö-Po assemblage. J) Photomicrograph showing a V ₂ -veinlet crosscutting Po ₂ . K) BSE image that shows Po ₂ as pressure shadow in garnet (Grt ₂ ?). L) BSE image showing free gold bordering Apy ₂ and Po ₂ . M) BSE image with base metal sulfide assemblage composed by Ccp, Gn and Ull. Apy – arsenopyrite; Bt – biotite; Ccp – chalcopyrite; Gn – galena; Grt – garnet; Lö – löllingite; Po – pyrrhotite; Py – pyrite; Sph – sphalerite.	117
Fig. 4-9. Plots showing EMP geochemistry of arsenopyrite from Apy ₁ (n = 73) and Apy ₂ (n = 34) in the Satinoco deposit. (A-B) relationship of S (wt.%) and Fe (wt.%) with As (wt.%) (C) Co (at.%) vs. Fe (wt.%) showing considerably high content of Co in Apy ₂ and the negative relationship between Fe and Co.	120
Fig. 4-10. X-ray mapping of representative arsenopyrite crystals which show the distribution of selected elements in sulfide stages I and II from Satinoco Deposit. (A-C, D-F, G-I, and J-L) are element mapping in counts from As, Fe, Ni, and Sb, respectively.	122
Fig. 4-11. Au and Bi element mapping of representative Apy ₂ rimmed by löllingite in the Satinoco deposit. (A-B) are element mapping in counts from As and Bi, respectively. (C) Gold content illustrating the gold enrichment along with the contact between Lö and Apy. Note the following features highlighted in the figures: (i) the green dashed lines highlight the contour of the löllingite and arsenopyrite; (ii) the white line in (A) refers to profile represented in (C); (iii) the yellow and the light blue arrows indicate gold and bismuth inclusions, respectively.	123
Fig. 4-12. Whisker and box diagrams of selected trace elements of Apy ₁ , Apy ₂ , and Py. The geometric mean (x), median (horizontal line), first quartile (Q1, lower limit of box) and third quartile (Q3, upper limit of box) are shown. Outlier values are shown as circles (see legend). The minor and trace elements composition can be found in Appendix Table A3.	125
Fig. 4-13. Summary of variations in the As/S ratio of the studied arsenopyrite (inserted histogram), expressed atomic % of As and estimated sulfur fugacity and temperature evolution during sulfide stage I and II. The phase boundaries and arsenic isopleths are based on the data of Kretschmar and Scott (1976).	128

Fig. 4-14. The hydrothermal alteration stages and the paragenetic sequence of ore and gangue minerals in Satinoco Deposit.....	133
Fig. 4-15. Geological evolution of the Satinoco deposit based on gold-bearing sulfide (re)crystallization. (A) Early sulfide phase. (B) Fe-rich sulfide phase. (C) Carbonate and base metal sulfide phase. Apy – arsenopyrite; Ccp – chalcopyrite; Gn – galena; Grt – garnet; Lö – löllingite; Po – pyrrhotite; Py – pyrite.	136
Fig. 4-16. Schematic diagram showing the temperature variation (Y axis) throughout the time (X axis). The noticeable geological events are represented by numbers 1-6 (see legend). The timing of the Casquilho granite is represented by pink balloon at the center of the diagram. Note that the geochronological data used are specified in letters (A-F). See text for more explanations.	146
Fig. 5-1. Geological map of the NW-Quadrilátero Ferrífero Subprovince in the southern region of the São Francisco craton. Note that the map of the NW Subprovince is represented as a yellow rectangle in the Quadrilátero Ferrífero area. Compiled and adapted after Renger et al. (1994), Brando Soares et al. (2018), Marinho et al. (2018), and Fabricio-Silva (2016).	164
Fig. 5-2. São Sebastião deposit. (A) Reflected light photomicrograph of arsenopyrite from sulfide assemblage II (Apy_2). (B) BSE SEM image showing visible fracture-filling gold. (C) EBSD phase colors map. (D) EBSD IPF map that highlights the different crystals within Apy aggregate. (E) Crystallographic misorientation angle in the range 0-8° (green). (F-K) Elemental As, Co, Sb, Ni, and Au X-ray maps from area represented as red box in D. Note that Ni and Au concentrations shows Apy_{2a} in the core of Apy_{2b} . (J) Histogram of Au and Ni that shows correlation only in higher Au grades (visible filling-fracture Au-Ni).....	179
Fig. 5-3. Turmalina deposit. (A) BSE SEM image of course grained arsenopyrite from sulfide assemblage II (Apy_2). (B) Crystallographic misorientation angle in the range 0-11°. (C-F) Elemental As, Ni, Au, and Co X-ray maps from area represented as white box in B. Yellow triangle indicate the LA-ICP-MS spot analyses. The white circles show the EMP spot analyses.	182
Fig. 5-4. Satinoco deposit. (A) BSE SEM image of course grained arsenopyrite from sulfide assemblage I (Apy_1). (B) Crystallographic misorientation angle in the range 0-20°. (C-F) Elemental As, Au, Co, and Ni X-ray maps from area represented as black	

box in A. Yellow triangle indicate the. The white circles show the LA-ICP-MS spot analyses. Note that the invisible gold forms Au-rich trends in the Apy-core.....	184
Fig. 5-5. Satinoco deposit. (A) BSE SEM image of course grained arsenopyrite from sulfide assemblage II (Apy ₂). (B) Crystallographic misorientation angle in the range 0-15°. (C-F) Elemental As, Au, Ni, and Co X-ray maps from area represented as black box in A. Yellow triangle indicate the. The white circles show the LA-ICP-MS spot analyses. Note that the invisible gold forms Au-rich zones in the Apy-core.	185
Fig. 5-6. Satinoco deposit. (A-B) Elemental X-ray mapping for As and Bi in a Apy ₂ that rims Lö (after Fabricio-Silva et al., 2020). (C) Crystallographic misorientation angle in the range 0-15°.	186
Fig. 5-7. Time-resolved LA-ICP-MS depth profiles for spot analyses of S, Fe, Co, Ni, Sb, Au, Pb and Bi of arsenopyrite and pyrite hosted in ores from Turmalina, Satinoco, and São Sebastião deposits from sulfide assemblages I (A-D), II (E-J), and III (K and L). Free gold particles are shown mainly in Apy ₂ from Satinoco deposit and Apy ₃ from São Sebastião deposit.	190
Fig. 5-8. Multi-element diagrams of arsenopyrite from Turmalina, Satinoco, and São Sebastião deposits showing median trace element values of the LA-ICP-MS analyses for specific sulfide assemblages. (A) Sulfide asssemblage I (Apy ₁) from the Turmalina and Satinoco deposits (grey region) showing similar trace element concentrations. In contrast, the sulfide assemblage II shows enrichment in Sb, Te, Pb, and Au, compared to assemblage I. (B) Relative similar patterns between assemblage II (beige region) from Turmalina and Satinoco and Apy ₃ (São Sebastião) and Py ₃ (Satinoco). Differences in Zn, Se, Mo, and Cu between assemblage II, considered to have formed in part from magmatic fluids, and the hydrothermal sulfide assemblage I. (C) Significant enrichment in Au, Sb, Te, Bi, and Ag in intragrain microfracture in Apy ₂ , compared to non-fractured crystals. (D) Median values after Brando Soares et al. (2018) aplied to the sulfide parageneses described here. Note that, although only few elements are above D.L. (detection limit), the later Py ₃ and Apy ₃ (this study) show enrichment in Au, Bi Pb and Sb, as observed in others studied deposits.....	192
Fig. 5-9. The São Sebastião Apy ₂ showing visible Au between the grain boundary (see Fig. 2D). The invisible gold occurs in Apy _{2a} -core (Apy _{2a}) and as remobilization lines in the Apy _{2b} -rim.	194

Fig. 5-10. Quantitative LA-ICP-MS elemental profiles (in ppm) aquired across an Apy₂ grain from Satinoco deposit. (A) Reflected light photomicrograph of the analyzed arsenopyrite grain. The dashed red lines represent micro-fractures identified. (B-C) Concentration profiles for selected elements in each spot ablated along the profile shown in image A. The spot 22 are over a fracture-filling visible Au.

.....196

Fig. 5- 11. The paragenetic sequence of sulfides in the studied deposits. The yellow circles represent the relative proportion of gold (free or invisible) in the indicated sulfides.....199

ÍNDICE DE TABELAS

Tabela 1-1. Relação dos depósitos de ouro estudados	25
Tabela 1-2. Trabalhos científicos relacionados ao desenvolvimento desse doutoramento.	27
Table 4-3. Summary of gold mineralization types observed in Satinoco deposit	118
Table 4-4. Summary of minor and trace element contents in sulfide minerals performed by LA-ICP-MS (data in ppm)	126
Table 4-5. Garnet and biotite electron microprobe analyses normalized to 12 O (garnet) and 22 O (biotite) used for the geothermometric calculations.	129
Table 4-6. Representative arsenopyrite composition obtained by electron microprobe analyses, minerals in equilibrium in the Fe-As-S system, and temperature calculation (according to Kretschmar and Scott, 1976; and Sharp et al., 1985)	130
Table 5-1. Summary table of the studied gold deposits showing temperature and pressures of metamorphism, sulfide assemblages and host rocks.	169
Table 5-2. Summary of electron microprobe results from arsenopyrite and pyrite of different assemblages from studied deposits.	175
Table 5-3. Summary of minor and trace element contents in sulfide minerals performed by LA-ICP-MS (data in ppm)	188

RESUMO

Arsenopirita (FeAsS) e pirita (FeS_2) são os sulfetos mais importantes associados à metalogênese do ouro. A estreita relação espacial entre Au e a mudança nas texturas desses sulfetos sugere que a transição metamórfica/hidrotermal dos processos de (re) cristalização resulta na concentração de ouro no sistema, por meio da liberação do elemento da trama cristalina (como partículas submicrônicas na forma de Au^0 ou como solução sólida na forma de Au^+). Esse metal é então transportado e (re)concentrado em processos comumente sincronizados com entrada de fluidos, intrusão magmática, deformação, entre outros. Essa pesquisa combina análise microestrutural por meio de técnicas de microssonda eletrônica, difração de elétron retroespelhado (EBSD), espectrometria de massa de plasma indutivamente acoplada por ablação a laser (LA-ICP-MS) e mapeamento composicional 2D para investigar a influência de eventos como magmatismo intrusivo, hidrotermalismo, metamorfismo e deformação na retenção, liberação ou captura de Au, e outros elementos-traço, dentro de arsenopirita e pirita de paragêneses sin-, tardi- e pós-tectônicas. Finalmente, combina-se mapeamento 2D de elementos-traço em microescala com avaliação 3D dos espectros de LA-ICP-MS para avaliar os mecanismos de remobilização e a cronologia relativa ao modelo de enriquecimento de Au. Foi documentada a assinatura geoquímica e microestruturas, principalmente de arsenopirita, de múltiplas paragêneses de Au em 9 depósitos de ouro brasileiros das classes ouro-orogênico e *intrusion-related*. Em geral, os nossos modelos para esses depósitos são consistentes com histórias evolutivas que compreendem, dentre outros: (i) Au concentrado durante a cristalização de arsenopirita pré-tectônica; (ii) substituição de arsenopirita por löllingita associada ao metamorfismo progrado relacionado à instalação de plúton granítico; (iii) fusão de sulfetos mediada por fluidos quentes ($>730\ ^\circ\text{C}$); (iv) deformação plástica intracristalina e difusão por volume; (v) dissolução-reprecipitação de Au em baixas temperaturas, possibilitada pela presença de elementos calcófilos de baixo ponto de fusão (notadamente Sb, Bi e Te). Todos esses processos foram capazes de concentrar ouro em diferentes fases metalogenéticas dos depósitos de ouro investigados, como ocorre comumente em depósitos de ouro-orogênico.

Esse trabalho reúne, de uma forma possivelmente inédita, o significado do zonamento composicional em arsenopirita para processos primários ligados à cristalização ou relacionados à remobilização e sugere uma abordagem onde a “idade da mineralização” pode não ter sentido direto quando se demonstra a mobilidade intracristalina do ouro.

Palavras-chave: ouro; arsenopirita; zonamento composicional; remobilização; idade de mineralização

1. INTRODUÇÃO

1.1 Escopo da Tese

A Tese apresenta-se estruturada na forma de artigos, separados em diferentes capítulos. Os capítulos com trabalhos publicados, submetidos ou preparados para submissão futura em periódicos internacionais, estão apresentados em Língua Inglesa.

O **Capítulo 1** apresenta as informações gerais da pesquisa: justificativa e importância do estudo; objetivos; relação dos depósitos de ouro estudados; a produção técnico-científica associada a este doutoramento; e a abordagem e métodos analíticos. Além deste subtópico, “Escopo da tese”.

Como introdução aos significados teóricos do zonamento composicional em sulfetos, o **Capítulo 2** contém o manuscrito “Zonamento em sulfetos: processos e condições para depósitos de ouro”, submetido no Periódico Série Científica – Geologia USP. Neste trabalho foram reunidos, possivelmente de forma inédita, os principais processos mineralógicos ligados à distribuição e mobilidade de elementos-traço em sulfetos auríferos. Também são abordadas e descritas as técnicas utilizadas em Nanogeoquímica de sulfetos de minério (inéditas no Brasil), como NanoSIMS e Atom Probe Tomography.

Com base nos diferentes processos de mobilidade de elementos-traço discutidos em trabalhos recentes, o **Capítulo 3** compõe um manuscrito no tipo *Express Letters* ou *Short Communications* com reflexões sobre o significado do termo “Idade de mineralização”, o qual definimos neste trabalho como um paradoxo. O trabalho se intitula “*Intragrain gold mobility and its significance for the ‘timing of mineralization’*” e

traz um panorama sobre os mecanismos de cristalização e remobilização para uma possível ressignificação dos resultados de geocronologia aplicada na metalogênese do ouro. Esse trabalho está em sua segunda versão, contemplando primeira revisão dos coautores, e deverá ser submetido ao periódico *Ore Geology Reviews* ou *Earth and Planetary Science Letters*.

O **Capítulo 4** traz o artigo publicado no periódico *Economic Geology*, intitulado “*Temperature-controlled ore evolution in orogenic gold systems related to synchronous granitic magmatism: an example from the Iron Quadrangle Province, Brazil*”. Nesse trabalho, demonstramos a relação cronológica entre as diferentes paragêneses de sulfeto com um granito intrusivo tardio a pós-tectônico. O trabalho sugere como a temperatura e a fonte de diferentes tipos de fluido resultam em composições e texturas específicas nos sulfetos.

O **Capítulo 5** exibe o trabalho intitulado “*How does arsenopyrite lose its primary geochemical signature? A glimpse from orogenic gold deposits in Brazil*”. Esse estudo aborda os resultados de deformação plástica e espectros 3D obtidos por LA-ICPMS em arsenopirita de diferentes paragêneses nos depósitos do Greenstone Belt Pitangui (NW-Quadrilátero Ferrífero). Dados apresentados sugerem que a arsenopirita da primeira geração (orogênica), perdeu quantidade significativa de Au após intrusão de granitos pós-tectônicos relativamente ao evento Arqueano. Esse trabalho está em preparação e deverá ser submetido ao periódico *Contributions to Mineralogy and Petrology*.

O **Capítulo 6** integra um compêndio com a evolução dos conhecimentos levantados durante o período de doutoramento aplicados ao desenvolvimento das técnicas analíticas apresentadas. Esse capítulo sequencia as informações metalogenéticas dos depósitos estudados, desde mapeamento de galerias, análise estrutural, definição de zonas de alteração hidrotermal, isótopos estáveis, química mineral, mapeamento em escala de grão, EBSD e LA-ICP-MS para elementos-traço. Está

estruturado na forma de resumos apresentados em congressos internacionais e nacionais.

O **Capítulo 7** contém uma síntese conclusiva da tese, a partir dos dados apresentados nos diferentes trabalhos, destacando a história evolutiva integrada e o significado dos resultados para o entendimento do comportamento dos sulfetos ricos em ouro, notadamente arsenopirita.

As referências bibliográficas específicas dos artigos e manuscritos correspondentes aos capítulos 2 a 6 encontram-se ao final de cada um deles. Já o **Capítulo 8** dispõe das referências dos outros capítulos e dos anexos.

A seção **ANEXOS** reúne dois tipos de arquivo: (*i*) resultados analíticos completos utilizados nos trabalhos publicados e submetidos e; (*ii*) resultados não utilizados nas publicações apresentadas nos capítulos 2 a 6, os quais serão utilizados em publicações futuras.

Especificamente, o **Anexo IV** apresenta os resultados LA-ICP-MS e EBSD, além de discussões preliminares sobre as formações de arsenopirita nos Greenstone Belts de Pilar de Goiás e Crixás. Esses cristais exibem sombras de pressão formadas por silicatos deformados plasticamente e evidenciam a capacidade da arsenopirita de manter a distribuição de elementos-traço quando submetidas a altas tensões. Esse trabalho está em preparação com o título “*Insights of ore genesis and gold remobilization mechanisms in gold-bearing arsenopyrite: a case of Pilar de Goiás e Crixás greentone belts, Brazil*” e deverá ser submetido ao periódico *American Mineralogist*.

1.2 Justificativa e importância do estudo

Depósitos de metais importantes são comumente associados a múltiplos eventos mineralizantes superpostos (e.g., Frost et al. 2002; Deol et al. 2012; Masurel et al. 2017; Kerr et al. 2018; Fabricio-Silva et al. 2019), mas é frequentemente muito difícil estabelecer quais desses estágios representam a adição ou a remobilização de metal pré-existente (Hastie et al. 2020) e qual a contribuição da fonte desse elemento (Tomkins 2013; Hu et al. 2018; Fielding et al. 2019; Vigneresse et al. 2019).

Depósitos de ouro são bastante estudados pelos geólogos econômicos (Lobato et al. 2001; Meinert et al. 2005; Morey et al. 2008; Frimmel and Hennigh 2015), mas pouco se sabe sobre como esse elemento se comporta na estrutura cristalina dos sulfetos (Palenik et al. 2004; Reich et al. 2005; Williams-Jones et al. 2009; Wu et al. 2019a; Xing et al. 2019), sobretudo quando o depósito é submetido a diferentes eventos de deformação, metamorfismo, deformação e etc.

O ouro pode se concentrar em uma grande variedade de tipos de depósitos por meio de um espectro amplo de processos magmáticos, hidrotermais e físicos (e.g., Larocque et al. 1995; Hagemann et al. 1998; Meinert et al. 2005; Vigneresse et al. 2019). Na grande maioria dos depósitos de ouro, os minerais-minério mais importantes são pirita e arsenopirita (Frimmel 2008) e a natureza refratária desses minerais traz um excelente potencial para preservar evidências da história da evolução dos corpos minerais, desde a precipitação primária (e.g. depósitos tipo VMS), passando por deformação pós-deposicional e metamorfismo (Barrie et al. 2010). Estudos recentes (Fougerouse et al. 2019; Gourcerol et al. 2020) sugerem que o ouro pode formar “clusters” e migrar de dentro da estrutura cristalina para fora do cristal de sulfeto dezenas ou centenas de milhões de anos após a cristalização desses minerais.

Esse estudo inova na abordagem da metalogênese do ouro fundamentada na textura e química dos sulfetos, aplicando conceitos modernos sobre processos de cristalização e mobilidade de elementos-traço em diferentes depósitos de ouro brasileiros conhecidos. Baseando-se em resultados de concentração e mobilidade de elementos traços em sulfetos oriundos principalmente de amostras do Quadrilátero Ferrífero (MG) e do *greenstone belt* Pilar de Goiás (GO), foi possível compreender os mecanismos e medir a taxa de remobilização para entender como foi o processo de enriquecimento e geração dos depósitos de ouro estudados. Também foi possível revisitar o termo “idade de mineralização” e atentar para uma apropriada abordagem dos métodos geocronológicos aplicados à geologia econômica.

1.3 Objetivo da tese

Essa tese trata de criteriosa análise textural e composicional de sulfetos portadores de ouro. Para tanto, foi feita uma reunião possivelmente inédita dos principais mecanismos e submecanismos de cristalização e remobilização de elementos-traço, notadamente Au, em sulfetos. Esses modelos foram aplicados em amostras contendo arsenopirita e pirita de 9 depósitos de ouro brasileiros com diferentes histórias tectono-termais e diferentes fontes de fluido para entender condições de formação e transformação de corpos minerais ao longo do tempo geológico.

1.4 Depósitos de ouro estudados

A relação dos depósitos de ouro amostrados durante essa pesquisa encontra-se na Tabela 1-1. Foram estudados os depósitos Turmalina, Satinoco e São Sebastião (principal área de estudo) pertencentes ao *greenstone belt* Pitangui (NW do Quadrilátero Ferrífero, Minas Gerais); os depósitos Carvoaria Velha e Laranjeiras, pertencentes ao Lineamento Córrego do Sítio (extremo leste do Quadrilátero Ferrífero); os depósitos de Crixás e Pilar de Goiás, pertencentes aos *greenstone belts* homônimos; além dos depósitos Fazenda Nova (um *Intrusion-related* do Arco Magmático de Arenópolis – Goiás) e Poconé, no distrito Baixada Cuiabana (Mato Grosso). As amostras obtidas incluem zonas mineralizadas com ocorrência de sulfatação disseminada com sulfetos e sulfo-arsenetos.

Embora a amostragem, descrição petrográfica e química mineral tenha sido realizada para todos os depósitos supracitados, os depósitos de Poconé, Fazenda Nova e os do Lineamento Córrego do Sítio não integram publicações, em periódicos científicos, relacionadas à essa Tese de Doutorado. Outrossim, as amostras e resultados obtidos são utilizadas como comparação, sobretudo no entendimento dos mecanismos de remobilização. Os resultados obtidos em microssonda eletrônica e EBSD para esses depósitos encontram-se na seção ANEXOS.

Tabela 1-1. Relação dos depósitos de ouro estudados

Depósito	Localização	Tipo de depósito	Rochas hospedeiras
Turmalina	NW do QF – greenstone belt Pitangui	Orogênico/Intrusion-related	Metatufo e metapelitos
Satinoco	NW do QF – greenstone belt Pitangui	Orogênico/Intrusion Related	Metavulcânicas ultramáficas e máficas
São Sebastião	NW do QF – greenstone belt Pitangui	Orogênico/Mesotermal	BIF
Carvoaria Velha	E do QF – greenstone belt Rio das Velhas	Orogênico	Rochas meta-sedimentares
Laranjeiras	E do QF – greenstone belt Rio das Velhas	Orogênico	Rochas meta-sedimentares
Pilar	Greenstone belt de Pilar, Goiás	Orogênico	Rochas meta-sedimentares
Crixás	Mina III - Greenstone belt de Pilar, Goiás	Orogênico	Rochas meta-sedimentares
Poconé	Alinhamento Cangas-Poconé – Distrito da Baixada Cuiabana	Orogênico	Rochas meta-sedimentares
Fazenda Nova	Arco Magmático de Arenópolis	Intrusion-related	Granitos

1.5 Produção técnico-científica associada

Os estudos relativos ao desenvolvimento desse doutoramento resultaram em algumas publicações, apresentações e submissões (Tabela 1-2). Essas publicações incluem trabalhos e parcerias com outros grupos de pesquisa, utilizando amostras e/ou análises obtidas por este projeto de doutorado.

Dentre os trabalhos na categoria “manuscritos não submetidos”, um trabalho intitulado *“Intragrain gold mobility and its significance for the ‘timing of mineralization”* está em sua versão revisada pelos coautores. Outros dois trabalhos, nomeadamente *“How does arsenopyrite lose its primary geochemical signature? A glimpse from orogenic gold deposits in Brazil”* e *“Insights of ore genesis and gold remobilization mechanisms in gold-bearing arsenopyrite: a case of Pilar de Goiás and Crixás greentone belts, Brazil”*, se encontram em versão preliminar.

A seção ANEXOS apresenta, ainda, dados sobre química mineral, geoquímica de rocha total, geotermometria, mapas de EBSD e análises de elementos-traço por LA-ICP-MS para os outros depósitos estudados, como se segue: (i) Carvoaria Velha; (ii) Laranjeiras; (iii) depósito Fazenda Nova e; (iv) Poconé. Esses resultados serão publicados em outra oportunidade.

Tabela 1-2. Trabalhos científicos relacionados ao desenvolvimento desse doutoramento.

Tipo de trabalho	Evento/Periódico	Título	Autores	Ano
Resumo	Goldschmidt (Boston, EUA)	Tectonothermal Evolution and Multiphase Ore-Forming Processes at Turmalina Gold Deposit, Quadrilátero Ferrífero, Brazil	Fabricio-Silva, W.; Rosiere, C.A.; Giustina, M.E.S.D.; Buhm, B.	2018
Resumo	49º Congresso Brasileiro de Geologia	Evolução tectono-termal e sua relação com as fases de mineralização aurífera no depósito Turmalina, Quadrilátero Ferrífero, Minas Gerais	Fabricio-Silva, W.; Rosiere, C.A.; Giustina, M.E.S.D.; Buhm, B.	2018
Paper	Mineralium Deposita	The shear zone-related gold mineralization at the Turmalina deposit, Quadrilátero Ferrífero, Brazil: structural evolution and the two stages of mineralization	Fabricio-Silva, W.; Rosière, C.A.; Bühn, B.	2018
Resumo	Goldschmidt (Barcelona, Espanha)	Multiple Mineralization Stages and Relative Timing of Gold Distribution in the Satinoco Deposit, NW of Quadrilátero Ferrífero, Brazil	Fabricio-Silva, W.; Giustina, M.E.S.D.; Frimmel, H.; Rosiere, C.A.	2019
Resumo	Goldschmidt (Barcelona, Espanha)	The Development of a Meso- to Neoarchean Rifting-Convergence-Collision-Collapse Cycle over an Ancient Thickened Protocontinent, South São Francisco Craton, Brazil	Brando Soares, M.; Correa Neto, A.V.; Fabricio-Silva, W.	2019
Resumo	SEG Conference (Santiago, Chile)	Gold Re Concentration by High Temperature Sulfide Recrystallization Supported by Re-Os Reset Ages: A New Mineralization Style for the Quadrilátero Ferrífero Area, Brazil	Brando Soares, M.; Correa Neto, A.V.; Fabricio-Silva, W.; Alves, F.E.A.	2019
Resumo	IV Simpósio Brasileiro de Metalogenia	Archean high-temperature orogenic gold deposits: a recently recognized mineralization style in the western part of the southern São Francisco Craton	Correa Neto, A.V.; Brando Soares, M.; Fabricio-Silva, W.; Rosiere, C.A.	2019

Paper	Precambrian Research	Euxinia in the Neoarchean: The starting point for early oxygenation in a Brazilian Craton	Bosco-Santos, A.; Gilhooly, W.P.; Fouskas, F.; Fabricio-Silva, W.; Oliveira, E.P.	2020
Paper	Gondwana Research	The development of a Meso- to Neoarchean rifting-convergence-collision-collapse cycle over an ancient thickened protocontinent in the south São Francisco craton, Brazil	Brando Soares, M.; Corrêa Neto, A.V.; Fabricio-Silva, W.	2020
Resumo	50º Congresso Brasileiro de Geologia	O paradigma 'Idade de Mineralização': porque precisamos revisitar este conceito à luz da nanogeochímica?	Fabricio-Silva, W.; Schutesky, M. E.; Frimmel, H.; Rosiere, C.A.	2020
Resumo	50º Congresso Brasileiro de Geologia	Depósitos de ouro orogênico e o papel do magmatismo granítico sincrônico: contribuição com fluido mineralizante ou apenas motor termodinâmico?	Fabricio-Silva, W.; Frimmel, H.; Schutesky, M.E.; Rosiere, C.A.	2020
Paper	Economic Geology	Temperature-Controlled Ore Evolution in Orogenic Gold Systems Related to Synchronous Granitic Magmatism: An Example from The Iron Quadrangle Province, Brazil	Fabricio-Silva, W.; Frimmel, H.; Schutesky, M.E.; Rosiere, C.A.; Massucatto, A.J.	2020
Manuscrito em revisão	Geoscience Frontiers	A change in atmospheric chemistry recorded in 2.76 Ga old sediments from the São Francisco Craton	Bosco-Santos, A.; Gilhooly, W.P; De Melo-Silva, P; Fouskas, F.; Fabricio-Silva, W.; Philippot, P; Oliveira, E.P.	
Manuscrito Submetido	Geologia USP - Serie Científica	Distribuição química intragrão e seu significado para sulfetos ricos em ouro	Fabricio-Silva, W.; Schutesky, M.E.	
Manuscrito em preparação	Ore Geology Reviews ¹	Intragrain gold mobility and its significance for the "timing of mineralization"	Fabricio-Silva, W.; Schutesky, M.E.; Frimmel, H.; Fougerouse, D.; Rosiere, C.A.; Bosco-Santos, A.	
Manuscrito em preparação	Contributions to Mineralogy and Petrology ¹	How does arsenopyrite lose its primary geochemical signature? A glimpse from orogenic gold deposits in Brazil	Fabricio-Silva, W.; Schutesky, M.E.; Frimmel, H.; Barbosa, P.; Fougerouse, D.; Lagoeiro, L.; Rosiere, C.A.; Brando Soares	

Manuscrito em
preparação

American Mineralogist¹

Insights of ore genesis and gold remobilization
mechanisms in gold-bearing arsenopyrite: a
case of Pilar de Goiás and Crixás greentone
belts, Brazil

Fabricio-Silva, W.; Schutesky, M.E.;
Frimmel, H.; Barbosa, P.; Fougerouse, D.;
Lagoeiro, L.; Oliveira, C. G.

¹ Trabalhos em preparação. Periódico a ser confirmado.

1.6 Abordagem e métodos analíticos

Baseado principalmente na textura, composição e paragêneses dos sulfetos de diferentes depósitos de ouro, o trabalho contou com os seguintes estudos e técnicas analíticas:

- Mapeamento de galerias subterrâneas e *logging* de furos de sondagem diamantadas
- Petrografia macro e microscópica
- Geoquímica de rocha-total por ICP-MS;
- Microssonda eletrônica em sulfetos;
- Mapeamento composicional em escala de grão por Raio-X;
- Mapas de deformação plástica utilizando EBSD;
- Análises de elementos traços em sulfetos por LA-ICP-MS.

Outros trabalhos em parceria com a UFRJ e a Unicamp, em amostras coletadas por este autor, incluem datação U-Pb em zircão, especiação de Fe e isótopos de S, todos relacionados com a mineralização de ouro nesses depósitos. A abordagem realizada para o estudo proposto está sumarizada na Figura 1-1.

Todas as abreviações minerais deste trabalho são posteriores a Whitney e Evans (2010).

As condições e parâmetros analíticos estão expressos nos manuscritos e publicações que integram essa Tese de Doutorado.

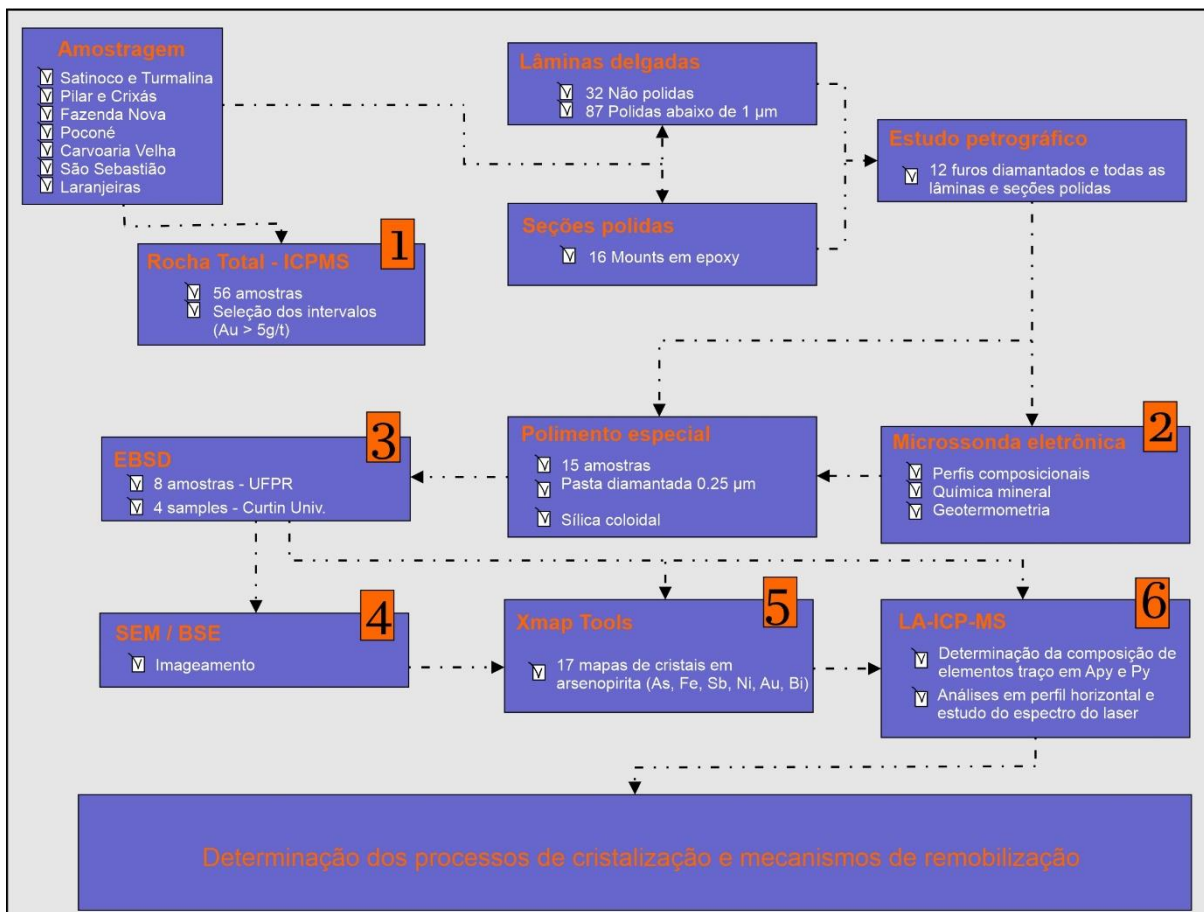


Fig. 1-1. Fluxograma da amostragem, métodos analíticos e tipos de abordagem aplicados no estudo.

1.6.1 Amostragem e geoquímica de rocha-total

Após a coleta de amostras nos depósitos de ouro, as amostras referentes aos depósitos do Quadrilátero Ferrífero foram analisadas nos laboratórios ALS em Lima (Peru). Os elementos maiores foram determinados por espectrometria ICP-AES, enquanto os elementos-traço foram determinados por ICP-MS, após fusão metaborato/tetraborato de lítio e digestão ácida. Os concentrados foram preparados a partir de amostras de 20 cm de metade dos testemunhos de sondagens de 5 cm de diâmetro. As amostras com teor de Au maior que 5 g/t foram selecionadas para laminação. Parte das análises de Rocha-Total, correspondentes aos granitoides

aflorantes nos depósitos Turmalina e Satinoco, foram cedidas e incorporadas nos trabalhos de Brando Soares et al. (2020). Os resultados são relatados em uma base anidra, recalculada para 100% do peso (ver Fabricio-Silva et al., 2020 e Brando Soares et al., 2020). Os dados inéditos e interpretações estão no ANEXO VII.

1.6.2 Microssonda Eletrônica

Após o estudo com microscópio petrográfico em seções (16) e lâminas polidas (129), as amostras selecionadas foram analisadas em Microssonda Eletrônica na Universidade de Brasília e, mais adiante, na *Würzburg Universität* (Alemanha). Os métodos e condições específicas estão descritos no Capítulo 4 (4.4 *Sampling and analytical methods*). Foram analisados sulfetos de diferentes associações em cada depósito. Os pontos de análises em microssonda foram preferencialmente dispostos em perfil, para definição de possíveis zonamentos composticionais. Os resultados analíticos representativos de cada depósito podem ser vistos no ANEXO III.

1.6.3 EBSD

Vinte e três amostras pré-selecionadas foram tratadas com polimento especial utilizando pasta diamantada ultrafina ($<0.25\text{ }\mu\text{m}$) e posteriormente com sílica coloidal. Esses procedimentos foram executados na Universidade Federal do Paraná, na *Curtin University* e na *Würzburg Universität*. Dessas amostras, 12 foram selecionadas para mapeamento intracristalino de deformação plástica por EBSD na *Curtin University* e na Universidade Federal do Paraná. A metodologia específica, o tratamento analítico e as condições dos equipamentos estão descritas no Capítulo 5

(5.4 *Methodology*). Os resultados obtidos para diferentes depósitos podem ser vistos no ANEXO V.

1.6.4 Mapas compositionais de cristais de sulfeto

Dezesete grãos de arsenopirita foram selecionados para mapeamento composicional de Raios-X para elementos como Fe, As, Co, Ni, Sb, Bi e Au. O software baseado em MatLab® (versão R2018b), XMapTools® versão 2.5.2 (Lanari et al., 2014), foi usado para gerar e tratar os mapas de raios-X. As condições e parâmetros específicos utilizados no XMapTools® podem ser consultados nos Capítulos 4 (4.4 *Sampling and analytical methods*) e 5 (5.4 *Methodology*).

1.6.5 Elementos-traço por LA-ICP-MS

Grãos de arsenopirita e pirita obtidos no mapeamento por Raios-X e selecionados após os perfis compositionais obtidos por Microssonda Eletrônica foram analisados na *University of Erlangen* para medição de concentrações de elementos-traço. Novamente, os pontos analíticos foram dispostos em perfis dentro de um mesmo grão com paragênese conhecida. Os métodos analíticos utilizados para LA-ICP-MS estão descritos no Capítulo 4 (4.4 *Sampling and analytical methods*) e 5 (5.4 *Methodology*). Os resultados representativos dos diferentes depósitos podem ser visualizados no ANEXO V e VI.

2. ZONAMENTO EM SULFETOS: PROCESSOS E CONDIÇÕES PARA DEPÓSITOS DE OURO

Wendell Fabricio-Silva^{1,2}, Maria Emilia Shutesky¹

¹ Universidade de Brasília, Instituto de Geociências, 70910-900, Brasília, Distrito Federal, Brasil (Fone: +55 61 3107 6973)

² Universität Würzburg, Bavarian Georesources Centre, Institute of Geography and Geology, Würzburg, Alemanha

* W. Fabricio-Silva – wendellsilva@aluno.unb.br (<https://orcid.org/0000-0002-5563-4866>)

* M. E. Schutesky – maria_emilia@unb.br (<https://orcid.org/0000-0001-8516-102X>)

2.1 Resumo

A composição química e as microestruturas constituem informação-chave para elucidar a evolução da mineralização relacionada às paragêneses de sulfetos ricos em Au. O zonamento composicional intracristalino pode representar: (i) processos primários ligados à cristalização e/ou; (ii) processos relacionados à remobilização. Para processos primários, alguns trabalhos recentes mostram como o zonamento químico marca tanto a interação fluido-rocha quanto a cinética de crescimento dos sulfetos. Esses fenômenos possuem diversas consequências no zonamento oscilatório do ouro. Já em termos de remobilização, as migrações intra-grão de elementos-traço na estrutura mineral dos sulfetos estão relacionadas a diversos mecanismos e sub-mecanismos, como difusão, fusão parcial e substituição mediada por fluido. Reconhecer e diferenciar o que representa o zonamento composicional passa pelo uso de técnicas analíticas com resolução espacial da ordem de nanômetros ou atômica, como NanoSIMS e *Atom Probe Tomography* (microscopia atômica). Este trabalho conceitua e reúne, de maneira inédita, os principais processos ligados ao zonamento em cristais de pirita e arsenopirita e demonstra a

importância das técnicas nanogeоquímicas para o entendimento da metalogênese do ouro.

Palavras-chave: Ouro; arsenopirita; pirita; nanopartícula; zonamento químico; remobilização.

2.2 Introdução

Sulfetos auríferos, mais notadamente pirita (FeS_2) e arsenopirita (FeAsS), estão entre os mais importantes minerais de interesse econômico da Terra, uma vez que estão relacionados às mineralizações de ouro na maioria de depósitos auríferos (Frimmel 2008). Grandes depósitos de ouro são comumente associados a múltiplos eventos mineralizantes superpostos (e.g., Masurel et al., 2017; Fabricio-Silva et al., 2019), mas é frequentemente muito difícil estabelecer se os estágios subsequentes representam a adição ou a remobilização de Au pré-existente (Hastie et al. 2020).

Além de eventos com novas adições de ouro relacionadas a processos geológicos distintos ou contínuos, a evidência de remobilização comumente apresenta um fator complicador para elucidar o modelo de mineralização em vários depósitos (Frost et al. 2002; Tooth et al. 2011; Gourcerol et al. 2018). E para entender esses processos de evolução do sistema mineral aurífero associado a sulfetos é necessário estabelecer as condições geológicas ligadas à interface cristal-fluido, bem como suas mudanças posteriores (i.e., remobilizações associadas).

Com o advento de técnicas analíticas de micro-, mas sobretudo as de nanoescala e escala atômica, tem-se dado um passo na direção de entender que existe grande, e pouco explorada, quantidade de mecanismos de cristalização, recristalização e remobilização. Essa informação tem se mostrado de fundamental importância para

compreender os processos geológicos e nos dão importante informação sobre o “*Au endowment*” (Gopon et al. 2019; Hastie et al. 2020).

Cristais de sulfeto apresentam comumente uma distribuição composicional heterogênea que representa uma distribuição areal de determinada concentração de elementos dentro do cristal. Essa distribuição pode ser oscilatória, em camadas cíclicas, setores e manchas irregulares (Wu et al. 2019a). As camadas ou zonas são da ordem de nanômetros ou micrômetros de espessura. Por meio da aplicação de técnicas sensitivas de imageamento convencionais, dezenas de minerais, formadores de rocha e acessórios, mostram zonamento químico, com destaque para silicatos, sulfetos e óxidos (Shore e Fowler, 1996). Essas técnicas convencionais, como BSE (*back-scattered electron imaging*), catodo luminescência, raios-X, EBSD (*electron back-scattered diffraction*; ou imagem de difração de elétrons retroespelhados) e outras, trouxeram grande avanço em mineralogia e geologia.

Entretanto, com o advento recente da nano geoquímica, tem sido possível entender e quantificar, sobretudo em escala nanométrica e atômica, o zonamento composicional com grande precisão. É possível observar, por exemplo, que o processo de remobilização é complexo e depende de mais variáveis do que se pensava quando (Marshall e Gilligan, 1987) postularam o “paradoxo da remobilização”, separando remobilização como dependente de escala (remobilização interna e externa). Empregando técnicas como o espectrômetro de massa de íons secundários em nano escala (*Nanoscale Secondary Ion Mass Spectrometer*; NanoSIMS), microscópio eletrônico de transmissão (*Transmission Electron Microscopy*; TEM) e a microssonda atômica (*Atom Probe Tomography*; APT), além do mapeamento composicional com LA-ICP-MS (*Laser Ablation - Inductively coupled plasma mass spectrometry*; espectrometria de massa por plasma acoplado), diversos autores (e.g., Ciobanu et al., 2010; Saintilan et al., 2017; Yan et al., 2018; Gopon et al., 2019; Stromberg et al., 2019) postularam modelos de evolução para diferentes depósitos no mundo. Como exemplo, em um modelo para o depósito de Witwatersrand na África do Sul, (Fougerouse et al. 2019)

demonstraram que o ouro foi remobilizado de dentro de grãos de pirita durante quase 1 Ga após a cristalização primária desse sulfeto (ver estudo de caso. Item 4.6).

Aqui, explora-se o significado de zonamento composicional e distribuição heterogênea, em virtude dos processos de cristalização e remobilização (mobilidade de elementos). Uma vez que esse estudo emprega técnicas analíticas modernas, poucos e recentes trabalhos abordam o tema. Neste sentido, este estudo reúne, de maneira inédita, as informações sobre os principais modelos e mecanismos de cristalização e remobilização em sulfetos e propõe uma divisão para a aplicação em depósitos de ouro.

2.3 Técnicas analíticas de alta resolução utilizadas em nanogeocquímica

As técnicas micro analíticas (em escalas mais precisas que 1 μ m) usam recursos de imagem, quantificação química e/ou variações estruturais (Pearce et al. 2018). Na escolha da técnica analítica a ser empregada, fatores como tipo de dado (e.g., químico ou estrutural), resolução espacial, limites de detecção, quantidade de elementos disponíveis, aspectos físicos (como destrutivos ou não) e valores analíticos (entre outros), devem ser sempre levados em consideração.

Inovações recentes têm feito com que a caracterização analítica chegue em escalas da ordem de nano ou atômicas. Essa escala de trabalho, aliada a baixíssimos limites de detecção, tem sido (talvez ainda informalmente) chamada de nanogeocquímica. Trabalhos que utilizam essas técnicas (como NanoSIMS e APT) são raros no Brasil, especialmente para as Geociências.

A Figura 2-1 exibe sumário com as principais técnicas analíticas de micro-, nanoescala e escala atômica, utilizadas a partir de escalas de depósitos minerais, relacionando resolução espacial com a máxima extensão da área analisada, além de exemplos gráficos de utilização dessas técnicas para arsenopirita e pirita auríferas. Mais detalhes sobre as técnicas analíticas de altíssima resolução espacial (NanoSIMS, TEM e APT) serão descritos a seguir.

2.3.1 NanoSIMS

O NanoSIMS é uma microssonda iônica comercial manufaturada pela Cameca que depois de vários anos de desenvolvimento, foi introduzido no campo da química mineral, no final dos anos 1990 (Hoppe 2006). Os dois primeiros instrumentos foram entregues à Universidade de Washington em St. Louis e ao Instituto de Química Max-Planck. No NanoSIMS, os íons secundários são produzidos por bombardeio da amostra com íons primários O⁻ ou Cs⁺. Na proximidade da amostra a óptica de íons coaxiais é comum aos íons primários e secundários, ou seja, as trajetórias de íons primários e secundários são antiparalelas. Os íons secundários são transferidos para um espectrômetro de massa de duplo foco e o layout do ímã permite raios iônicos entre 130 e 550 nm (Hoppe et al. 2013). O NanoSIMS apresenta três características fundamentais: (i) resolução lateral alta até 50 nm para íons primários Cs⁺. Esta é uma ordem de magnitude melhor do que pode ser alcançado com as microssondas de íons IMSxf; (ii) alta sensibilidade para íons secundários, cerca de 30 vezes maiores do que com o Cameca IMS3f para condições utilizadas para medições de O-isotópicas; (iii) Detecção simultânea de até seis isótopos com cinco multiplicadores de elétrons em miniatura, quatro dos quais são móveis, e um copo de Faraday que está ligado ao elétron multiplicador no raio mais baixo. Além disso, há um multiplicador de elétrons convencional no maior raio. A separação mínima de massa entre os detectores móveis é M / 30 o que significa que isótopos até a massa 30 (Si) podem ser medidos simultaneamente.

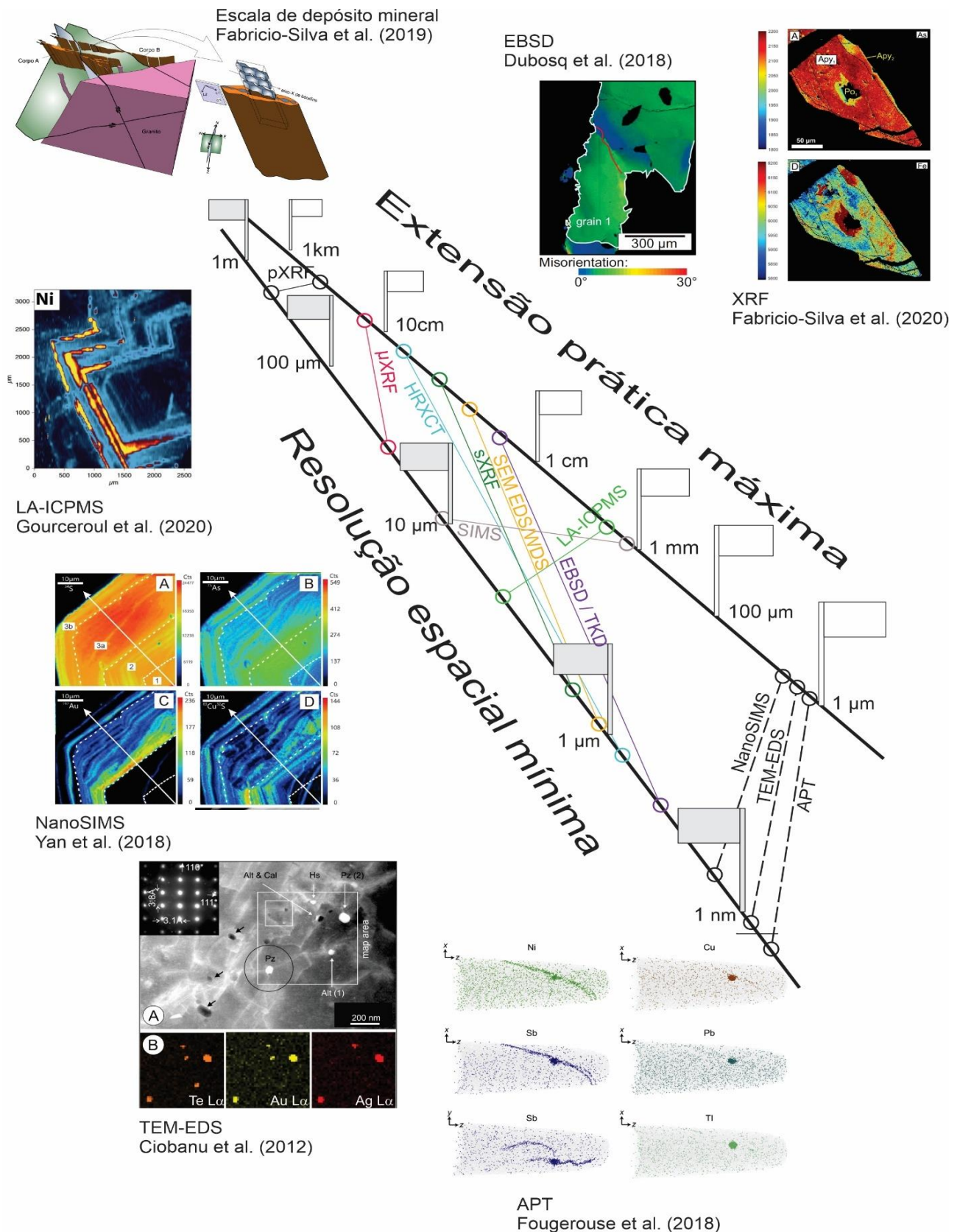


Fig. 2-1. Diagrama esquemático modificado de Pearce et al. (2018) com ênfase em técnicas analíticas mais utilizadas em nanogeоquímica. Mostra a resolução espacial

mínima em função da maior extensão aérea prática de cada técnica (linhas espessas). As linhas com cores indicam as diferentes técnicas analíticas. As linhas tracejadas indicam as técnicas de altíssima resolução espacial. As figuras no entorno do diagrama representam exemplos de trabalhos com aplicação de técnicas utilizando sulfetos (pirita e arsenopirita) em depósitos de ouro (Ciobanu et al. 2012; Dubosq et al. 2018; Yan et al. 2018; Fabricio-Silva et al. 2019; Fougerouse et al. 2019; Fabricio-Silva et al. 2020; Gourcerol et al. 2020). Abreviações: pXRF – Fluorescência de raios-X picoescala; μ XRF – Micro fluorescência de raios-X; HRXCT - Tomografia computadorizada de raio-X de alta resolução CT; sXRF – Fluorescência de raio-X sincrotron; SIMS - espectrometria de massa de íons secundários; SEM – Microscopia eletrônica; WDS – espectroscopia de raios-X dispersiva de comprimento de onda; TEM – microscopia eletrônica de transmissão; TKD – Difração de transmissão de Kikuchi.

2.3.2 TEM-EDS

O microscópio eletrônico de transmissão é uma ferramenta muito utilizada em mineralogia. Nele, um feixe de elétrons de alta energia é emitido através de uma amostra muito fina, e as interações entre os elétrons e os átomos podem ser usadas para observar características como a estrutura cristalina e características na estrutura como deslocamentos e contornos de grão (Williams e Carter, 1996). A análise química também pode ser realizada. TEM pode ser usado para estudar o crescimento de camadas, sua composição e defeitos em minerais (e.g., Ciobanu et al., 2012). O TEM opera nos mesmos princípios básicos do microscópio de luz, porém, usando elétrons. Como o comprimento de onda dos elétrons é muito menor do que o da luz, a resolução ideal atingível para imagens TEM é muitas ordens de magnitude melhor. Assim, os TEM podem revelar os detalhes mais detalhados da estrutura interna ou da trama cristalina tão pequenos quanto átomos individuais (Williams e Carter, 1996).

2.3.3 Atom Probe Tomography

A microssonda atômica (APT) é uma técnica analítica destrutiva, com recursos exclusivos para revelar o arranjo 3D e a distribuição dos elementos dentro de um pequeno volume de um material sólido (Gault 2016). Embora esta técnica tenha completado 50 anos em 2017, ela passou por uma série de revoluções: de 1D a 3D e de restrita a condutores a isoladores e semicondutores. Contudo, foi nos últimos 10 anos que rompeu uma média de 100 publicações anuais em todo o mundo (em 2015 passou de 450 incluindo todas as ciências; Gault, 2016; o que é ainda muito pouco). Os estudos atuais estão cada vez mais fazendo uso de vasta gama de técnicas de caracterização, em múltiplas escalas, com o objetivo de correlacionar informações de microscopia eletrônica e espectroscopia óptica (De Geuser et al. 2006; Rigutti et al. 2013; Herbig et al. 2015). Muito recentemente, a técnica tem sido empregada em materiais geológicos (e.g., Valley et al., 2014), permitindo relacionar a composição local à história, cristalografia, deformação e idade do mineral. A APT deriva do microscópio de íons de campo equipado com um espectrômetro de massa de tempo de voo desenvolvido por Erwin Müller e seus colegas de trabalho em 1967 a 1968 (Gault 2016).

A Figura 2-2 ilustra a construção e obtenção de dados de uma APT. A técnica usa um campo elétrico intenso, da ordem de 10^{10} Vm⁻¹, para ionizar átomos nas proximidades da superfície do espécimen. O espécimen tem o formato de uma agulha afiada, com raio de curvatura usualmente menor que 100 nm, o que permite a geração de campos elétricos de magnitude adequada, levando o espécimen para alguns quilovolts. A amostra é mantida em baixa temperatura (20 a 80 K; ou menor que -195 °C) para evitar a migração da superfície e melhorar o controle sobre o processo de evaporação do campo. Essa análise ocorre em condições de ultra alto vácuo ($\approx 10^{-8}$ Pa). Os feixes de íons gerados próximos à superfície são projetados em uma tela, sob o efeito do campo elétrico muito intenso, e a imagem formada revela a topografia da superfície do corpo de prova até o nível atômico (Müller 1956). Em experimentos com APT, nenhum gás de imagem é usado. São os átomos da

própria amostra que são removidos sucessivamente na forma de íons (Herbig et al. 2015; Gault 2016). A partida dos íons permite a identificação elementar de cada íon evaporado por espectrometria de massa de tempo de voo. O espécimen é destruído progressivamente, praticamente átomo a átomo, e o microscópio de sonda atômica coleta o tempo de voo e a posição de impacto de cada íon (Fig. 2). O processamento dos dados traduz o tempo de voo em uma razão massa-carga, e a posição é usada para construir uma imagem tomográfica atomicamente resolvida do volume evaporado (Gault, 2016; e.g., Gopon et al., 2019), representada como uma nuvem de pontos em que cada ponto é um átomo que foi identificado de forma elementar e reposicionado com alto grau de precisão (Gault 2016).

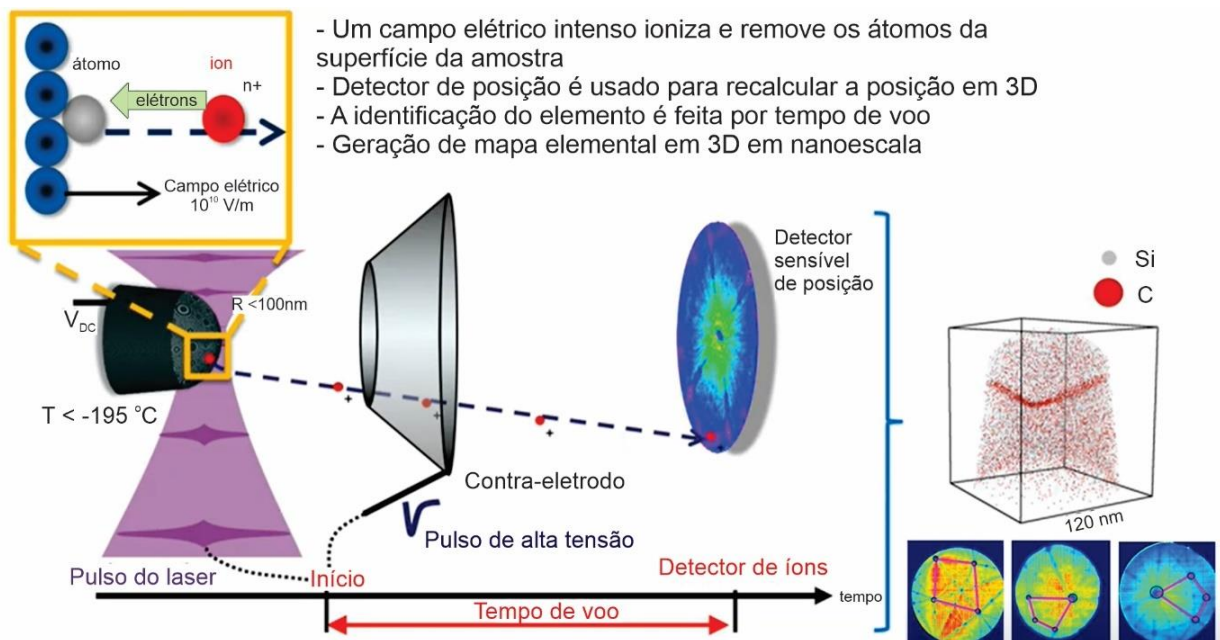


Fig. 2-2. Visão esquemática de um microscópio atômico (APT). O espécimen amostral é congelado ($T < -195^{\circ}\text{C}$), submetido a um campo de alta tensão (V_{DC}) e iluminado por pulsos de laser, desencadeando a evaporação do campo de íons, que voam através de um contra eletrodo e são coletados pelo detector sensível de posição. O detector também registra o tempo de voo, o que permite a identificação do elemento (Modificado e adaptado de Gault, 2016).

2.4 A cristalização de sulfetos na formação do zonamento

O zonamento químico em sulfetos registra dois aspectos da fase de cristalização: o grau e tipo da interação fluido-rocha; e a taxa de crescimento do cristal (Wu et al. 2019a). O ouro é incorporado nesses sulfetos como partículas (ou “clusters”) submicrônicas na forma de Au^0 e/ou como solução sólida (Au^+), presente na estrutura cristalina desses minerais (Palenik et al. 2004).

As hipóteses para a presença de zonamento primário (i.e., durante o crescimento do cristal) de ouro em pirita e arsenopirita dependem da dinâmica da interface cristal-fluido, o que determina a incorporação de elementos-traço nas fases minerais em crescimento. Fougerouse et al. (2016b) diviram as hipóteses para a concentração de nanopartículas de ouro em pirita e arsenopirita em quatro mecanismos diferentes: (i) imiscibilidade de fase durante a precipitação de sulfeto, a partir da afinidade de partículas de ouro com domínios altamente enriquecidos (Reich et al. 2005); (ii) associação de ouro com sulfeto policristalino orientado aleatoriamente, refletindo na exsolução de Au pós-cristalização durante o metamorfismo (Palenik et al. 2004). Os modelos (i) e (ii) estão fortemente ligados à solubilidade máxima do ouro em sulfetos contendo arsênio, estudados analiticamente por Palenik et al. (2004) e Reich et al. (2005). Acima do limite máximo de solubilidade, o Au excedente precipitará como nanopartículas de ouro. Ao contrário, abaixo deste limite, o Au formará solução sólida dentro da estrutura cristalina do sulfeto. A solubilidade máxima de Au em pirita e arsenopirita em solução sólida foi estimada em aproximadamente 1 e 2% em peso, respectivamente (Reich et al. 2005; Deditius et al. 2011); (iii) formação de nanopartículas de ouro e subsequente transporte em fase fluida, com a precipitação na superfície de minerais de sulfeto (Saunders 1990; Hough et al. 2011). Hough et al. (2011) analisaram amostras de ouro de depósitos supergênicos montadas em nanoplaças triangulares por TEM e demonstraram o transporte de ouro em nanopartículas coloidais, sendo este um mecanismo ativo para o transporte de ouro; (iv) modelo dependente das propriedades eletroquímicas e semicondutoras da superfície do sulfeto e da capacidade do Au de se adsorver da solução (Widler e

Seward, 2002; Mikhlin et al., 2006; Becker et al., 2007). Aqui, o Au adsorvido na superfície do mineral hospedeiro, que inicialmente se liga à matriz de sulfeto, pode se difundir e criar ligações covalentes com outros átomos de Au vindos de locais de adsorção vizinhos ou dissolvidos em solução.

Discriminar entre esses diferentes modelos tem sido difícil porque as relações espaciais e texturais entre as fases de ouro e sulfeto em nanoescala permanecem enigmáticas. A análise da estrutura de borda próxima à absorção de raios-X demonstrou que os átomos de ouro se ligam à estrutura do cristal como Au^+ ou existem como *clusters* na forma de Au^0 metálico (Genkin et al. 1998). Estudos de microscopia eletrônica de transmissão de alta resolução combinada com análise de energia dispersiva de raios-X (TEM-EDX) registraram a ocorrência, a forma bidimensional e a distribuição de nanopartículas de ouro metálico (Reich et al. 2005; Deditius et al. 2011; Ciobanu et al. 2012). No entanto, a incapacidade dos sistemas TEM-EDX mais antigos de detectar elementos-traço em baixas concentrações compromete a medição do ouro ligado à rede.

Para resolver esse problema e discriminar entre os quatro modelos supracitados, Fougerouse et al. (2016b) fizeram estudo combinado de microscopia de fluorescência de raios-X (XFM) e APT em arsenopirita para verificar a distribuição 3D de Au em nanoescala. Esses autores verificaram que o processo de distribuição de Au durante o crescimento da arsenopirita não necessita de grandes mudanças na composição química do fluido em contato com o cristal. O fator determinante, então, é que o desequilíbrio da interface fluido-mineral (que ocasiona o zonamento químico de ouro na arsenopirita) ocorre pelas diferenças na velocidade de crescimento do cristal, conforme ilustrado na Figura 2-3.

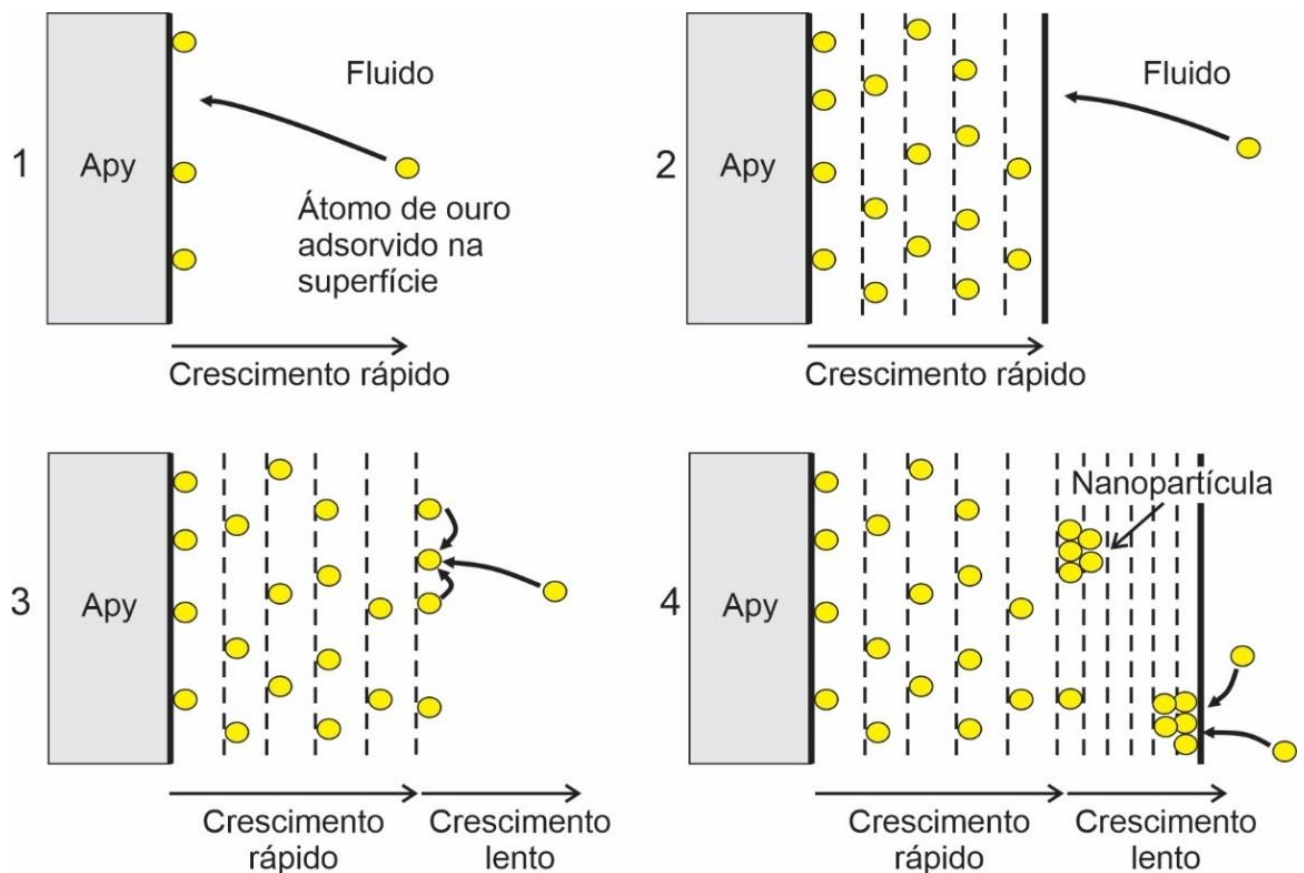


Fig. 2-3. Diagrama esquemático mostrando o efeito da taxa de crescimento do cristal de arsenopirita (Apy) e sua resposta na distribuição de Au. Crescimento rápido resulta numa maior tendência de distribuição homogênea de ouro. Crescimento lento facilita a difusão de átomos em superfícies, resultando na formação de nanopartículas de ouro. Adaptado e traduzido de Fougerouse et al. (2016b).

Complementarmente, (Wu et al. 2019a) combinaram NanoSIMS e APT para estudar o zonamento composicional de elementos-traço, notadamente Au, em pirita aurífera do Orógeno West Qinling, China. Esses autores demonstraram que múltiplos processos geológicos resultaram em diferentes domínios de zonamento químico em cristal de pirita e que essas diferenças significam diferentes mecanismos e submecanismos. Cronologicamente, esses mecanismos e submecanismos dentro de um mesmo cristal são (Figura 4 deles): (i) zona concêntrica formada como resultado da mudança da composição do fluido durante fraturamento hidráulico dinâmico; (ii) Em escala ainda menor, em domínio rico em Au, outro zonamento concêntrico foi controlado pela superfície do cristal conforme modelo supracitado de Fougerouse et al. (2016b); (iii) com a distribuição irregular de Au, As e Cu em microescala e

transições (de homogênea para heterogênea) formaram-se "ilhas" como consequência do crescimento heteroepitaxial de Stranski-Krastanov (crescimento SK; Mo et al., 1990). Esse fenômeno é baseado na incompatibilidade da rede cristalina de abarcar a precipitação de um elemento de forma homogênea em uma camada. Isso ocorreria porque a alta energia iônica da superfície concentra átomos e causa deformação e formação dessas "ilhas" irregulares (Mo et al. 1990). Esse fenômeno seria responsável pelo acúmulo de átomos de Au intercamadado, como demonstrado na figura 3; e, (iv) finalmente, o zonamento oscilatório em nanoscala de Au é interpretado como consequência de processos de auto-organização limitados por difusão na interface cristal-fluido (similares àqueles definidos por Palenik et al., 2004).

Em termos de escala, os mecanismos que explicam padrões de zonamento podem ser mais facilmente entendidos se divididos genericamente em extrínsecos, relacionados a mudanças em condições externas (i.e., nos fluidos) e intrínsecos, ligados a mudanças em nível cristalino (Wu et al. 2019a). Essa divisão favorece o entendimento do processo de acumulação de ouro em um evento geológico. Genericamente, mecanismos extrínsecos envolvem mudanças de condições nos fluidos (e.g., P, T, composição) durante a cristalização dos sulfetos (Shore e Fowler, 1996; Deditius et al., 2011), enquanto os mecanismos intrínsecos são dirigidos por efeitos cinéticos de crescimento (e.g., Fougerouse et al., 2016b) ou por efeitos de auto-organização cristalina (e.g., Putnis et al., 1992).

As diferenciações entre esses mecanismos permanecem relativamente confusas, mas (Wu et al. 2019a) observaram que zonamentos maiores, de escalas micro a milimétricas, tendem a registrar mudanças nas condições do fluido (e.g., Fowler et al., 2002). Contrariamente, zonamentos em nanoscala e escala atômica (como aquelas obtidas por APT; ver Fougerouse et al., 2019; Gopon et al., 2019) estariam muitas vezes relacionados com mecanismos intrínsecos. Adicionalmente, (Wu et al. 2019a) ainda concluem que mudanças compostionais muito bruscas em zonamentos intra-grão, mesmo no limite entre bandas menores, comumente indicam

flutuações na composição do fluido. Logo, o reconhecimento do tipo de mecanismo passa pela utilização de técnicas nanogeоquímicas de alta resolução.

Já o zonamento cíclico em escala de mícron tem ainda sido interpretado como provenientes do registro da flutuação das condições (principalmente composição) do fluido hidrotermal (Deditius et al. 2011), embora exista clara importância da cinética de crescimento (e.g., Fougerouse et al., 2016b) e da deformação cristal-plástica (e.g., Dubosq et al., 2018) para distribuição de nanopartículas. O zonamento associado à deformação plástica e recristalização está relacionado com mecanismos exclusivos de remobilização e serão vistos separadamente no item 2.5, adiante.

Mecanismos extrínsecos, como ciclos de mudanças induzidos por pressão, temperatura e composição, são inconsistentes com zonamento cristalino em setores, bandas compostionais internas ou “caminhos”, uma vez que esses mecanismos tendem a produzir zonas paralelas com a borda de crescimento do sulfeto. Os zonamentos compostionais avaliados tridimensionalmente por Wu et al. (2019) em setores e “caminhos” internos da pirita mostra a incorporação dos referidos elementos-traço particionados segundo {110} e {111} na rede da pirita. O modo de crescimento SK é consistente com manchas irregulares de Au e a transição de distribuição em escala atômica, de homogênea para heterogênea, padrão comumente observado, quando não associados a mecanismos de deformação cristal-plástica ou difusão em cristais fraturados.

2.5 Mecanismos de remobilização

A remobilização tem a capacidade de transportar e concentrar metais para formar (ou enriquecer depósitos existentes), e tem início com a transferência desses metais a partir da escala de grão. Marshall e Gilligan (1987; 1993) separaram a remobilização de metais em remobilização interna e externa. A remobilização interna

é a transferência de metais que ocorre dentro dos limites do próprio corpo mineral. O minério original muda as fases originais e/ou a distribuição interna, mas mantém sua relação espacial com a rocha encaixante. A remobilização externa resulta em mudanças de teor total e de volume dos corpos de minério originais uma vez que acontece o transporte de metais para fora dos limites do minério. Neste caso pode ocorrer a formação de novos corpos de minério ou enriquecimento dos corpos de minério existentes.

Após Marshall e Gilligan (1993), diversos trabalhos postularam mecanismos como responsáveis pela remobilização de metais (Mumin et al., 1994; Larocque et al., 1995; Tomkins et al., 2007; Fougerouse et al., 2016a; dentre outros). Na tentativa de separar os processos ligados à remobilização de elementos-traço (principalmente Au) em sulfetos, Fougerouse et al. (2016a) separam os mecanismos em três grupos: (i) difusão intra-grão; (ii) fusão parcial e; (iii) substituição mediada por fluido.

A difusão intra-grão ocorre por meio de ampla gama de sub-mecanismos, sendo os três mais importantes a difusão de volume (*volume diffusion*), difusão pelo par deslocamento-impurezas (*dislocation-impurity pair DIP*) e a difusão por caminhos de alta difusividade (*high-diffusivity pathway diffusion - HDPD*) (Reddy et al. 2007; Plümper et al. 2012). A difusão de volume é um mecanismo pelo qual os elementos agregados na trama cristalina (preferencialmente homogênea) migram lentamente por um gradiente químico potencial em temperaturas usualmente maiores que 500 °C (Vukmanovic et al. 2014). A difusão pelo DIP ocorre pela migração de deslocamentos cristalinos contendo elementos-traço (impurezas). Essas impurezas também podem formar barreiras (e “armadilhas”) desde que a energia de ativação não seja superada pela energia gerada pela deformação ou aumento de temperatura, ocorrendo a mobilidade do deslocamento (Vukmanovic et al. 2014; Dubosq et al. 2018). Já o modelo HDPD é definido como migração preferencial de elementos em bordas de grão de baixo ângulo (*low-angle grain boundaries*) (Barrie et al. 2010; Dubosq et al. 2018), também definido como tubos (*pipes*; Vukmanovic et

al. 2014). A fonte do elemento-traços pode ser nanopartículas de Au no cristal ou introdução de fluido em microfraturas.

Para a migração de elementos de raios atômicos grandes (como o ouro em sulfetos), o sub-mecanismo que melhor explica a difusão intra-grão é o HDPD e DIP (e.g., Fougerouse et al., 2016c; Dubosq et al., 2019). A deformação plástica como fator importante para a remobilização foi demonstrada por Barrie et al. (2010), Dubosq et al. (2018) e outros. Usando mapas de NanoSIMS associados a mapas de EBSD, Fougerouse et al. (2016a) observaram que a arsenopirita perde ouro da estrutura cristalina em regiões específicas da matriz de deformação, por meio de percolação de fluidos ao longo das bordas de grão recém formadas.

A fusão parcial de minérios de sulfeto é um processo comum em depósitos minerais de condições metamórficas de alto grau onde o *melt* gerado tem a capacidade de remover metais dos minerais (Tomkins et al. 2007). Esse processo pode ser favorecido pela presença de elementos calcófilos de baixo ponto de fusão (*Low Melting Point Chalcophile Elements – LMCE*) (Ciobanu et al. 2006), como Bi, Te, Sb e Hg. No modelo desses autores, quando presentes em sulfetos, os LMCEs abaixam consideravelmente o ponto de fusão e permitem que a fusão parcial possa ser eficiente na remobilização de Au e possibilitar a fusão parcial em condições de fácies xisto verde (Frost et al. 2002). Esses autores propuseram que, em sulfetos e arsenietos de Fe, a fusão parcial pode começar com temperaturas de 281 °C. Posteriormente, Tooth et al. (2011), utilizando imagens de TEM, atestaram experimentalmente essa teoria.

Por fim, reações de substituição mineral mediadas por fluidos, ou reações de dissolução-reprecipitação acoplada (*coupled dissolution-reprecipitation – CDR*; Putnis 2009), são um mecanismo bastante eficaz para modificações de elementos maiores e traços em minerais (Harlov et al. 2011; Hastie et al. 2020). Essa reação ocorre quando elementos introduzidos por fluido fazem com que uma fase mineral

seja substituída por nova composição da mesma fase ou por fase inteiramente nova (Putnis 2009; Harlov et al. 2011). Uma vez iniciada, a reação é autoperpetuante (Harlov et al. 2011) e a fase filha pode ser caracterizada por nano e micro porosidade interligadas, permitindo a infiltração de líquido para a frente de reação. Em alguns exemplos (Harlov et al. 2011), nos estágios avançados da reação a nano e micro porosidade interconectadas não são preservadas devido à completa recristalização da fase filha e à vedação da porosidade (Hastie et al. 2020).

Qualquer que seja o sub-mecanismo, como resultado da migração de elementos em sulfetos, a distribuição composicional dos elementos-traço é parcialmente ou totalmente alterada, enquanto as composições de elementos maiores permanecem inalteradas.

O transporte do ouro liberado pelos mecanismos aqui mencionados é parte integrante do processo completo de remobilização. Esse processo integrado inclui a perda de Au a partir do mineral, o transporte (milímetros ou centenas de metros) e sua precipitação em nova localidade. Existem dois modelos para transporte de Au, após a sua remoção da fonte primária: Au em solução (e.g., Williams-Jones et al. 2009; Fougerouse et al. 2016a) e Au como parte de “*melt*” poli metálico (e.g., Frost et al. 2002; Tomkins et al. 2007; Tooth et al. 2011). Existe uma série de mecanismos e sub-mecanismos para a perda (liberação/remoção) e transporte (comumente por fluidos ou material fundido, que será tratado aqui como “*melt*”) de ouro.

De maneira geral, mecanismos de remobilização e transporte relacionado ao Au em solução são mais abordados como responsáveis pela mobilidade desse elemento (Hastie et al. 2020), em que o transporte seria em complexos tendo HS⁻ e Cl⁻ como ligantes (conforme postulado por Williams-Jones et al., 2009). A deposição ou precipitação do Au (primário ou como produto de remobilização) ocorreria após a desestabilização desses complexos como resultado de “*boiling*”, reações ligadas à sulfetação, oxidação ou resfriamento (ver Williams-Jones et al., 2009).

Entretanto, o modelo de remobilização de ouro em solução encontra dois obstáculos ainda não superados (Hastie et al. 2020): (i) se o fluido modelo de liberação de ouro for o mesmo fluido do transporte (transporte em solução), o processo passa a ter que ser contínuo, o que causaria uma interação geoquímica complexa entre reações e processos; (ii) é difícil explicar as altas concentrações de ouro livre (e.g., em veios) uma vez que a solubilidade do Au em fluidos hidrotermais é muito baixa.

Em ambos os modelos teóricos (i e ii) as concentrações de Au no fluido variam entre 0.001 e 1 ppm (cf., Williams-Jones et al., 2009; Wagner et al., 2016; Fabricio-Silva et al., 2020). Hastie et al. (2020) usaram valores microtermométricos médios de inclusões fluidas em sistemas auríferos (Th_{CO_2} , salinidade, volume de CO_2) para calcular a densidade de fluido de $1 \pm 0.04 \text{ g/cm}^3$ com XCO_2 de 7 a 14. Assim, usando a densidade de fluido de 1 g/cm^3 e a máxima concentração de Au (1 ppm) em solução, 10-Moz precisa de um mínimo de 0.311 km^3 de fluido. Volumes de fluidos para depósitos com baixas concentrações de ouro (como 1 a 100 ppb; Williams-Jones et al., 2009) requereria volumes de fluido ainda muito maiores (da ordem de 3.11 a 311 km^3). É um problema de balanço de massa. Volumes de fluido dessa natureza podem ocorrer em processos de mineralização primária, principalmente em sistemas magmáticos (Phillips e Powell, 2009). Já para casos de fluidos de fonte metamórfica, de acordo com Phillips e Powell (2009), o volume de rochas “fonte” deve ser pelo menos 10 vezes maior que o volume da rocha mineralizada gerada. Todavia, é pouco provável que, para casos de remobilização, uma quantidade de fluido igualmente grande seja transportada uma segunda vez.

Um mecanismo de remobilização por fluido mais eficiente para o transporte de Au em grandes concentrações envolve o transporte como nanopartículas (ou coloides). Nesse processo uma solução rica em Au e Si se torna supersaturada, sendo transportada na forma de sílica gel amorfa com ouro suspenso (cf., Saunders, 1990). Tooth et al. (2011) defendem que fluidos hidrotermais poli metálicos com presença

de LMCE podem remover Au de mineralizações preexistentes pelo mecanismo de CDR.

De acordo com Putnis (2009), CDR é a principal reação de substituição mineral e o contato do fluido com a superfície não substituída do mineral é favorecido pelo desenvolvimento de porosidade. Baseado em Putnis (2009), Hastie et al. (2020) ilustraram essa reação contínua do fluido com o mineral substituído usando pirita (Fig. 2-4). O estágio de desenvolvimento de porosidade precede a eliminação desses poros com a nova fase mineral. Se o tempo de reação for suficientemente grande, ocorre a completa substituição do mineral, por nova fase.

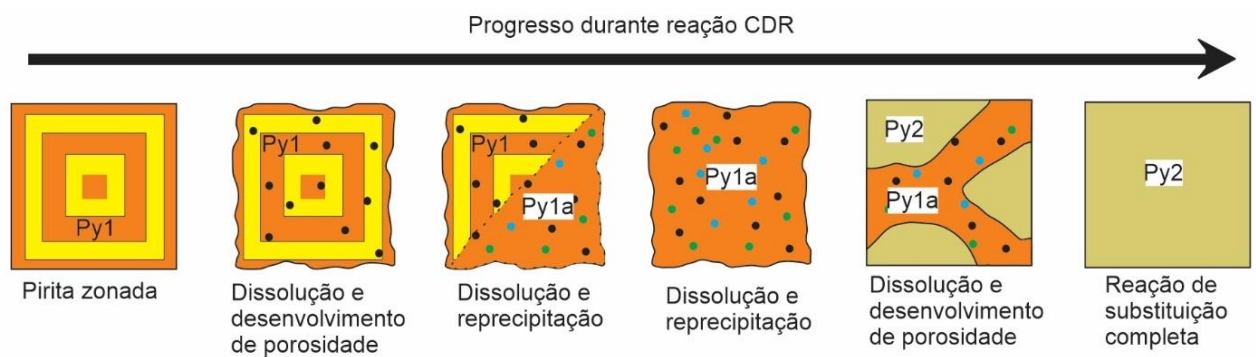


Fig. 2-4. Estágios do mecanismo de CDR para pirita (Py). Adaptado e traduzido de Hastie et al. (2020) usando conceitos de reações de substituição mineral de Putnis (2009). Os pontos coloridos representam inclusões. A fase de Py1a é híbrida entre a pirita de primeira geração (Py1) e a substituição da pirita de segunda geração (Py2).

O modelo de fusão mediada por fluido de Tooth et al. (2011) difere do modelo de fusão parcial proposto por Frost et al. (2002) e Tomkins et al. (2007) pelo fato de as reações de CDR promoverem a formação de fusão em condições de fácies xisto verde ($250^{\circ} - 400^{\circ}\text{C}$), em vez de fusão parcial sem fluido que domina em condições de fácies anfibolito e acima (i.e., $> 500^{\circ}\text{C}$). Independentemente das diferenças, cada um deles envolve *melts* polimetálicos e pode ser responsável pela abundância de ouro visível - como os de granulação grossa encontrada em muitos depósitos, Hastie et al. (2020) -, além de ouro preenchendo fraturas tardias em veios de quartzo. Os

problemas potenciais com esse mecanismo são que os minerais contendo LMCEs nem sempre estão presentes e, quando observados, nem sempre mostram texturas que indicam sincronicidade paragenética. Todos os mecanismos discutidos acima podem remobilizar Au. A questão é qual mecanismo, ou combinação de mecanismos, pode melhor explicar as características observadas em depósitos de Au de alto teor.

2.6 Recentes avanços em remobilização e suas aplicações

A importância do emprego de técnicas analíticas para nanogeoquímica no estudo de sulfetos ricos em ouro é bem retratada no trabalho de Fougerouse et al. (2019). Portanto, abordamos este trabalho utilizando APT em pirita do depósito Witwatersrand (África do Sul) como estudo de caso.

Para investigar os mecanismos de mobilidade de elementos-traço em uma pirita deformada, os autores combinaram EBSD e APT. Foi selecionado um mapa de orientação cristalográfica e ângulo de borda de grão em pirita aurífera. Em seguida, foram feitas amostragens em três pontos de borda de grão de baixo ângulo para as análises multielementares em APT.

Foi possível calcular as composições isotópicas do Pb e separá-las por planos cristalográficos na pirita. Chumbo, Sb, Ni, Tl e Cu são elementos que estão comumente trapeados em determinadas tramas cristalográficas devido a núcleos de deslocamentos (que formam anteparos à difusão de elementos traço). Esses deslocamentos preservaram a composição isotópica do Pb da pirita no momento do crescimento (~3 Ga) e mostraram que as intersecções de deslocamento, provavelmente comuns em minerais deformados, limitam a mobilidade dos elementos-traço. Em contraste, Pb, As, Ni, Co, Sb e Bi marcam um contorno de borda grão de alto ângulo que se formou logo após a cristalização por recristalização

por rotação de sub-grão. A composição isotópica de Pb dentro das bordas de grão indica a adição de Pb e outros elementos-traço, como o Au, derivado externamente e durante o metamorfismo em ~2 Ga.

Assim, esse estudo foi possibilitado pela avaliação quantitativa de elementos-traço na escala atômica e, ainda, diferenciando as concentrações dos elementos em diferentes planos cristalográficos. Os autores concluem que o ouro e outros elementos-traço migraram da parte externa do grão quase 1 Ga após a ocorrência da deformação, o que desconecta a idade da cristalização do sulfeto com episódios de mineralização. Eles ilustram que os limites de grãos podem permanecer sistemas abertos para a mobilidade de elementos-traço muito tempo após sua formação e que o entendimento da distribuição intra-grão desses elementos é de fundamental importância.

2.7 Discussões e conclusões

Os processos multi-estágios para a metalogênese do ouro têm sido considerados como responsáveis pela formação de depósitos de alto teor em muitos depósitos minerais. Esses processos são reunidos aqui de maneira inédita. Em geral, os processos ligados à cristalização somados aos processos relacionados à remobilização produzem concentrados de metais, formando (ou enriquecendo) os depósitos minerais.

O estudo do zonamento e distribuição de elementos-traço (notadamente Au) em pirita e arsenopirita guarda informações relevantes sobre os processos responsáveis pela mineralização. Os mecanismos ligados ao zonamento desses elementos são distribuídos em um amplo espectro entre primários (aqueles ligados à cristalização) e secundários (aqueles ligados a remobilização).

Em cristalização, geralmente os mecanismos têm relação com mecanismos extrínsecos (mudanças de P, T, composição, fugacidade...) ou intrínsecos (efeitos cinéticos, efeitos de estrutura da superfície do cristal, crescimento heteroepitaxial tipo SK ou auto-organização limitada por difusão). Já em remobilização na escala de grão, os mecanismos estão geralmente ligados a fusão parcial de minério de sulfeto, difusão intra-grão, ou substituição mineral por fluido. Esses mecanismos ocorrem separadamente ou em conjunto. Dos diversos mecanismos capazes de gerar minérios de elevado teor (i.e., substituição mediada por fluido, fusão parcial e difusão intra-grão), destacamos um sub-mecanismo de remobilização por fluido muito eficiente para o transporte de Au em grandes concentrações envolve o transporte como nanopartículas (ou coloides). Esse transporte ocorre como consequência de fluidos polimetálicos com presença de LMCE, que removem Au de mineralizações preexistentes pelo sub-mecanismo de CDR.

Estudos com nanogeоquímica e sulfetos se tornaram dependentes de técnicas analíticas modernas, como APT, TEM e NanoSIMS (também destaque para mapas com LA-ICPMS), em conjunto com ferramentas mais convencionais. Entendemos que esses estudos podem trazer excelentes ganhos no entendimento da evolução da mineralização e geração de minérios auríferos em depósitos brasileiros, especialmente aqueles ligados com processos multiestágios como observado nas regiões do Quadrilátero Ferrífero, Bloco Arqueano de Goiás, Carajás, dentre outras.

2.8 Agradecimentos

Este estudo foi financiado em parte pela Coordenação de Aperfeiçoamento de Pessoal de Nível Superior - Brasil (CAPES) – Código de Financiamento 001. W. Fabricio-Silva também agradece à CAPES pela bolsa PDSE (nº 88881.188398/2018-01) e todos os colegas do Departamento de Pesquisa em Geodinâmica e Geomateriais da Würzburg Universität.

2.9 Referências

- Alkmim F.F., Marshak S. 1998. Transamazonian Orogeny in the Southern São Francisco Craton Region, Minas Gerais, Brazil: Evidence for Paleoproterozoic collision and collapse in the Quadrilátero Ferrífero. Precambrian Research, **70**:29–58.
- Almeida F.F.M. 1977. O Cráton do São Francisco. Revista Brasileira de Geociências, **7**:349–364.
- Bajwah Z.U., Seccombe P.K., Offler R. 1987. Trace element distribution, Co: Ni ratios and genesis of the Big Cadia iron-copper deposit, New South Wales, Australia.

Mineralium Deposita, **22**:292–300.

- Baltazar O.F., Zucchetti M. 2007. Lithofacies associations and structural evolution of the Archean Rio das Velhas greenstone belt, Quadrilátero Ferrífero, Brazil: A review of the setting of gold deposits. *Ore Geology Reviews*, **32**:471–499.
- Barnicoat A.C., Fare R.J., Groves D.I., McNaughton N.J. 1991. Synmetamorphic lode-gold deposits in high-grade Archean settings. *Geology*, **19**:921–924.
- Barrie C.D., Boyle A.P., Cook N.J., Prior D.J. 2010. Pyrite deformation textures in the massive sulfide ore deposits of the Norwegian Caledonides. *Tectonophysics*, **483**:269–286.
- Becker U., Reich M., Utsunomiya S., Wang J., Kesler S., Wang L., Ewing R.C. 2007. Nanoparticle-host interactions in natural systems. *AGU FM*, **2007**:B31F-04.
- Berman R.G. 1991. Thermobarometry using multi-equilibrium calculations; a new technique, with petrological applications. *The Canadian Mineralogist*, **29**:833–855.
- Bierlein F.P., Reynolds N., Arne D., Bargmann C., McKeag S., Bullen W., Al-Athbah H., McKnight S., Maas R. 2016. Petrogenesis of a Neoproterozoic magmatic arc hosting porphyry Cu-Au mineralization at Jebel Ohier in the Gebeit Terrane, NE Sudan. *Ore Geology Reviews*, **79**:133–154.
- Bosco-Santos A., Gilhooly W.P., Fouskas F., Fabricio-Silva W., Oliveira E.P. 2020. Euxinia in the Neoarchean: The starting point for early oxygenation in a Brazilian Craton. *Precambrian Research*, **341**:105655.
- Brando Soares M., Corrêa Neto A.V., Zeh A., Cabral A.R., Pereira L.F., Prado M.G.B. do, Almeida A.M. de, Manduca L.G., Silva P.H.M. da, Mabub R.O. de A., Schlichta T.M. 2017. Geology of the Pitangui greenstone belt, Minas Gerais, Brazil: Stratigraphy, geochronology and BIF geochemistry. *Precambrian Research*, **291**:17–41.
- Brando Soares M., Corrêa Neto A.V., Bertolino L.C., Alves F.E.A., de Almeida A.M., Montenegro da Silva P.H., Mabub R.O. de A., Manduca L.G., Araújo I.M.C. de P. 2018. Multistage mineralization at the hypozonal São Sebastião gold deposit, Pitangui greenstone belt, Minas Gerais, Brazil. *Ore Geology Reviews*, **102**:618–

- Brando Soares M., Corrêa Neto A.V., Fabricio-Silva W. 2020. The development of a Meso- to Neoarchean rifting-convergence-collision-collapse cycle over an ancient thickened protocontinent in the south São Francisco craton, Brazil. *Gondwana Research*, **77**:40–66.
- Bühn B., Santos R. V., Dardenne M.A., de Oliveira C.G. 2012. Mass-dependent and mass-independent sulfur isotope fractionation (δ 34S and δ 33S) from Brazilian Archean and Proterozoic sulfide deposits by laser ablation multi-collector ICP-MS. *Chemical Geology*, **312–313**:163–176.
- Caddick M.J., Konopásek J., Thompson A.B. 2010. Preservation of Garnet Growth Zoning and the Duration of Prograde Metamorphism. *Journal of Petrology*, **51**:2327–2347.
- Carneiro M.A. 1992. O Complexo Metamórfico Bonfim Setentrional (Quadrilátero Ferrífero, MG): Litoestratigrafia e evolução geológica de um segmento de crosta continental do Arqueano: Universidade de São Paulo: 233 p.
- Chemale F., Rosière C.A., Endo I. 1994. The tectonic evolution of the Quadrilátero Ferrífero, Minas Gerais, Brazil. *Precambrian Research*, **65**:25–54.
- Ciobanu C.L., Cook N.J., Damian F., Damian G. 2006. Gold scavenged by bismuth melts: An example from Alpine shear-remobilizes in the Highiș Massif, Romania. *Mineralogy and Petrology*, **87**:351–384.
- Ciobanu C.L., Birch W.D., Cook N.J., Pring A., Grundler P. V 2010. Petrogenetic significance of Au–Bi–Te–S associations: the example of Maldon, Central Victorian gold province, Australia. *Lithos*, **116**:1–17.
- Ciobanu C.L., Cook N.J., Utsunomiya S., Kogagwa M., Green L., Gilbert S., Wade B. 2012. Gold-telluride nanoparticles revealed in arsenic-free pyrite. *American Mineralogist*, **97**:1515–1518.
- Cooke R.A., O'Brien P.J., Carswell D.A. 2000. Garnet zoning and the identification of equilibrium mineral compositions in high-pressure-temperature granulites from the Moldanubian Zone, Austria. *Journal of Metamorphic Geology*, **18**:551–569.

- Deditius A.P., Utsunomiya S., Reich M., Kesler S.E., Ewing R.C., Hough R., Walshe J. 2011. Trace metal nanoparticles in pyrite. *Ore Geology Reviews*, **42**:32–46.
- Deol S., Deb M., Large R.R., Gilbert S. 2012. LA-ICPMS and EPMA studies of pyrite, arsenopyrite and loellingite from the Bhukia-Jagpura gold prospect, southern Rajasthan, India: Implications for ore genesis and gold remobilization. *Chemical Geology*, **326–327**:72–87.
- Dorr J.V.N. 1969. Physiographic, stratigraphic, and structural development of the Quadrilatero Ferrífero, Minas Gerais, Brazil:, accessed at US Geological Survey - Professional Paper 614-A at <http://pubs.er.usgs.gov/publication/pp641A>.
- Dubosq R., Lawley C.J.M., Rogowitz A., Schneider D.A., Jackson S. 2018. Pyrite deformation and connections to gold mobility: Insight from micro-structural analysis and trace element mapping. *Lithos*, **310–311**:86–104.
- Dubosq R., Rogowitz A., Schweinar K., Gault B., Schneider D.A. 2019. A 2D and 3D nanostructural study of naturally deformed pyrite: assessing the links between trace element mobility and defect structures. *Contributions to Mineralogy and Petrology*, **174**:1–16.
- Fabricio-Silva W. 2016. Evolução tectono-metamórfica aplicada aos processos responsáveis pela mineralização no depósito de ouro Turmalina, Quadrilátero Ferrífero, Brasil: geologia, análise estrutural e isótopos de enxofre: Universidade Federal de Minas Gerais: 113 p.
- Fabricio-Silva W., Rosière C.A., Bühn B. 2019. The shear zone-related gold mineralization at the Turmalina deposit, Quadrilátero Ferrífero, Brazil: structural evolution and the two stages of mineralization. *Mineralium Deposita*, **54**:347–368.
- Fabricio-Silva W., Frimmel H.E., Shutesky M.E., Rosière C.A., Massucatto A.J. 2020. Temperature-controlled ore evolution in orogenic-gold systems related to synchronous granitic magmatism: An example from the Iron Quadrangle Province, Brazil. *Economic Geology*, .
- Fielding I.O.H., Johnson S.P., Meffre S., Zi J., Sheppard S., Large R.R., Rasmussen B. 2019. Linking gold mineralization to regional-scale drivers of mineral systems

using in situ U–Pb geochronology and pyrite LA-ICP-MS element mapping. *Geoscience Frontiers*, **10**:89–105.

Fougerouse D., Micklēthwaite S., Tomkins A.G., Mei Y., Kilburn M., Guagliardo P., Fisher L.A., Halfpenny A., Gee M., Paterson D., Howard D.L. 2016a. Gold remobilisation and formation of high grade ore shoots driven by dissolution-reprecipitation replacement and Ni substitution into auriferous arsenopyrite. *Geochimica et Cosmochimica Acta*, **178**:143–159.

Fougerouse D., Reddy S.M., Saxe D.W., Rickard W.D.A., Van Riessen A., Micklēthwaite S. 2016b. Nanoscale gold clusters in arsenopyrite controlled by growth rate not concentration: Evidence from atom probe microscopy. *American Mineralogist*, **101**:1916–1919.

Fougerouse D., Micklēthwaite S., Halfpenny A., Reddy S.M., Cliff J.B., Martin L.A.J., Kilburn M., Guagliardo P., Ulrich S. 2016c. The golden ark: Arsenopyrite crystal plasticity and the retention of gold through high strain and metamorphism. *Terra Nova*, **28**:181–187.

Fougerouse D., Reddy S.M., Kirkland C.L., Saxe D.W., Rickard W.D., Hough R.M. 2019. Time-resolved, defect-hosted, trace element mobility in deformed Witwatersrand pyrite. *Geoscience Frontiers*, **10**:55–63.

Fowler A., Prokoph A., Stern R., Dupuis C. 2002. Organization of oscillatory zoning in zircon: analysis, scaling, geochemistry, and model of a zircon from Kipawa, Quebec, Canada. *Geochimica et Cosmochimica Acta*, **66**:311–328.

Frimmel H.E. 2008. Earth's continental crustal gold endowment. *Earth and Planetary Science Letters*, **267**:45–55.

Frimmel H.E., Hennigh Q. 2015. First whiffs of atmospheric oxygen triggered onset of crustal gold cycle. *Mineralium Deposita*, **50**:5–23.

Frizzo C., Takai V., Scarpelli W. 1991. Auriferous mineralization at Pitangui, Minas Gerais. *Brazil Gold '91 - Ladeira*, E. A. (ed), 579–583.

Frost B.R., Mavrogenes J.A., Tomkins A.G. 2002. Partial melting of sulfide ore deposits during medium- and high-grade metamorphism. *The Canadian Mineralogist*, **40**:1–18.

- Gault B. 2016. A brief overview of atom probe tomography research. *Applied Microscopy*, **46**:117–126.
- Genkin A.D., Bortnikov N.S., Cabri L.J., Wagner F.E., Stanley C.J., Safonov Y.G., McMahon G., Friedl J., Kerzin A.L., Gamyanin G.N. 1998. A multidisciplinary study of invisible gold in arsenopyrite from four mesothermal gold deposits in Siberia, Russian Federation. *Economic Geology*, **93**:463–487.
- De Geuser F., Lefebvre W., Blavette D. 2006. 3D atom probe study of solute atoms clustering during natural ageing and pre-ageing of an Al-Mg-Si alloy. *Philosophical Magazine Letters*, **86**:227–234.
- Goldfarb R.J., Groves D.I. 2015. Orogenic gold: Common or evolving fluid and metal sources through time. *Lithos*, **233**:2–26.
- Gopon P., Douglas J.O., Auger M.A., Hansen L., Wade J., Cline J.S., Robb L.J., Moody M.P. 2019. A Nanoscale Investigation of Carlin-Type Gold Deposits: An Atom-Scale Elemental and Isotopic Perspective. *Economic Geology*, **114**:1123–1133.
- Gourcerol B., Kontak D.J., Thurston P.C., Petrus J.A. 2018. Results of LA-ICP-MS sulfide mapping from Algoma-type BIF gold systems with implications for the nature of mineralizing fluids, metal sources, and deposit models. *Mineralium Deposita*, **53**:871–894.
- Gourcerol B., Kontak D.J., Petrus J.A., Thurston P.C. 2020. Application of LA ICP-MS analysis of arsenopyrite to gold metallogeny of the Meguma Terrane, Nova Scotia, Canada. *Gondwana Research*, **81**:265–290.
- Groves D.I., Goldfarb R.J., Gebre-Mariam M., Hagemann S.G., Robert F. 1998. Orogenic gold deposits: a proposed classification in the context of their crustal distribution and relationship to other gold deposit types. *Ore Geology Reviews*, **13**:7–27.
- Groves D.I., Santosh M., Goldfarb R.J., Zhang L. 2018. Structural geometry of orogenic gold deposits: Implications for exploration of world-class and giant deposits. *Geoscience Frontiers*, **9**:1163–1177.
- Groves D.I., Santosh M., Deng J., Wang Q., Yang L., Zhang L. 2019. A holistic model

for the origin of orogenic gold deposits and its implications for exploration. *Mineralium Deposita*, 1–18.

Hagemann S.G., Brown P.E., Ridley J., Stern P., Fournelle J. 1998. Ore petrology, chemistry, and timing of electrum in the Archean hypozonal Transvaal lode gold deposit, Western Australia. *Economic Geology*, **93**:271–291.

Harlov D.E., Wirth R., Hetherington C.J. 2011. Fluid-mediated partial alteration in monazite: the role of coupled dissolution–reprecipitation in element redistribution and mass transfer. *Contributions to Mineralogy and Petrology*, **162**:329–348.

Hart C.J.R., McCoy D.T., Goldfarb R.J., Smith M., Roberts P., Hulstein R., Bakke A.A., Bundtzen T.K. 2002. Geology, exploration, and discovery in the Tintina Gold Province, Alaska and Yukon. Special Publication - Society of Economic Geologists, **9**:241–274.

Hastie E.C.G., Kontak D.J., Lafrance B. 2020. Gold Remobilization: Insights from Gold Deposits in the Archean Swayze Greenstone Belt, Abitibi Subprovince, Canada. *Economic Geology*, **115**:241–277.

Hazarika P., Mishra B., Lochan Pruseth K. 2017. Trace-element geochemistry of pyrite and arsenopyrite: ore genetic implications for late Archean orogenic gold deposits in southern India. *Mineralogical Magazine*, **81**:661–678.

Herbig M., Choi P., Raabe D. 2015. Combining structural and chemical information at the nanometer scale by correlative transmission electron microscopy and atom probe tomography. *Ultramicroscopy*, **153**:32–39.

Hofmann A.W. 1988. Chemical differentiation of the Earth: the relationship between mantle, continental crust, and oceanic crust. *Earth and Planetary Science Letters*, **90**:297–314.

Hoppe P. 2006. NanoSIMS: A new tool in cosmochemistry. *Applied Surface Science*, **252**:7102–7106.

Hoppe P., Cohen S., Meibom A. 2013. NanoSIMS: Technical Aspects and Applications in Cosmochemistry and Biological Geochemistry. *Geostandards and Geoanalytical Research*, **37**:111–154.

- Hough R.M., Noble R.R.P., Reich M. 2011. Natural gold nanoparticles. *Ore Geology Reviews*, **42**:55–61.
- Hu X., Gong Y., Zeng G., Zhang Z., Wang J., Yao S. 2018. Multistage pyrite in the Getang sediment-hosted disseminated gold deposit, southwestern Guizhou Province, China: Insights from textures and in situ chemical and sulfur isotopic analyses. *Ore Geology Reviews*, **99**:1–16.
- Jaguar Mining I. 2020. Technical report on the Turmalina mine Complex, Minas Gerais State, Brasil.:
- Kerr M.J., Hanley J.J., Kontak D.J., Morrison G.G., Petrus J., Fayek M., Zajacz Z. 2018. Evidence of upgrading of gold tenor in an orogenic quartz-carbonate vein system by late magmatic-hydrothermal fluids at the Madrid Deposit, Hope Bay Greenstone Belt, Nunavut, Canada. *Geochimica et Cosmochimica Acta*, **241**:180–218.
- Kretschmar U., Scott S.D. 1976. Phase relations involving arsenopyrite in the system Fe-As-S and their application. *The Canadian Mineralogist*, **14**:364–386.
- Lana C., Alkmim F.F., Armstrong R., Scholz R., Romano R., Nalini H.A. 2013. The ancestry and magmatic evolution of Archaean TTG rocks of the Quadrilátero Ferrífero province, southeast Brazil. *Precambrian Research*, **231**:157–173.
- Lanari P., Vidal O., De Andrade V., Dubacq B., Lewin E., Grosch E.G., Schwartz S. 2014. XMapTools: A MATLAB©-based program for electron microprobe X-ray image processing and geothermobarometry. *Computers & Geosciences*, **62**:227–240.
- Large R.R., Danyushevsky L., Hollit C., Maslennikov V., Meffre S., Gilbert S., Bull S., Scott R., Emsbo P., Thomas H., Singh B., Foster J. 2009. Gold and Trace Element Zonation in Pyrite Using a Laser Imaging Technique: Implications for the Timing of Gold in Orogenic and Carlin-Style Sediment-Hosted Deposits. *Economic Geology*, **104**:635–668.
- Larocque A.C.L., Hodgson C.J., Cabri L.J., Jackman J.A. 1995. Ion-microprobe analysis of pyrite, chalcopyrite and pyrrhotite from the Mobrun VMS deposit in northwestern Quebec; evidence for metamorphic remobilization of gold. *The*

Canadian Mineralogist, **33**:373–388.

- Lobato L.M., Ribeiro-Rodrigues L.C., Vieira F.W.R. 2001. Brazil's premier gold province. Part II: geology and genesis of gold deposits in the Archean Rio das Velhas greenstone belt, Quadrilátero Ferrífero. *Mineralium Deposita*, **36**:249–277.
- Machado N., Schrank A., Noce C.M., Gauthier G. 1996. Ages of detrital zircon from Archean-Paleoproterozoic sequences: Implications for Greenstone Belt setting and evolution of a Transamazonian foreland basin in Quadrilátero Ferrífero, southeast Brazil. *Earth and Planetary Science Letters*, **141**:259–276.
- Marinho M.S., Silva M.A., Lombello J.C., Di Salvio L.P., Silva R.N., Féboli W.L., Brito D.C. 2018. Projeto ARIM - Áreas de Relevante Interesse Mineral - Noroeste do Quadrilátero Ferrífero - Mapa Geológico Integrado do Sinclínio Pitangui. 1 mapa colorido. Escala 1:75.000. 1.
- Marshall B., Gilligan L.B. 1987. An introduction to remobilization: information from ore-body geometry and experimental considerations. *Ore Geology Reviews*, **2**:87–131.
- Marshall B., Gilligan L.B. 1993. Structural Setting and Controls on Mineral Deposits Remobilization, syn-tectonic processes and massive sulphide deposits. *Ore Geology Reviews*, **8**:39–64.
- Masurel Q., Thébaud N., Miller J., Ulrich S., Hein K.A.A., Cameron G., Béziat D., Bruguier O., Davis J.A. 2017. Sadiola Hill: A world-class carbonate-hosted gold deposit in Mali, West Africa. *Economic Geology*, **112**:23–47.
- McQueen K.G. 2005. Ore deposit types and their primary expressions. *Regolith Expression of Australian Ore Systems*: ..., 1–14.
- Meinert L.D., Dipple G.M., Nicolescu S. 2005. World Skarn Deposits. *Economic Geology 100th Anniversary Volume*.
- de Melo-Silva P., da Silva Amaral W., Oliveira E.P. 2019. Geochronological evolution of the Pitangui greenstone belt, southern São Francisco Craton, Brazil: Constraints from U-Pb zircon age, geochemistry and field relationships. *Journal of South American Earth Sciences*, .

- de Melo-Silva P., Amaral W. da S., Oliveira E.P. 2020. Geochronological evolution of the Pitangui greenstone belt, southern São Francisco Craton, Brazil: Constraints from U-Pb zircon age, geochemistry and field relationships. *Journal of South American Earth Sciences*, **99**:
- Mériaud N., Jébrak M. 2017. From intrusion-related to orogenic mineralization: The Wasamac deposit, Abitibi Greenstone Belt, Canada. *Ore Geology Reviews*, **84**:289–308.
- Mikhlin Y.L., Romanchenko A.S., Asanov I.P. 2006. Oxidation of arsenopyrite and deposition of gold on the oxidized surfaces: A scanning probe microscopy, tunneling spectroscopy and XPS study. *Geochimica et Cosmochimica Acta*, **70**:4874–4888.
- Mishra B., Pruseth K.L., Hazarika P., Chinnasamy S.S. 2018. Nature and source of the ore-forming fluids associated with orogenic gold deposits in the Dharwar Craton. *Geoscience Frontiers*, **9**:715–726.
- Mo Y.-W., Savage D.E., Swartzentruber B.S., Lagally M.G. 1990. Kinetic pathway in Stranski-Krastanov growth of Ge on Si (001). *Physical Review Letters*, **65**:1020.
- Morey A.A., Tomkins A.G., Bierlein F.P., Weinberg R.F., Davidson G.J. 2008. Bimodal distribution of gold in pyrite and arsenopyrite: Examples from the archean boorara and bardoc shear systems, Yilgarn Craton, Western Australia. *Economic Geology*, **103**:599–614.
- Müller E.W. 1956. Resolution of the atomic structure of a metal surface by the field ion microscope. *Journal of Applied Physics*, **27**:474–476.
- Mumin A.H., Fleet M.E., Chryssoulis S.L. 1994. Gold mineralization in As-rich mesothermal gold ores of the Bogosu-Prestea mining district of the Ashanti Gold Belt, Ghana: remobilization of “invisible” gold. *Mineralium Deposita*, **29**:445–460.
- Neumayr P., Cabri L.J., Groves D.I., Mikucki E.J., Jackman J.A. 1993. The mineralogical distribution of gold and relative timing of gold mineralization in two Archean settings of high metamorphic grade in Australia. *The Canadian Mineralogist*, **31**:711–725.
- Noce C.M., Tassinari C., Lobato L.M. 2007. Geochronological framework of the

- Quadrilátero Ferrífero, with emphasis on the age of gold mineralization hosted in Archean greenstone belts. *Ore Geology Reviews*, **32**:500–510.
- Oliveira E.P., McNaughton N.J., Zincone S.A., Talavera C. 2020. Birthplace of the São Francisco Craton, Brazil: Evidence from 3.60 to 3.64 Ga Gneisses of the Mairi Gneiss Complex. *Terra Nova*, **32**:281–289.
- Palenik C.S., Utsunomiya S., Reich M., Kesler S.E., Wang L., Ewing R.C. 2004. “Invisible” gold revealed: Direct imaging of gold nanoparticles in a Carlin-type deposit. *American Mineralogist*, **89**:1359–1366.
- Palme H., Jones A. 2003. Solar system abundances of the elements. *TrGeo*, **1**:711.
- Pearce M.A., Godel B.M., Fisher L.A., Schoneveld L.E., Cleverley J.S., Oliver N.H.S., Nugus M. 2018. Microscale data to macroscale processes: A review of microcharacterization applied to mineral systems. *Geological Society Special Publication*, **453**:7–39.
- Petrakakis K. 1986. Metamorphism of high-grade gneisses from the Moldanubian zone, Austria, with particular reference to the garnets. *Journal of Metamorphic Geology*, **4**:323–344.
- Phillips G.N., Powell R. 2009. Formation of gold deposits: Review and evaluation of the continuum model. *Earth-Science Reviews*, **94**:1–21.
- Phillips G.N., Powell R. 2010. Formation of gold deposits: A metamorphic devolatilization model. *Journal of Metamorphic Geology*, **28**:689–718.
- Plümper O., King H.E., Vollmer C., Ramasse Q., Jung H., Austrheim H. 2012. The legacy of crystal-plastic deformation in olivine: high-diffusivity pathways during serpentinization. *Contributions to Mineralogy and Petrology*, **163**:701–724.
- Putnis A. 2009. Mineral replacement reactions. *Reviews in mineralogy and geochemistry*, **70**:87–124.
- Putnis A., Fernandez-Diaz L., Prieto M. 1992. Experimentally produced oscillatory zoning in the (Ba, Sr) SO₄ solid solution. *Nature*, **358**:743–745.
- Reddy S.M., Timms N.E., Pantleon W., Trimby P. 2007. Quantitative characterization of plastic deformation of zircon and geological implications. *Contributions to*

Mineralogy and Petrology, **153**:625–645.

- Reich M., Kesler S.E., Utsunoyiya S., Palenik C.S., Chryssoulis S., Ewing R.C. 2005. Solubility of gold in arsenian pyrite: *Geochemica et Cosmochimica Acta*, vol. 69.
- Renger F.E., Noce C.M., Romano A.W., Machado N. 1994. Evolução Sedimentar Do Supergrupo Minas: 500 Ma. De Registro Geológico No Quadrilátero Ferrífero, Minas Gerais, Brasil. *Geonomos*, **2**:1–11.
- Ribeiro-Rodrigues L.C., de Oliveira C.G., Friedrich G. 2007. The Archean BIF-hosted Cuiabá Gold deposit, Quadrilátero Ferrífero, Minas Gerais, Brazil. *Ore Geology Reviews*, **32**:543–570.
- Rigutti L., Vella A., Vurpillot F., Gaillard A., Sevelin-Radiguet N., Houard J., Hideur A., Martel G., Jacopin G., Bugallo A.D.L. 2013. Coupling atom probe tomography and photoluminescence spectroscopy: Exploratory results and perspectives. *Ultramicroscopy*, **132**:75–80.
- Romano A.W. 1993. Parte, O Supergrupo Rio das Velhas da Faixa Mateus Leme-Pitangui - meridional do Cráton de São Francisco, MG - e seu sistema de alteração hidrotermal. *Geonomos*, **1**:16–32.
- Romano A.W. 2007. Programa Geologia do Brasil. Folha Pará de Minas, SE-23-Z-C-I. Escala 1:100.000 relatório final. UFMG-CPRM, Belo Horizonte. 74 p.
- Romano R., Lana C., Alkmim F.F., Stevens G., Armstrong R. 2013. Stabilization of the southern portion of the São Francisco craton, SE Brazil, through a long-lived period of potassic magmatism. *Precambrian Research*, **224**:143–159.
- Saintilan N.J., Stephens M.B., Spikings R., Schneider J., Chiaradia M., Spangenberg J.E., Ulianov A., Fontboté L. 2017a. Polyphase vein mineralization in the Fennoscandian Shield at Åkerlandet, Järvsand, and Laisvall along the erosional front of the Caledonian orogen, Sweden. *Mineralium Deposita*, **52**:823–844.
- Saintilan N.J., Creaser R.A., Spry P.G., Hnatyshin D. 2017b. Re-Os Systematics of löllingite and arsenopyrite in granulite-facies garnet rocks: Insights into the metamorphic history and thermal evolution of the broken hill block during the early mesoproterozoic (New South Wales, Australia). *Canadian Mineralogist*, **55**:29–44.

- Saunders J.A. 1990. Colloidal transport of gold and silica in epithermal precious-metal systems: Evidence from the Sleeper deposit, Nevada. *Geology*, **18**:757–760.
- Sharp Z.D., Essene E.J., Kelly W.C. 1985. A re-examination of the arsenopyrite geothermometer: Pressure considerations and applications to natural assemblages. *The Canadian Mineralogist*, **23**:517–534.
- Shore M., Fowler A.D. 1996. Oscillatory zoning in minerals; a common phenomenon. *The Canadian Mineralogist*, **34**:1111–1126.
- Silva G.P.A., Carneiro M.A. 2009. The metatholeiitic suite of the Rio Manso metavolcanosedimentary sequence, Iron Quadrangle (MG). *Revista da Escola de Minas de Ouro Preto*, **62**:423–430.
- Spear F.S. 1991. Temperatures in Light of Garnet Diffusion During Cooling. *Journal of Metamorphic Geology*, **9**:379–388.
- Stromberg J.M., Barr E., Van Loon L.L., Gordon R.A., Banerjee N.R. 2019. Fingerprinting multiple gold mineralization events at the Dome mine in Timmins, Ontario, Canada: Trace element and gold content of pyrite. *Ore Geology Reviews*, **104**:603–619.
- Tassinari C.C.G., Mateus A.M., Velásquez M.E., Munhá J.M.U., Lobato L.M., Bello R.M., Chiquini A.P., Campos W.F. 2015. Geochronology and thermochronology of gold mineralization in the Turmalina deposit, NE of the Quadrilátero Ferrífero Region, Brazil. *Ore Geology Reviews*, **67**:368–381.
- Teixeira W., Ávila C.A., Dussin I.A., Corrêa Neto A. V., Bongiolo E.M., Santos J.O., Barbosa N.S. 2015. A juvenile accretion episode (2.35–2.32 Ga) in the Mineiro belt and its role to the Minas accretionary orogeny: Zircon U-Pb-Hf and geochemical evidences. *Precambrian Research*, **256**:148–169.
- Thorman C.H., DeWitt E., Maron M.A., Ladeira E.A. 2001. Major brazilian gold deposits - 1982 to 1999. *Mineralium Deposita*, **36**:218–227.
- Tomkins A.G. 2013. On the source of orogenic gold. *Geology*, **41**:1255–1256.
- Tomkins A.G., Mavrogenes J.A. 2001. Redistribution of gold within arsenopyrite and

- löllingite during pro- and retrograde metamorphism: Application to timing of mineralization. *Economic Geology*, **96**:525–534.
- Tomkins A.G., Pattison D.R.M., Zaleski E. 2004. The Hemlo Gold Deposit, Ontario: An Example of Melting and Mobilization of a Precious Metal-Sulfosalt Assemblage during Amphibolite Facies Metamorphism and Deformation. *Economic Geology*, **99**:1063–1084.
- Tomkins A.G., Pattison D.R.M., Frost B.R. 2007. On the initiation of metamorphic sulfide anatexis. *Journal of Petrology*, **48**:511–535.
- Tooth B., Ciobanu C.L., Green L., O'Neill B., Brugger J. 2011. Bi-melt formation and gold scavenging from hydrothermal fluids: An experimental study. *Geochimica et Cosmochimica Acta*, **75**:5423–5443.
- Tuccillo M.E., Essene E.J., van der Pluijm B.A. 1990. Growth and retrograde zoning in garnets from high-grade, metapelites: Implications for pressure-temperature paths. *Geology*, **18**:839–842.
- Valley J.W., Cavosie A.J., Ushikubo T., Reinhard D.A., Lawrence D.F., Larson D.J., Clifton P.H., Kelly T.F., Wilde S.A., Moser D.E. 2014. Hadean age for a post-magma-ocean zircon confirmed by atom-probe tomography. *Nature Geoscience*, **7**:219–223.
- Verma S.K., Oliveira E.P., Silva P.M., Moreno J.A., Amaral W.S. 2017. Geochemistry of komatiites and basalts from the Rio das Velhas and Pitangui greenstone belts, São Francisco Craton, Brazil: Implications for the origin, evolution, and tectonic setting. *Lithos*, **284–285**:560–577.
- Vial D.S., DeWitt E., Lobato L.M., Thorman C.H. 2007. The geology of the Morro Velho gold deposit in the Archean Rio das Velhas greenstone belt, Quadrilátero Ferrífero, Brazil. *Ore Geology Reviews*, **32**:511–542.
- Vigneresse J.L., Truche L., Richard A. 2019. How do metals escape from magmas to form porphyry-type ore deposits? *Ore Geology Reviews*, **105**:310–336.
- Vukmanovic Z., Reddy S.M., Godel B., Barnes S.J., Fiorentini M.L., Barnes S.-J., Kilburn M.R. 2014. Relationship between microstructures and grain-scale trace element distribution in komatiite-hosted magmatic sulphide ores. *Lithos*, **184**:42–

- Wagner T., Fusswinkel T., Wölle M., Heinrich C.A. 2016. Microanalysis of Fluid Inclusions in Crustal Hydrothermal Systems using Laser Ablation Methods. *Elements*, **12**:323–328.
- Widler A.M., Seward T.M. 2002. The adsorption of gold (I) hydrosulphide complexes by iron sulphide surfaces. *Geochimica et Cosmochimica Acta*, **66**:383–402.
- Williams-Jones A.E., Bowell R.J., Migdisov A.A. 2009. Gold in Solution. *Elements*, **5**:281–287.
- Williams D.B., Carter C.B. 1996. *Transmission Electron Microscopy: Spectrometry*. IV. Plenum Press.
- Wu Y.F., Fougerouse D., Evans K., Reddy S.M., Saxe D.W., Guagliardo P., Li J.W. 2019a. Gold, arsenic, and copper zoning in pyrite: A record of fluid chemistry and growth kinetics. *Geology*, **47**:641–644.
- Wu Y.F., Evans K., Li J.W., Fougerouse D., Large R.R., Guagliardo P. 2019b. Metal remobilization and ore-fluid perturbation during episodic replacement of auriferous pyrite from an epizonal orogenic gold deposit. *Geochimica et Cosmochimica Acta*, **245**:98–117.
- Xing Y., Brugger J., Tomkins A., Shvarov Y. 2019. Arsenic evolution as a tool for understanding formation of pyritic gold ores. *Geology*, **47**:335–338.
- Xue Y., Campbell I., Ireland T.R., Holden P., Armstrong R. 2013. No mass-independent sulfur isotope fractionation in auriferous fluids supports a magmatic origin for Archean gold deposits. *Geology*, **41**:791–794.
- Yan J., Hu R., Liu S., Lin Y., Zhang J., Fu S. 2018. NanoSIMS element mapping and sulfur isotope analysis of Au-bearing pyrite from Lannigou Carlin-type Au deposit in SW China: New insights into the origin and evolution of Au-bearing fluids. *Ore Geology Reviews*, **92**:29–41.

3. INTRAGRAIN GOLD MOBILITY AND ITS SIGNIFICANCE FOR THE “TIMING OF MINERALIZATION”

Wendell **Fabricio-Silva**^{1,2,*}, Maria Emília **Shutesky**¹, Hartwig E. **Frimmel**^{2,3}, Carlos A. **Rosière**⁴, Denis **Fougerouse**⁵, Alice **Bosco-Santos**⁶

¹ Geosciences Institute, University of Brasília, 70910-900, Brasília, Brazil

² Bavarian Georesources Centre, Dept. of Geodynamics & Geomaterials Research, Institute of Geography and Geology, University of Würzburg, 97074, Würzburg, Germany

³ Department of Geological Sciences, University of Cape Town, 7700, Rondebosch, South Africa

⁴ Geosciences Institute, Federal University of Minas Gerais, 31270-901, Belo Horizonte, Brazil

⁵ School of Earth and Planetary Sciences, The Institute for Geoscience Research (TIGeR), Curtin University, GPO Box U1987, Perth, 6845, Australia

⁶ Department of Geology and Natural Resources, University of Campinas, 13083-855, Campinas, Brazil

* Corresponding author: e-mail, wendellfabricio@gmail.com

3.1 Abstract

The chemical composition and the microstructures are key information to clarify mineralization evolution related to gold-bearing sulfides parageneses. Compositional zoning can represent: (i) primary processes associated with crystallization and/or (ii) processes related to remobilization. For the former, some recent work shows how chemical zoning marks both the fluid-rock interaction and the growth kinetics of sulfides. These occurrences have several consequences on the oscillatory zoning of gold. For the latter, intra-grain migrations of trace elements in the sulfide mineral structure are related to several mechanisms and sub-mechanisms. Recognizing and

differentiating what compositional zoning represents requires analytical techniques such as nanometer or atomic spatial resolution. Considering variable amounts of Au remobilized, the asynchronicity between crystallization episodes and remobilization, and the unknown momentum when the remobilized volume was large enough to define a mineral deposit, we question the use of the term "timing of mineralization". We use examples of how the intracrystalline mechanisms of gold (and other metals) mobility can help to use geochronological data to understand the history of the deposit and that the age of mineralization may not be absolute or even not exist.

Keywords: Timing of mineralization; remobilization, sulfide zoning; gold

3.2 Introduction

Determining the age of ore mineralization is an active area of research because it is strategic to understand the mechanisms responsible for the formation of mineral deposits and it is used to develop exploration strategies in broader metallogenic provinces. However, studying the genesis of metallic deposits is complex, as settlement of the metal source, control of ore location and age is often equivocal. A particular challenge is related to multiple superimposed mineralizing events, commonly associated with large deposits (Frimmel 2008; Fougerouse et al. 2017). In those deposits, it is often exceedingly complex to establish which events represent significant increases in volume and concentration of the commodity. The so-called "mineralization age" assignment to any event can bring incomplete or misguided information of the metallogenetic processes.

To help overcome unknowns associated with the history of mineralization and mineralizing events, the study of sulfide minerals is a remarkable informative tool. These crystals commonly present a heterogeneous compositional distribution and record mobility of trace elements throughout the mineral deposit history. In this

context, the combination of chemical and textural screening is becoming essential. Advances in high-resolution microanalytical techniques applied to sulfide minerals (down to the atomic scale) have enabled our understanding of numerous processes such as crystallization mechanisms, recrystallization, and remobilization, providing vital information about the “endowment” (e.g., Palenik et al. 2004; Gopon et al. 2019; Hastie et al. 2020).

The heterogeneous and systematic distribution of chemical elements in a crystal determines intra-grain zoning. This distribution can be oscillatory, in cyclical bands, sectors, and as irregular stains (e.g., Cook et al. 2016; Morishita et al. 2018; Wu et al. 2019). Bands or zones of nano to micrometers thick can be the result of primary processes related to the diffusion of the elements during crystallization (Mumin et al. 1994; Fougerouse et al. 2016a; Augustin and Gaboury 2019) or remobilization/recrystallization of the sulfide (Tomkins and Mavrogenes 2001; Dubosq et al. 2018; Kerr et al. 2018).

The point of uncertainties for the age of mineralization definition is related to the variability of gold, or other commodities, concentrations throughout a deposit history. The fact is if the accumulation of a reasonable amount of metal in a specific location (to define an orebody) happened in a markable time. Here we review the mechanisms responsible for gold incorporation in sulfides and remobilization to place them in the context of using geochronological methods applied to metallogenesis. Thus, we illustrate some weaknesses and complications in the indiscriminate use of the term “timing of mineralization”.

3.3 Primary zoning

The hypotheses for the presence of primary zoning in gold-bearing sulfides depend on the dynamics of the crystal-fluid interface, which determines the incorporation of trace elements in the growing mineral phases. The mechanisms that explain zoning patterns can be broadly divided into extrinsic, related to changes in external conditions (i.e., fluids), and intrinsic, linked to changes at the crystalline scale (Wu et al. 2019). Overall, extrinsic mechanisms involve changes in tectonic stress and thermodynamic conditions (i.e., P, T, fluid composition) during sulfide crystallization (Deditius et al. 2009; Xing et al. 2019), while intrinsic mechanisms are drove by kinetic growth effects (Fougerouse et al. 2016b) or crystalline self-organization (Putnis et al. 1992).

Gold is incorporated into sulfides as nanoparticles (or "clusters") in the form of Au^0 and/or as a solid solution (Au^+) in the crystalline mineral structure (Palenik et al. 2004). The occurrence of Au nanoparticles in sulfides seems to be decisive for the formation of high-grade deposits. Several theories try to explain the presence of nanoparticles. Palenik et al. (2004) and Reich et al. (2005) presented models based on immiscibility and exsolution linked to the maximum gold solubility. In their models, the Au nanoparticles precipitation in the sulfides reflects the excess of gold concerning its maximum solubility.

Fougerouse et al. (2016b) proposed that the gold distribution process during arsenopyrite growth does not require significant changes in the chemical composition of the fluid in contact with the crystal. In this scenario, the determining factor is the imbalance of the fluid-mineral interface (which causes the chemical zoning of gold), which occurs due to differences in the crystal's growth rate. The slow growth allows the Au atoms, when adhering to the crystal surface, to group together, forming nanoparticles. Detailed thermodynamic models proposed by Xing et al. (2019) also suggested that time is fundamental regarding gold concentration in sulfides. These

models established that the high concentration of gold in hydrothermal pyrite depends on a prolonged fluid-rock interaction without the requisition of original Au-rich fluid.

Variations in composition within the same growth layer (forming micro islands or nucleation) can be explained by heteroepitaxy growth phenomena (Herman et al. 2004). This growth phenomenon is based on the incompatibility of the crystalline network to encompass the precipitation of an element homogeneously within a layer. In this case, the lattice mismatch and formation of irregular islands would result from the surface's high ionic energy concentrating atoms (Mo et al. 1990). Heteroepitaxial growth is an active process in gold-bearing pyrite and was observed by Wu et al. (2019), using atom probe tomography. Herman et al. (2004; and references therein) show that the energy is related to the surface immediately below and to the degree of lattice mismatch, which the clustering of Au atoms can explain (most favored by slow growth, Fougerouse et al. 2016b).

Other crystallization models seek to explain the formation of colloidal nanoparticles (Saunders 1990; Hough et al. 2011). The formation of nanoparticles before adhering to the growing crystal surface is presented as an active mechanism, but it is understood here as a process for transport in the fluid phase. The models that explain processes of nanoparticle transport are discussed below linked to remobilization.

3.4 Changes in metal content during remobilization

The complete remobilization process involves three stages, which can occur cyclically (Fig. 3-1): liberation, transport, and deposition. The liberation is described as a grain-scale remobilization stage, where the gold is removed and made available for transport. Once concentrated, the deposit can be enriched or depleted through

remobilization. To separate the processes related to the liberation of trace elements in sulfides, Fougerouse et al. (2016a) discriminated the mechanisms into three groups: (i) intra-grain diffusion; (ii) partial melting; and (iii) fluid-mediated replacement.

Intra-grain diffusion occurs through a wide range of sub-mechanisms, the three most important being *volume diffusion*, *dislocation-impurity pair (DIP)*, and *high-diffusivity pathway diffusion* (HDPD; Reddy et al. 2007; Plümper et al. 2012). Volume diffusion is a mechanism by which the elements aggregated in the crystalline lattice (preferably homogeneous) and migrate slowly through a potential chemical gradient at temperatures usually above 500°C (Vukmanovic et al. 2014). Diffusion by *DIP* occurs through the migration of crystalline dislocations containing trace elements (impurities). These impurities can also form traps as long as the activation energy is not overcome by the energy generated by the deformation or by increased temperature, resulting in displacement mobility (Vukmanovic et al. 2014; Dubosq et al. 2018). The HDPD model is defined as preferential migration of elements in grain boundaries (Barrie et al. 2010; Dubosq et al. 2018), also defined as pipes (Vukmanovic et al. 2014). The trace elements source can be Au nanoparticles in the crystal or fluid introduced in microfractures.

For the migration of large atomic radii elements (such as gold in sulfides), the sub-mechanisms that best explain intra-grain diffusion are HDPD and DIP (Fougerouse et al. 2016a; Dubosq et al. 2018). Plastic deformation as an important factor for remobilization was previously demonstrated, among others, by Barrie et al. (2010) and Dubosq et al. (2018). Using maps of NanoSIMS combined with EBSD ones, Fougerouse et al. (2016c) observed that arsenopyrite releases gold from the crystalline lattice in specific deformation matrix regions through the percolation of fluids along the newly formed grain boundaries.

In mineral deposits of high-grade metamorphic conditions where the melt generated can remove (and transport, see below) metals from the minerals, partial melting of sulfide ores is the most common process (Tomkins et al. 2007). This process can be favored by the presence of Low Melting Point Chalcophile Elements (LMCE, Ciobanu et al. 2006), such as Bi, Te, Sb, and Hg. Throughout this model, when present in sulfides, the LMCEs considerably decrease the melting point allowing partial melting to be efficient in gold remobilization under greenschist metamorphic facies (Frost et al. 2002). In the Fe-As-S system, partial melting can begin at 281 °C (Frost et al. 2002), as experimentally demonstrated by TEM images (Tooth et al. 2011).

Finally, fluid-mediated mineral substitution reactions, or coupled dissolution-reprecipitation reactions (CDR; Putnis 2009), are a very effective mechanism for modifying major and trace elements in minerals (Harlov et al. 2011; Hastie et al. 2020). This reaction occurs when a fluid introduces elements resulting in a mineral phase replacement by a new composition from the same phase or an entirely new phase (Putnis 2009; Harlov et al. 2011). Once initiated, the reaction is self-perpetuating, and the daughter phase can be characterized by interconnected nano and microporosity. Such interconnection allows the infiltration of liquid to the reaction front. In some examples (Harlov et al. 2011), interconnected nano and microporosity are not preserved in the advanced stages of the reaction due to the complete recrystallization of the daughter phase and porosity sealing (Hastie et al. 2020).

The transport of the gold released by the mentioned mechanisms can be divided into internal and external (Marshall and Gilligan 1987; 1993). Internal remobilization is the transfer of metals within the limits of the orebody itself. The original ore changes the original phases and/or the internal metals distribution but preserves its spatial relationship with the host rocks. External remobilization transports metals outside the ore limits changing the original total content and volume. In this case, new orebodies formation or the enrichment of existing ones may occur.

There are two models for transporting gold after removal from the primary source: as part of a polymetallic melt (e.g., Frost et al. 2002; Tomkins et al. 2007; Tooth et al. 2011); and in solution (Williams-Jones et al. 2009). Overall, the transport of the gold in solution would be in complexes having HS- and Cl- as ligands (Williams-Jones et al. 2009). Gold deposition or precipitation (primary or as a remobilization product) would occur after the destabilization of these complexes due to boiling reactions linked to sulfidation, oxidation, or cooling (Williams-Jones et al. 2009).

3.5 The age of mineralization and the other half of the history

Reviewing crystallization and grain-scale remobilization mechanisms previously described in the literature, we created a diagram (Fig. 3-1). All the mechanisms discussed here can concentrate, remobilize and re-concentrate gold. But it is often a combination of these mechanisms that best explains the features of high-grade gold deposits.

The use of the term “timing of Mineralization” with accuracy has been the subject of several debates in economic geology and mineral exploration publications. Analytical improvement headed by nanoscale techniques, as exemplified before, opens numerous limitations for the indiscriminate use of the term. As “timing of mineralization” can be understood as the accumulation/concentration of metal in processes with multiple tectonic, metamorphic, and hydrothermal events, defining it becomes not only a complex but an inaccurate process.

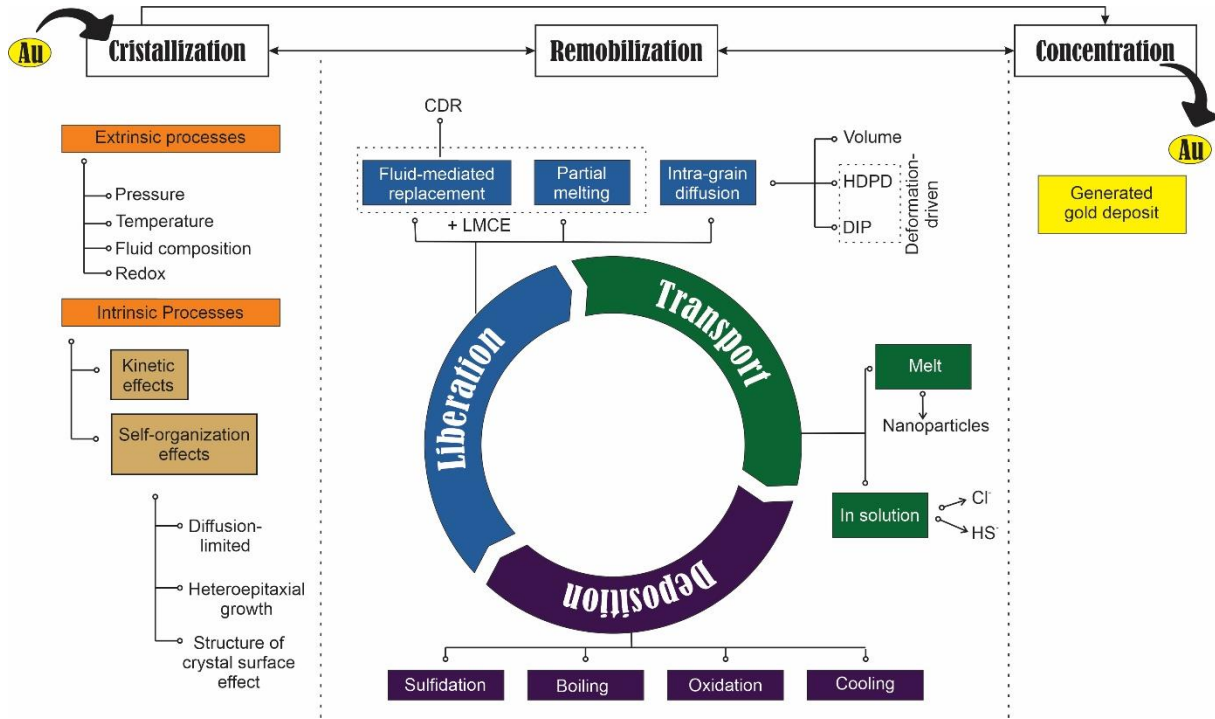


Fig. 3-1. Diagram with the set of crystallization mechanisms and remobilization as processes of generation and enrichment of gold deposits associated with sulfides. Gold-bearing sulfides crystallize by intrinsic or extrinsic processes (often a combination of both). After crystallization, the gold present in the sulfides can be remobilized through liberation, transport, and deposition, in a cyclic and usually continuous process.

A source of inaccuracy was showed with atom probe tomography data from Witwatersrand pyrite crystals (Fougerouse et al. 2019). The data indicate that part of the invisible gold has been liberated from the core and concentrated as free gold on the rims of the crystal almost 1 Ga after the sulfide crystallization. Furthermore, a later hydrothermal/metamorphic event seems to have taken part of the gold (e.g., Frimmel 2018), previously trapped in the sulfide structure, to recrystallize associated with other minerals.

Growth kinetics of gold pyrite (e.g., Wu et al. 2019; Gourcerol et al. 2020) suggest that the crystallization of sulfides can take hundreds of thousands of years, presenting another potential inaccuracy. Wu et al. (2019) combined NanoSIMS and APT to study the compositional zoning of trace elements, notably gold, in a single pyrite grain and demonstrated that its history of crystallization represents multiple

processes and mechanisms (oscillation in fluid composition, domains controlled by the crystal's surface in a slow-growth stage, SK growth, and self-organization processes limited by diffusion at the crystal-fluid interface). Whatever the mechanism and the thermodynamic conditions for the growth of the sulfide to be efficient in the capture (sequestration) of gold, a preponderant variable is “time”. Multiple hydrothermal events separated by long periods are observed in deposits from different parts of the world (e.g., Morey et al. 2008; Martins et al. 2016; Kerr et al. 2018).

Studies in the gold-orogenic deposits of the NW-Quadrilátero Ferrífero Subprovince demonstrate that the ore concentration process had components between > 2730 and ~ 2000 Ma (Brando Soares et al. 2018; Fabricio-Silva et al. 2019; 2020). This broad process is registered in changes in the crystal growth kinetics, remobilization associated with plastic deformation, partial melting mediated by late to post-tectonic granitic intrusion, intra-grain diffusion, and CDR with the entry of new fluids. In general, a sulfide paragenesis cut by apophysis of a $2694 \pm$ Ma granite (U-Pb zircon age; de Melo-Silva et al. 2020) shows evidence of remobilization and is almost completely depleted in gold (LA-ICP-MS trace elements; Fabricio-Silva et al. 2020). Post-granite sulfide assemblages suggest a new redistribution and expulsion of gold from the arsenopyrite core through partial sulfide melting (similar to Tomkins and Mavrogenes 2001). The rhenium-osmium (Re-Os) isotopic system was used for dating arsenopyrite from the newest sulfide assemblage and returned values of 1986 ± 72 Ma (Brando Soares et al. 2021). Re-Os data for the older paragenesis show a very large initial variation and indicate a Paleoproterozoic disturbance.

Several processes would be responsible for remobilization and (re) crystallization with possible transport and concentration (enrichment?) of gold in this wide range of time. In the NW-Quadrilátero Ferrífero Subprovince deposits, the definition of mineralization age loses its meaning in the face of mobility episodes and (re?) entry of gold into the mineral system. Therefore, defining a mineralization age for these

deposits, based on the momentum when the gold concentration was large enough to determine a mineral body, became difficult.

Finally, as the focus should be placed on describing the processes responsible for the mobility of gold (and the consequent concentration of the ore) over a defined geological time, we challenge the use of the term “timing of mineralization”, especially in cases of multistage mineralization. We suggest keeping using the term mineralization stage (I, II, III ...). The focus should be placed on describing the processes responsible for the mobility of gold (and the consequent concentration of the ore) over a defined geological time. Everything is about time. Not only can the crystallization process belong and go through different stages of fluid entry, but the remobilization and reconcentration of gold can be millions (or billions) of years detached from the original sulfide mineral carrier.

3.6 Considerations on the use of geochronology

In economic geology, date crystallization processes are essential. Silicates commonly associated with gold-bearing sulfides used to be dated by Rb-Sr, Sm-Nd, K-Ar, and $^{40}\text{Ar}/^{39}\text{Ar}$ methods. These chronometers are currently understated due to their higher susceptibility to chemical and thermal disturbances (Krohe and Wawrzenitz 2000) compared to U-Th-Pb and Re-Os methods. The former techniques present a particular challenge in deposits where multiple hydrothermal, magmatic, and metamorphic activity phases are observed.

U-Pb dating in situ techniques in zircon, monazite, titanite, and xenotime crystals are widely used in gold metallogenesis. The most crucial advantage of punctual mineral crystals dating is the possibility of crossing geochronology the results with observed petrographic texture (e.g., overgrowth during metamorphism episodes; Krohe and

Wawrzenitz 2000), allowing a better understanding of the processes involved. However, during solid-state recrystallization, Pb (and other trace elements) mobilization between individual crystal margins (Stein et al. 2001; Fougerouse et al. 2019) represents a method reservation. Re-Os isotopic system high closing temperature in molybdenite and rare loss or incorporation of radiogenic Os can provide reliability to this chronometer when applied to mineral deposits (Selby and Creaser, 2001). The Re-Os geochronological method can also directly date sulfides, which is very useful for discriminating metamorphic and magma-hydrothermal events when associated with other methods (e.g., U-Pb in metamorphic titanite; Stein et al. 2001).

However, many times, when dating a gold-rich sulfide crystal, mineralization is not necessarily dating. The recent recognition of Re-Os chronometer thermal disturbance in gold sulfides (~2.0 Ga, Brando Soares et al., 2021) due to the minerals partial melting and fluid-mediated replacement by CDR (Fabricio-Silva et al. 2020; Fabricio-Silva et al. *in prep*) associated with crosscutting granitic apophyses (~2.7 Ga, Fabricio-Silva et al. 2020) challenge this method. In this case, Re-Os age in sulfides represented a point-in-time for a gold remobilization event of two sulfide paragenesis, older than 2.6 Ga (Fabricio-Silva et al. 2020), in the Paleoproterozoic.

We propose that for metallogenetic purposes dating methods should always be combined with sulfide grains imaging to build reliable discrimination between crystallization, hydrothermal, magmatic, and metamorphic events.

3.7 Acknowledgments

This study was financed in part by the Coordenação de Aperfeiçoamento de Pessoal de Nível Superior - Brasil (CAPES) - Finance Code 001. W. Fabricio-Silva also thanks CAPES for PDSE (n° 88881.188398/2018-01) doctoral scholarship.

3.8 References

- Augustin J., Gaboury D. 2019. Multi-stage and multi-sourced fluid and gold in the formation of orogenic gold deposits in the world-class Mana district of Burkina Faso – Revealed by LA-ICP-MS analysis of pyrites and arsenopyrites. *Ore Geology Reviews*, **104**:495–521.
- Barrie C.D., Boyle A.P., Cook N.J., Prior D.J. 2010. Pyrite deformation textures in the massive sulfide ore deposits of the Norwegian Caledonides. *Tectonophysics*, **483**:269–286.
- Brando Soares M., Corrêa Neto A.V., Bertolino L.C., Alves F.E.A., de Almeida A.M., Montenegro da Silva P.H., Mabub R.O. de A., Manduca L.G., Araújo I.M.C. de P. 2018. Multistage mineralization at the hypozonal São Sebastião gold deposit, Pitangui greenstone belt, Minas Gerais, Brazil. *Ore Geology Reviews*, **102**:618–638.
- Ciobanu C.L., Cook N.J., Damian F., Damian G. 2006. Gold scavenged by bismuth melts: An example from Alpine shear-remobilizes in the Highiș Massif, Romania. *Mineralogy and Petrology*, **87**:351–384.
- Cook N., Ciobanu C.L., George L., Zhu Z.Y., Wade B., Ehrig K. 2016. Trace element analysis of minerals in magmatic-hydrothermal ores by laser ablation inductively-coupled plasma mass spectrometry: Approaches and opportunities. *Minerals*, **6**:
- Deditius A.P., Utsunomiya S., Ewing R.C., Chryssoulis S.L., Venter D., Kesler S.E. 2009. Decoupled geochemical behavior of As and Cu in hydrothermal systems.

Geology, **37**:707–710.

- Dubosq R., Lawley C.J.M., Rogowitz A., Schneider D.A., Jackson S. 2018. Pyrite deformation and connections to gold mobility: Insight from micro-structural analysis and trace element mapping. *Lithos*, **310–311**:86–104.
- Fabricio-Silva W., Rosière C.A., Bühn B. 2019. The shear zone-related gold mineralization at the Turmalina deposit, Quadrilátero Ferrífero, Brazil: structural evolution and the two stages of mineralization. *Mineralium Deposita*, **54**:347–368.
- Fabricio-Silva W., Frimmel H.E., Shutesky M.E., Rosière C.A., Massucatto A.J. 2020. Temperature-controlled ore evolution in orogenic-gold systems related to synchronous granitic magmatism: An example from the Iron Quadrangle Province, Brazil. *Economic Geology*, .
- Fougerouse D., Micklenthwaite S., Tomkins A.G., Mei Y., Kilburn M., Guagliardo P., Fisher L.A., Halfpenny A., Gee M., Paterson D., Howard D.L. 2016a. Gold remobilisation and formation of high grade ore shoots driven by dissolution-reprecipitation replacement and Ni substitution into auriferous arsenopyrite. *Geochimica et Cosmochimica Acta*, **178**:143–159.
- Fougerouse D., Reddy S.M., Saxy D.W., Rickard W.D.A., Van Riessen A., Micklenthwaite S. 2016b. Nanoscale gold clusters in arsenopyrite controlled by growth rate not concentration: Evidence from atom probe microscopy. *American Mineralogist*, **101**:1916–1919.
- Fougerouse D., Micklenthwaite S., Halfpenny A., Reddy S.M., Cliff J.B., Martin L.A.J., Kilburn M., Guagliardo P., Ulrich S. 2016c. The golden ark: Arsenopyrite crystal plasticity and the retention of gold through high strain and metamorphism. *Terra Nova*, **28**:181–187.
- Fougerouse D., Micklenthwaite S., Ulrich S., Miller J., Godel B., Adams D.T., McCuaig T.C. 2017. Evidence for two stages of mineralization in West Africa's largest gold deposit: Obuasi, Ghana. *Economic Geology*, **112**:3–22.
- Fougerouse D., Reddy S.M., Kirkland C.L., Saxy D.W., Rickard W.D., Hough R.M. 2019. Time-resolved, defect-hosted, trace element mobility in deformed

- Witwatersrand pyrite. *Geoscience Frontiers*, **10**:55–63.
- Frimmel H.E. 2008. Earth's continental crustal gold endowment. *Earth and Planetary Science Letters*, **267**:45–55.
- Frimmel H.E. 2018. Episodic concentration of gold to ore grade through Earth's history. *Earth-Science Reviews*, **180**:148–158.
- Frost B.R., Mavrogenes J.A., Tomkins A.G. 2002. Partial melting of sulfide ore deposits during medium- and high-grade metamorphism. *The Canadian Mineralogist*, **40**:1–18.
- Gopon P., Douglas J.O., Auger M.A., Hansen L., Wade J., Cline J.S., Robb L.J., Moody M.P. 2019. A Nanoscale Investigation of Carlin-Type Gold Deposits: An Atom-Scale Elemental and Isotopic Perspective. *Economic Geology*, **114**:1123–1133.
- Gourcerol B., Kontak D.J., Petrus J.A., Thurston P.C. 2020. Application of LA ICP-MS analysis of arsenopyrite to gold metallogeny of the Meguma Terrane, Nova Scotia, Canada. *Gondwana Research*, **81**:265–290.
- Harlov D.E., Wirth R., Hetherington C.J. 2011. Fluid-mediated partial alteration in monazite: the role of coupled dissolution–reprecipitation in element redistribution and mass transfer. *Contributions to Mineralogy and Petrology*, **162**:329–348.
- Hastie E.C.G., Kontak D.J., Lafrance B. 2020. Gold Remobilization: Insights from Gold Deposits in the Archean Swayze Greenstone Belt, Abitibi Subprovince, Canada. *Economic Geology*, **115**:241–277.
- Herman M.A., Richter W., Sitter H. 2004. Heteroepitaxy; Growth Phenomena. *Epitaxy*, 389–421.
- Hough R.M., Noble R.R.P., Reich M. 2011. Natural gold nanoparticles. *Ore Geology Reviews*, **42**:55–61.
- Kerr M.J., Hanley J.J., Kontak D.J., Morrison G.G., Petrus J., Fayek M., Zajacz Z. 2018. Evidence of upgrading of gold tenor in an orogenic quartz-carbonate vein system by late magmatic-hydrothermal fluids at the Madrid Deposit, Hope Bay Greenstone Belt, Nunavut, Canada. *Geochimica et Cosmochimica Acta*,

- Krohe A., Wawrzenitz N. 2000. Domainal variations of U–Pb monazite ages and Rb–Sr whole-rock dates in polymetamorphic paragneisses (KTB Drill Core, Germany): influence of strain and deformation mechanisms on isotope systems. *Journal of Metamorphic Geology*, **18**:271–291.
- Marshall B., Gilligan L.B. 1987. An introduction to remobilization: information from ore-body geometry and experimental considerations. *Ore Geology Reviews*, **2**:87–131.
- Marshall B., Gilligan L.B. 1993. Remobilization, syn-tectonic processes and massive sulphide deposits. *Ore Geology Reviews*, **8**:39–64.
- Martins B. de S., Lobato L.M., Rosière C.A., Hagemann S.G., Santos J.O.S., Villanova F.L. dos S.P., Figueiredo e Silva R.C., de Ávila Lemos L.H. 2016. The Archean BIF-hosted Lamego gold deposit, Rio das Velhas greenstone belt, Quadrilátero Ferrífero: Evidence for Cambrian structural modification of an Archean orogenic gold deposit. *Ore Geology Reviews*, .
- de Melo-Silva P., Amaral W. da S., Oliveira E.P. 2020. Geochronological evolution of the Pitangui greenstone belt, southern São Francisco Craton, Brazil: Constraints from U-Pb zircon age, geochemistry and field relationships. *Journal of South American Earth Sciences*, **99**:
- Mo Y.-W., Savage D.E., Swartzentruber B.S., Lagally M.G. 1990. Kinetic pathway in Stranski-Krastanov growth of Ge on Si (001). *Physical Review Letters*, **65**:1020.
- Morey A.A., Tomkins A.G., Bierlein F.P., Weinberg R.F., Davidson G.J. 2008. Bimodal distribution of gold in pyrite and arsenopyrite: Examples from the archean boorara and bardoc shear systems, Yilgarn Craton, Western Australia. *Economic Geology*, **103**:599–614.
- Morishita Y., Shimada N., Shimada K. 2018. Invisible gold in arsenian pyrite from the high-grade Hishikari gold deposit, Japan: Significance of variation and distribution of Au/As ratios in pyrite. *Ore Geology Reviews*, **95**:79–93.
- Mumin A.H., Fleet M.E., Chryssoulis S.L. 1994. Gold mineralization in As-rich mesothermal gold ores of the Bogosu-Prestea mining district of the Ashanti Gold

- Belt, Ghana: remobilization of “invisible” gold. *Mineralium Deposita*, **29**:445–460.
- Palenik C.S., Utsunomiya S., Reich M., Kesler S.E., Wang L., Ewing R.C. 2004. “Invisible” gold revealed: Direct imaging of gold nanoparticles in a Carlin-type deposit. *American Mineralogist*, **89**:1359–1366.
- Plümper O., King H.E., Vollmer C., Ramasse Q., Jung H., Austrheim H. 2012. The legacy of crystal-plastic deformation in olivine: high-diffusivity pathways during serpentinization. *Contributions to Mineralogy and Petrology*, **163**:701–724.
- Putnis A., Fernandez-Diaz L., Prieto M. 1992. Experimentally produced oscillatory zoning in the (Ba, Sr) SO₄ solid solution. *Nature*, **358**:743–745.
- Reddy S.M., Timms N.E., Pantleon W., Trimby P. 2007. Quantitative characterization of plastic deformation of zircon and geological implications. *Contributions to Mineralogy and Petrology*, **153**:625–645.
- Reich M., Kesler S.E., Utsunoyiya S., Palenik C.S., Chryssoulis S., Ewing R.C. 2005. Solubility of gold in arsenian pyrite: *Geochimica et Cosmochimica Acta*, vol. 69.
- Saunders J.A. 1990. Colloidal transport of gold and silica in epithermal precious-metal systems: Evidence from the Sleeper deposit, Nevada. *Geology*, **18**:757–760.
- Selby D., Creaser R.A. 2001. Re-Os geochronology and systematics in molybdenite from the Endako porphyry molybdenum deposit, British Columbia, Canada. *Economic Geology*, **96**:197–204.
- Stein H.J., Markey R.J., Morgan J.W., Hannah J.L., Scherstén A. 2001. The remarkable Re–Os chronometer in molybdenite: how and why it works. *Terra Nova*, **13**:479–486.
- Tomkins A.G., Mavrogenes J.A. 2001. Redistribution of gold within arsenopyrite and löllingite during pro- and retrograde metamorphism: Application to timing of mineralization. *Economic Geology*, **96**:525–534.
- Tomkins A.G., Pattison D.R.M., Frost B.R. 2007. On the initiation of metamorphic sulfide anatexis. *Journal of Petrology*, **48**:511–535.
- Tooth B., Ciobanu C.L., Green L., O’Neill B., Brugger J. 2011. Bi-melt formation and

gold scavenging from hydrothermal fluids: An experimental study. *Geochimica et Cosmochimica Acta*, **75**:5423–5443.

Vukmanovic Z., Reddy S.M., Godel B., Barnes S.J., Fiorentini M.L., Barnes S.-J., Kilburn M.R. 2014. Relationship between microstructures and grain-scale trace element distribution in komatiite-hosted magmatic sulphide ores. *Lithos*, **184**:42–61.

Williams-Jones A.E., Bowell R.J., Migdisov A.A. 2009. Gold in Solution. *Elements*, **5**:281–287.

Wu Y.F., Fougerouse D., Evans K., Reddy S.M., Saxy D.W., Guagliardo P., Li J.W. 2019. Gold, arsenic, and copper zoning in pyrite: A record of fluid chemistry and growth kinetics. *Geology*, **47**:641–644.

Xing Y., Brugger J., Tomkins A., Shvarov Y. 2019. Arsenic evolution as a tool for understanding formation of pyritic gold ores: REPLY. *Geology*, **47**:e492–e492.

4. TEMPERATURE-CONTROLLED ORE EVOLUTION IN OROGENIC-GOLD SYSTEMS RELATED TO SYNCHRONOUS GRANITIC MAGMATISM: AN EXAMPLE FROM THE IRON QUADRANGLE PROVINCE, BRAZIL

Wendell **Fabricio-Silva**^{1,2,*}, Hartwig E. **Frimmel**^{2,3}, Maria Emilia **Shutesky**¹, Carlos A. **Rosière**⁴, Armando J. **Massucatto**⁵

1 Geosciences Institute, University of Brasília, 70910-900, Brasília, Brazil

2 Bavarian Georesources Centre, Dept. of Geodynamics & Geomaterials Research, Institute of Geography and Geology, University of Würzburg, 97074, Würzburg, Germany

3 Department of Geological Sciences, University of Cape Town, 7700, Rondebosch, South Africa

4 Geosciences Institute, Federal University of Minas Gerais, 31270-901, Belo Horizonte, Brazil

5 Jaguar Mining Inc., 35960-000, Belo Horizonte, Brazil

* Corresponding author: e-mail, wendellfabricio@gmail.com

4.1 Abstract

Against the background of an ongoing debate on the genetic relationship between orogenic gold and granitic magmatism, we studied the evolution of a gold-mineralizing system in shear zone-hosted veins that are spatially associated with a syn- to late-tectonic 2.69 Ga granite at the Satinoco deposit in the Archean Pitangui greenstone belt (Iron Quadrangle, Brazil). Detailed underground mine mapping, petrography, laser ablation-inductively coupled plasma-mass spectrometry (LA-ICPMS), and elemental mapping of sulfide grains revealed a complex polyphase

history, with at least three gold-bearing stages: (*i*) A syn-tectonic arsenopyrite (Apy₁)-löllingite-pyrrhotite assemblage I that formed during prograde metamorphism from c. 475 to 650 °C at 3-4 kb; (*ii*) further fluid circulation during syn- to late-tectonic retrograde metamorphism from c. 510 to 445 °C, which led to a pyrrhotite-arsenopyrite (Apy₂) ± löllingite ± galena assemblage II; and (*iii*) a pyrite-pyrrhotite-galena ± chalcopyrite ± sphalerite ± ullmannite assemblage III formed during a later post-tectonic brittle deformation event from c. 350 to 300 °C at 1-2 kb. Ascending granitic magma acted as a heat engine for peak metamorphic temperatures locally, that is at the immediate contact, reaching as much as 730 °C and, together with the dehydration of mafic and ultramafic host rocks, generated the sulfide assemblage I. Cross-cutting field relationships, together with existing S isotope data, indicate a metamorphic origin for all the sulfide stages with a contribution from granite-derived magmatogenic fluids to the mineralizing system at stage II. New X-ray element maps together with LA-ICPMS spot analyses document oscillatory zoning of As, Fe, and Ni in Apy₁ and enrichment in Ni, Mn, Zn, and V. The large amount of pyrrhotite in assemblage II is explained by granite-related Fe-metasomatism. This stage led to an enrichment in Co, Sb, and Pb and the redistribution of Au. Assemblage III involved the formation of pyrite veins and precipitation of free gold and Pb-Sb-Cu-Zn sulfides in micro-fractures of this pyrite. This stage was likely responsible for the remobilization of Ni, Cu, Zn, and Bi-Te minerals. Based on existing geochronological data, at least most of the gold formed between ~2.72 and 2.68 Ga. This study revealed that gold mineralization took place over a wide range of temperatures – a finding that might be not only specific to the Satinoco deposit but possibly to other orogenic-type gold deposits elsewhere as well.

Keywords: Arsenopyrite – Sulfide mapping – Gold mineralization – LA-ICPMS

4.2 Introduction

Although no doubt exists about the hydrothermal nature of so-called orogenic-type gold deposits (Groves et al. 1998), the source of the mineralizing fluids as well as that of the metals transported by them remains enigmatic (e.g., Phillips and Powell, 2009). The prevailing view is that metamorphic rocks are the source of the gold-mineralizing fluids (Phillips and Powell 2010; Tomkins 2013), but other authors (e.g., Xue et al., 2013; Kerr et al., 2018) have suggested that the Au-rich fluid could be magmatic in origin. However, even in deposits in which magmatogenic hydrothermal fluids may have contributed to the mineralization, the spatial, temporal and genetic relationship between intruding magma and orebodies remains uncertain (Groves et al. 2019). In this regard, deposits with a clear spatial association to intrusive bodies are the ideal targets for testing the genetic relationship between gold-mineralizing fluids and magmatism. A prime example of such a target is the Pitangui gold district in Brazil, which is located in an orogenic terrane that hosts gold-bearing sulfide deposits with a polyphase history.

Sulfide chemistry has been used as an effective proxy for monitoring hydrothermal fluid composition in order to better understand the mineralization history in many gold deposits (e.g. Hazarika et al., 2017; Saintilan et al., 2017; Yan et al., 2018; Stromberg et al., 2019). The distribution of trace elements, such as gold, in sulfides records changes in the fluid chemistry across a wide range of temperatures (Large et al. 2009), from as low as 300 °C (Frost et al. 2002; Ciobanu et al. 2006), through to moderate temperatures at upper greenschist and lower amphibolite-facies conditions (Frost et al., 2002; Hazarika et al., 2017), and high temperatures (> 600 °C; Neumayr et al., 1993; Fabricio-Silva et al., 2019). Reconstructing the history of mineralizing fluids is not an easy task, as a number of mechanisms (such as partial melting, fluid-mediated replacement, and intra-grain diffusion) can affect the primary distribution of elements in sulfides during deformation (Fougerouse et al. 2016c) and metamorphism (Tomkins et al. 2004).

In the southern São Francisco Craton (Fig. 4-1A), the Iron Quadrangle Province (known as Quadrilátero Ferrífero) contains one of the largest Fe and Au metallogenic provinces in the world (Thorman et al. 2001). The Iron Quadrangle hosts numerous orogenic gold deposits, including the giant Morro Velho deposit, which is, with a cumulative gold production of about 470 t (Vial et al., 2007), the largest gold deposit in Brazil (Lobato et al. 2001). These deposits are structurally controlled and the ore therein occur as (*i*) disseminated sulfides associated with hydrothermal alteration along shear zones, and (*ii*) gold-bearing veins composed of quartz, carbonate, and sulfides in mafic, ultramafic, felsic volcanic, and clastic sedimentary rocks (Lobato et al. 2001; Ribeiro-Rodrigues et al. 2007). The deposits of the Iron Quadrangle are similar to others in Archean cratons worldwide, being hosted by greenschist- to amphibolite-facies greenstone belts (Lobato et al. 2001; Vial et al. 2007) (Lobato et al., 2001; Vial et al., 2007). The most common host rocks are oxide- and carbonate-banded iron formation (e.g., the world-class Cuiabá gold deposit) and quartz–dolomite to quartz–ankerite rocks (e.g., world-class Morro Velho gold deposit). Most of the other gold deposits are hosted by metabasalt.

The Satinoco (also known locally as “Corpo C”) gold deposit (total resource estimated at 1591 t Au, at an average grade of 4.31 g/t Au; Jaguar Mining Inc, 2020) is located within the Pitangui greenstone belt (northwestern Iron Quadrangle), which comprises a set of intensely deformed and hydrothermally overprinted rocks, correlated to the Rio das Velhas greenstone belt (Romano 2007; Brando Soares et al. 2017; Brando Soares et al. 2020). The Satinoco ore shoots are strongly enriched in sulfides, occupying as much as 10 vol %. Although the sulfide mineralogy in the gold deposits of the Pitangui ore district has been described before (Frizzo et al. 1991; Brando Soares et al. 2018; Fabricio-Silva et al. 2019), the paragenetic sequence still remains controversial. Due to its complex ore mineralogy and an intimate spatial relationship between the orebodies and high-K granite bodies, the Satinoco deposit was chosen to test the genetic relationship between hydrothermal orogenic gold deposition and granitic magmatism. To this effect, sulfide texture and

mineral composition and zonation were determined to characterize the hydrothermal phases and their genetic affiliation. It will be shown that the deposit records a complex evolution with a multi-stage gold-bearing sulfide (re-) crystallization related to the thermo-structural evolution. Our study supports the importance of multiple fluid sources and a magmatic heat source for the formation of at least some orogenic-type gold deposits, such as Satinoco.

4.3 Geological setting

4.3.1 Iron Quadrangle area

The southern São Francisco Craton (Fig. 4-1A) is composed of a Meso- to Neoarchean trondhjemite-tonalite-granodiorite (TTG) basement (Dorr 1969; Lana et al. 2013) covered by Neoarchean metavolcano-sedimentary units, exposed in the Rio das Velhas, Pitangui and Rio Manso greenstone belts (Dorr 1969; Baltazar and Zucchetti 2007; Silva and Carneiro 2009; Brando Soares et al. 2017). These are unconformably overlain by metasedimentary rocks of the Paleo- to Mesoproterozoic Minas and Espinhaço supergroups (Renger et al. 1994; Alkmim and Marshak 1998), and Neoproterozoic carbonate-siliciclastic rocks of the Bambuí Group (Almeida 1977). Several Neoarchean TTG to potassic granitoid bodies were emplaced along the contact between the greenstone belts and the TTG blocks (Romano 2007; Romano et al. 2013; Teixeira et al. 2015; Brando Soares et al. 2020).

The rocks in the southern São Francisco Craton record three orogenic events: (*i*) the 2750-2670 Ma Rio das Velhas orogeny (Carneiro 1992; Baltazar and Zucchetti 2007); (*ii*) Paleoproterozoic deformation at ca. 2100 Ma with mostly southeast-directed strain markers (Alkmim and Marshak 1998; Teixeira et al. 2015); and (*iii*) the Neoproterozoic Brasiliano Pan-African orogeny from 650 to 0.50 Ga, evident only

in the eastern portion of the São Francisco Craton (Chemale et al. 1994; Alkmim and Marshak 1998).

Recently the Pitangui greenstone belt (Fig. 4-1B), which forms a NW-trending synclinorium, was recognized to represent a distinct rock succession, separate from the well-known Rio das Velhas greenstone belt (Brando Soares et al. 2020). Its stratigraphy has been divided by Marinho et al. (2018) into the basal Pitangui Group and the overlying Antimes Formation. The Pitangui Group consists of three formations, from bottom to top: (*i*) the Rio Pará Formation, a succession of komatiite to tholeiitic metabasalt, interbedded with metapelites and metatuffs; (*ii*) the Rio São João Formation, composed of rhythmites interbedded with quartzite, metabasalt and banded iron formation (BIF); and (*iii*) the Onça do Pitangui Formation, consisting of phyllite, black shale, arkose and intercalations of metaconglomerate, metachert and BIF. The geology and geochemistry of the mafic magmatism in the Pitangui greenstone belt reveal an E-MORB to N-MORB signature with a back-arc affinity (Verma et al. 2017; Brando Soares et al. 2020; de Melo-Silva et al. 2020). The Pitangui Group dominates the regional geology and, based on lithostratigraphic correlations, the rocks therein are equivalent to those of the Nova Lima Group in the Rio das Velhas greenstone belt (Romano 2007; Brando Soares et al. 2017; Fabricio-Silva et al. 2019). The Antimes Formation is composed mainly of fine to coarse-grained quartzites, metaconglomerates, and interbedded metapelites.

The Pitangui greenstone belt is surrounded by the Divinópolis and Belo Horizonte complexes (Fig. 4-1A), which represent the TTG terrane in the continental crust of the São Francisco Craton (Machado et al. 1996; Noce et al. 2007; Brando Soares et al. 2020). The TTG-greenstone terranes were intruded by late- to post-tectonic granitic magmas (Renger et al. 1994; Alkmim and Marshak 1998; Noce et al. 2007; Romano 2007), resulting in TTG rocks that range in age from c. 2750 to 2695 Ga (Romano et al. 2013; Marinho et al. 2018; de Melo-Silva et al. 2020) and younger, high-K calc-alkaline granites, which include the 2694.7 ± 9 Ma (U-Pb zircon age; de Melo-Silva et al., 2019) Casquilho pluton (Fig. 4-1B). The latter is exposed in the

underground workings within the Turmalina and Satinoco deposits (Fabricio-Silva et al. 2019).

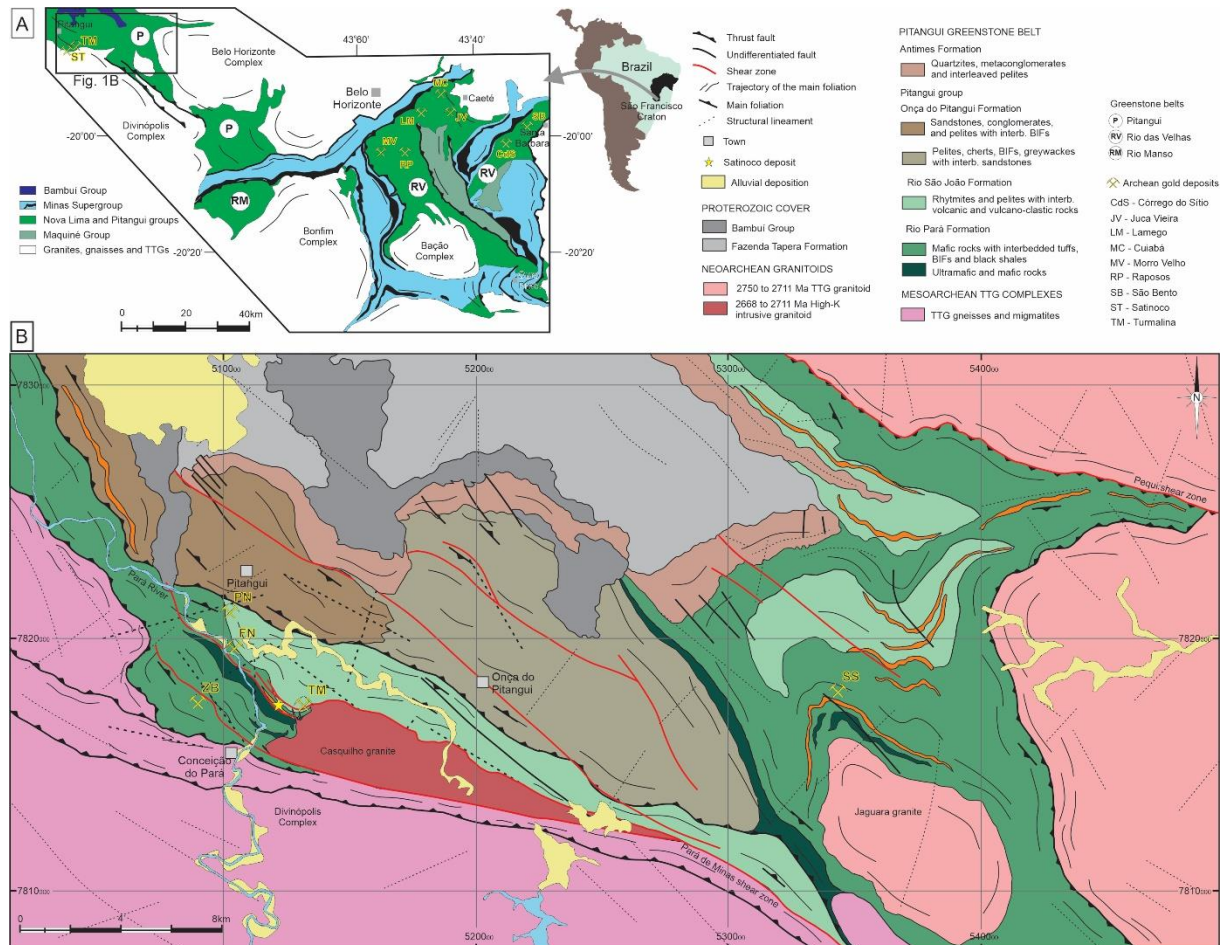


Fig. 4-1. Regional geology schematic map of the southern region of the São Francisco Craton. (A) Schematic geological map of the Iron Quadrangle (Minas Gerais / Brazil) showing the Archean greenstone belts, as well as some of the major Archean gold deposits. Compiled and adapted after Dorr (1969) and Renger et al. (1994). (B) Map of the Pitangui geological region (modified and adapted after Fabricio-Silva, 2016; Brando Soares et al., 2017; Marinho et al., 2018).

4.3.2 The age of the TTG-Pitangui greenstone belt terrane

The most primitive crust known from the São Francisco Craton is made up of 3.6 Ga gneisses (Oliveira et al. 2020) and cratonization took place in the course of several

TTG magmatic events mainly between 3.2-2.7 Ga (Lana et al. 2013). The Belo Horizonte complex was formed initially via magmatic addition of juvenile felsic rocks at c. 3.212-3.210 Ga, but most of the TTG rocks exposed today are c. 2.93-2.90 Ga in age (Lana et al., 2013; and references therein). Emplacement of the Divinópolis complex near the contact with the Pitangui greenstone belt, south of the Satinoco deposit, has been dated by a U-Pb zircon age at 2878.5 ± 5.7 Ma (de Melo-Silva et al., 2020).

Based on detrital zircon grains from a metasandstone layer interbedded with volcanic rocks (Pará de Minas Formation), Brando Soares et al. (2017) suggested an age of 2859 ± 11 Ma for the basal komatiite, which is slightly younger than basal Rio das Velhas magmatism (Baltazar and Zucchetti 2007; Noce et al. 2007).

Detrital zircon from the sedimentary rocks gave ages in the range of 3252-2680 Ma with prominent age modes at 2980 and 2730 Ma (Romano 2007; Marinho et al. 2018; de Melo-Silva et al. 2020). Brando Soares et al. (2017) obtained a maximum depositional age of 2765 ± 12 Ma for metasandstone from the Rio São João Formation (their intermediate unit). Similarly, the maximum depositional age for micaschist and metagraywacke from the intermediate unit has been constrained at 2769.8 ± 8.9 Ma (de Melo-Silva et al. 2020) and 2788 ± 4 Ma (Marinho et al. 2018), respectively. For quartzite in the upper units of the Pitangui Group in the vicinity of our study area, , a maximum depositional age of 2684 Ma (Marinho et al. 2018) has been determined. According to Brando Soares et al. (2020) and de Melo-Silva et al. (2020), most of the detrital zircon ages cluster at 2790-2730 Ma and suggest that the main source of detrital sediments from intermediate units could have been TTG complexes. Correspondingly, the zircon grains from the upper sedimentary units of the Pitangui Group were derived mainly from the greenstone sequences.

The timing of the earlier event of the late- to post-tectonic felsic magmatism coincides with the latest TTG event in the south São Francisco craton (see Lana et al., 2013;

Romano et al., 2013; Marinho et al., 2018; Brando Soares et al., 2020; de Melo-Silva et al., 2020). This intrusive magmatism (Fig. 4-1B) is represented mainly by two batholiths and three plutons: the Florestal (U-Pb zircon age of 2755 ± 8 Ma; Romano et al., 2013) and Pequi (U-Pb zircon age of 2750 ± 13 Ma; Romano et al., 2013) batholiths in addition to the Jaguara, Casquilho, and Caio Martins plutons. The Jaguara pluton (TTG-like signature), which was emplaced into the metavolcano-sedimentary sequence neighboring the São Sebastião gold deposit, revealed ages between 2747 ± 7 Ma (U-Pb zircon age; Marinho et al., 2018) and 2719 ± 11 Ma (U-Pb zircon age; Brando Soares et al., 2020). The U-Pb zircon data from the high-K Casquilho granite indicate a crystallization age of 2694.7 ± 9 Ma (de Melo-Silva et al., 2020) and 2711 ± 4 Ma (U-Pb zircon age; Marinho et al., 2018). The samples for the latter came from surface outcrops whereas those for the former age determination come from the exact same apophysis referred to in our study from underground exposures of the Satinoco deposit. The youngest episode of late-tectonic magmatism is represented by the Caio Martins granite, dated at 2593 ± 19 Ma (U-Pb zircon age; Romano, 1993).

4.4 Sampling and analytical methods

Systematic face mapping was performed in all accessible underground stopes of the Satinoco mine. Section logging was undertaken and included 12 horizontal diamond drill holes that had been chosen to represent the main structural, lithological, and mineralogical variations. We selected two representative drill holes (FTS1406 and FTS1562) from the Central (C) orebody and Southeast (SE) orebody, respectively, for systematic sampling. More than 80 samples were collected from the diamond drill cores and the underground galleries, including the mineralized zones, hydrothermally altered zones, and unaltered country rocks, and these served as the basis for ore microscopy and petrography of mineralized and barren rocks. All the mineral abbreviations are after Whitney and Evans (2010).

Quantitative in-situ microanalyses of several selected sulfide grains were performed with a JEOL-8230 electron microprobe (EMP) at the Geoscience Institute of the University of Brasilia. The analytical conditions were set as 20 kV accelerating voltage for sulfides and 15 kV for silicates, and a beam current of 25 nA. The beam was either slightly defocused to 5 µm or fully focused (<1 µm). Spot sulfide and garnet analyses were conducted along lines and grids, in order to identify possible compositional variations between cores and rims. A set of 13 elements was chosen for EMP spot sulfide (As, Se, S, Pb, Bi, Te, Fe, Co, Cu, Ni, Au, Ag, and Sb) and 13 elements for silicates (Na, Mg, Al, Si, O, Ca, K, Ti, Cr, Mn, Ni, Fe, V, and Zr) analyses. The detection limits for each element are given in the electronic supplementary material (Appendix) Table A1 (silicates) and Table A2 (sulfides). The following standards were used for calibration of elemental X-ray intensities: gallium arsenide (As), pyrite (S, Fe), copper (Cu), antimony (Sb), cobalt (Co), tellurium (Te), Selenium (Se), nickel (Ni), bismuth (Bi), gold (Au), galena (Pb), and silver (Ag). The resulting data were corrected off-line using a ZAF correction procedure (samples: Offline_0001_QNT and Offline_0003_QNT).

A MatLab®-based (version R2018b) software, XMapTools®, version 2.5.2 (Lanari et al. 2014), was used to generate qualitative As, Fe, Ni, Sb, and Pb X-ray maps of the arsenopyrite crystals from two gold-bearing sulfide assemblages for subsequent modeling of compositional variation and hydrothermal conditions. The element maps were acquired by EMP with an acceleration voltage of 20 KV, 200 nA beam current, and 100 ms dwell time.

In-situ microanalyses of 77 arsenopyrite grains associated with gold-bearing sulfide and 12 pairs of garnet-biotite (which appear in textural equilibrium) were carried out to calculate the temperatures of equilibration. The arsenopyrite geothermometer (Kretschmar and Scott 1976; Sharp et al. 1985), which is based on the As content in arsenopyrite, was used to model the temperatures for each sulfide assemblages; whereas garnet-biotite thermometry based on the TWQ thermodynamic database

(version 2.10; Berman, 1991) was used to constrain metamorphic temperatures. Spot analyses in garnet-biotite pairs and compositional profiles (rim-core-rim) were performed on several garnet porphyroblasts.

Laser ablation ICP-MS on polished thick sections was carried out at the GeoZentrum Nordbayern, University of Erlangen, for measurement of trace-element concentrations. Prior to LA-ICP-MS analyses, the quantitative EPMA spot analyses were combined with qualitative X-ray mapping to display the potential patterns of trace element distribution in arsenopyrite and pyrite crystals. The analyses were performed with a single collector quadrupole AGILENT 7500c ICP-MS equipped with a laser unit (Analyte Excite, Teledyne, photon machines, Excimer laser 193nm). The carrier gas used was He and Ar. For external calibration, Po724 B2 SRM (sulfide standard for Au, Memorial University Newfoundland) and MASS-1 (Polymetal sulfide; USGS; for V, Mn, Fe, Co, Ni, Cu, Zn, Se, Mo, Ag, Sn, Sb, Te, Pb, and Bi) were used. The on-line data reduction was done by GLITTER Version 4.4.4 (Macquarie Research Ltd.), using S as the internal standard and monitoring Si, V, Mn, Sn for possible interferences. The laser beam was fired at 20 Hz repetition rate (fluence 4.04 J/cm²). The spot size was 20 µm in diameter. Integration time for ²⁹Si was set to 10 ms, for ³⁴S, ⁵⁷Fe, ⁶³Cu, ⁶⁷Zn, ⁶⁸Zn to 25 ms, for ⁵¹V, ⁵⁵Mn, ⁵⁹Co, ⁶⁰Ni, ⁶¹Ni, ⁷⁷Se, ⁹⁵Mo, ⁹⁷Mo, ¹⁰⁹Ag, ¹¹⁷Sn, ¹²¹Sb, ¹²⁵Te, ¹⁹⁷Au, ²⁰⁸Pb, and ²⁰⁹Bi to 55 ms, and for ¹⁹⁷Au to 45 ms on the maximum peak. Total acquisition time was 40 s, background time was 20 s. Copper, Co, As, Zn, Mo, Ag, Te, Bi, Hg, Pb, and Si were measured as relative concentrations in counts per seconds (cps), as there was no well-calibrated standard available for these elements. The average of 23 analyses of the standard Po724 B2 SRM during our analysis period yielded a Au concentration of 47.1 ppm, consistent with the 47.3 ppm measured by quadrupole ICP-MS at Memorial University.

4.5 Results

4.5.1 Geology of the Satinoco deposit

Satinoco belongs to the Turmalina mine Complex and is one of the largest gold deposits in the Pitangui greenstone belt. It was the first mine to produce in an open pit (1989) in the NW-Iron Quadrangle and since 2010 has been operated as an underground mine. The deposit is hosted by metabasalt and metakomatiite interbedded with metatuff, BIF, and black shales of the lowermost units of the Pitangui Group (Fig. 4-2A), the Rio Pará Formation. The shear zone-related orebodies have a lenticular shape and consist of three 2 to 4 m-thick auriferous corridors extending over 350 m. The lenses follow a NW-SE trend with a NE-dip (around 60°) and constitute sub-bodies referred to as Satinoco-NW (C-NW), Satinoco-Central (C-Central), and Satinoco-SE (C-SE).

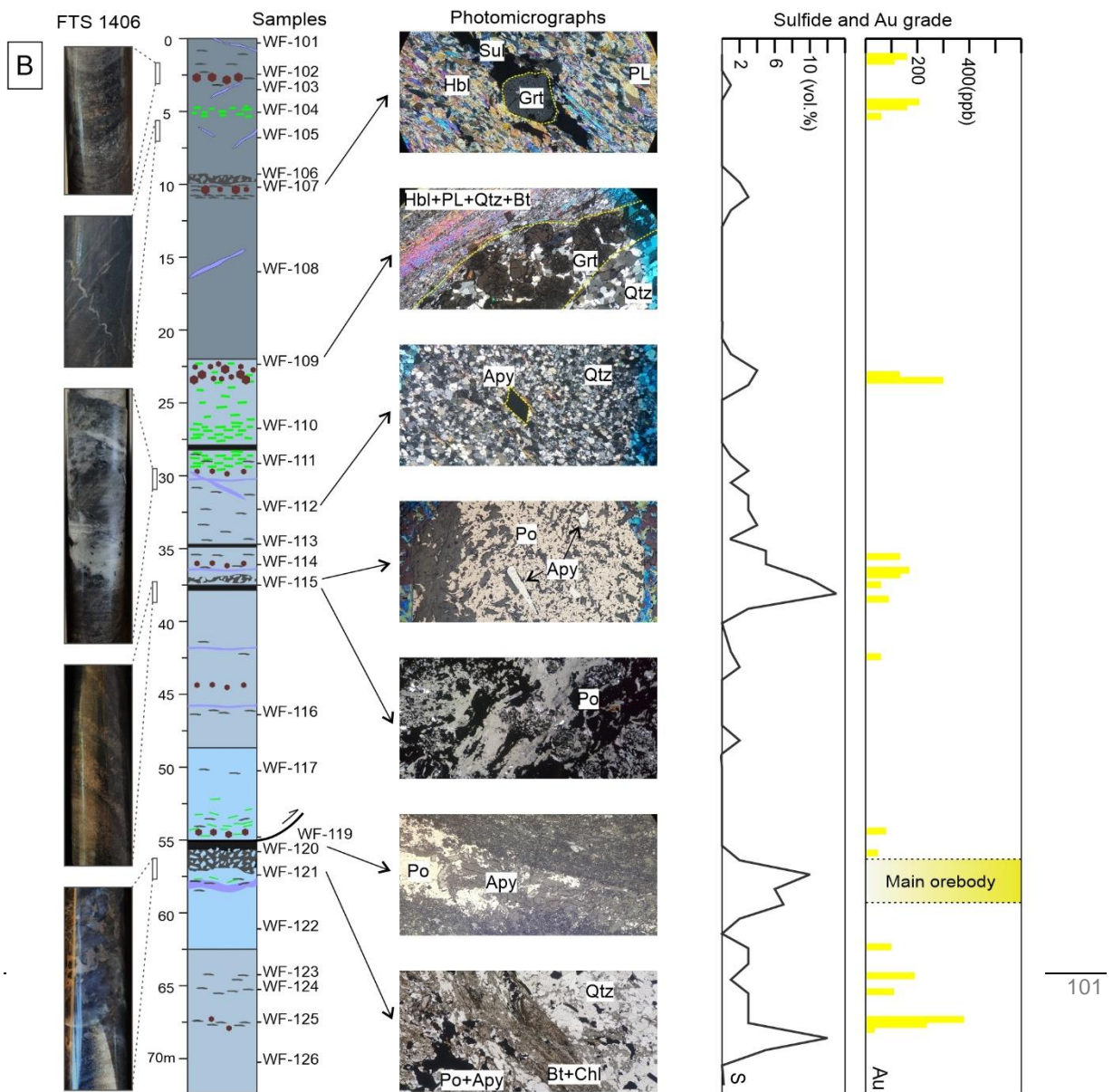
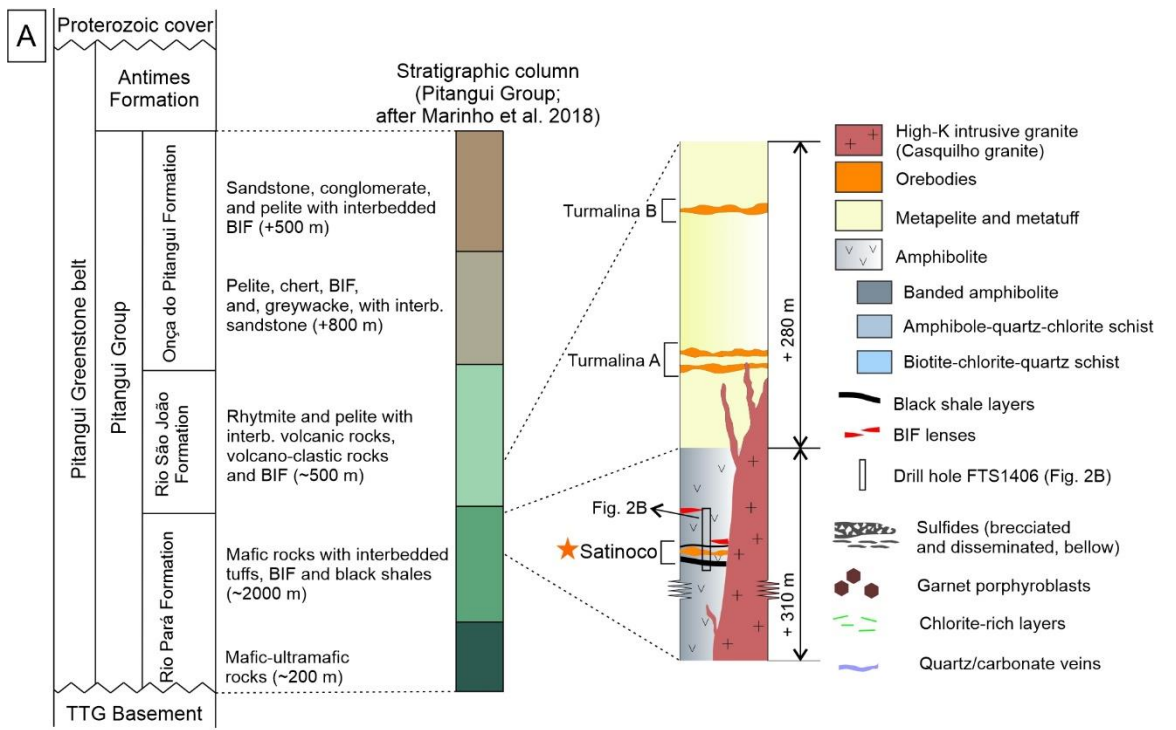


Fig. 4-2. (A) Stratigraphic column of the host rocks in the Satinoco deposit and their relation to the regional stratigraphic column of the Pitangui greenstone belt and Turmalina-A and Turmalina-B orebodies. (B) Horizontal drill hole FTS-1406 logging of the C-Central orebody with representatives macroscopic and microscopic photos. The left column represents photos of some selected samples. In the schematic drill hole, the color intensity is disproportionate with the amount of hydrothermal silica (grey: less silica; light blue: more silica). The other schematic local mineral enrichments are shown as: garnet, chlorite, sulfide (light grey layers and ellipses, representing brecciated and disseminated, respectively), quartz ± carbonate veins, and black shales bands. The two columns in the right side represent, respectively, estimated total sulfides (vol %) and the gold content (in ppm) based in whole-rock ICP-MS analyses.

The host rocks are cut by a series of granitic apophyses (Fig. 4-3). Brando Soares et al. (2020) demonstrated that the apophyses have the same geochemical signature (high-K granitic) as the main batholith of the Casquilho granite exposed on the surface (Fig. 4-1). The granite is leucocratic, coarse-grained and composed mainly of quartz (40 to 55 vol %), Ca-rich plagioclase (partially saussuritized; 25 vol %), microcline (15 to 20 vol %), and biotite (10 to 15 vol %; partially chloritized). Some of these discordant apophyses become parallel to the orebodies (and consequently to the shear zones) where they are in proximity. In this case, they are partially deformed, forming mainly pinch-and-swell structures, which is taken as evidence of a close spatial and temporal relationship between the granitic magma intrusion and mineralization (Fig. 4-3).

High-grade and sulfide-rich (10 vol %) ore is associated with quartz veins. The sulfides occur within, or disseminated in, cm-thick bands parallel to the quartz veins or as matrix of hydraulic breccias (Fig. 4-2B). Arsenopyrite is a visual indicator of high-grade gold, although gold is also commonly associated with pyrrhotite and pyrite. The gold occurs mainly as visible gold inclusion, $> 0.1 \mu\text{m}$ in size, and as “invisible gold” (i.e., optically undetectable) within arsenopyrite and löllingite.

The rocks of the Satinoco area were affected by at least three deformation events (D_1 , D_2 , and D_3). The oldest observable structures, related to D_1 , developed during a

stage of compression and are represented by isoclinal regional folds and associated S₁ WNW-ESE-striking axial-planar foliation (with an average of 62/012) that obliterated primary compositional banding. The second deformational event (D₂) resulted in NW-SE-striking and NE-dipping ductile shear zones (which host the orebodies), quartz veins, and the generation of an Ls₂ stretching lineation (mean plunge at 25/085) and S₂ crenulation cleavage (striking between NNW and NNE; dipping 65 to 75° towards W). The D₃ event is reflected by meter-sized open folds (with axial plane dipping around 60° NE and axis plunging 65/325) and several reverse faults, most commonly found in the Satinoco-SE orebody. The reverse faults cut the open folds, strike mainly NW-SE and dip 50 to 60° to the NE.

The distribution of metamorphic mineral assemblages has a clear spatial relationship with the D₂ shear zones and the granite stock (Fig. 4-4; for photomicrographs with alteration minerals see supplementary online appendix Fig A1). The shear zones are approximately orthogonal to the contact between the granite and the host rocks and the highest metamorphic grades are observed in these areas. The hydrothermal mineral assemblage proximal to the orebodies indicates recrystallization under amphibolite-facies conditions. Peak metamorphic minerals are also overprinted by other lower grade metamorphic minerals. In the proximal zone, the metamorphic mineral assemblage in the metabasalt is quartz-garnet-cummingtonite-actinolite ± biotite; whereas the metatuff is characterized by quartz-garnet-cummingtonite-ilmenite ± staurolite. Staurolite and larger (>25 mm) garnet crystals are most common in close proximity to the granite contact in the western area of the deposit. In an intermediate zone, the metamorphic mineral assemblage reflects a markedly lower grade: at a distance of c. 7 m from the orebodies, the typical assemblage is quartz-chlorite ± garnet, reflecting upper greenschist-facies conditions. At an even greater distance, the regional metamorphic mineral assemblage is quartz-chlorite-calcite ± muscovite, reflecting lower greenschist facies (Romano, 2007). This low-grade regional metamorphism affected both the higher grade contact metamorphic aureole in the vicinity of the granite, where chlorite ± calcite ± muscovite developed as retrograde phases, and the granite itself, in which biotite became chloritized and quartz partly recrystallized.

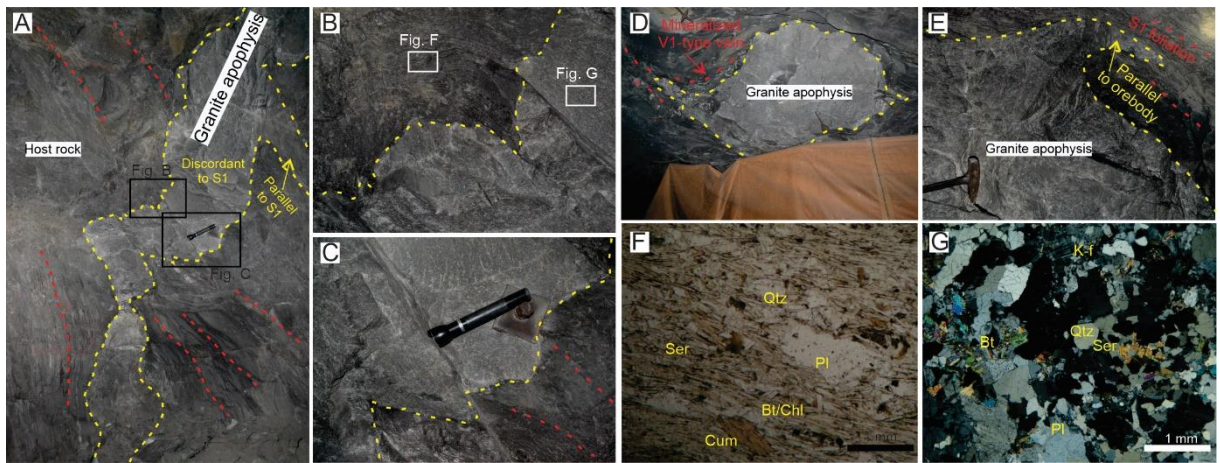


Fig. 4-3. (A-E) Pictures illustrating underground representative granite apophysis and their structural relationship with the host rocks and orebodies. (F) Photomicrograph of metamorphic host rock (garnet-biotite-chlorite-quartz schist) seen in B. Transmitted light, parallel polarizers. (G) Photomicrograph of representative texture seen in the granite apophysis showed in B. Equigranular granite with quartz, k-feldspar (microcline), plagioclase (partially sericitized) and biotite. Transmitted light, crossed polarizers.

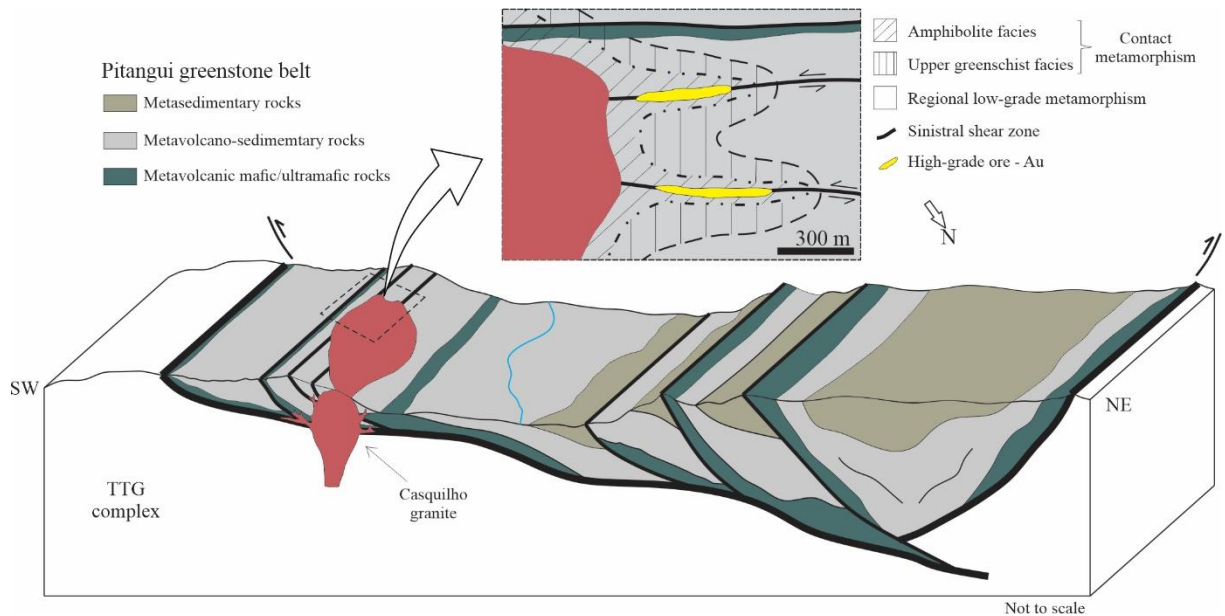


Fig. 4-4. Schematic cartoon illustrating the Neoarchean late-tectonic intrusive magmatism at the Pitangui greenstone belt and its relationship between the thrust/shear zones and gold mineralization. Note the spatial distribution of the contact metamorphism and the metamorphic facies. Modified after Brando Soares et al. (2020). See photomicrographs containing the alteration minerals for each metamorphic paragenesis in App. Fig. A1 – In Economic Geology).

4.5.2 Hydrothermal alteration and mineralization styles

Several types of hydrothermal alteration have been recognized in the Satinoco deposit and these are distributed, in general, parallel to the S_1 foliation in association with the mineralized envelope (Fig. 4-2B). Hydrothermal alteration zones form halos with gradational contacts with the host rocks around the orebodies. The hydrothermal minerals include mainly quartz, carbonate, chlorite, arsenopyrite, löllingite, pyrrhotite, galena, pyrite, and sericite, in addition to grunerite, biotite, tourmaline, and epidote. Less common hydrothermal minerals are gold, chalcopyrite, sphalerite, ullmannite, monazite, rutile, magnetite, and hematite.

Silicification is the dominant alteration type. It led to the formation of milky and smoky quartz veins and granoblastic quartz that is moderately sheared and recrystallized. In the shear zones, quartz shows limited subgrain development and undulose extinction but, in general, it is completely recrystallized. Carbonate alteration left behind cm-thick calcite veins associated with pyrrhotite and pyrite, in places in the form of breccias, or as interstitial ankerite and calcite associated with bands of sericite and recrystallized quartz. The sulfide alteration is represented by at least three assemblages that developed as disseminated grains in bands, breccias, or along the margin of quartz veins. Chloritization (up to 40 vol %) was pervasive and associated with sericitization. Tourmaline is concentrated in layers (sub)parallel to the S₁ foliation near the orebodies, where euhedral fine-grained crystals are associated with sericite. In places, tourmaline crystals contain inclusions of quartz, cummingtonite, and sulfide (mainly pyrrhotite, subordinately arsenopyrite). Incipient hydrothermal alteration in the mafic host rocks is evident by grunerite, biotite, epidote, magnetite, hematite, and monazite.

Vein systems and quartz textures

At least three generations of veins were identified in the deposit (V₁, V₂, and V₃; Fig. 4-5). They are made up of quartz, carbonate, and sulfides, with a minor amount of feldspar, tourmaline, grunerite, biotite, and actinolite.

The V₁ forms the main vein system, are parallel to S₁ (Fig. 4-5B) and developed pre-to synkinematically with regard to the ductile D₂ event. These veins are composed of milky to smoky quartz and contain 5 to 10 vol % gold-bearing sulfides. Their ore grade is 3-7 g/t Au. The V₁ veins are oriented NW-SE and display laminated and brecciated textures, also containing inclusion bands that are up to 5 cm wide and oriented subparallel to the vein walls. These inclusion bands contain amphibolite and sulfide-rich rock fragments. The milky quartz constitutes 40 to 70 % of total quartz

and is dominant where the veins have greater thickness, whereas the smoky quartz occurs mainly in the boudin boundaries or in the “necks” of pinch-and-swell structures.

The V₂ veins (Fig. 4-5C) are 10 to 25 cm wide, extensional shear-related, mainly comprising milky quartz (80-90 vol %), carbonate (<5 vol %), and sulfide (5 vol %). These veins fill reverse faults and cut across most of the granite apophyses (Fig. 4-5E). They also cut the main shear zone and V₁ veins. The V₂ veins occur at low angles to the shear zone corridors or are oriented along the S₂ foliation. These extensional-shear veins contain coarse-grained (about 1 to 2 cm-large) euhedral to subhedral quartz, in places forming growth fibers that are oriented both perpendicular and oblique to vein margins. Some of these veins are weakly mineralized, with Au contents ranging from 0.1 to 0.5 g/t. Therefore, these veins are not a target for current mining. The V₂ veins also occur frequently as veinlets (1 to 2 mm-thick) and cut S₁ and V₁ veins (Fig. 4-5F). They usually contain fine-grained, euhedral to subhedral milky quartz, carbonate grains (up to 20 vol %, mainly ankerite), and gold-bearing sulfides.

The barren V₃ vein system is represented by extensional veins that are 1 to 15 cm thick and consist of coarse-grained, euhedral, milky quartz and calcite. These veins are sulfide-poor (pyrite-chalcopyrite, with no gold content) and randomly oriented.

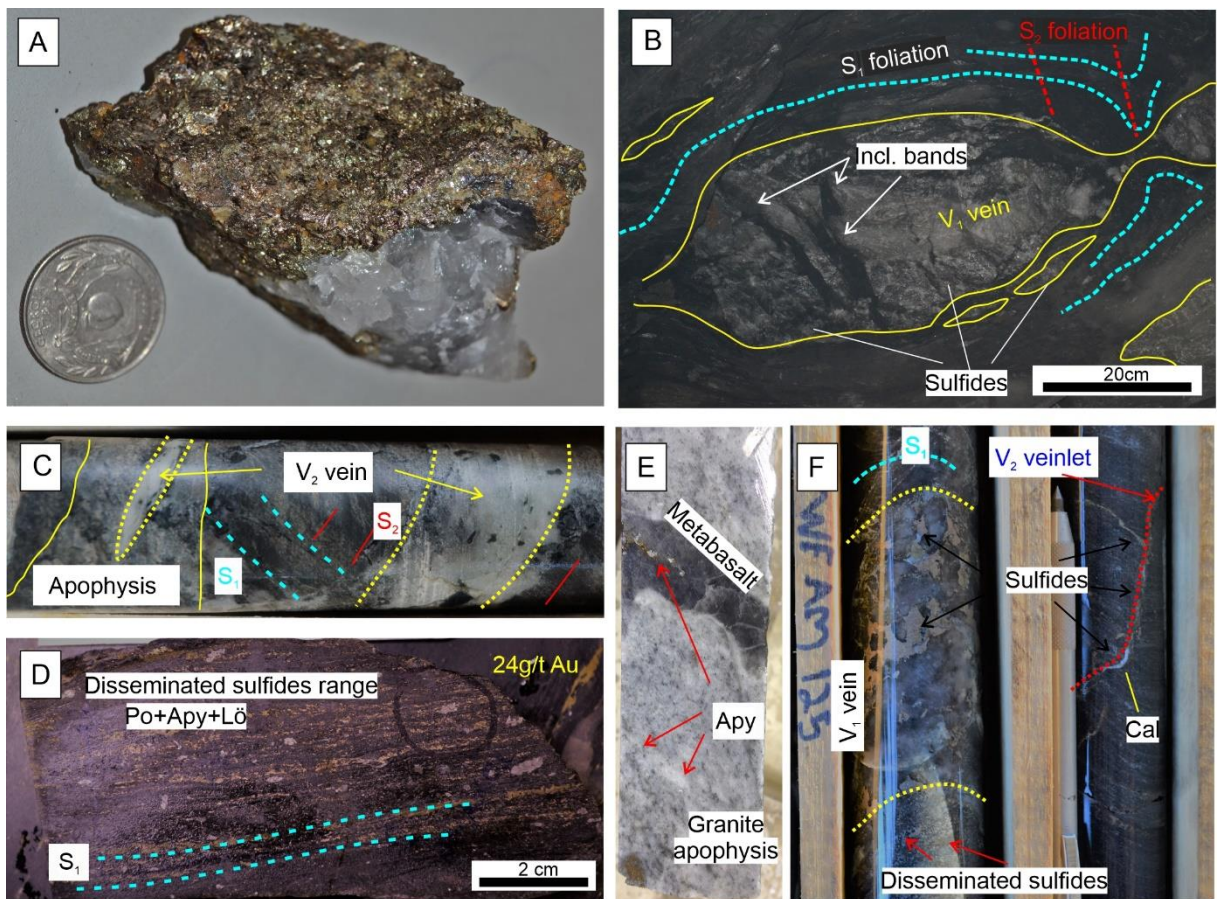


Fig. 4-5. Vein systems at the Satinoco deposit. (A) V₁ vein showing milky quartz rimmed by recrystallized smoky quartz and sulfides. (B) Underground stope ceiling displaying pinch-and-swell structures in V₁ vein. Note deformed vein contains inclusion bands with preserved S₁ foliation (weakly developed) in metabasalt. (C) Drill core with quartz-carbonate V₂ vein crosscutting S₁, S₂, and granite apophysis. (D) Disseminated gold-bearing sulfide range parallel to V₁ vein. (E) Drill core showing granite apophysis with a xenolith of metabasalt. Note arsenopyrite grains in both granite and metabasalt. (F) Drill core showing aggregates of sulfides forming hydraulic breccias in V₁ vein, disseminated sulfide range, and V₂ veinlets with sulfide and carbonate. Apy – arsenopyrite; Cal – calcite; Po – pyrrhotite; Lö – löllingite.

Alteration halos developed around V₁ veins

Based on diamond drill logging and sampling, petrography, and mineral chemistry, we divided the hydrothermal alteration halos into five zones: (*i*) main lodes, represented by V₁ veins and surrounding sulfide-enriched zones that contain the highest Au grade; (*ii*) proximal quartz-chlorite-carbonate-sericite-grunerite-biotite-garnet-sulfide±epidote±tourmaline zone; (*iii*) proximal- intermediate quartz-chlorite-carbonate-sericite ± sulfide ± biotite ± garnet ± grunerite ± epidote zone; (*iv*) distal-intermediate quartz-chlorite-carbonate±sericite zone; and (*v*) distal quartz-carbonate-chlorite ± sericite zone. Note that the distal versus proximal location of these alteration zones are relative to the main lode. Similar zonation is observed, though on a smaller scale, around smaller satellite orebodies (see gold-bearing sulfide layers in Fig. 4-2B). The spatial distribution of the hydrothermal assemblages and alteration zones are summarized in Table 1 and illustrated in photomicrographs in App. Fig. 4-A1.

The 1 to 2 m-thick main lode contains a high proportion of V₁ quartz veins. These veins tend to be sulfide-rich in the main lode and also contain rare tourmaline. The margins of the veins and the inclusion bands in the main lode are rich in biotite, garnet, plagioclase, and grunerite. Both the main lode and extensive V₁ veins are boudinaged and transposed within the D₂ shear zone.

Table 4-1. Schematic geographic distribution of the hydrothermal alteration types in the Turmalina deposit

Primary phases	Hydrothermal alteration zones and assemblages				
	Distal zone	Intermediate-distal zone	Intermediate-proximal zone	Proximal zone	V ₁ vein (main lode)
	Quartz-carbonate-chlorite ± sericite	Quartz-chlorite-carbonate ± sericite	Quartz-chlorite-carbonate-sericite ± sulfide ± biotite ± grunerite ± epidote	Quartz-chlorite-carbonate-sericite-grunerite-biotite-sulfide ± epidote ± tourmaline	Quartz-carbonate-sulfide ± tourmaline
Biotite	Partly replaced by chlorite and, rarely, muscovite		Most times replaced by hydrothermal biotite, chlorite, and carbonate (in V ₂ veins)		Replaced by chlorite
Pyroxene	Unstable, almost completely replaced by cummingtonite/actinolite (metamorphic)		Where present, completely replaced by actinolite and grunerite		
Garnet and Grt ₂	Grt ₁	Absent	Unstable, partly replaced by chlorite and sericite	Unstable, partly replaced by chlorite, sericite, quartz, sulfides and iron oxides	Rare, unstable
Apatite	Less common. Replaced by rutile		Replaced by rutile and monazite		Absent
Feldspar	Unstable, partly replaced by sericite		Unstable, plagioclase almost completely replaced by sericite or occasionally by epidote and carbonate		
Quartz	Partly stable		Hydrothermal milky quartz more or less recrystallized		Hydrothermal quartz recrystallized, mainly as smoky quartz
Rutile	Partly replaced by ilmenite and titanite				Absent
Amphibole	Stable cummingtonite and actinolite	Cummingtonite, actinolite, and grunerite. Sometimes altered into sericite and chlorite		Most times replaced by grunerite	Rare, most grunerite
Total opaques	Accessory hematite and pyrrhotite, <4 vol %		Mainly sulfides (<6 vol %)	Sulfides (2 – 15 vol %), hematite and magnetite (<3 vol %)	Mainly sulfides (5 – 15 vol %)
Thickness	> 30 m	15-25 m	7-15 m	3-7 m	1-2 m

The proximal alteration zone occurs around the V₁ main lode vein within 3 to 7 m. This zone is rich in quartz, chlorite and carbonate, with subordinate sericite, grunerite, biotite, sulfides, and lesser amounts of epidote and tourmaline. This alteration zone is marked by a high amount of milky quartz (>50 vol %) and the preferential replacement of an initial assemblage of cummingtonite-actinolite-biotite-plagioclase ± hematite ± rutile by, firstly, an assemblage of garnet-biotite-grunerite-sulfide and then by a lower temperature assemblage of chlorite-sericite-ankerite-sulfide-calcite ± epidote ± titanite ± tourmaline. Carbonate in the proximal zone is ankerite and calcite. Whereas ankerite is observed mainly in the interstices between

quartz grains, calcite is present as coarse-grained crystals in the V₂ veinlets and “calcite eye bands”. Chlorite occurs both in chlorite-rich layers (10 to 20 cm-thick; >35 vol % chlorite) and as replacement of biotite and garnet. Sericite developed by the almost complete replacement of plagioclase besides the common association with the chlorite-rich layers.

The proximal-intermediate alteration zone is similar to the proximal alteration zone but differs mainly by the presence of preserved cummingtonite and actinolite, as metamorphic phases (and hornblende as igneous phase), besides a lower proportion of quartz (about 30 vol %) and the absence of hematite and magnetite. The width of this alteration zone is approximately 7 to 15 m.

The intermediate-distal alteration zone and the distal alteration zone are distinguished by the least amount of hydrothermal milky quartz (up to 30 vol % in the intermediate-distal zone and between 5 and 15 % in the distal zone) and by the dominance of amphiboles and sericitized plagioclase. The boundaries among these zones are gradational over a few meters and these alteration zones are characterized by their green color (darker in the distal zone) related to the occurrence of cummingtonite and actinolite, which are partially replaced by chlorite. In the intermediate-proximal alteration zone, cummingtonite is typically replaced by grunerite, which is absent in the distal zone.

4.5.3 Garnet porphyroblasts: textures, generations, and compositions

Based on chemical composition (App. Table A1) and inclusion trail relations, at least two generations of garnet porphyroblasts (Grt₁ and Grt₂) can be distinguished in the schists of the Satinoco deposit (Fig. 4-6). Both garnet generations are concentrated

in narrow bands (10 to 20 cm wide) parallel to the S_1 foliation and close to the orebodies.

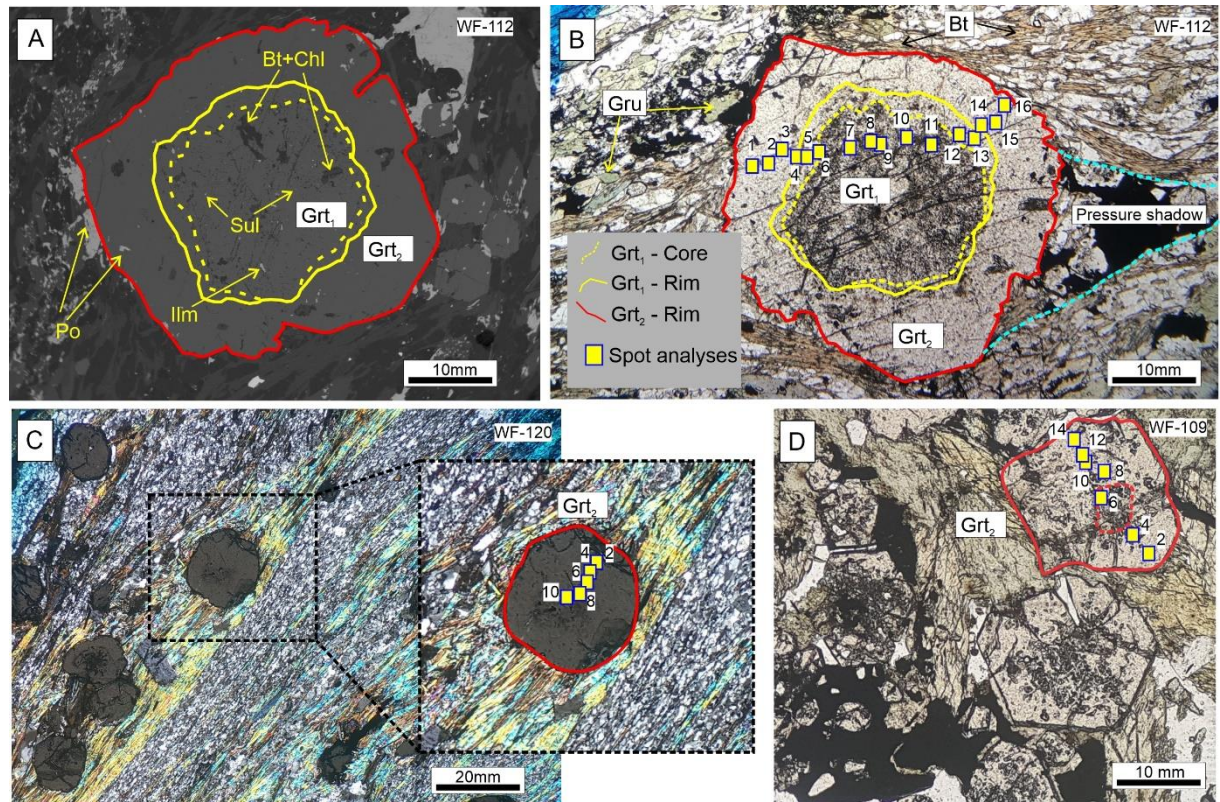


Fig. 4-6. Photomicrographs of representative garnet porphyroblasts from the two generations (Grt₁ and Grt₂). The compositional profiles are indicated by yellow squares (spot analysis location) and the garnet domains (core and rims) are highlighted in lines yellow and red (see legend).

The Grt₁ occurs as euhedral crystals that can reach up to 30 mm in diameter (on average 10 mm). It contains numerous inclusions, mainly in the cores. The inclusions are arranged as straight or complex circular trails (in places helicitic), define an internal foliation ($S_{1\text{int}}$), and are composed of quartz, arsenopyrite, pyrrhotite, chlorite, biotite, and rutile. The porphyroblasts exhibit strain shadows that are essentially composed of quartz, biotite, arsenopyrite, pyrite, and pyrrhotite. Such patterns indicate rotation of porphyroblasts during syntectonic deformation. The external foliation S_1 deflects around the garnet external grain boundaries with the development of strain shadows.

The Grt_2 occurs as overgrowth around Grt_1 (in this case, crystals of up to 25 mm diameter) or as separate euhedral individual crystals (mainly 5 mm in size). The Grt_2 grew over undeflected (or weakly deflected) S_1 foliation late to post-kinematically with regard to D_2 . It contains few inclusions of arsenopyrite, pyrrhotite, quartz, biotite, chlorite, and ilmenite.

The EMP data reveal compositional zonation for both garnet generations, characterized by an increase in Fe and Mg and a corresponding decrease in Ca and Mn from the core to the rim (Fig. 4-7; App. Table A1). In terms of composition, Grt_2 is distinguished from Grt_1 by a high amount of spessartine and a lower amount of almandine at the rims (Alm63Grs4Prp8Sps25 against Alm85Grs3Prp7Sps4 in Grt_1).

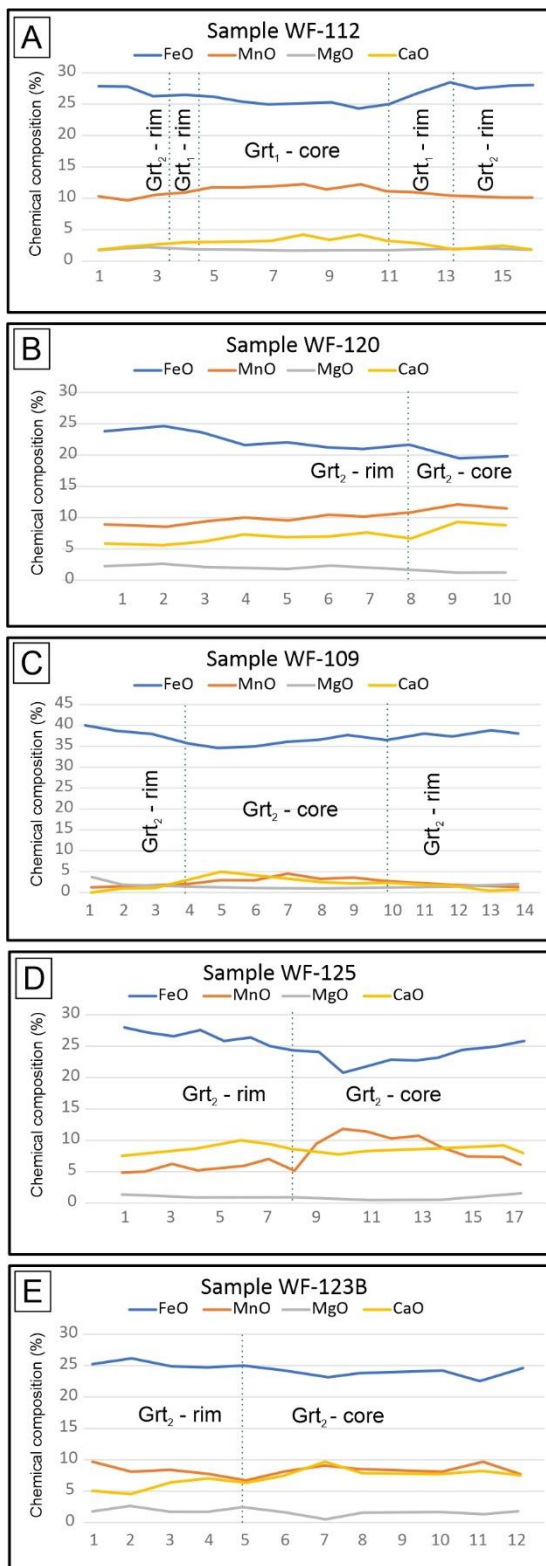


Fig. 4-7. Chemical profiles of representative garnet porphyroblasts from the FTS-1406 drill hole. The pseudo sections and the spot analysis locations are shown in figure 6 and the chemical composition values can be found in Appendix Table A1.

4.5.4 The sulfide assemblages and gold mineralization

The bulk of the gold in the Satinoco deposit is intimately associated with sulfides. The gold-bearing sulfides occur disseminated with quartz at V₁ vein margins (Fig. 4-5A, B) or, less commonly, along tourmaline stringers. Disseminated sulfide is the main mineralization style, in which the Au grade can reach as much as 24 g/t (Fig. 4-5D). When associated with veins, the sulfides are commonly concentrated at the “necks” of pinch-and-swell structures (Fig. 4-5B) or form the matrix of hydraulic breccias.

Based on texture, composition, and cross-cutting relationships, three generations of gold-bearing sulfide assemblages are distinguished (Fig. 4-8): (*i*) A first As-rich arsenopyrite-pyrrhotite-löllingite assemblage I; (*ii*) a subsequent Fe-rich pyrrhotite-arsenopyrite ± galena assemblage II; and (*iii*) a base metal-rich pyrite-pyrrhotite ± galena ± chalcopyrite ± sphalerite ± ullmannite assemblage III. The last assemblage is related to the V₃ veins. As this is not gold-bearing, it is not further considered here.

The early As-rich sulfide assemblage I is characterized by arsenopyrite (c. 60 vol %) + pyrrhotite (30 to 35 vol %) + löllingite (c. 5 vol %). This assemblage contains relatively rare disseminated sulfides in cm-wide bands along the S₁ foliation (Fig. 4-8A) or in the V₁ veins as aggregates or in breccias. Arsenopyrite (Apy₁) is present as disseminated oriented euhedral or subhedral crystals (c. 100 to 300 µm) or as aggregates of subhedral to anhedral grains (up to 300 µm). It is weakly zoned and rich in inclusions close to the grain margins. The inclusions are mostly pyrrhotite, quartz, hornblende, löllingite, and gold (Fig. 4-8C). The rims are typically altered, with variable degrees of crystal embayment that likely reflect mineral dissolution and re-precipitation reactions. Pyrrhotite (Po₁; 10 to 50µm) is present mainly as grains rich in inclusions of quartz, biotite, and arsenopyrite, and commonly replaces Apy₁. Preserved löllingite (Lö) is uncommon and occurs as anhedral grains usually as relicts rimming Apy₁ (Fig. 4-8F, G) or in the Apy₂ cores (Fig. 4-8H).

The second sulfide assemblage II is dominated by pyrrhotite (>80 vol % of the sulfides), arsenopyrite (>5 vol %), and subordinately galena and gold. It reflects the second gold-forming event and comprises recrystallized aggregates transposed within the S₂ foliation and locally affected by syn-D₂ shearing (Fig. 4-8J). The abundant pyrrhotite (Po₂) consists of fine-grained porous grains containing silicate and sulfide inclusions of the earlier sulfide assemblage. Arsenopyrite (Apy₂; 200 to 500 µm in size) has an euhedral-subhedral habit and cracked surface (Fig. 4-8H, J). It occurs commonly as single fine-grained crystals (10 to 100 µm), associated or intergrown with subhedral Po₂. Apy₂ also occurs as a recrystallization product of Apy₁ and Lö (Fig. 4-8H). Galena was observed with visible gold as inclusions in Apy₂.

The gold-bearing metal-rich sulfide assemblage III comprises pyrite-pyrrhotite ± chalcopyrite ± galena and Sb-Ni-Cu-Zn sulfides (Fig. 4-8B, L). Pyrite (Py; >65 vol %) occurs as semi-massive aggregates associated with V₂ veinlets (Fig. 4-8B) or isolated well-developed crystals overprinting the Fe-oxides. It is mostly coarse-grained with a euhedral to subhedral habit, ranging in size from 0.5 to 10 mm. These pyrite grains are commonly rich in inclusions of pyrrhotite, sphalerite, quartz and biotite, and formed at the expense of Po₂, mainly in sulfide breccias from assemblage II. Pyrrhotite (Po₃; 25-30 vol %) occurs as recrystallized rims of Po₂, normally devoid of inclusions. This base metal-rich sulfide assemblage also includes fine-grained chalcopyrite (2-5 vol %), galena (<1 vol %), sphalerite (rare), and rare ullmannite (Fig. 4-8M). Chalcopyrite usually fills fractures and/or replaced pyrite and pyrrhotite (Po₂ and Po₃). Ullmannite was observed in chalcopyrite and pyrite fractures and associated with galena.

Gold in the Satinoco deposit is mainly associated with arsenopyrite (Apy₁ and Apy₂) and pyrite. Gold contains trace amounts of Bi, Sb, and Ag (quantified by LA-ICP-MS; Table 3) and is found as free gold mainly at the contact between arsenopyrite and other sulfides, or as inclusions in pyrrhotite and other sulfides. Native bismuth occurs as inclusions together with gold particles (Fig. 4-8H). The visible gold can be divided into four textural types (Fig. 4-8; Table 2): (*i*) inclusions of gold along the boundaries

of arsenopyrite and löllingite of assemblage I; (ii) free gold in silicates, in most cases bordering Apy₂. This type corresponds to the more common visible gold type; (iii) inclusions in Po₂ and Apy₂; (iv) remobilized fracture-controlled gold associated with pyrite from sulfide assemblage III and arsenopyrite and pyrrhotite from earlier sulfide assemblages. Rare free gold also occurs within the tourmaline stringers.

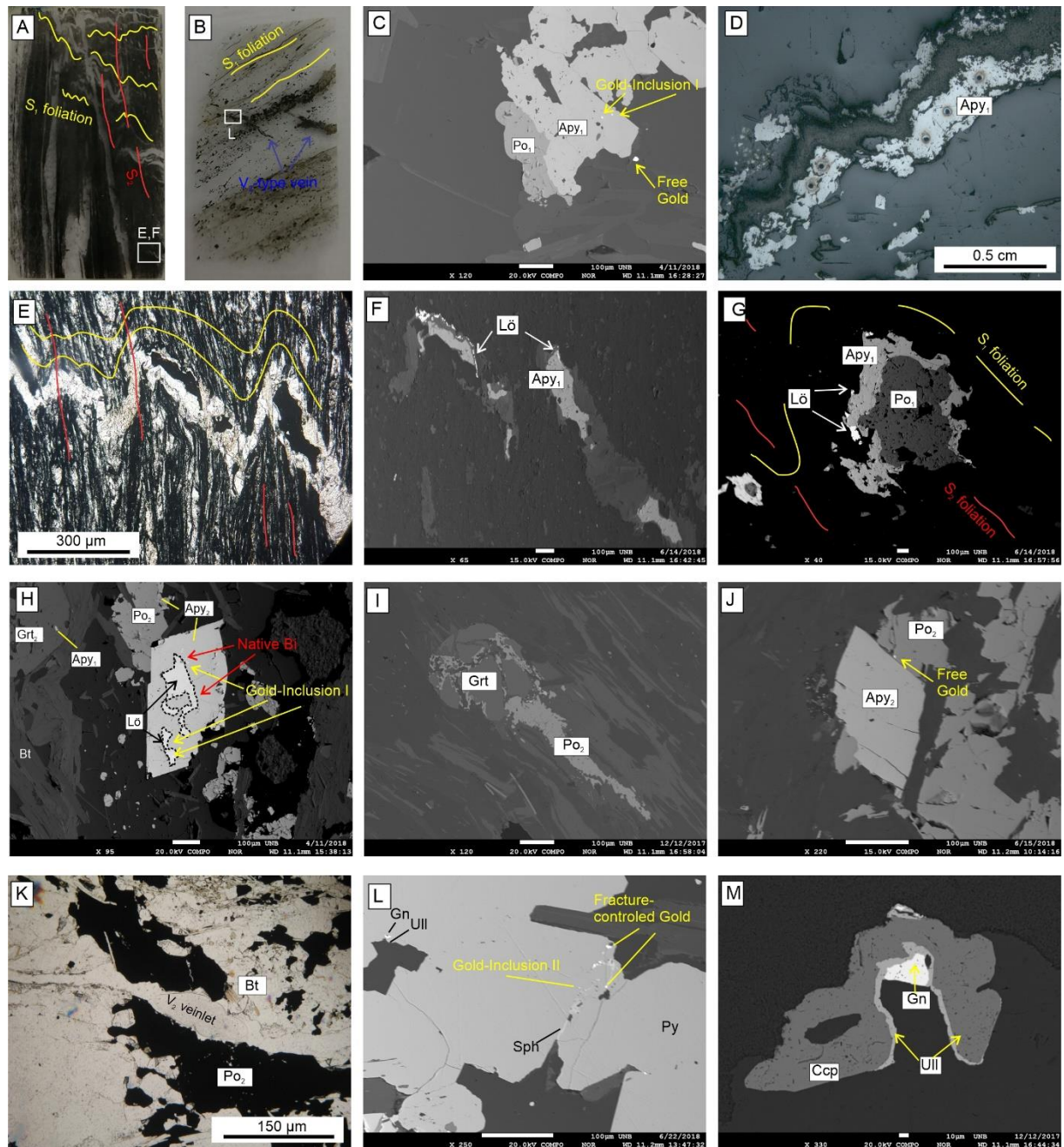


Fig. 4-8. Au-bearing sulfide stages and gold mineralization types at the Satinoco deposit. A) BSE image of sulfides from sulfide stage I and gold grains as inclusion I

and free. B) BSE image of Apy₂ replacing löllingite and Apy₁ as inclusion in Grt₂. Note that the gold inclusions rims a löllingite crystal. C) Photomicrograph with reflected light showing Apy₁. D) BSE image of pyrite and fracture-controlled gold and gold inclusion II associated with sphalerite. E) Polished thin section showing pyrite crosscutting sulfides parallel to S₁ foliation (yellow lines). The white square indicates the position of the (D). F) Polished thin section that shows deformed black shale and sulfides from assemblage I associated with foliation S₁. The white square indicates the position of the (G) and (H). G) Photomicrograph showing the detail of the V₁ vein deformed by S₂ crenulation cleavage (red lines). H) BSE image of (G) showing Apy₁ and Lö related to the V₁ vein. I) BSE image of Apy-Lö-Po assemblage. J) Photomicrograph showing a V₂-veinlet crosscutting Po₂. K) BSE image that shows Po₂ as pressure shadow in garnet (Grt₂?). L) BSE image showing free gold bordering Apy₂ and Po₂. M) BSE image with base metal sulfide assemblage composed by Ccp, Gn and Ull. Apy – arsenopyrite; Bt – biotite; Ccp – chalcopyrite; Gn – galena; Grt – garnet; Lö – löllingite; Po – pyrrhotite; Py – pyrite; Sph – sphalerite.

Table 4-1. Summary of gold mineralization types observed in Satinoco deposit

Type	Texture	Association
I Inclusion I	5 to 30 µm, typically in porous surfaces and irregular shapes	Within arsenopyrite (Apy ₁) crystals associated with incomplete retrograde metamorphism of löllingite
II Free gold	Irregular shapes, 10-60 µm	The most common type of visible gold. With silicates, such as quartz, biotite, and tourmaline, bordering arsenopyrite grains
III Inclusion II	Commonly > 30 µm, typically in round shapes and smooth surfaces	Together galena within pyrrhotite (Po ₂), associated with arsenopyrite (Apy ₁ and Apy ₂)
IV Free/fracture-controlled	10 to 50 µm, in acicular shapes and smooth surfaces	Fracture-filling within arsenopyrite and pyrite. Associated with pyrite and base metals, such as chalcopyrite and sphalerite

4.5.5 Compositional variation of gold-bearing sulfide assemblages

EMP mapping and spot analyses

Representative major and minor element concentrations of the analyzed sulfides are listed in Appendix Table A2. Concentrations below the detection limit were considered as zero in the statistical calculations. The EMP data indicate that arsenopyrite has an average As content of 49.43 wt.%, with a predictable negative correlation with S and Fe (Fig. 4-9A, B). The Co content of the analyzed arsenopyrite (Fig. 4-9C) is highly variable. Apy₁ shows no correlation between Co and Fe, whereas Apy₂ is Co-rich (between 0.67 and 2.65 wt.%) with a negative correlation with Fe. Both arsenopyrite generations have similar Sb contents (on average 0.33 and 0.30 wt.%, respectively) but a slightly positive correlation with As was noted only in Apy₂.

Although the lower limit of detection of the EMP is relatively high for gold (300 ppm) and other trace elements, it was possible to study some compositional variation between sulfide grains. The gold distribution within arsenopyrite grains also reveals similar contents between Apy₁ and Apy₂. The average Au concentration in the Apy₁ and Apy₂ are, respectively, 101 ppm (max. 960 ppm) and 149 ppm (max. 1113 ppm).

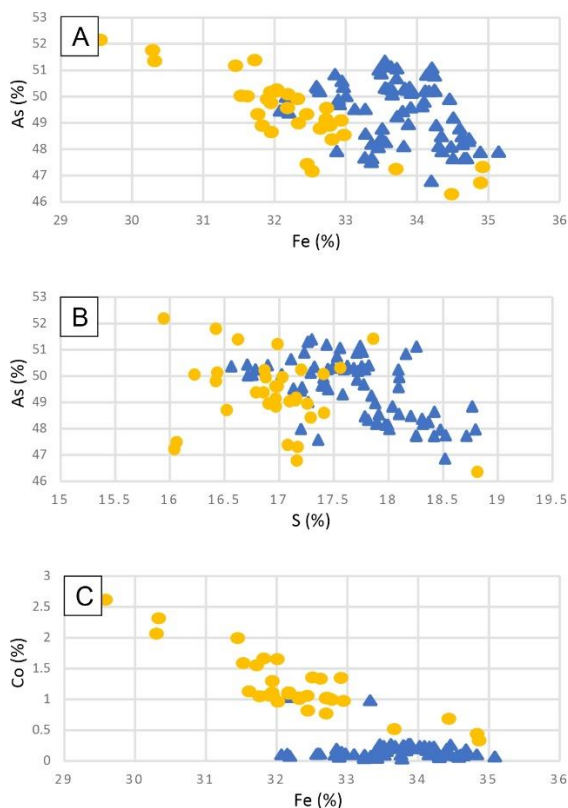


Fig. 4-9. Plots showing EMP geochemistry of arsenopyrite from Apy₁ (n = 73) and Apy₂ (n = 34) in the Satinoco deposit. (A-B) relationship of S (wt.%) and Fe (wt.%) with As (wt.%) (C) Co (at.%) vs. Fe (wt.%) showing considerably high content of Co in Apy₂ and the negative relationship between Fe and Co.

The modal proportion of löllingite and its intimate association with visible gold (observed by optical microscopy) is also reflected by the trace Au content within the crystals (highest value is 1119 ppm, with an average of 451 ppm). Arsenic concentrations are >73 wt.%, besides the high concentration of Ni (average of 2.3 wt.%) and Bi-Te (average of 0.2 wt.%).

Gold-bearing pyrite belongs to assemblage III. The pyrite grains display a weak oscillatory compositional zonation and are characterized mainly by a high concentration of Pb (940-3040 ppm) and Cu (BDL-0.477 wt.%) and low As (on average 0.04 wt.%) and Ni concentrations (<0.2 wt.%). No correlation exists between Au and As in this pyrite, analogous to other gold deposits in the Iron Quadrangle.

Along the fracture surfaces, the pyrite is enriched in Sb, Ni, Cu, Zn, and Au (App. Table A2).

EMP mapping and spot analyses at multiple scales illustrate the heterogeneity of gold-bearing Apy₁ and Apy₂. Based on cross-sections through several grains, three arsenopyrite grains were selected to show the results of elemental X-ray mapping (Figs. 10 and 11). Note that it was not possible to separate Apy₁ grains from pyrrhotite or löllingite reliably for X-ray mapping. Thus, all grains show a pyrrhotite reaction front and the description of the elemental maps (Fig. 4-10A, D, G, and J – first column) will be done disregarding the close contact between these minerals. In addition, two maps with Apy₂ crystals are shown: a smaller disseminated grain (Fig. 4-8B, E, H, and K – second column) and a grain that coexists with löllingite and pyrrhotite (Fig. 4-10C, F, I, and L - last column).

The element distribution in Apy₁ shows a complex and irregular As, Fe and Ni zonation, whereas no significant zonation was observed with regard to Sb (Fig. 4-10). In general, the recognizable compositional variation reflects, from core to rim, increasing As and decreasing Fe contents. An isolated crystal of Apy₂ reveals a uniform distribution of As and Ni (Fig. 4-10B and H) and discrete compositional zoning for Fe and Sb (Fig. 4-10E, and K). Core and rim are slightly enriched in Fe and Sb, respectively. Arsenopyrite grains that are in contact with löllingite reveal a wide variation in As, Fe, and Sb contents. Their cores are As- (Fig. 4-10C) and Sb-rich (Fig. 4-10L) and correspondingly poor in Fe. However, Apy₂, with or without löllingite in its vicinity, is homogeneous with regard to Ni. The zone between arsenopyrite and löllingite is rimmed by a thin line showing a sharp increase in Bi and Au (also detected by spot analyses in many samples), followed by a sharp decrease in the content of these elements (Fig. 4-11).

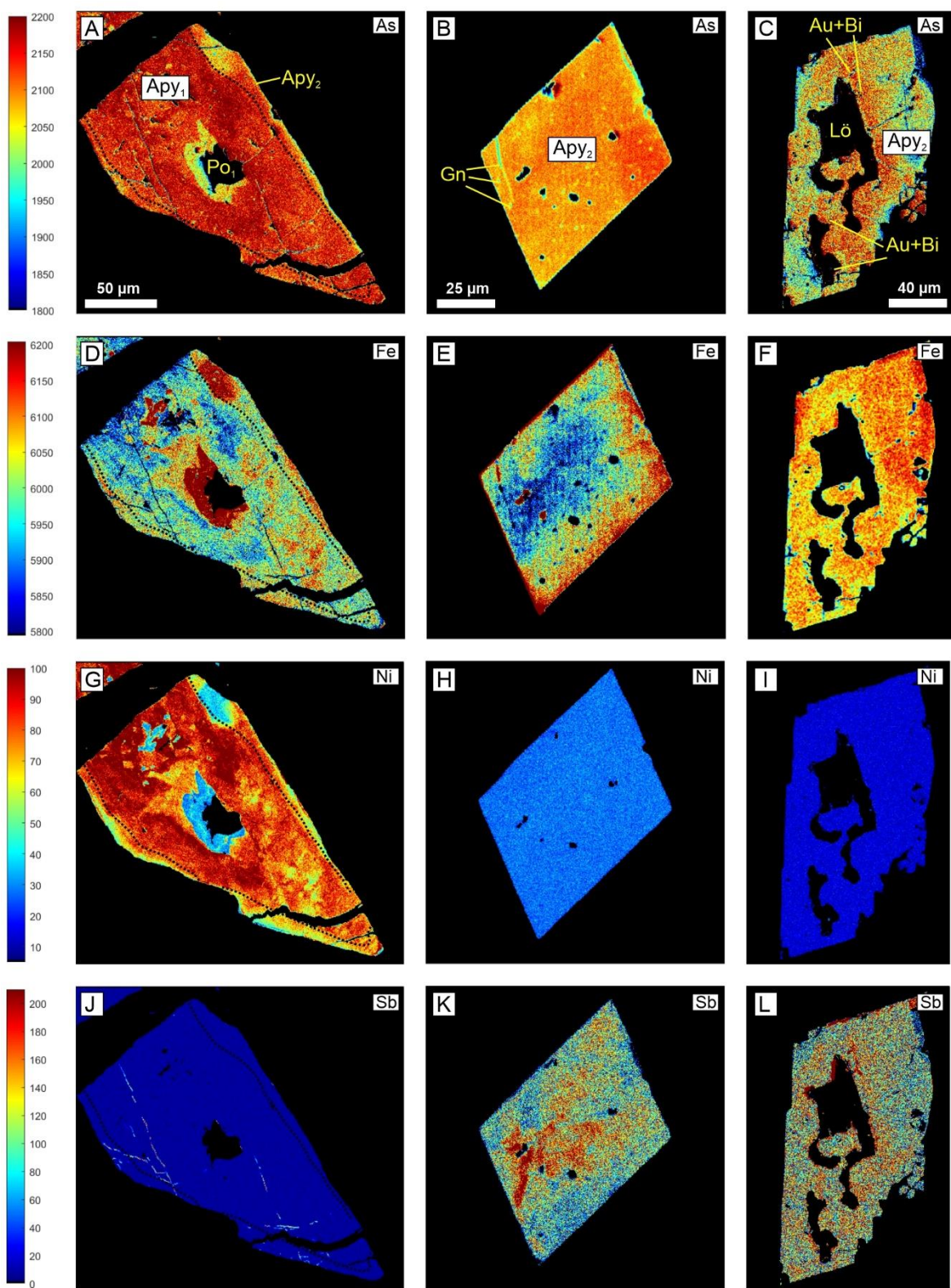


Fig. 4-10. X-ray mapping of representative arsenopyrite crystals which show the distribution of selected elements in sulfide stages I and II from Satinoco Deposit. (A-C, D-F, G-I, and J-L) are element mapping in counts from As, Fe, Ni, and Sb, respectively.

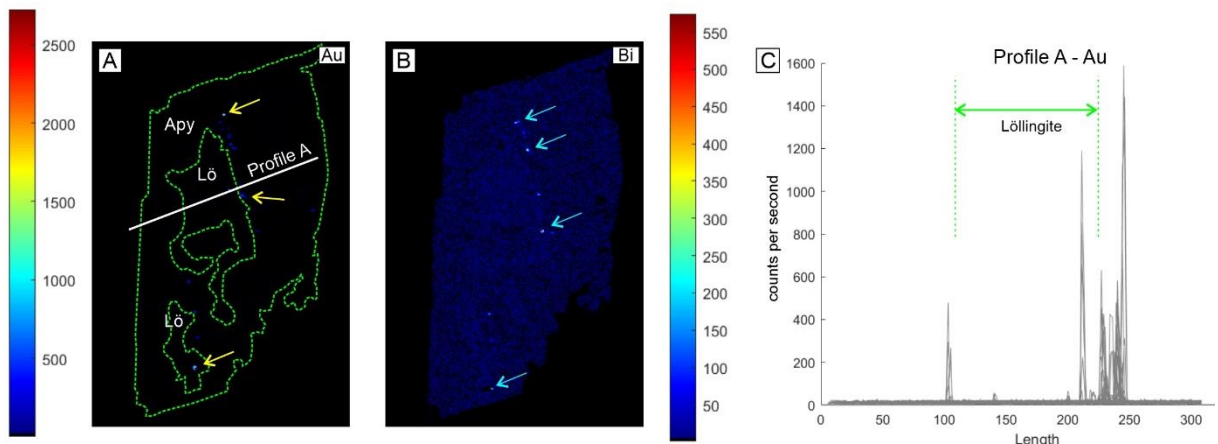


Fig. 4-11. Au and Bi element mapping of representative Apy_2 rimmed by löllingite in the Satinoco deposit. (A-B) are element mapping in counts from As and Bi, respectively. (C) Gold content illustrating the gold enrichment along with the contact between Lö and Apy. Note the following features highlighted in the figures: (i) the green dashed lines highlight the contour of the löllingite and arsenopyrite; (ii) the white line in (A) refers to profile represented in (C); (iii) the yellow and the light blue arrows indicate gold and bismuth inclusions, respectively.

LA-ICP-MS data

The trace element distribution in arsenopyrite and pyrite crystals differs in different sulfide assemblages (Fig. 4-12). The minor and trace element contents of the analyzed sulfides are summarized in Table 3 and all results are presented in App. Table A3. Note that the elements with the highest concentrations (i.e., Ni, Co, and Sb) and most of those with the lowest concentrations are consistent with the EMP results.

Trace elements contained in Apy_1 are dominated by Ni (2689-4901 ppm) and Mn (8.73-1700 ppm), in addition to Co (96.57-209 ppm), Zn (BDL-239 ppm), and V (BDL-83.74 ppm). Apy_1 has lower concentrations of Se (11.58-16.38 ppm), Pb (0.74-10.69), Bi (0.731-8.78 ppm), and Ag (0.35-1.67 ppm). All analyzed Apy_1 spots are

devoid of detectable Au. Compared to Apy₁ crystals, the Apy₂ contains higher abundances of Sb (0.86-2.1 wt.%), Co (194-524 ppm), Pb (BDL-1657 ppm), Au (0.21-794 ppm), and Ag (BDL-9 ppm) but lower contents of Zn (BDL-112.44), Se (BDL-7.13 ppm), Bi (BDL-3.64 ppm), and Cu (BDL-2.93 ppm). Representing the systematic Au-microfracture association with the low-melting point chalcophile elements (LMCE; Hg, Te, Sb, and Bi; as seen in Fig. 4-8J and L), one spot analysis in an intragrain microfracture within Apy₂ exposed high values of Au (21 wt.%), Sb (54 wt.%), and Ni (2.5 wt.%). This spot was not considered in the whisker and box diagrams of the Figure 12. Pyrite returned higher Cu (BDL-78.01 ppm), Se (9.77-36.81 ppm), Bi (0.04-33.51 ppm), Te (BDL- 7.04 ppm), and Ag contents (BDL-4.06 ppm) than Apy₁ and Apy₂.

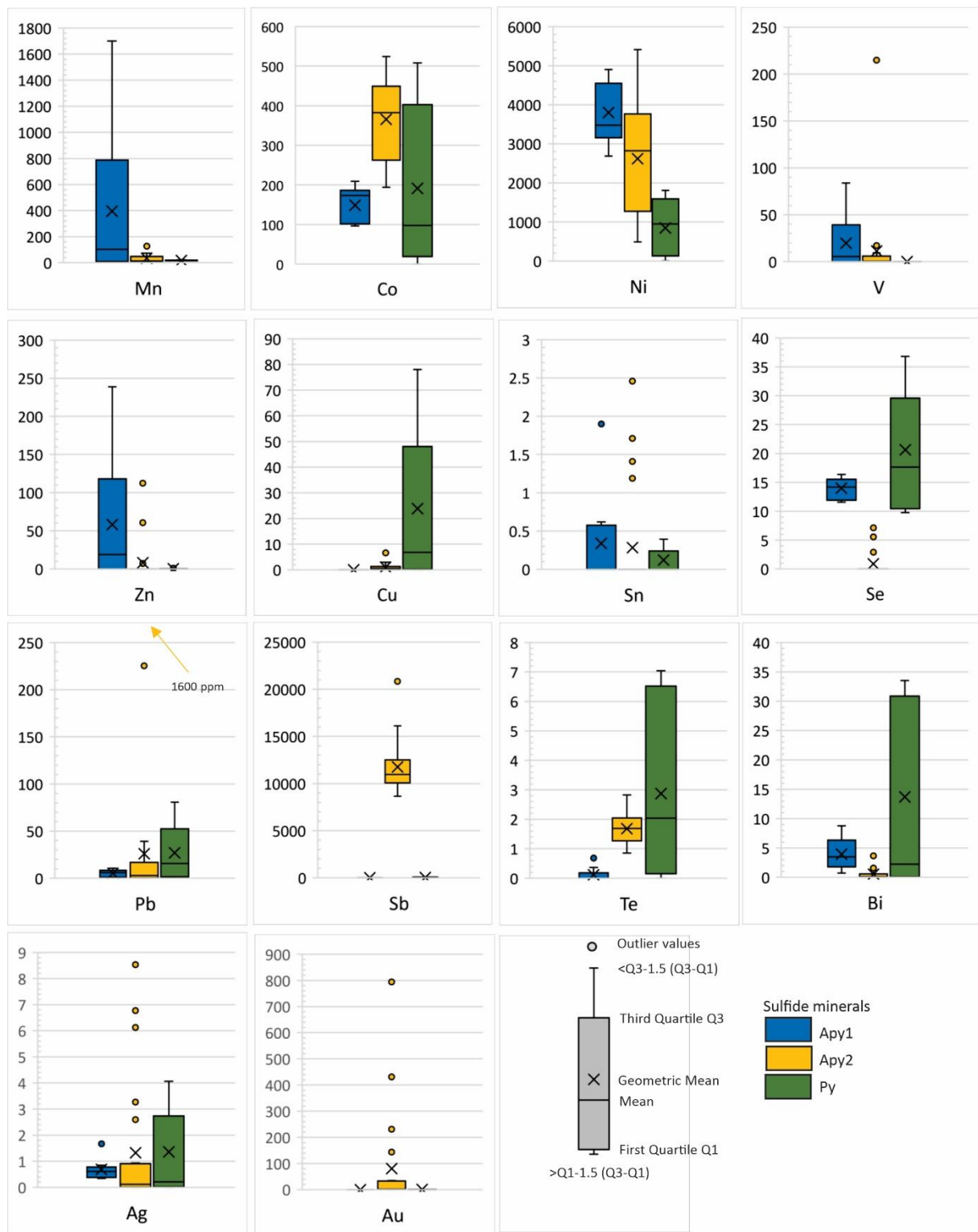


Fig. 4-12. Whisker and box diagrams of selected trace elements of Apy₁, Apy₂, and Py. The geometric mean (x), median (horizontal line), first quartile (Q1, lower limit of box) and third quartile (Q3, upper limit of box) are shown. Outlier values are shown as circles (see legend). The minor and trace elements composition can be found in Appendix Table A3.

Table 4-2. Summary of minor and trace element contents in sulfide minerals performed by LA-ICP-MS (data in ppm)

Mineral	V	Mn	Co	Ni	Cu	Zn	Se	Mo	Ag	Sn	Sb	Te	Pb	Bi	Au
Apy₁ (9)															
Mean	19.62	396.38	148.72	3803.12	BDL	58.04	14.00	BDL	0.69	BDL	0.69	0.12	5.29	3.94	BDL
Maximum	83.74	1700.53	209.06	4901.07	BDL	238.77	16.38	0.98	1.67	1.90	1.17	0.68	10.69	8.78	BDL
Minimum	0.00	8.73	96.57	2688.86	BDL	BDL	11.58	BDL	0.35	BDL	0.07	BDL	0.74	0.73	BDL
Standard deviation	29.73	611.37	45.87	806.81	-	83.77	1.82	-	0.41	-	0.38	-	3.63	2.87	-
Apy₂ (25)															
Mean	11.44	33.77	365.77	2618.78	0.74	8.06	BDL	BDL	1.33	0.28	11764.53	1.69	93.99	0.54	80.51
Maximum	214.76	164.82	524.20	5413.72	2.93	112.44	7.13	0.76	8.53	2.46	20838.09	2.83	1657.35	3.64	794.00
Minimum	BDL	10.83	194.00	488.00	BDL	BDL	BDL	BDL	BDL	BDL	8659.49	0.85	BDL	BDL	0.21
Standard deviation	43.51	39.71	106.01	1467.91	0.94	25.53	2.13	0.25	2.42	0.67	2717.98	0.52	338.86	0.92	186.23
Apy₂ fract (1)															
	BDL	26.88	455.86	25780.23	6.58	10.87	BDL	BDL	35.76	BDL	541413.63	30.00	16.77	107.93	213803.00
Py (7)															
Mean	0.07	17.54	191.40	844.74	23.88	BDL	20.64	0.22	1.36	0.12	22.55	2.87	26.90	13.71	0.33
Maximum	0.09	22.17	508.02	1805.81	78.01	0.94	36.81	0.38	4.06	0.39	67.74	7.04	80.63	33.51	0.74
Minimum	0.05	14.82	0.42	9.03	BDL	BDL	9.77	0.15	BDL	BDL	0.17	BDL	0.54	0.03	0.01
Standard deviation	0.02	2.41	202.98	724.13	29.58	-	11.09	0.08	1.69	-	30.83	2.88	30.54	16.28	0.29

BDL: below detection limit.

Zero values were used for statistical calculations of samples with values below detection limit

Numbers in parentheses refer to number of analyses

' refer to meaningless standard deviation, due to insufficient data exceeding detection limit

4.5.6 Geothermometry

Twelve pairs of the two garnet generations in equilibrium with biotite in different samples from the drill hole FTS-1406 (Table 4-4) were used to calculate the equilibrium temperature based on the exchange between the end-members almandine, grossular, spessartine, and pyrope, employing the TWQ thermodynamic database (version 2.10; Berman, 1991). We found several biotite inclusions in Grt₁ cores (Fig. 4-6A, B) but none of them were used for geothermometry because of their small size and partial chloritization. Using a pressure estimate of 3-4 kbar (Tassinari et al. 2015; Brando Soares et al. 2017; Fabricio-Silva et al. 2019), the temperatures calculated for each garnet generation were (Table 4-4) between 532 and 572 °C for Grt₁ rims, 618 to 640 °C for the Grt₂ cores, and 681 to 734 °C for Grt₂ rims. Note that the Grt₂ rims (Table 4: pairs SAT-3 to SAT-5) having reached values greater than 650 °C, might have undergone some resetting by volume diffusion (Spear 1991). Although several studies (Petrakakis 1986; Tuccillo et al. 1990; Cooke et al. 2000) claim that initial garnet compositions remained unchanged at peak temperatures of >650 °C, Caddick et al. (2010) argued that garnet, in order to preserve high-grade P-T conditions, should be at least 5 mm in diameter. In this study, the garnets used to calculate equilibrium temperatures reach as much as 25 mm in diameter. The rim-core-rim compositional profiles also show a very linear variation in Ca, Fe, Mg, and Mn distribution, suggesting that post-crystallization volume diffusion was insignificant.

The arsenopyrite analyses were used to estimate the equilibrium temperatures for each gold-bearing sulfide assemblage (Table 4-5; Fig. 4-13) according to the geothermometer proposed by Kretschmar and Scott (1976) and Sharp et al. (1985). Forty-one Apy₁ analyses with As contents ranging from 34.8 to 37.6 at. % were used and these yielded temperatures between 475 and 650 °C. In contrast to Apy₁, the Apy₂

compositions do not meet the reliability criteria for this geothermometer, because their combined concentrations of Co, Sb and Ni are >1 wt.%. Of the 36 analyses obtained, with As contents ranging from 33.6 to 35.1 at. % (Table 5), only four grains meet the above requirements and these yielded temperatures between 445 and 510 °C.

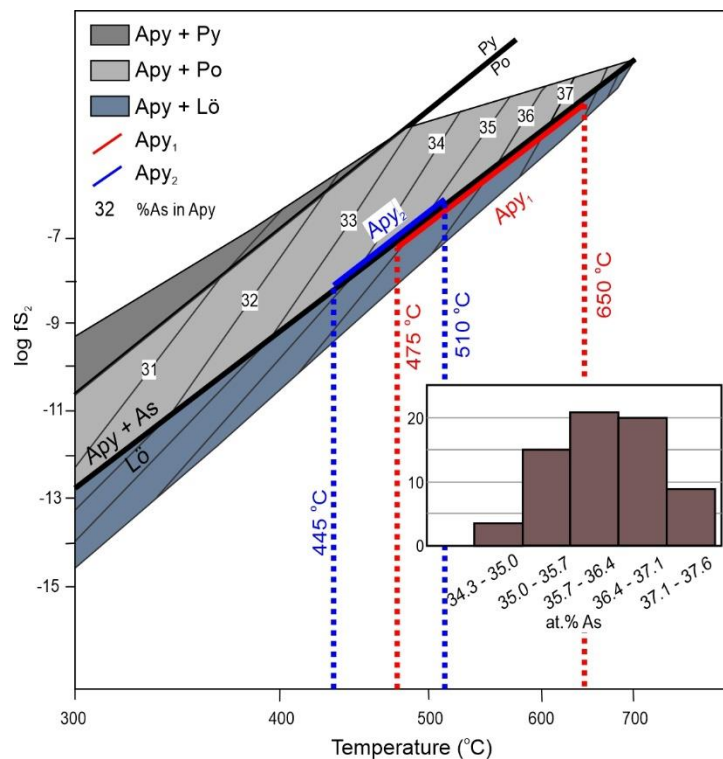


Fig. 4-13. Summary of variations in the As/S ratio of the studied arsenopyrite (inserted histogram), expressed atomic % of As and estimated sulfur fugacity and temperature evolution during sulfide stage I and II. The phase boundaries and arsenic isopleths are based on the data of Kretschmar and Scott (1976).

Table 4-3. Garnet and biotite electron microprobe analyses normalized to 12 O (garnet) and 22 O (biotite) used for the geothermometric calculations.

Pair	SAT-1	SAT-2	SAT-3	SAT-4	SAT-5	SAT-6	SAT-7	SAT-8	SAT-9	SAT-10	SAT-11	SAT-12	
Grt Generation	Grt ₂ core	Grt ₂ core	Grt ₂ rim	Grt ₂ rim	Grt ₁ rim	Grt ₂ core							
T (°C)	640	629	734	681	696	532	560	560	568	572	570	618	
Garnet analyses	SiO ₂	36.90	34.52	36.67	36.56	36.30	36.18	36.57	36.73	36.72	36.31	36.16	36.56
	Al ₂ O ₃	20.04	20.98	21.35	21.38	21.15	20.67	20.78	20.76	20.64	20.77	20.72	19.83
	FeO	24.17	33.68	23.82	23.62	21.98	38.31	37.24	38.47	38.06	35.48	36.45	27.88
	MnO	8.69	6.12	8.92	9.42	10.18	1.73	1.70	1.63	1.34	1.59	2.07	10.31
	MgO	1.38	1.96	2.25	2.12	1.79	1.66	1.81	1.88	2.04	1.69	1.59	1.78
	CaO	8.34	1.83	6.28	6.16	7.63	1.04	1.10	1.12	0.66	2.08	1.49	1.80
	Total	99.88	99.64	99.37	99.50	99.30	99.90	99.27	100.77	99.58	98.01	98.62	98.21
	Si	2.99	2.86	2.96	2.95	2.94	2.96	3.00	2.98	3.00	3.00	2.99	3.03
	Al	1.91	2.05	2.03	2.03	2.02	1.99	2.00	1.98	1.99	2.02	2.01	1.94
	Fe	1.64	2.33	1.61	1.59	1.49	2.63	2.55	2.61	2.60	2.45	2.52	1.93
	Mn	0.60	0.43	0.61	0.64	0.69	0.12	0.12	0.11	0.09	0.11	0.14	0.72
	Mg	0.17	0.24	0.27	0.25	0.22	0.20	0.22	0.23	0.25	0.21	0.20	0.22
	Ca	0.72	0.16	0.55	0.54	0.66	0.09	0.10	0.10	0.06	0.18	0.13	0.16
	Xalm	50.25	70.85	51.50	51.50	46.37	86.01	85.46	85.37	86.65	83.13	84.19	62.69
	Xgrs	19.88	1.61	15.64	17.46	20.79	1.68	2.98	1.52	1.64	5.68	4.01	1.70
	Xprp	5.58	8.44	9.13	8.62	6.88	6.86	7.39	7.62	8.31	6.96	6.57	7.43
	Xsps	19.95	15.03	20.61	21.83	25.39	4.04	3.94	3.75	3.06	3.72	4.85	24.47
Biotite analyses	SiO ₂	30.99	33.44	32.46	34.23	35.58	34.72	33.39	35.10	33.23	33.39	31.34	33.35
	TiO ₂	1.10	1.43	1.00	1.03	1.12	0.91	1.14	0.87	0.57	1.23	1.14	0.98
	Al ₂ O ₃	18.34	17.68	18.79	17.90	17.25	17.25	17.26	16.99	17.48	16.17	17.46	16.35
	FeO	29.11	29.77	28.91	28.45	28.33	28.52	28.91	27.91	27.93	29.35	30.20	29.97
	MnO	1.25	0.63	0.05	0.14	0.24	0.21	0.27	0.22	0.23	0.34	0.57	0.68
	MgO	7.34	7.43	7.35	8.06	7.02	7.14	7.65	7.46	7.97	7.91	7.32	7.96
	CaO	0.09	0.09	0.21	0.78	0.23	0.10	0.09	0.05	0.29	0.12	0.13	0.15
	Na ₂ O	0.01	0.04	0.08	0.03	0.05	0.06	0.04	0.08	0.03	0.02	0.06	0.03
	K ₂ O	4.61	5.01	3.99	3.11	4.55	4.80	3.42	5.15	4.46	4.16	4.59	3.46
	Cr ₂ O ₃	0.39	0.33	0.34	0.02	0.28	0.32	0.34	0.33	0.30	0.34	0.31	0.20
	NiO	0.03	0.01	0.00	0.06	0.05	0.03	0.06	0.05	0.05	0.08	0.01	0.02
	Total	93.25	95.86	93.17	93.81	94.69	94.04	92.56	94.21	92.53	93.11	93.11	93.14
	Si	5.02	5.24	5.17	5.36	5.54	5.47	5.34	5.51	5.33	5.36	5.09	5.35
	Ti	0.13	0.17	0.12	0.12	0.13	0.11	0.14	0.10	0.07	0.15	0.14	0.12
	Al	3.50	3.26	3.53	3.30	3.17	3.20	3.25	3.15	3.30	3.06	3.34	3.09
	Fe	3.94	3.90	3.85	3.73	3.69	3.76	3.87	3.67	3.75	3.94	4.10	4.02
	Mn	0.17	0.08	0.01	0.02	0.03	0.03	0.04	0.03	0.03	0.05	0.08	0.09
	Mg	1.77	1.73	1.74	1.88	1.63	1.68	1.82	1.75	1.90	1.89	1.77	1.90
	Ca	0.02	0.02	0.04	0.13	0.04	0.02	0.02	0.01	0.05	0.02	0.02	0.03
	Na	0.00	0.01	0.02	0.01	0.01	0.02	0.01	0.02	0.01	0.01	0.02	0.01
	K	0.95	1.00	0.81	0.62	0.90	0.97	0.70	1.03	0.91	0.85	0.95	0.71
	Total	19.55	19.45	19.34	19.18	19.19	19.29	19.23	19.32	19.39	19.37	19.56	19.34

Table 4-4. Representative arsenopyrite composition obtained by electron microprobe analyses, minerals in equilibrium in the Fe-As-S system, and temperature calculation (according to Kretschmar and Scott, 1976; and Sharp et al., 1985)

Stage	Composition (wt.%)								Composition (at.%)		
	Co	Ni	Sb	Pb	Fe	As	S	Total	Fe	S	As
I	0.50	0.41	0.10	0.02	33.70	47.29	17.15	99.16	33.77	29.94	35.33
I	0.06	0.05	0.17	0.00	34.51	47.70	18.24	100.72	33.81	31.14	34.84
I	0.20	0.14	0.14	0.00	33.71	49.24	17.56	101.00	33.23	30.16	36.18
I	0.21	0.21	0.03	0.10	33.87	48.95	17.24	100.62	33.59	29.79	36.18
I	0.07	0.13	0.44	0.02	33.49	48.44	18.19	100.78	32.93	31.17	35.51
I	0.07	0.58	0.53	0.02	32.06	49.46	17.11	99.83	32.19	29.92	37.01
I	0.02	0.06	0.14	0.15	33.26	47.72	18.52	99.86	32.83	31.85	35.12
I	0.05	0.58	0.61	0.10	32.18	49.95	16.69	100.16	32.37	29.24	37.45
I	0.08	0.70	0.39	0.15	32.62	50.17	16.76	100.87	32.62	29.09	37.31
I	0.09	0.48	0.25	0.07	32.99	49.98	17.00	100.86	32.80	29.44	37.05
I	0.04	0.36	0.05	0.11	32.90	49.69	17.39	100.54	32.67	30.09	36.79
I	0.12	0.42	0.15	0.07	32.88	49.85	17.39	100.88	32.63	29.96	36.81
I	0.08	0.31	0.27	0.04	33.12	49.51	17.19	100.51	33.02	29.86	36.70
I	0.04	0.00	0.30	0.14	33.36	47.69	18.41	99.94	32.96	31.69	35.13
I	0.00	0.05	0.03	0.18	33.81	48.14	18.31	100.52	33.24	31.36	35.29
I	0.02	0.07	0.63	0.00	33.45	48.11	17.98	100.24	33.11	31.01	35.49
I	0.07	0.09	0.41	0.15	33.55	48.29	17.80	100.35	33.23	30.71	35.66
I	0.05	0.12	0.43	0.00	33.36	48.22	17.88	100.07	33.06	30.87	35.63
I	0.09	0.76	0.14	0.11	32.59	50.28	16.53	100.50	32.66	28.86	37.56
II	0.07	0.01	0.83	0.10	34.20	46.85	18.51	100.57	33.57	31.66	34.29
II	0.67	0.30	0.14	0.09	34.49	46.36	18.81	100.86	33.53	31.86	33.60
II	0.31	0.49	0.02	0.00	34.92	47.36	17.05	100.15	34.67	29.50	35.06
II	0.41	0.42	0.49	0.12	34.90	46.78	17.14	100.26	34.65	29.65	34.63

4.6 Discussion

4.6.1 Paragenetic sequence of the hydrothermal alteration minerals

At least four hydrothermal alteration stages can be differentiated (Fig. 4-14): (i) an early stage I that affected the host rocks by silicification, sulfidation and biotitization; (ii) an Fe-rich metasomatic stage II; (iii) stage III, involving carbonate alteration with introduction of base metal-rich sulfides; and (iv) a post-ore carbonatization and chloritization stage IV.

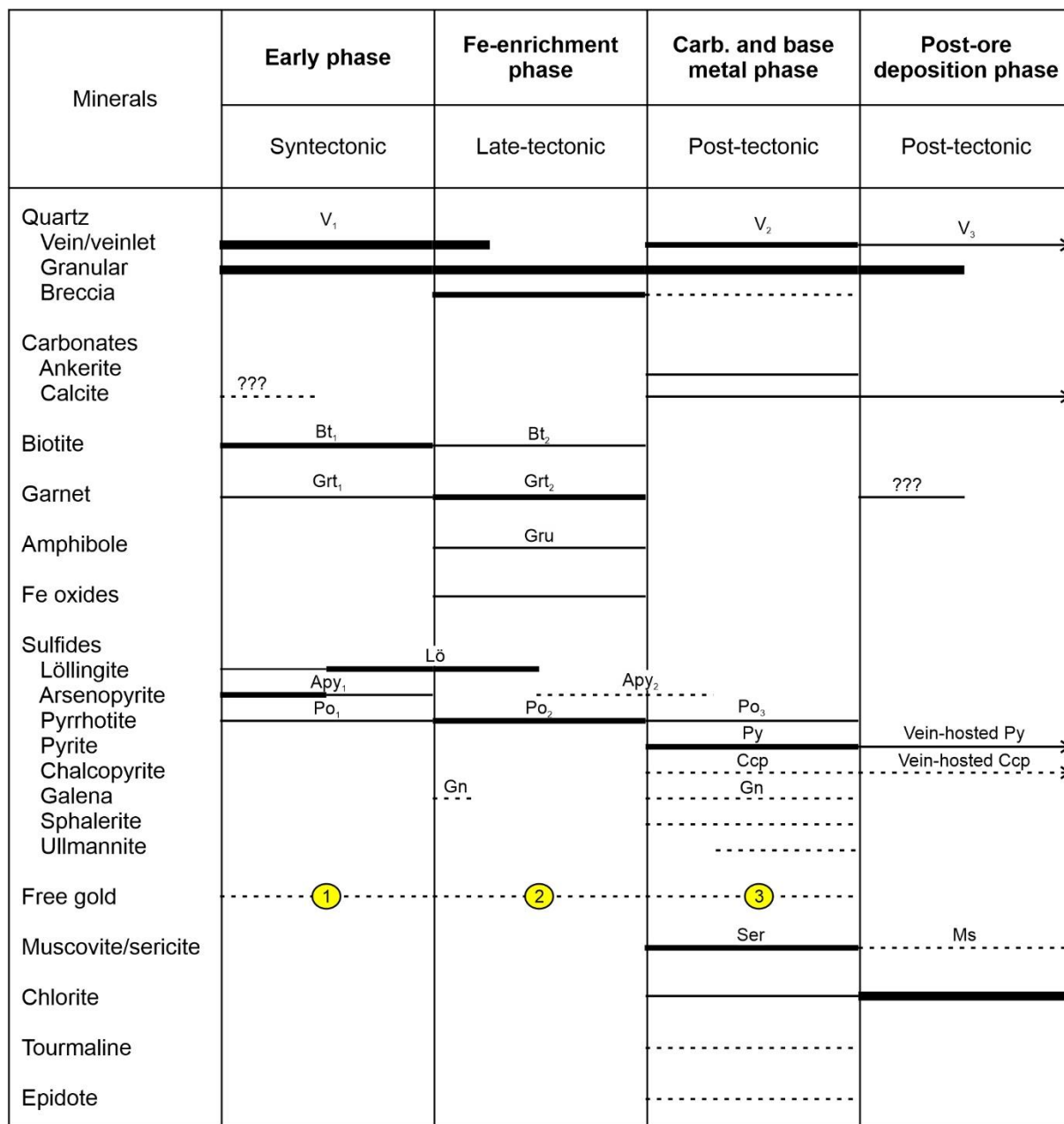
The early hydrothermal stage I is marked by a large volume of silica resulting from the formation of V₁ veins and quartz precipitation. It is also manifested by the crystallization of the gold-bearing arsenopyrite-pyrrhotite-löllingite sulfide assemblage I and hydrothermal phlogopite (Bt₁). The first stage of hydrothermal alteration is spatially restricted to the proximal alteration zone and occurred during the progressive D₁₋₂ event, evidenced by: (i) the strong structural control and V₁ vein stretching, with the generation of the boudin and pinch-and-swell structures; (ii) crosscutting relationship of the sulfide assemblage I; and (iii) structural relation of garnet Grt₁ with the S₁ foliation.

The second and most voluminous hydrothermal alteration (stage II) is represented by the Fe-rich mineral assemblage pyrrhotite (Po₂) + grunerite + biotite (Bt₂) ± magnetite besides quartz, tourmaline and gold-bearing sulfide assemblage II (Po₂-Apy₂-Gn). Grunerite replaced cummingtonite and S₁-parallel actinolite, thus resulting in a lepidoblastic fabric. Eastonite and phlogopite were overprinted by siderophyllite that defines the S₂ foliation. This stage is related to the last phases of D₂, as indicated by: (i)

absence of ductile deformation in the Casquilho granite; (ii) the porphyroblast-matrix relations of Grt_2 ; and (iii) the fact that the granite stock (and the most of the apophyses) cut the pinch-and-swell structures.

The carbonate and base metal-rich alteration stage III formed the quartz-sericite-ankerite-chlorite-calcite-sulfide (pyrite-pyrrhotite-chalcopyrite \pm galena \pm sphalerite \pm ullmannite) assemblage III and also involved the growth of epidote in the alteration zones. This stage partially replaced the Fe-rich phases of stage II in the proximal zone and proximal-intermediate zones. The stage III caused a large amount of carbonate and sericite, with recrystallization of earlier formed sulfides. The sericite-rich bands, which contain epidote, cut the S_2 foliation, suggesting that the epidote post-dates both D_2 and the mineralization stages I and II.

The post-ore alteration stage IV is characterized mainly by the generation of the quartz-calcite V_3 veins and by the formation of chlorite and muscovite. Sulfide alteration at this stage was restricted to the barren assemblage of pyrite-chalcopyrite within the V_3 veins. It was not possible to accurately establish the temporal relationship of the chlorite-muscovite assemblage and the generation of these veins. Presumably, the most voluminous chloritization occurred at a post- D_{1-2} re-equilibration stage, and the discordant V_3 quartz veins are younger but probably still Neoarchean in age.



<5 vol.% ----- 10-15 vol.% ——————
 5-10 vol.% —————— >15 vol.% ——————

(1) Gold mineralization stage I (3) Gold mineralization stage III
 (2) Gold mineralization stage II

Fig. 4-14. The hydrothermal alteration stages and the paragenetic sequence of ore and gangue minerals in Satinoco Deposit.

4.6.2 The sulfide assemblages

P-T constraints and sulfide paragenesis

This study made it possible to better understand the temporal relation between multiple hydrothermal alteration stages and sulfide assemblages as illustrated in Figure 15. The peak metamorphism at the Satinoco deposit reached more than 730 °C and overprinted the sulfide assemblage I but preceded sulfide stage II, as shown above.

We suggest that Apy₁ and its subsequent replacement by löllingite and pyrrhotite occurred during prograde metamorphism, following the reaction $2\text{FeAsS} \rightarrow \text{FeAs}_2 + \text{FeS} + 0.5\text{S}_2$ (Barnicoat et al., 1991). This reaction was simulated experimentally by Tomkins and Mavrogenes (2001) using pressure and temperature conditions (3 to 5 kbars, 300 to 650 °C) similar to those established for Satinoco and other nearby deposits (Tassinari et al. 2015; Brando Soares et al. 2018). According to Tomkins and Mavrogenes (2001), all prograde experiments produced löllingite and pyrrhotite at or above 550 °C. This temperature is compatible with that obtained in this study for Apy₁ (475 - 650 °C, mean = 580 °C; see histogram in Fig. 4-13).

The compositional zonation noted in the garnet, that is, the decrease in spessartine component from core to rim, is typical of growth under prograde metamorphic conditions, with the late-tectonic Grt₂-rims recording the highest temperatures (691 - 734 °C). As Apy₁ grew syn-kinematically with regards to S₁ foliation (and as inclusions in the cores of Grt₂), the sulfide assemblage I must pre-date the metamorphic peak. This early assemblage was associated with progressive D₁₋₂, as demonstrated by the

circular and helicitic sulfide inclusions in Grt₁ and Grt₂, as well as in the overlap of the temperatures obtained by garnet-biotite and arsenopyrite geothermometry. During this stage, some of the arsenopyrite grains were replaced by löllingite and only the larger grains or those included in garnet survived as relicts.

We regard löllingite as product of the prograde reaction between Apy₁ + Po₁, as indicated by löllingite rims around Apy₁ grains (Fig. 4-8F, G). During retrograde metamorphism, such löllingite is expected to be completely consumed to form arsenopyrite (our Apy₂, see below) as experimentally demonstrated by Tomkins and Mavrogenes (2001) and observed at other localities (Deol et al., 2012; Saintilan et al., 2017) via the reaction $\text{FeAs}_2 + (1/x)\text{FeS}(1 + x) \rightarrow 2\text{FeAsS} + ([1+x]/x)\text{FeS}$ (Neumayr et al., 1993).

The sulfide assemblage II developed during post-peak metamorphic cooling. Our results indicate that Apy₂ replacement started at temperature >500 °C and continued down to at least 445 °C. Based on the textural relationship and the absence of Apy₂ inclusions in Grt₂, this temperature probably represents the final phase of crystallization of the sulfide stage II. The replacement of löllingite and pyrrhotite by Apy₂ is also critical in this regard. Löllingite replacement during retrograde metamorphism invariably led to Co enrichment in Apy₂, because Lö is richer in Co than Apy₁; Appendix Table A2) and uneven distribution of Bi (Fig. 4-8H and 11B) and Pb (Fig. 4-10). A similar redistribution of elements and enrichment in Co of retrograde arsenopyrite has been reported from the Broken Hill Block (Saintilan et al. 2017b). The brittle deformation conditions observed in the Apy₂ crystals, associated with X-ray compositional maps, indicate that fracturing occurred in the final stages of löllingite replacement and before the stage III. Therefore, the late stage II took place at the brittle-ductile transition, which was reached at estimated temperatures and pressures of 550-450 °C and 2-1.5 kbar, respectively.

The Satinoco deposit is also marked by a large amount of pyrite from the alteration stage III. Pyrite in the sulfidic equilibrium assemblage pyrite-pyrrhotite \pm chalcopyrite \pm galena \pm Sb-Ni-Cu-Zn-sulfides cuts minerals from stage II, in places associated with S_2 foliation or V_2 quartz-carbonate veins. Fluid inclusion microthermometry performed in the neighboring Turmalina deposit (Tassinari et al. 2015) shows that the earlier (high-temperature aqueous-carbonic) metamorphogenic fluids were subjected to repeated boiling and mixing with cooler aqueous solutions at approximately 1-2 kb and 300-350 °C. The mineralogy and temperatures obtained by Tassinari et al. (2015) are equivalent to the sulfide assemblage III here and were also observed by Fabricio-Silva et al. (2019) and Brando Soares et al. (2018) in the Turmalina and São Sebastião deposits, respectively.

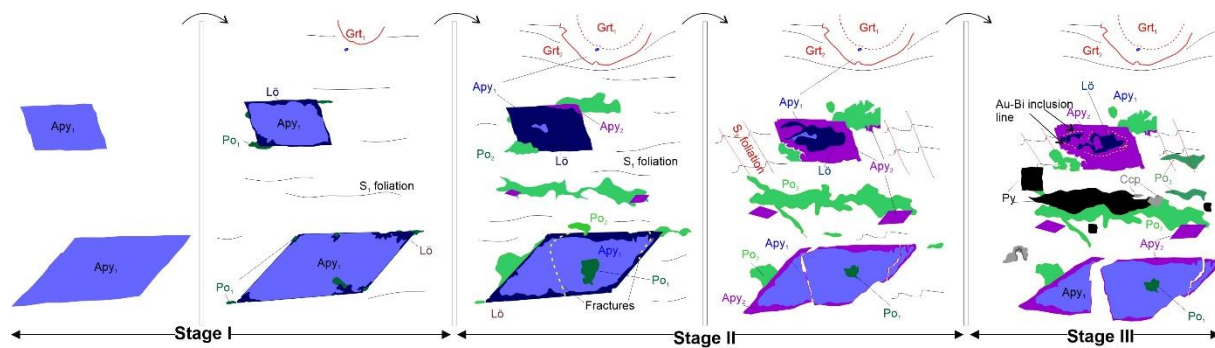


Fig. 4-15. Geological evolution of the Satinoco deposit based on gold-bearing sulfide (re)crystallization. (A) Early sulfide phase. (B) Fe-rich sulfide phase. (C) Carbonate and base metal sulfide phase. Apy – arsenopyrite; Ccp – chalcopyrite; Gn – galena; Grt – garnet; Lö – löllingite; Po – pyrrhotite; Py – pyrite.

Pre-metamorphic pyrite

Although the oldest sulfide observed in the orebodies is Apy₁, this arsenopyrite is unlikely to have been the starting material in the protolith but may have been derived from a previous pre-hydrothermal pyrite (assemblage 0). Such pyrite occurs in black shales outside of the mineralized zone of Satinoco. Recently, Bosco-Santos et al. (2020) suggested a syngenetic origin for the Satinoco pyrite in these marine shales farther away from the ore shoots, based on iron speciation, the distribution of trace redox-sensitive metals, and sulfur isotope ratios ($\delta^{34}\text{S}$, $\Delta^{33}\text{S}$, and $\Delta^{36}\text{S}$), all of which indicate early inputs of sulfate from an oxidative environment.

In the mineralized zone, this syngenetic pyrite probably was completely replaced by the syntectonic Apy₁. This is suggested by the observed coexistence of arsenopyrite with löllingite where the orebodies cut across the black shales. Based on a textural relationship, Frizzo et al. (1991) described a sulfide paragenesis with pyrite and arsenopyrite in other prospects in the Pitangui greenstone belt where it did not experience amphibolite-facies conditions. Note that pyrite and löllingite cannot coexist at any P-T conditions (Kretschmar and Scott, 1976). Further support for Apy₁-formation at the expense of syngenetic pyrite comes from the straight inclusion trails in Grt₁, which indicate that the As-S-Fe gold-bearing sulfide assemblage I had already existed at the early stage of D₁.

Au and elemental composition of the sulfides

Our LA-ICP-MS and EMP data indicate that there are at least three auriferous sulfide assemblages. The compositional zonation observed in the arsenopyrite and pyrite grains reflects, at least in parts, metal availability during the growth and metamorphism of these grains.

The oscillatory distribution of As in Apy₁ may be due to short-lived variations in the Fe and As concentrations of the mineralizing fluid. With progressive deformation and shearing at increasing temperature, the rims of Apy₁ became enriched in As and replaced by löllingite. The features noted in regard to minor and trace element distribution in the various parageneses show that the early hydrothermal stage, responsible for the sulfide stage I, involved an enrichment in Ni, Mn, Zn, and V, with lesser Bi and Se. Circulation of new Fe-rich fluids generated the pyrrhotite-dominated hydraulic breccias and was concomitant with the transformation of löllingite-pyrrhotite to Apy₂ during subsequent cooling of the host rocks. These Fe-rich fluids were also responsible for a notable enrichment in Co, Sb, and Pb during the gold mineralization stage II, besides Ag and Au.

Finally, the carbonate alteration and base metal stage fluids were enriched in Cu, Se, Bi, and Te, and to a lesser extent in Pb and Sb. During this stage, dissolution-reprecipitation of pyrite led to the release of Au and precipitation of gold in microfractures under greenschist-facies conditions.

In combination with textural observations, the EMP data and X-ray mapping indicate that Au was initially concentrated in Apy₁. However, the Au contents in Apy₁ were below

the detection limit of the LA-ICPMS. This may be an artifact of the smaller number of analyzes in Apy₁ obtained by LA-ICPMS ($n = 9$) as opposed to those by EMP ($n = 73$), of which only 13 points returned values above the detection limit. We also emphasize the dominance of the occurrence of gold as micro inclusions in Apy₁. The relationship between the texture of löllingite rimmed by Apy₂ and the trend of Au and Bi inclusions (Fig. 4-11B) indicates that invisible gold must have been present in Apy₁. During retrograde metamorphism, Apy₂ formed gold-rich rims around löllingite, implying the exsolution of gold during the retrograde stage (cf. Neumayr et al., 1993; Tomkins and Mavrogenes, 2001). This interpretation is also supported by the profiles of EMP spot analyses on the arsenopyrite grains and Sb-Ni- and Au-rich microfractures observed in LA-ICPMS data (Table 3). As arsenopyrite commonly rims the löllingite, the highest average gold contents are now in the Apy₂.

4.6.3 Age of the TTG-greenstone terrane and timing of gold mineralization

The relative sequence of mineralization stages established in this study, combined with several, partly very recent, publications on the geochronology of the study area, makes it possible to better constrain the chronology of gold mineralization in the Satinoco deposit. Gold mineralization and associated hydrothermal minerals are spatially related with, and hosted within, D₂ shear zones. The first deformation event recorded in the basal komatiites in the Iron Quadrangle (Rio das Velhas and Pitangui greenstone belts) occurred in a collisional phase between 2780 and 2730 Ma (Baltazar and Zucchetti 2007; Brando Soares et al. 2020). The tectonic collapse between the Belo Horizonte and Divinópolis TTG complexes started at c. 2730 to 2720 Ma (Brando Soares et al. 2020) and corresponds to D₂. Based on our observed relationship between sulfide assemblages, garnet porphyroblasts and S₁ foliation, the gold mineralization stage I must predate 2720 Ga (D₂). Additionally, inclusion bands (Fig. 4-5B) show that the S₁ foliation is older than the V₁ veins, which implies that the sulfide assemblage I predates the D₂ pinch-and-swell structures. Thus, the age of the V₁ veins and the shear zones can be confined between that of the S₁ foliation and the granite intrusion (Figs. 3, 5B).

As the mineralization stage II comprises recrystallized sulfide aggregates transposed within the S₂ foliation, the main gold-bearing event must have started after (or maybe during) D₂ but before the Casquilho granite emplacement (Fig. 4-5D, F), i.e., between c. 2720 and 2695 Ma. This is further supported by some V₂ veins being cut by granite apophyses. Mapping of the surface above the nearby Turmalina deposit (Fabricio-Silva, 2016; Fabricio-Silva et al., 2019) revealed that some granite apophyses are cut by faults that are filled with quartz veins analogous to the V₂ veins at Satinoco. Thus, a temporal relationship between granite emplacement, especially late-magmatic apophyses, and the development of these veins can be inferred. Yet, as indicated by the somewhat

lower temperatures obtained for Apy₂ and the observed alteration assemblages, the mineralization stage II continued to lower temperatures as the granitic body cooled, i.e., after 2695 Ma. However, the stage II probably occurred before 2684 Ma, the maximum depositional age of non-mineralized upper units of the Pitangui Group.

The subsequent gold-bearing sulfide assemblages III formed during retrograde metamorphism. Considering the fracture-controlled texture of stage III, the final gold stage took place after the ductile to brittle deformation transition in the upper part of the Pitangui Group had been reached. This implies that the gold mineralization stage III occurred after the maximum depositional age (2684 Ma; Marinho et al., 2018) of the quartzite in the upper units of the Pitangui greenstone belt.

Based on the available geochronological data, we advocate that the mineralization process in the Satinoco deposit lasted for at least 36 million years (2720-2684 Ma). However, considering the age of the last felsic magmatism in the area as represented by the Caio Martins granodiorite (2593 ± 19 Ma; Romano, 1993), it is possible that the sulfide assemblage III is even younger and/or might represent a short-lived, separate, event at around 2600 Ma. In that case, the multi-stage hydrothermal history (sulfide assemblages I, II, and III) might have lasted for more than 100 Myr (>2720 to c. 2600 Ma).

4.6.4 Role of granite in the mineralization history

The tectonic settings of orogenic gold deposits are relatively well-established thanks to a large number of studies (e.g., review by Groves et al., 2018) but the genesis of this

deposit type remains a matter of debate. Most researchers argue for gold having been introduced into the host rocks by metamorphic fluids (e.g., Tomkins, 2013; Goldfarb and Groves, 2015) during the accretion and/or collision of orogenic belts. The role of granitic magmatism in the formation of orogenic gold deposits is, however, uncertain and contested. Although many orogenic belts contain voluminous intrusive magmatic bodies, a derivation of gold and/or the mineralizing fluids from such bodies has been questioned because the suspected causative granite bodies are located, in most cases, several kilometers away from the gold deposits (Groves et al. 2019). The Satinoco deposit (this study) and the nearby Turmalina deposit (Fabricio-Silva et al., 2019) provide good examples of a close spatial, and possibly temporal, relationship between granitic magmatism and gold mineralization.

Our results indicate an increase in the temperature recorded after D₂ ductile deformation and before the D₃ ductile-brittle event at Satinoco. Together with geochronological data discussed above, we suggest that granitic magmatism, peak metamorphism, and the generation of considerable volumes of hydrothermal fluids were broadly coeval.

Granitic magma ascended in the final stage of D₂, synchronously with the gold-bearing sulfide stage I, and locally caused contact metamorphism (Fig. 4-4). The peak metamorphic assemblages in the immediate vicinity of the orebodies (Qtz + Grt + Cum + Act + Bt in the metabasalt and Qtz + Grt + Cum + Ilm ± Str in the interleaved metatuffs) is of a distinctly higher grade than in the intermediate zone (upper greenschist facies) about 7 m from the orebodies, and the regional metamorphism (lower greenschist facies) farther away. Staurolite, and most large garnet, is restricted to the contact metamorphic assemblage, both at Satinoco (in the easternmost area of the deposit) as well as the adjacent Turmalina deposit (Fabricio-Silva et al. 2019). The Qtz + Chl ± Grt assemblage, described from the intermediate zone, represents a cooler

phase relative to the metamorphic peak in the proximal halo. Finally, regional metamorphism in the Satinoco deposit must be younger than the granitic magmatism because it can be related, on textural grounds, to the replacement of contact metamorphic garnet, biotite, and staurolite by chlorite.

Bosco-Santos et al. (2020) analyzed S isotopes in sulfides along a drill hole from the Satinoco deposit. They observed that, in general, the $\delta^{34}\text{S}$ ratios increase from -5 to 8 ‰ and $\Delta^{33}\text{S}$ from -1 to 5‰ with proximity to the mineralized zone. Combined with iron speciation and $\Delta^{36}\text{S}$, the authors argued for a mixture of S from metamorphic fluids and S from the original sediments. The observation of photolytic S fractionation (S-MIF) produced in an anoxic Archean atmosphere support an incomplete overprint by metamorphic- and/or magmatic-hydrothermal alteration through the drill core, with primary S source preserved (as sulfide assemblage 0) farthest from the orebodies. Thus, their data show an increase of higher S-MIF closer to the ore shoots and the values increase proportionally with proximity to the ore shoots. Elsewhere in the Iron Quadrangle, Bühn et al. (2012) studied the S isotopic composition of gold-bearing sulfides in the Cuiabá ($\delta^{34}\text{S} = 3.8$ to 5.1‰) and São Bento ($\delta^{34}\text{S} = 2.9$ to 6.1‰) deposits (eastern Iron Quadrangle) and concluded that the source of the S was metamorphic. There is no late intrusive magmatism surrounding the Cuiabá and São Bento deposits and their data show less variable and overall higher average ratios ($\delta^{34}\text{S} = 4.45$ and 4.5‰ , respectively, against 1.5‰ in Satinoco) than in the Satinoco deposit. Considering the synchronism of granite apophyses related to the mineralization stage II, this observation indicates that the mixture of fluids (also based on iron speciation and $\delta^{36}\text{S}$ ratios; cf. Bosco-Santos et al., 2020) probably incorporated magmatic-derived ones, bringing the S isotope ratios closer to zero.

Sulfur isotope data in sulfides from the nearby Turmalina deposit have been used to suggest a mixed magmatic and metamorphic S source (Fabricio-Silva et al. 2019).

Additionally, the highly ferruginous nature of stage II assemblage (garnet-pyrrhotite-grunerite-siderophyllite) and a relatively low base metal content, as documented by our LA-ICPMS data for Apy₂, are in line with a derivation of the mineralizing fluid from granitic magma. Thus, the Fe-metasomatic alteration stage II can be interpreted as the product of mixing of late magmatic and metamorphic fluids, at T-P conditions of 550-450 °C and 2-1.5 kbar. This process is ascribed to crustal uplift and/or exhumation, synchronously with the late phase of the granite emplacement. Stage II mineralization was likely associated with significant hydrothermally activity as generated by both prograde metamorphic dehydration reactions and the addition of magmatic fluids to the mineralizing system.

Higher Co:Ni ratios (usually greater than 1) are commonly associated with hydrothermal Fe-sulfides (Bajwah et al. 1987), although Bierlein et al. (2016) cautioned that geological evidence should be given priority because some hydrothermal pyrite can have a Co:Ni ratio of less than 1. In the Satinoco deposit, the Co:Ni ratio ranges as follows (App. Table A3): Apy₁ (0.02 – 0.07, average 0.18); Apy₂ (0.02 – 0.48; average 0.04), and Py (0.05 – 0.35; average 0.19). The high values of Ni concentration can be explained by fluid/rock interaction, because ultramafic and mafic rocks have concentrations on the order of c. 2200 (Palme and Jones 2003) and c. 150 ppm (Hofmann 1988), respectively. However, in the case of Satinoco, while the fluid volume increased, Ni concentrations progressively decreased from the sulfide stage I to stage II, which can be explained by the presence of hydrothermal fluids derived from acidic magmatism.

Magmatogenic hydrothermal deposits are usually regarded as having formed over a relatively short time span, depending on the cooling rate of the causative intrusive body (e.g., Tomkins, 2013). From our observations we conclude that mineralization at Satinoco involved magmatogenic fluids, at least for stage II, the timing of which can be

constrained between c. 2695 Ma, the crystallization age of the causative granite (de Melo-Silva et al., 2020) and 2684 Ma, the best available age for the Pitangui Group (Marinho et al., 2018). The true period of stage II mineralization within this time window was probably much shorter.

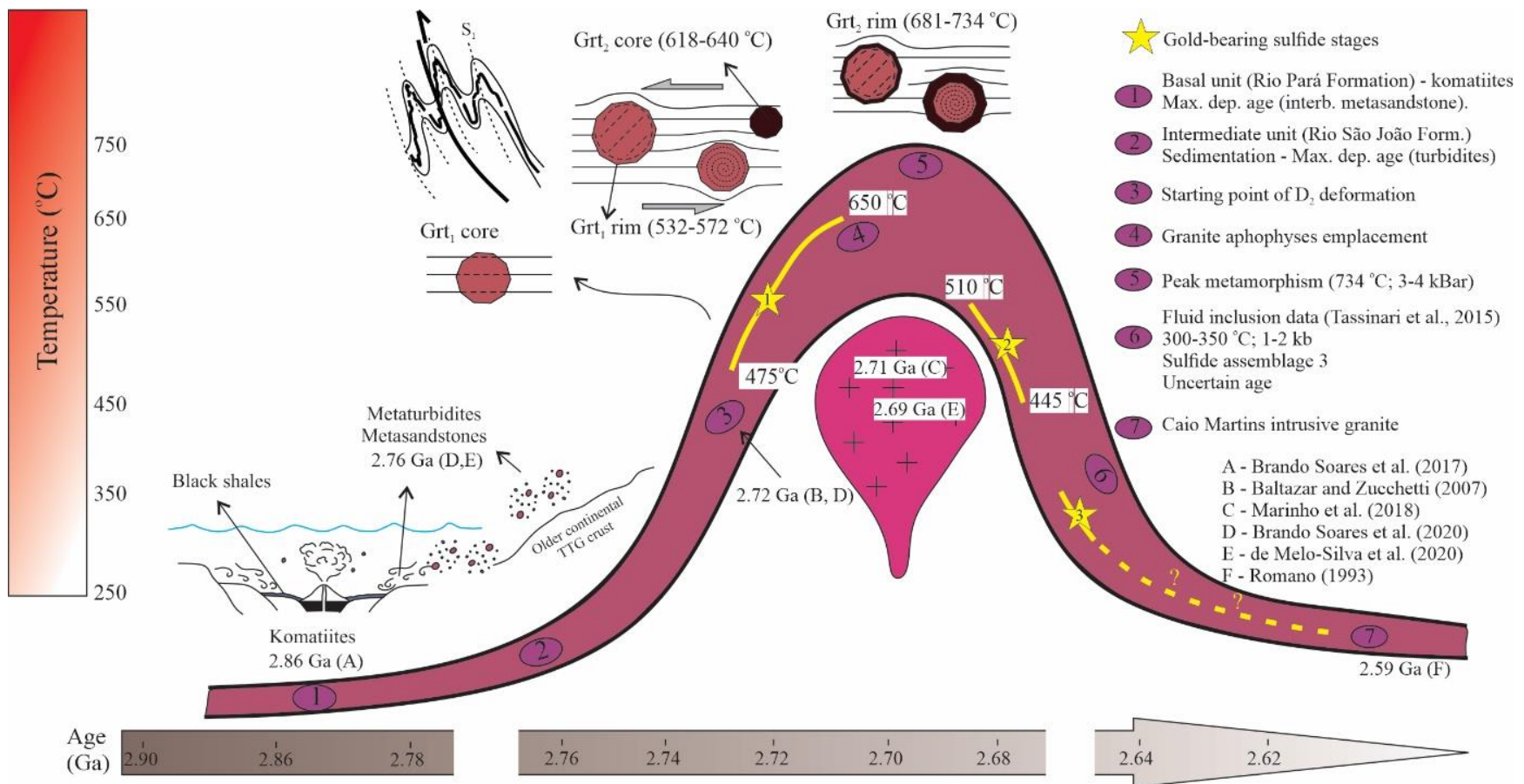


Fig. 4-16. Schematic diagram showing the temperature variation (Y axis) throughout the time (X axis). The noticeable geological events are represented by numbers 1-6 (see legend). The timing of the Casquilho granite is represented by pink balloon at the center of the diagram. Note that the geochronological data used are specified in letters (A-F). See text for more explanations.

4.6.5 Metallogenetic classification

It is evident that the Satinoco is a structurally controlled, shear zone-hosted gold deposit that initially formed above the brittle-ductile transition in a collisional orogen. In this sense it appears similar to orogenic-type gold deposits. It shows, however, some notable differences from typical orogenic-gold deposits as defined by Groves et al. (1998): (i) the formation temperature of ore minerals of stages I (mainly) and II are above those registered in most classic orogenic-type deposits in the world and the eastern Iron Quadrangle (see Lobato et al., 2001); (ii); Fe-rich hydrothermal assemblages can be interpreted as contact metasomatism, similar to skarn deposits; and (iii) magmatic fluids seem to have been involved at some stage of the mineralizing system, that is, at stage II.

Recently, Brando Soares et al. (2018) classified the São Sebastião deposit as hypozonal, mainly due to its association with amphibolite-facies rocks. According to these authors, the deposit would have formed in the lower crustal section of the Pitangui greenstone belt. However, the higher temperatures recorded in this greenstone belt are spatially restricted to c. 2700 Ma intrusive bodies. As demonstrated above, the older hydrothermal gold-bearing sulfide stage I took place before the peak metamorphism under conditions of c. 3 to 4 kb. In addition, the metamorphic paragenesis and the porphyroblast-matrix relations of Grt_2 indicate that the peak metamorphism occurred after the D_2 deformation, i.e., the granite had to be responsible for the locally high temperatures.

The Fe-rich nature of the hydrothermal stage II, the distinctive Au-Co-Bi-Te-S association, and its relatively low base metal content are in line with the derivation of the mineralizing fluid from granitic magma, akin to Au-skarn mineralization. The highly potassic composition of the Casquilho granite (Brando Soares et al. 2020) is, however, not typical of skarn systems (cf. Meinert et al., 2005).

The demonstrated Au-Co-Bi-Te-S metal association in the multistage mineralization process at Satinoco, coupled with granite-derived fluid input for stage II, also raises the possibility of explaining the deposit as intrusion-related gold systems (IRGS), such as the Maldon in the Victorian gold province (Ciobanu et al. 2010). Hydrothermal fluids associated with intrusion-related gold systems and some orogenic gold deposits share some similarities (Goldfarb and Groves 2015), but their alteration halos are distinct. Due to thermal disequilibrium with the wall rocks, the IRGSs generate a characteristic zonation around the causative intrusion (Hart et al. 2002). The early phase of the D₂ event at Satinoco clearly predates the granite. Still, the observation of the occurrence of highest metamorphic assemblages in the vicinity of the intrusion indicates contact metamorphism and shows a halo related to the geometry of the granite and older shear zones.

4.7 Conclusions

Underground mapping of the Satinoco deposit, drill core examination, petrographic, electron microprobe and LA-ICPMS analyses, including mineral-scale element mapping, made it possible, in combination with previously published geochronological, S isotope and fluid inclusion data, to draw the following conclusions:

- i) Gold mineralization took place over a period at least from c. 2720 to 2684 Ga prior, during and after the emplacement of granitic magma. Between 2720 and 2695 Ma, WNW-striking shear zones appear to be a critical factor controlling ore deposit location and ore shoot geometry during the early pre-granite stage of hydrothermal fluid infiltration, associated alteration and mineralization stage I;
- ii) A second Fe-rich stage of mineralization stage (stage II) was late- to post-magmatic with regards to the Casquilho granite, i.e., between c. 2695 and >2684 Ma, and involved metasomatism by late-magmatic Fe-rich fluids;
- iii) Intrusion of granitic magma may have driven dehydration of the host rocks and thus generated a mixture of metamorphic and magmatic fluids with a high fluid/rock, essential for mineralization;
- iv) During later post-granite uplift and/or exhumation and accompanying decrease in temperature, a third stage led to the recrystallization and remobilization of sulfides and gold.

The metallogenetic model proposed here for the Satinoco deposit provides an example of overlapping orogenic-type and intrusion-related gold systems features. This model has some major implications for future mineral exploration, as it emphasizes the role of late magmatic fluids in the formation of orogenic gold systems. As faults and shear zones mark higher temperature zones capable of concentrating hydrothermal fluids, favoring the generation of new deposits or upgrading the gold grade of earlier gold-bearing veins, their recognition is of critical importance in exploration, especially when a temporal and causal link to nearby granitic magmatism can be established. This conclusion can be applied to other deposits in the Iron Quadrangle and elsewhere, especially to those that have experienced temperatures above 600 °C.

4.8 Acknowledgments

This study was financed in part by the Coordenação de Aperfeiçoamento de Pessoal de Nível Superior - Brasil (CAPES) - Finance Code 001. W. Fabricio-Silva thanks CAPES for PDSE (n° 88881.188398/2018-01) doctoral scholarship and all the colleagues from the Department of Geodynamics and Geomaterials Research of the University of Würzburg. We also thank Jaguar Mining Inc. for supporting the field trips and sampling. Valuable discussion with Alice Bosco-Santos, Denis Fougerouse, Mahyra Tedeschi, Vitor Silveira, Daniel Kontak, Isabela Moreno, Mariana Brando Soares, Raul Chaves, Alexander Kawohl, and William Campos are also gratefully acknowledged. Insightful comments from Dr. James Lambert-Smith, Dr. Christopher Lawley, and Dr. Larry Meinert greatly helped us improving this paper.

4.9 References

- Alkmim, F. F., and Marshak, S., 1998, Transamazonian Orogeny in the Southern São Francisco Craton Region, Minas Gerais, Brazil: Evidence for Paleoproterozoic collision and collapse in the Quadrilátero Ferrífero: Precambrian Research, v. 70, p. 29–58.
- Almeida, F. F. M., 1977, O Cráton do São Francisco: Revista Brasileira de Geociências, v. 7, p. 349–364.
- Bajwah, Z. U., Seccombe, P. K., and Offler, R., 1987, Trace element distribution, Co: Ni ratios and genesis of the Big Cadia iron-copper deposit, New South Wales, Australia: Mineralium Deposita, v. 22, p. 292–300.

- Baltazar, O. F., and Zucchetti, M., 2007, Lithofacies associations and structural evolution of the Archean Rio das Velhas greenstone belt, Quadrilátero Ferrífero, Brazil: A review of the setting of gold deposits: *Ore Geology Reviews*, v. 32, p. 471–499.
- Barnicoat, A. C., Fare, R. J., Groves, D. I., and McNaughton, N. J., 1991, Synmetamorphic lode-gold deposits in high-grade Archean settings: *Geology*, v. 19, p. 921–924.
- Berman, R. G., 1991, Thermobarometry using multi-equilibrium calculations; a new technique, with petrological applications: *The Canadian Mineralogist*, v. 29, p. 833–855.
- Bierlein, F. P., Reynolds, N., Arne, D., Bargmann, C., McKeag, S., Bullen, W., Al-Athbah, H., McKnight, S., and Maas, R., 2016, Petrogenesis of a Neoproterozoic magmatic arc hosting porphyry Cu-Au mineralization at Jebel Ohier in the Gebeit Terrane, NE Sudan: *Ore Geology Reviews*, v. 79, p. 133–154.
- Bosco-Santos, A., Gilhooly, W. P., Fouskas, F., Fabricio-Silva, W., and Oliveira, E. P., 2020, Euxinia in the Neoarchean: The starting point for early oxygenation in a Brazilian Craton: *Precambrian Research*, v. 341, p. 105655.
- Brando Soares, M., Corrêa Neto, A. V., Zeh, A., Cabral, A. R., Pereira, L. F., Prado, M. G. B. do, Almeida, A. M. de, Manduca, L. G., Silva, P. H. M. da, Mabub, R. O. de A., and Schlichta, T. M., 2017, Geology of the Pitangui greenstone belt, Minas Gerais, Brazil: Stratigraphy, geochronology and BIF geochemistry: *Precambrian Research*, v. 291, p. 17–41.
- Brando Soares, M., Corrêa Neto, A. V., Bertolino, L. C., Alves, F. E. A., de Almeida, A. M., Montenegro da Silva, P. H., Mabub, R. O. de A., Manduca, L. G., and Araújo, I. M. C. de P., 2018, Multistage mineralization at the hypozonal São Sebastião gold deposit, Pitangui greenstone belt, Minas Gerais, Brazil: *Ore Geology Reviews*, v. 102, p. 618–638.

- Brando Soares, M., Corrêa Neto, A. V., and Fabricio-Silva, W., 2020, The development of a Meso- to Neoarchean rifting-convergence-collision-collapse cycle over an ancient thickened protocontinent in the south São Francisco craton, Brazil: *Gondwana Research*, v. 77, p. 40–66.
- Bühn, B., Santos, R. V., Dardenne, M. A., and de Oliveira, C. G., 2012, Mass-dependent and mass-independent sulfur isotope fractionation (δ 34S and δ 33S) from Brazilian Archean and Proterozoic sulfide deposits by laser ablation multi-collector ICP-MS: *Chemical Geology*, v. 312–313, p. 163–176.
- Caddick, M. J., Konopásek, J., and Thompson, A. B., 2010, Preservation of Garnet Growth Zoning and the Duration of Prograde Metamorphism: *Journal of Petrology*, v. 51, p. 2327–2347.
- Carneiro, M. A., 1992, O Complexo Metamórfico Bonfim Setentrional (Quadrilátero Ferrífero, MG): Litoestratigrafia e evolução geológica de um segmento de crosta continental do Arqueano: Universidade de São Paulo: 233 p.
- Chemale, F., Rosière, C. A., and Endo, I., 1994, The tectonic evolution of the Quadrilátero Ferrífero, Minas Gerais, Brazil: *Precambrian Research*, v. 65, p. 25–54.
- Ciobanu, C. L., Cook, N. J., Damian, F., and Damian, G., 2006, Gold scavenged by bismuth melts: An example from Alpine shear-remobilizes in the Hăghiș Massif, Romania: *Mineralogy and Petrology*, v. 87, p. 351–384.
- Ciobanu, C. L., Birch, W. D., Cook, N. J., Pring, A., and Grundler, P. V., 2010, Petrogenetic significance of Au–Bi–Te–S associations: the example of Maldon, Central Victorian gold province, Australia: *Lithos*, v. 116, p. 1–17.
- Cooke, O'Brien, and Carswell, 2000, Garnet zoning and the identification of equilibrium mineral compositions in high-pressure-temperature granulites from the Moldanubian Zone, Austria: *Journal of Metamorphic Geology*, v. 18, p. 551–569.

- Deol, S., Deb, M., Large, R. R., and Gilbert, S., 2012, LA-ICPMS and EPMA studies of pyrite, arsenopyrite and loellingite from the Bhukia-Jagpura gold prospect, southern Rajasthan, India: Implications for ore genesis and gold remobilization: *Chemical Geology*, v. 326–327, p. 72–87.
- Dorr, J. V. N., 1969, Physiographic, stratigraphic, and structural development of the Quadrilatero Ferrifero, Minas Gerais, Brazil:, accessed at US Geological Survey - Professional Paper 614-A at <http://pubs.er.usgs.gov/publication/pp641A>.
- Fabricio-Silva, W., 2016, Evolução tectono-metamórfica aplicada aos processos responsáveis pela mineralização no depósito de ouro Turmalina, Quadrilátero Ferrífero, Brasil: geologia, análise estrutural e isótopos de enxofre: Universidade Federal de Minas Gerais: 113 p.
- Fabricio-Silva, W., Rosière, C. A., and Bühn, B., 2019, The shear zone-related gold mineralization at the Turmalina deposit, Quadrilátero Ferrífero, Brazil: structural evolution and the two stages of mineralization: *Mineralium Deposita*, v. 54, p. 347–368.
- Fougerouse, D., Micklethwaite, S., Halfpenny, A., Reddy, S. M., Cliff, J. B., Martin, L. A. J., Kilburn, M., Guagliardo, P., and Ulrich, S., 2016, The golden ark: Arsenopyrite crystal plasticity and the retention of gold through high strain and metamorphism: *Terra Nova*, v. 28, p. 181–187.
- Frizzo, C., Takai, V., and Scarpelli, W., 1991, Auriferous mineralization at Pitangui, Minas Gerais, in Brazil Gold '91 - Ladeira, E. A. (ed): Balkema, Rotterdam, p. 579–583.
- Frost, B. R., Mavrogenes, J. A., and Tomkins, A. G., 2002, Partial melting of sulfide ore deposits during medium- and high-grade metamorphism: *The Canadian Mineralogist*, v. 40, p. 1–18.
- Goldfarb, R. J., and Groves, D. I., 2015, Orogenic gold: Common or evolving fluid and metal sources through time: *Lithos*, v. 233, p. 2–26.

Groves, D. I., Goldfarb, R. J., Gebre-Mariam, M., Hagemann, S. G., and Robert, F., 1998, Orogenic gold deposits: a proposed classification in the context of their crustal distribution and relationship to other gold deposit types: *Ore Geology Reviews*, v. 13, p. 7–27.

Groves, D. I., Santosh, M., Goldfarb, R. J., and Zhang, L., 2018, Structural geometry of orogenic gold deposits: Implications for exploration of world-class and giant deposits: *Geoscience Frontiers*, v. 9, p. 1163–1177.

Groves, D. I., Santosh, M., Deng, J., Wang, Q., Yang, L., and Zhang, L., 2019, A holistic model for the origin of orogenic gold deposits and its implications for exploration: *Mineralium Deposita*, p. 1–18.

Hart, C. J. R., McCoy, D. T., Goldfarb, R. J., Smith, M., Roberts, P., Hulstein, R., Bakke, A. A., and Bundtzen, T. K., 2002, Geology, exploration, and discovery in the Tintina Gold Province, Alaska and Yukon: Special publication-society of Economic Geologists, v. 9, p. 241–274.

Hazarika, P., Mishra, B., and Lochan Pruseth, K., 2017, Trace-element geochemistry of pyrite and arsenopyrite: ore genetic implications for late Archean orogenic gold deposits in southern India: *Mineralogical Magazine*, v. 81, p. 661–678.

Hofmann, A. W., 1988, Chemical differentiation of the Earth: the relationship between mantle, continental crust, and oceanic crust: *Earth and Planetary Science Letters*, v. 90, p. 297–314.

Jaguar Mining, I., 2020, Technical report on the turmalina mine complex , minas gerais state , Brasil.:

Kerr, M. J., Hanley, J. J., Kontak, D. J., Morrison, G. G., Petrus, J., Fayek, M., and Zajacz, Z., 2018, Evidence of upgrading of gold tenor in an orogenic quartz-carbonate vein system by late magmatic-hydrothermal fluids at the Madrid Deposit, Hope Bay Greenstone Belt, Nunavut, Canada: *Geochimica et Cosmochimica Acta*, v. 241, p. 180–218.

- Kretschmar, U., and Scott, S. D., 1976, Phase relations involving arsenopyrite in the system Fe-As-S and their application: *The Canadian Mineralogist*, v. 14, p. 364–386.
- Lana, C., Alkmim, F. F., Armstrong, R., Scholz, R., Romano, R., and Nalini, H. A., 2013, The ancestry and magmatic evolution of Archaean TTG rocks of the Quadrilátero Ferrífero province, southeast Brazil: *Precambrian Research*, v. 231, p. 157–173.
- Lanari, P., Vidal, O., De Andrade, V., Dubacq, B., Lewin, E., Grosch, E. G., and Schwartz, S., 2014, XMapTools: A MATLAB©-based program for electron microprobe X-ray image processing and geothermobarometry: *Computers & Geosciences*, v. 62, p. 227–240.
- Large, R. R., Danyushevsky, L., Hollit, C., Maslennikov, V., Meffre, S., Gilbert, S., Bull, S., Scott, R., Emsbo, P., Thomas, H., Singh, B., and Foster, J., 2009, Gold and Trace Element Zonation in Pyrite Using a Laser Imaging Technique: Implications for the Timing of Gold in Orogenic and Carlin-Style Sediment-Hosted Deposits: *Economic Geology*, v. 104, p. 635–668.
- Lobato, L. M., Ribeiro-Rodrigues, L. C., and Vieira, F. W. R., 2001, Brazil's premier gold province. Part II: geology and genesis of gold deposits in the Archean Rio das Velhas greenstone belt, Quadrilátero Ferrífero: *Mineralium Deposita*, v. 36, p. 249–277.
- Machado, N., Schrank, A., Noce, C. M., and Gauthier, G., 1996, Ages of detrital zircon from Archean-Paleoproterozoic sequences: Implications for Greenstone Belt setting and evolution of a Transamazonian foreland basin in Quadrilátero Ferrífero, southeast Brazil: *Earth and Planetary Science Letters*, v. 141, p. 259–276.
- Marinho, M. S., Silva, M. A., Lombello, J. C., Di Salvio, L. P., Silva, R. N., Féboli, W. L., and Brito, D. C., 2018, Projeto ARIM - Áreas de Relevante Interesse Mineral - Noroeste do Quadrilátero Ferrífero - Mapa Geológico Integrado do Sinclínorio Pitangui. 1 mapa colorido. Escala 1:75.000: p. 1.

- Meinert, L. D., Dipple, G. M., and Nicolescu, S., 2005, World Skarn Deposits. Economic Geology 100th Anniversary Volume:
- de Melo-Silva, P., da Silva Amaral, W., and Oliveira, E. P., 2019, Geochronological evolution of the Pitangui greenstone belt, southern São Francisco Craton, Brazil: Constraints from U-Pb zircon age, geochemistry and field relationships: Journal of South American Earth Sciences.
- de Melo-Silva, P., Amaral, W. da S., and Oliveira, E. P., 2020, Geochronological evolution of the Pitangui greenstone belt, southern São Francisco Craton, Brazil: Constraints from U-Pb zircon age, geochemistry and field relationships: Journal of South American Earth Sciences, v. 99.
- Neumayr, P., Cabri, L. J., Groves, D. I., Mikucki, E. J., and Jackman, J. A., 1993, The mineralogical distribution of gold and relative timing of gold mineralization in two Archean settings of high metamorphic grade in Australia: The Canadian Mineralogist, v. 31, p. 711–725.
- Noce, C. M., Tassinari, C., and Lobato, L. M., 2007, Geochronological framework of the Quadrilátero Ferrífero, with emphasis on the age of gold mineralization hosted in Archean greenstone belts: Ore Geology Reviews, v. 32, p. 500–510.
- Oliveira, E. P., McNaughton, N. J., Zincone, S. A., and Talavera, C., 2020, Birthplace of the São Francisco Craton, Brazil: Evidence from 3.60 to 3.64 Ga Gneisses of the Mairi Gneiss Complex: Terra Nova, v. 32, p. 281–289.
- Palme, H., and Jones, A., 2003, Solar system abundances of the elements: TrGeo, v. 1, p. 711.
- Petrakakis, K., 1986, Metamorphism of high-grade gneisses from the Moldanubian zone, Austria, with particular reference to the garnets: Journal of Metamorphic Geology, v. 4, p. 323–344.
- Phillips, G. N., and Powell, R., 2009, Formation of gold deposits: Review and evaluation

- of the continuum model: *Earth-Science Reviews*, v. 94, p. 1–21.
- Phillips, G. N., and Powell, R., 2010, Formation of gold deposits: A metamorphic devolatilization model: *Journal of Metamorphic Geology*, v. 28, p. 689–718.
- Renger, F. E., Noce, C. M., Romano, A. W., and Machado, N., 1994, Evolução Sedimentar Do Supergrupo Minas: 500 Ma. De Registro Geológico No Quadrilátero Ferrífero, Minas Gerais, Brasil: *Geonomos*, v. 2, p. 1–11.
- Ribeiro-Rodrigues, L. C., de Oliveira, C. G., and Friedrich, G., 2007, The Archean BIF-hosted Cuiabá Gold deposit, Quadrilátero Ferrífero, Minas Gerais, Brazil: *Ore Geology Reviews*, v. 32, p. 543–570.
- Romano, A. W., 1993, Parte, O Supergrupo Rio das Velhas da Faixa Mateus Leme-Pitangui - meridional do Cráton de São Francisco, MG - e seu sistema de alteração hidrotermal: *Geonomos*, v. 1, p. 16–32.
- Romano, A. W., 2007, Programa Geologia do Brasil. Folha Pará de Minas, SE-23-Z-C-I. Escala 1:100.000 relatório final. UFMG-CPRM, Belo Horizonte: 74 p.
- Romano, R., Lana, C., Alkmim, F. F., Stevens, G., and Armstrong, R., 2013, Stabilization of the southern portion of the São Francisco craton, SE Brazil, through a long-lived period of potassic magmatism: *Precambrian Research*, v. 224, p. 143–159.
- Saintilan, N. J., Creaser, R. A., Spry, P. G., and Hnatyshin, D., 2017, Re-Os Systematics of löllingite and arsenopyrite in granulite-facies garnet rocks: Insights into the metamorphic history and thermal evolution of the broken hill block during the early mesoproterozoic (New South Wales, Australia): *Canadian Mineralogist*, v. 55, p. 29–44.
- Sharp, Z. D., Essene, E. J., and Kelly, W. C., 1985, A re-examination of the arsenopyrite geothermometer: Pressure considerations and applications to natural assemblages: *The Canadian Mineralogist*, v. 23, p. 517–534.

- Silva, G. P. A., and Carneiro, M. A., 2009, The metatholeiitic suite of the Rio Manso metavolcanosedimentary sequence, Iron Quadrangle (MG): *Revista da Escola de Minas de Ouro Preto*, v. 62, p. 423–430.
- Spear, F. S., 1991, Temperatures in Light of Garnet Diffusion During Cooling: *Journal of Metamorphic Geology*, v. 9, p. 379–388.
- Stromberg, J. M., Barr, E., Van Loon, L. L., Gordon, R. A., and Banerjee, N. R., 2019, Fingerprinting multiple gold mineralization events at the Dome mine in Timmins, Ontario, Canada: Trace element and gold content of pyrite: *Ore Geology Reviews*, v. 104, p. 603–619.
- Tassinari, C. C. G., Mateus, A. M., Velásquez, M. E., Munhá, J. M. U., Lobato, L. M., Bello, R. M., Chiquini, A. P., and Campos, W. F., 2015, Geochronology and thermochronology of gold mineralization in the Turmalina deposit, NE of the Quadrilátero Ferrífero Region, Brazil: *Ore Geology Reviews*, v. 67, p. 368–381.
- Teixeira, W., Ávila, C. A., Dussin, I. A., Corrêa Neto, A. V., Bongiolo, E. M., Santos, J. O., and Barbosa, N. S., 2015, A juvenile accretion episode (2.35-2.32Ga) in the Mineiro belt and its role to the Minas accretionary orogeny: Zircon U-Pb-Hf and geochemical evidences: *Precambrian Research*, v. 256, p. 148–169.
- Thorman, C. H., DeWitt, E., Maron, M. A., and Ladeira, E. A., 2001, Major brazilian gold deposits - 1982 to 1999: *Mineralium Deposita*, v. 36, p. 218–227.
- Tomkins, A. G., 2013, On the source of orogenic gold: *Geology*, v. 41, p. 1255–1256.
- Tomkins, A. G., and Mavrogenes, J. A., 2001, Redistribution of gold within arsenopyrite and löllingite during pro- and retrograde metamorphism: Application to timing of mineralization: *Economic Geology*, v. 96, p. 525–534.
- Tomkins, A. G., Pattison, D. R. M., and Zaleski, E., 2004, The Hemlo Gold Deposit, Ontario: An Example of Melting and Mobilization of a Precious Metal-Sulfosalt Assemblage during Amphibolite Facies Metamorphism and Deformation: *Economic*

Geology, v. 99, p. 1063–1084.

Tuccillo, M. E., Essene, E. J., and van der Pluijm, B. A., 1990, Growth and retrograde zoning in garnets from high-grade, metapelites: Implications for pressure-temperature paths: *Geology*, v. 18, p. 839–842.

Verma, S. K., Oliveira, E. P., Silva, P. M., Moreno, J. A., and Amaral, W. S., 2017, Geochemistry of komatiites and basalts from the Rio das Velhas and Pitangui greenstone belts, São Francisco Craton, Brazil: Implications for the origin, evolution, and tectonic setting: *Lithos*, v. 284–285, p. 560–577.

Vial, D. S., DeWitt, E., Lobato, L. M., and Thorman, C. H., 2007, The geology of the Morro Velho gold deposit in the Archean Rio das Velhas greenstone belt, Quadrilátero Ferrífero, Brazil: *Ore Geology Reviews*, v. 32, p. 511–542.

Xue, Y., Campbell, I., Ireland, T. R., Holden, P., and Armstrong, R., 2013, No mass-independent sulfur isotope fractionation in auriferous fluids supports a magmatic origin for Archean gold deposits: *Geology*, v. 41, p. 791–794.

Yan, J., Hu, R., Liu, S., Lin, Y., Zhang, J., and Fu, S., 2018, NanoSIMS element mapping and sulfur isotope analysis of Au-bearing pyrite from Lannigou Carlin-type Au deposit in SW China: New insights into the origin and evolution of Au-bearing fluids: *Ore Geology Reviews*, v. 92, p. 29–41.

5. HOW DOES ARSENOPYRITE LOSE ITS PRIMARY GEOCHEMICAL SIGNATURE? A GLIMPSE FROM OROGENIC GOLD DEPOSITS IN BRAZIL

Wendell **Fabricio-Silva**, Maria Emilia **Schutesky**, Hartwig E. **Frimmel**, Denis **Fougerouse**, Paola **Barbosa**, Carlos A. **Rosière**, Leonardo **Lagoeiro**, Mariana **Brando Soares**

5.1 Introduction

Arsenopyrite (FeAsS) is the most abundant arsenic-bearing sulfide mineral in lithosphere (Tomkins et al. 2004) and is the most important gold-bearing sulfide mineral in the several gold deposits in Brazil (Lobato et al. 2001). Understanding arsenopyrite behavior across a range of deformation and metamorphism conditions provide useful information about evolutionary history of a gold deposit.

In those deposit, to fully understand the behavior of an orebody throughout the metallogenetic interval, it is essential to analyse the conditions of the arsenopyrite crystallization and the following remobilization (s) mechanism (s). The close spatial relationship between Au and the changing in arsenopyrite textures has led researchers to suggest that the metamorphic/hydrothermal transition of arsenopyrite processes results in gold upgrading through the liberation of lattice-bound and nano-particulate metals hosted within early, Au-rich sulfide minerals (Craig and Vokes, 1993; Tomkins and Mavrogenes, 2001). The metals are then remobilized and concentrated into late, high-grade ore shoots and macro- to microscale observations at these deposits suggest

that late, Au mineralization is synchronous with hydrothermal fluids (e.g., Mishra et al., 2018; Wu et al., 2019), magmatism (e.g., Mériaud and Jébrak, 2017; Kerr et al., 2018), and deformation (e.g., Fougerouse et al., 2016; Dubosq et al., 2018).

In this study, we document arsenopyrite microstructures and multiple Au paragenesis that are consistent with a syn- to post-peak metamorphic and deformation-driven Au-upgrading model, where Au and other trace elements are introduced, released from crystal lattice and remobilized into fluid and deformation-induced substructures within arsenopyrite.

Peak metamorphic conditions at the NW-Iron Quadrangle Subprovince, reached 730 °C and 3-4 kbar (Fabricio-Silva et al. 2020), which fall within the range of pressure-temperature conditions expected for arsenopyrite crystal plastic deformation prior to two more hydrothermal assemblages thus making its gold deposits an ideal area to test the model. Herein we combine microstructural analysis via electron backscatter diffraction (EBSD) techniques, laser ablation inductively coupled plasma mass spectrometry (LA-ICPMS), and 2D element mapping to further investigate the influence of intrusive magmatism, hydrothermalism, metamorphism, and deformation on the retention, release or capture of Au and other trace elements within arsenopyrite and pyrite from syn-, late-, and post-tectonic assemblages.

Finally, we combine 2D microscale trace element mapping with 3D time-resolved LA-ICP-MS spectra to evaluate the remobilization mechanisms and the relative chronology to the significance of the Au-upgrading model.

5.2 Geological background

The Pitangui greenstone belt (PGB - Frizzo et al., 1991; Brando Soares et al., 2017) is located within the southern São Francisco craton (Almeida 1977), as part of the well-known Quadrilátero Ferrífero mining district (QF; translated as “Iron Quadrangle”). The QF is one of the largest Fe and Au metallogenic provinces in the world and accommodates the world-class Morro Velho and Cuiabá gold deposits amongst several other important deposits and minor occurrences. The Pitangui greenstone belt (PGB; Fig. 1) is an NW-SE-striking belt, covering an area of c. 700 sq. km, and is confined between Mesoarchean (3.2 – 2.8 Ga) TTG-granite complexes. The PGB show a rough stratigraphic and chronological correspondence with the famous Rio das Velhas greenstone belt in the central and eastern QF but is considered to represent a separate geological entity (Brando Soares et al. 2020).

The PGB rocks consist predominantly of metakomatiite with minor metapelites, banded iron formation (BIF) and black shales at the base, followed by metarhythmites and metapelites with interbedded volcanic- and volcano-clastic rocks comprised within the Pitangui Group (Romano 2007; Marinho et al. 2018). The Antimes formation, to the top, is mostly comprised of quartzite, metaconglomerate, iron-rich meta-pelite and metachert with interbedded BIF and metagreywackes. Medium to coarse-grained calc-alkaline (TTG-like) to high-K granitoids have intruded the Pitangui Group in the southern part of the PGB (Romano 2007; Brando Soares et al. 2020). Two of the main intrusive granitoids are the Jaguara (2.71 Ga, Brando-Soares et al., 2020) and Casquilho (2.69 Ga, de Melo-Silva et al., 2019) plutons considered to represent the response of a protracted TTG magmatism over an overthickened collisional belt and its stabilization, respectively.

Metamorphism in the PGB generally displays greenschist-facies mineral assemblages characterized by talc-antigorite-actinolite-chlorite-carbonate in volcanic meta-mafic rocks and by quartz-kyanite-muscovite-chloritoid in meta-sedimentary rocks (Romano, 2007). Surrounding the intrusive granitoids and at the margins of the PGB the metamorphic grade is described to increase up to amphibolite-facies (Brando Soares et al. 2018; Fabricio-Silva et al. 2019; Fabricio-Silva et al. 2020) where phases like staurolite, hornblende and Fe-rich garnet are identified.

At least three deformational episodes have affected the PGB (Romano, 2007). The second episode (D_2) corresponds to the main compressional deformation constrained at c. 2720 to 2695 Ma (Brando Soares et al., 2020; Fabricio-Silva et al., 2020), which is a transition from purely compressive (D_1 ; at c. 2780 to 2720 Ma; Brando Soares et al., 2020) to oblique compression (Fabricio-Silva et al., 2019). The D_2 episode is responsible to the generation of shear zones and is chronologically associated with granitoid intrusions to the peak metamorphism (Fabricio-Silva et al., 2020). The third deformation episode (D_3) took place after the ductile to brittle deformation (Fabricio-Silva et al., 2020) and is represented mainly by reverse faults that is, according to these authors, younger than the maximum depositional age of 2684 Ma obtained by Marinho et al. (2018). Both Casquilho and Jaguara plutons have intruded the PGB. Roughly contemporaneous with D_2 deformation, high-K (e.g., Casquilho pluton) and calc-alkaline (e.g., TTG-like Jaguara pluton) granitoids intruded the PGB. Dating constrains these granitoids to between 2694.7 ± 9 Ma (U-Pb zircon age; de Melo-Silva et al., 2020; Casquilho granite) and 2719 ± 11 Ma (U-Pb zircon age; Brando Soares et al., 2020; Jaguara).

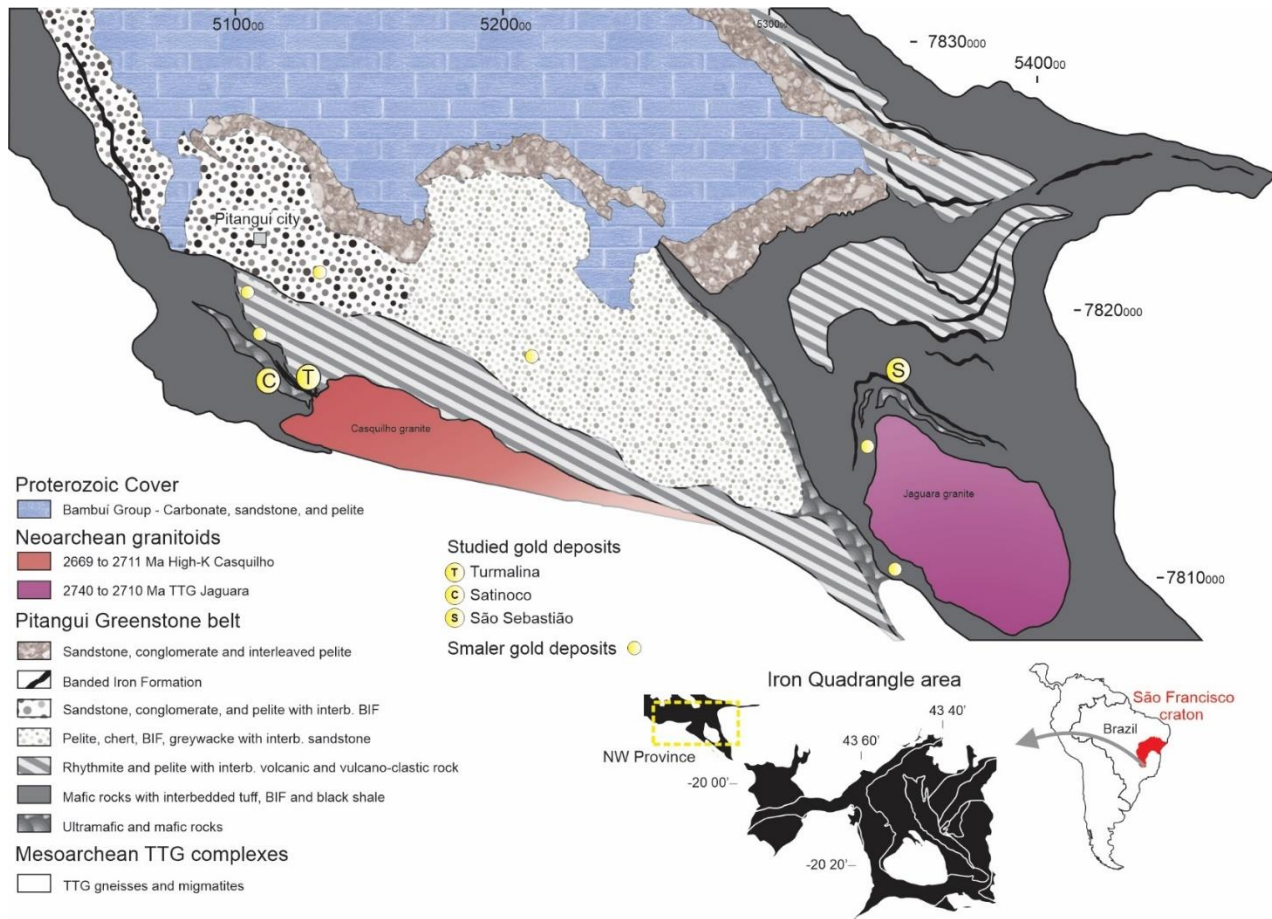


Fig. 5-1. Geological map of the NW-Quadrilátero Ferrífero Subprovince in the southern region of the São Francisco craton. Note that the map of the NW Subprovince is represented as a yellow rectangle in the Quadrilátero Ferrífero area. Compiled and adapted after Renger et al. (1994), Brando Soares et al. (2018), Marinho et al. (2018), and Fabricio-Silva (2016).

5.3 Individual Au deposits

The São Sebastião deposit is located within the eastern sector of the PGB being hosted by BIFs at the base of the Pitangui Group (Fig. 5-1; Brando Soares et al., 2017, 2018). The base of the Pitangui group is intruded by the Jaguara granitoid, which outcrops 2 km away from the deposit. Several granitoid apophyses are described to occur in depth intercepting mafic and ultramafic rocks up to a few meters from the mineralized bodies.

The two main mineralized BIFs intervals are sulfide-rich and separated by a metavolcanic ultramafic layer. These orebodies (Biquinho and Pimentão) are developed in the northeast limb of the Jaguara anticline (Fig. 5-1) and display a strata-confined sulfide replacement within BIF where pyrrhotite is the most abundant phase. A number of studies have been recently performed at the São Sebastião deposit. These studies were mainly focused on its complex ore mineralogy (e.g., Cabral and Corrêa Neto, 2015; Brando Soares et al., 2018) composed by Bi-enriched accessory phases and a distinctive native Au – native Bi association, geochronology and geochemistry (e.g., Brando Soares et al., 2017; Brando Soares et al., 2020).

Brando Soares et al. (2018) have identified three (I, II and III) sulfide assemblages at the São Sebastião deposit (Table 1) comprising a (I) pyrrhotite (Po_1) - chalcopyrite assemblage related to an early tectonic compressional stage; (II) arsenopyrite (Apy_2) and arsenian pyrite (Py_2); overgrowths replacing Po_1 , and an (III) assemblage comprising fine-grained arsenopyrite (Apy_3) and pyrite (Py_3), with lower amounts of pyrrhotite (Po_3) and chalcopyrite. Gold occurs as inclusions in Py_3 , Apy_2 , Apy_3 and filling fractures of minerals from assemblage III.

Although assemblage I is syntectonic and older than the 2747 ± 7 Ma (U-Pb zircon age; Marinho et al., 2018) Jaguara pluton and its apophyses, recent Re-Os data obtained for assemblage III Brando Soares et al., (2021) returned results at ca. 2.0 Ga and was interpreted as related to extensional movements at the waning stages of Minas Orogeny (Alkmim and Teixeira, 2017). According to Brando Soares et al. (2021), high initial variations of $^{187}\text{Os}/^{188}\text{Os}$ for assemblages I and II indicate a disturbance in the Re-Os system at ~ 2.0 Ga caused by hot fluids responsible for the crystallization of assemblage III.

The Turmalina and Satinoco deposits are part of the Turmalina Mining Project (Jaguar Mining Inc.) and are located at southwest section of the PGB (Fig. 1). The deposits share similar structural evolution and ore geometry, but the host rocks and hydrothermal evolution are quite different (Frizzo et al., 1991; Fabricio-Silva et al., 2019; Fabricio-Silva et al., 2020). Both deposits are controlled by a series of WNW-ESE- to NW-SE-trending and steeply NNE to NE-dipping shear zones. In the eastern domain, the shear zones show a horsetail geometry termination and ends few meters far from the Casquilho pluton (see Fig. 9 from Fabricio-Silva, 2016).

The Turmalina deposit comprises two subparallel orebodies hosted in an interleaved package of meta-pelite, meta-rhythmite and meta-tuffs. Widespread hydrothermal alteration haloes propagate from extensive sulfide-rich quartz veins. Gold-bearing sulfides occur either disseminated in cm-wide bands parallel to the vein margins and as aggregates at the borders of these veins, being particularly abundant at the “necks” of pinch-and-swell structures.

Fabricio-Silva et al. (2019) have defined two Archean gold-bearing sulfide assemblages in the Turmalina deposit (Table 1): (I) an early pyrrhotite-arsenopyrite ($\text{Apy}_1 \pm \text{löllingite}$

\pm chalcopyrite assemblage which has precipitated during prograde metamorphism conditions at ca. 598 ± 19 °C, associated with the development of main foliation and the 2.69 Ga Casquilho granite intrusion; and a (II) second pyrrhotite-pyrite-arsenopyrite (Apy_2) \pm chalcopyrite assemblage, associated with a late- to post-tectonic Archean event under cooling conditions between 442 and 510 °C.

The Satinoco deposit (also known locally as “Corpo C”) is hosted within amphibolitic rocks (chlorite-quartz-amphibole schist) interbedded with BIF and black shales from the lowermost Pitangui Group (Frizzo et al., 1991; Fabricio-Silva et al., 2020). The gold-bearing sulfides at Satinoco occur forming the matrix of massive hydraulic breccias and as disseminated in cm-wide bands parallel to the lenses of black shales.

Recently, Fabricio-Silva et al. (2020) have described three gold-bearing sulfide assemblages for the Satinoco deposit (Table 1): an assemblage (I) with timing between 2720 and 2695 Ma formed by syntectonic arsenopyrite (Apy_1), löllingite and pyrrhotite (Po_1) genetically related to prograde metamorphism at ca. 475 to 650 °C temperature conditions; an (II) assemblage comprised of an association of pyrrhotite (Po_2)-arsenopyrite (Apy_2) \pm löllingite \pm galena formed under retrograde metamorphic conditions of metamorphism from ca. 510 to 445 °C coeval with the emplacement of the Casquilho granitoid and a late assemblage (III) of pyrite-pyrrhotite (Po_3), galena \pm chalcopyrite \pm sphalerite \pm ullmannite formed during a late post-tectonic brittle deformation event at temperature conditions of 350 to 300 °C at 1 to 2 kbars. Assuming that the ultimate felsic magmatism affecting the PGB is represented by the granodiorites with ages similar to that of the Caio Martins body (2593 ± 19 Ma; Romano, 1993), it is possible that the sulfide assemblage III has crystallized at ~ 2600 Ma or represents a short-lived isolated sulfide event younger than this age possibly correlating to the paleoproterozoic ages found at São Sebastião. In terms of fluid sources, crosscutting

field relationships together with Fe speciation and $\Delta^{33}\text{S}$, $\delta^{34}\text{S}$, and $\Delta^{36}\text{S}$ ratios (Bosco-Santos et al. 2020) indicate a metamorphic origin for all the sulfide stages in Turmalina and Satinoco, having a contribution from granite-derived magmatogenic fluids coeval to the (re) crystallization of assemblage II (Fabricio-Silva et al., 2020).

Table 5-1. Summary table of the studied gold deposits showing temperature and pressures of metamorphism, sulfide assemblages and host rocks.

Deposit	Sulfide assemblages						References
	Peak temp.	Pressure	Au-bearing stages	Relative timing with Archean def. event	Host rocks		
São Sebastião	~ 600 °C	>4 kbar	Po-Ccp	Pre- to late-tectonic			
			Apy-ArPy	Late to post-tectonic	Banded Iron Formations	Brando Soares et al. (2018; 2020)	
			Apy-Py-Po±ISS±Ccp	Post-tectonic			
Turmalina	610-633 °C	3-4 kbar	Po-Apy±Lö±Ccp	Syn to late-tectonic			Frizzo et al. (1993); Fabricio-Silva (2016); Tassinari et al. (2015);
			Po-Py-Apy±Ccp	Late to post-tectonic	Rhythmic pelitic rocks interb. with metatuffs		Fabricio-Silva et al. (2019)
			Py-Po	Post-tectonic			
Satinoco	681-734 °C	3-4 kbar	Apy-Lö-Po	Early-tectonic	Metabasalt and		
			Po-Apy±Lö±Gn	Late to post-tectonic	metakomatiite interb. with metatuffs and black	Frizzo et al. (1993); Fabricio-Silva (2016); Fabricio Silva et al. (2020)	
			Py-Po-Gn±Ccp±Sph±Ull	Post-tectonic	shales		

5.4 Methodology

Samples used in this study are from drillcores and underground (mine) outcrops. Sampling was conducted after deposit-scale mapping and extensive diamond drill hole logging at the São Sebastião, Satinoco and Turmalina deposits. Approximately 140 samples were selected and prepared as polished blocks or thin sections for reflected light microscopy.

Quantitative in-situ microanalyses of several selected sulfide grains were performed with a JEOL 8230 and a JEOL JXA 8800 electron microprobe (EMP) at Geoscience Institute of the University of Brasilia (Brazil) and at Institute of Geography and Geology of the University of Würzburg (Germany), respectively. Analytical conditions were set as 20 kV accelerating voltage and a beam current of 25 nA. A set of 13 elements (As, Se, S, Pb, Bi, Te, Fe, Co, Cu, Ni, Au, Ag, and Sb) was chosen for spot EMP analyses in sulfides. The following standards were used for calibration of elemental X-ray intensities: gallium arsenide (As), pyrite (S, Fe), copper (Cu), antimony (Sb), cobalt (Co), tellurium (Te), Selenium (Se), nickel (Ni), bismuth (Bi), gold (Au), galena (Pb), and silver (Ag). The resulting data were corrected off-line using a ZAF correction procedure (samples: Offline_0001_QNT and Offline_0003_QNT). A MatLab®-based (version R2018b) software, XMapTools®, version 2.5.2 (Lanari et al., 2014), was used to generate qualitative As, Fe, Ni, Sb, and Pb X-ray maps of the arsenopyrite crystals from different gold-bearing sulfide assemblages for subsequent modeling of compositional variation and hydrothermal conditions. The element maps were acquired by EMP with an acceleration voltage of 20 KV, 200 nA beam current, and 100 to 150 ms dwell time.

Samples chosen used for electron backscatter diffraction (EBSD) were further polished using a suspension of colloidal silica. Prior to EBSD analyses, the quantitative EMP spot analyses were combined with qualitative X-ray mapping to display the potential patterns of element distribution in arsenopyrite and pyrite crystals. The EBSD data were collected: (i) at the CSIRO Earth Science and Resource Engineering in Kensington (Australia) using a Bruker e-flash detector for EBSD and a Bruker XFlash 5030 silicon drift detector for EDS, all fitted on a Zeiss Ultraplus FEG SEM; (ii) at the Lactec Institute in the Federal University of Paraná (Brazil) using a MIRA 3RM SCAN-SEM. Both instruments were operated at 20 kV accelerating voltage, 12.10 nA beam current and a tilting angle of 70°. The Oxford Instruments/HKL Channel 5 software was used for data treatment. EBSD color maps show the full crystal orientation, from the crystallographic centre of each grain.

Laser ablation ICP-MS on polished thin sections was carried out at the GeoZentrum Nordbayern, University of Erlangen, for measurement of trace-element concentrations. Prior to LA-ICP-MS analyses, the quantitative EMP spot analyses were combined with qualitative X-ray mapping to display the potential patterns of trace element distribution in arsenopyrite and pyrite crystals. The analyses were performed with a single collector quadrupole AGILENT 7500c ICP-MS equipped with a laser unit (Analyte Excite, Teledyne, photon machines, Excimer laser 193nm). The carrier gas used was He and Ar. For external calibration, Po724 B2 SRM (sulfide standard for Au, Memorial University Newfoundland) and MASS-1 (Polymetal sulfide; USGS; for V, Mn, Fe, Co, Ni, Cu, Zn, Se, Mo, Ag, Sn, Sb, Te, Pb, and Bi) were used. The on-line data reduction was done by GLITTER Version 4.4.4 (Macquarie Research Ltd.), using S as the internal standard and monitoring Si, V, Mn, Sn for possible interferences. The laser beam was fired at 20 Hz repetition rate (fluence 4.04 J/cm²). The spot size was 20 µm in diameter. Integration time for ²⁹Si was set to 10 ms, for ³⁴S, ⁵⁷Fe, ⁶³Cu, ⁶⁷Zn, ⁶⁸Zn to 25 ms, for ⁵¹V, ⁵⁵Mn, ⁵⁹Co, ⁶⁰Ni, ⁶¹Ni, ⁷⁷Se, ⁹⁵Mo, ⁹⁷Mo, ¹⁰⁹Ag, ¹¹⁷Sn, ¹²¹Sb, ¹²⁵Te, ¹⁹⁷Au, ²⁰⁸Pb, and

^{209}Bi to 55 ms, and for ^{197}Au to 45 ms on the maximum peak. Total acquisition time was 40 s, background time was 20 s. Copper, Co, As, Zn, Mo, Ag, Te, Bi, Hg, Pb, and Si were measured as relative concentrations in counts per seconds (cps), as there was no well-calibrated standard available for these elements. The average of 23 analyses of the standard Po724 B2 SRM during our analysis period yielded an Au concentration of 47.1 ppm, consistent with the 47.3 ppm measured by quadrupole ICP-MS at Memorial University. Some time-resolved spectra for trace elements from São Sebastião and Satinoco deposits was obtained after LA-ICP-MS performed by Brando Soares et al. (2018) and Fabricio-Silva et al. (2020), respectivelly.

5.5 Arsenopyrite: textures and elemental composition

An overview of the results of the EPM is organized following the paragenetic stages for São Sebastião, Turmalina and Satinoco, as well as syngenetic pyrite (from Satinoco deposit), is provide as a summary in Table 5-2, including mean values, maximum, minimum and percentage of analyses below detection (% BDL). For the electron probe spot analyses, the concentrations below the detection limit were considered as zero in the statistical calculations. All results are presented as Electronic Appendix. The spot analysis used here were distributed using two criteria: points in the inner part of the crystals from each assemblage and sequential points forming linear profiles throughout the crystal. The locations of the spot analyses (used in Table 5-2) avoid proximity to fractures and grain boundaries.

Although the lower limit of detection of the EMP is relatively high for trace elements (e.g., Au: 300 ppm; Te: 210 ppm; Sb: 140 ppm; Ni: 180 ppm; Table 5-2), it was possible to study some compositional variation between sulfide grains (see X-ray maps and line analyses) in addition to comparing with LA-ICP-MS data.

The Euler map and the inverse pole figure are characterized by the sudden and linear color variation with orientation changing about 1° within the crystal lattice. These color variations correspond to the microcracks and microfractures. The equally lower hemisphere pole figures showed minimal orientation variation. As described above, Apy is characterized by well-developed microfractures.

LA-ICPMS provided by Brando Soares et al. (2018) and Fabricio-Silva et al. (2020) are after the EBSD and X-ray mapping. The time-resolved spectras related to each sulfide

parageneses are described for the first time here. The trace element distribution in arsenopyrite and pyrite crystals differs in different sulfide assemblages. The minor and trace element contents of the analyzed sulfides are summarized in Table 5-3 and all results are presented in Electronic Appendix. Note that the elements with the highest concentrations (e.g., Ni, Co, and Sb) and most of those with the lowest concentrations are consistent with the EMP results. In order to distinguish between evenly distributed nano-inclusions and elements within the crystal structure, we analyzed the mass spectra of LA-ICP-MS spot analyses. The integration intervals selected for quantitative trace element analysis represent the ablated sulfide without inclusions. By contrast, element inclusion likely reflects spectral peaks in a width of 1-3 s and signal at least an order of magnitude higher than background (e.g., Román et al. 2019). All results for time-resolved spectra are presented in Electronic Appendix.

Table 5-2. Summary of electron microprobe results from arsenopyrite and pyrite of different assemblages from studied deposits.

Analysis	Sulfide	N	As	Se	S	Pb	Bi	Te	Fe	Co	Cu	Ni	Au	Ag	Sb
São Sebastião	Apy2a	10													
Mean			43.51	0.24	18.93	0.03	0.06	0.05	36.49	0.02	0.02	0.16	0.03	0.01	0.01
Maximum			43.54	0.24	18.95	0.07	0.98	0.10	36.53	0.04	0.04	0.17	0.07	0.01	0.03
Minimum*			43.48	0.23	18.92	0.00	0.00	0.00	36.46	0.00	0.00	0.15	0.00	0.00	0.00
% BDL			0	0	0	30	40	50	0	50	10	0	30	30	30
São Sebastião	Apy2b	68													
Mean			43.22	0.23	19.12	0.04	0.09	0.05	36.16	0.02	0.06	0.04	0.02	0.01	0.02
Maximum			43.84	0.25	20.29	0.11	1.76	0.18	36.62	0.10	0.11	0.17	0.09	0.06	0.11
Minimum*			40.28	0.21	18.15	0.00	0.00	0.00	35.49	0.00	0.01	0.00	0.00	0.00	0.00
% BDL			0	0	0	32	37	50	0	46	6	28	68	39	44
São Sebastião	Apy3	26													
Mean			46.16	0.09	15.91	0.08	0.11	0.00	29.49	3.82	0.02	0.61	0.02	0.00	0.03
Maximum			48.32	0.28	16.48	0.17	1.24	0.03	33.08	12.86	0.07	7.01	0.07	0.02	0.10
Minimum*			43.13	0.00	14.25	0.00	0.00	0.00	18.83	1.26	0.00	0.00	0.00	0.00	0.00
% BDL			0	62	0	31	54	85	0	0	38	31	69	76	84
Turmalina	Apy1	131													
Mean			49.16	0.00	17.62	0.08	0.01	0.01	33.44	0.10	0.00	0.27	0.01	0.01	0.36
Maximum			50.79	0.00	18.76	0.19	0.07	0.05	34.73	0.25	0.05	0.76	0.10	0.03	1.38
Minimum*			46.85	0.00	16.53	0.00	0.00	0.00	32.06	0.00	0.00	0.00	0.00	0.00	0.00
% BDL			0	100	0	12	68	48	0	0	81	3	77	44	1
Turmalina	Apy2	111													
Mean			44.89	0.25	19.28	0.00	0.00	0.04	35.38	0.03	0.02	0.08	0.04	0.01	0.04
Maximum			46.69	0.30	20.38	0.03	0.07	0.22	36.44	0.14	0.11	0.22	0.11	0.08	0.15
Minimum*			40.16	0.20	17.59	0.00	0.00	0.00	31.52	0.00	0.00	0.00	0.00	0.00	0.00
% BDL			0	0	0	91	67	61	0	0	41	10	45	43	33
Satinoco	Py0	5													
Mean			0.00	0.06	51.57	0.17	0.00	0.00	45.92	0.08	0.01	0.01	0.01	0.01	0.00
Maximum			0.00	0.12	54.02	0.28	0.00	0.00	47.00	0.10	0.02	0.02	0.03	0.02	0.01
Minimum*			0.00	0.01	50.27	0.09	0.00	0.00	45.32	0.07	0.00	0.00	0.00	0.00	0.00
% BDL			100	0	0	0	100	100	0	0	20	60	80	20	80
Satinoco	Apy1	73													
Mean			49.41	0.00	17.70	0.09	0.01	0.01	33.72	0.15	0.00	0.24	0.01	0.00	0.33
Maximum			51.28	0.00	18.79	0.23	0.09	0.10	35.15	1.03	0.05	1.23	0.08	0.03	0.81

Minimum*		46.85	0.00	16.53	0.00	0.00	0.00	32.06	0.00	0.00	0.00	0.00	0.00	0.00
% BDL		0	100	0	19	56	62	0	0	74	5	51	41	10
Satinoco	Apy2	139												
Mean		48.99	0.00	16.96	0.05	0.02	0.01	32.41	1.09	0.00	1.03	0.01	0.00	0.15
Maximum		50.14	0.00	18.81	0.15	0.11	0.05	34.49	1.67	0.02	1.79	0.09	0.02	0.74
Minimum*		46.36	0.00	16.00	0.00	0.00	0.00	31.51	0.67	0.00	0.30	0.00	0.00	0.00
% BDL		0	100	0	21	60	49	0	0	87	0	66	32	24
Satinoco	Py3	14												
Mean		0.11	0.03	52.59	0.20	0.16	0.00	45.86	0.06	0.07	0.03	0.02	0.02	0.01
Maximum		0.45	0.09	53.46	0.33	1.28	0.00	46.58	0.09	0.48	0.17	0.08	0.07	0.05
Minimum*		0.00	0.00	50.65	0.04	0.00	0.00	44.83	0.04	0.00	0.00	0.00	0.00	0.00
% BDL		64	21	0	0	58	100	0	0	21	50	64	43	50
Detection Limit		0.0306	0.0304	0.0085	0.0135	0.0429	0.0207	0.0168	0.0121	0.021	0.0176	0.03	0.017	0.0135

Values in wt. %

N = Number of analyses

5.5.1 São Sebastião deposit

Three varieties of arsenopyrite have been identified on basis of their textures and composition (Apy_{2a}, Apy_{2b}, and Apy₃). Apy_{2a} and Apy_{2b} are present as subhedral coarse-grained crystals disseminated within sulfide bands along the main foliation, whereas Apy₃ is present as disseminated fine-grained grains with sub-rounded outlines or occur within masses of pyrrhotite (Po₃).

Apy_{2a} and Apy_{2b} (Fig. 5-2) fit in the sulfide assemblage II and correspond to coarse-grained arsenopyrite from Brando Soares et al. (2018). Here, the EMP mapping reveal compositional zonation for Apy₂ and the phase Apy_{2a} correspond to the inner part of the some large Apy_{2b} grains. EMP spot analyses show that, in comparison to Apy_{2b}, the Apy_{2a} has a relatively higher abundance of Ni (average 0.16 against 0.04 wt.%) and lower Cu (average 0.024 against 0.058 wt.%). Respectively, Apy_{2a} and Apy_{2b} contains distinctly higher average S (18.93 and 19.12 wt.%), Fe (36.49 and 36.16 wt.%), and Se (0.23 and 0.23 wt.%). The percentage of analyses below detection (% BDL) is zero or relativelly low in the following trace elements: Se (0%), Cu (<10%), Pb (<32%).

The disseminated fine-grained Apy₃ contain relatively high average Co (3.82 wt.%), Ni (0.61 wt.%), Bi (0.11 wt.%), Se (0.93 wt.%), and Pb (0.83 wt.%) along with other element concentrations as follows: As (46.2 wt.%), S (15.9 wt.%), Sb (0.03 wt.%), and Cu (0.02 wt.%). The

Previous LA-ICP-MS spot analyses by Brando Soares et al. (2018) have shown that the trace elements contained in Apy₂ are dominated by Co (average 95.67 ppm) and lower concentrations of Sb (average 10.44 ppm), Ni (average 3.66 ppm), and Bi (average

1.27 ppm). All analyzed Apy₂ spots are devoid of detectable Au. The new LA-ICP-MS reveal that, compared to Apy₂ crystals, the Apy₃ contains higher abundances of Ni (average 1075.69 ppm), Pb (average 268.09 ppm), Co (average 211.79 ppm), and Bi (average 19.79 ppm), but slight lower contents of Sb (average 9.12 ppm). The Apy₃ grains contain a relatively high abundance of Zn (average 23.56 ppm), Bi (average 19.79 ppm), Au (average 17.23 ppm), and Mn (average 21.26 ppm) in addition to minor V, Cu, Ag, and Te. Two spot analysis in intragrain microfractures within Apy₂ exposed higher average values of Bi (52.59 ppm) and Sb (18.73 ppm), compared to fracture-free Apy₂ spots. Pyrite returned higher Cu (1.37 ppm), Ag (2.02 ppm), Bi (11.70 ppm), and Pb (0.95 ppm) average contents than Ap₂, but lower than Apy₃.

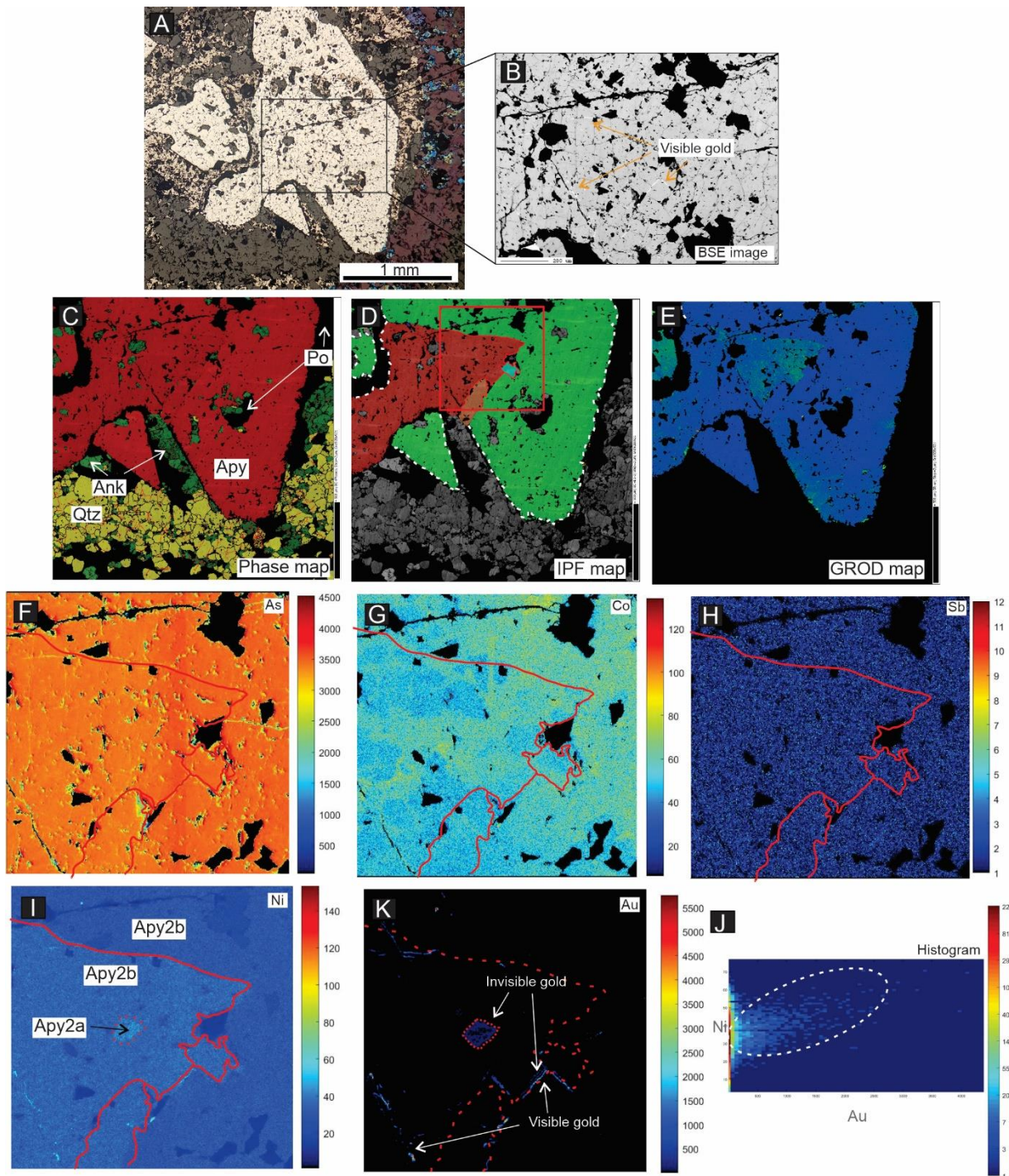


Fig. 5-2. São Sebastião deposit. (A) Reflected light photomicrograph of arsenopyrite from sulfide assemblage II (Apy_2). (B) BSE SEM image showing visible fracture-filling gold. (C) EBSD phase colors map. (D) EBSD IPF map that highlights the different

crystals within Apy aggregate. (E) Crystallographic misorientation angle in the range 0-8° (green). (F-K) Elemental As, Co, Sb, Ni, and Au X-ray maps from area represented as red box in D. Note that Ni and Au concentrations shows Apy_{2a} in the core of Apy_{2b}. (J) Histogram of Au and Ni that shows correlation only in higher Au grades (visible filling-fracture Au-Ni).

5.5.2 Turmalina deposit

Three arsenopyrite types (Apy_{1a} , Apy_{1b} , and Apy_2) were defined in the Turmalina deposit based on their texture, X-ray mapping, and EBSD data and are consistent with the recognized sulfide assemblages by Fabricio-Silva et al. (2019; Fig. 5-3). The Apy_{1a} presents as subhedral, fine-grained, acicular grains disseminated along the main foliation and the Apy_{1b} occurs as prismatic polycrystalline aggregates foliation-parallel or in the quartz vein margins. The Apy_2 is characterized by a main foliation-discordant disseminated that grow up to 300 μm in size, usually replacing the existing sulfides.

Generally, the EMP results show that the Apy_{1a} and Apy_{1b} have similar contents. Nevertheless, compared to Apy_1 , Apy_2 grains present a greater number of minor and trace elements, but a lower As (average 44.9 against 49.2 wt.%) and Sb (0.044 against 0.36 wt.%). The Apy_2 grains contain a relatively higher average abundance of Se (0.23 wt.%), Te (0.04 wt.%; max at 0.215 wt.%), Cu (0.02 wt.%; max at 0.11 wt.%) and Au (0.039 wt.%; max at 0.11 wt.%). In the Apy_2 , the percentage of analyses below detection (% BDL) of the following trace elements are: Se (0%), Te (61%), Cu (41%), and Au (45%).

Based on LA-ICP-MS, Apy_1 returned lower trace elements contents, compared to Apy_2 . The average results for Apy_1 and Apy_2 are, respectively: Co (197.70 and 315.52 ppm), Cu (BDL and 0.82 ppm), Se (27.77 and 345.54 ppm), Sb (6.94 and 570.86 ppm), Te (0.19 and 12.38 ppm), Pb (1.09 and 6.38 ppm), and Au (BDL and 3.17 ppm). However, Apy_1 contains higher Ni (average 1755 ppm), V (9.68 ppm), and Bi (2.74 ppm), compared to Apy_2 .

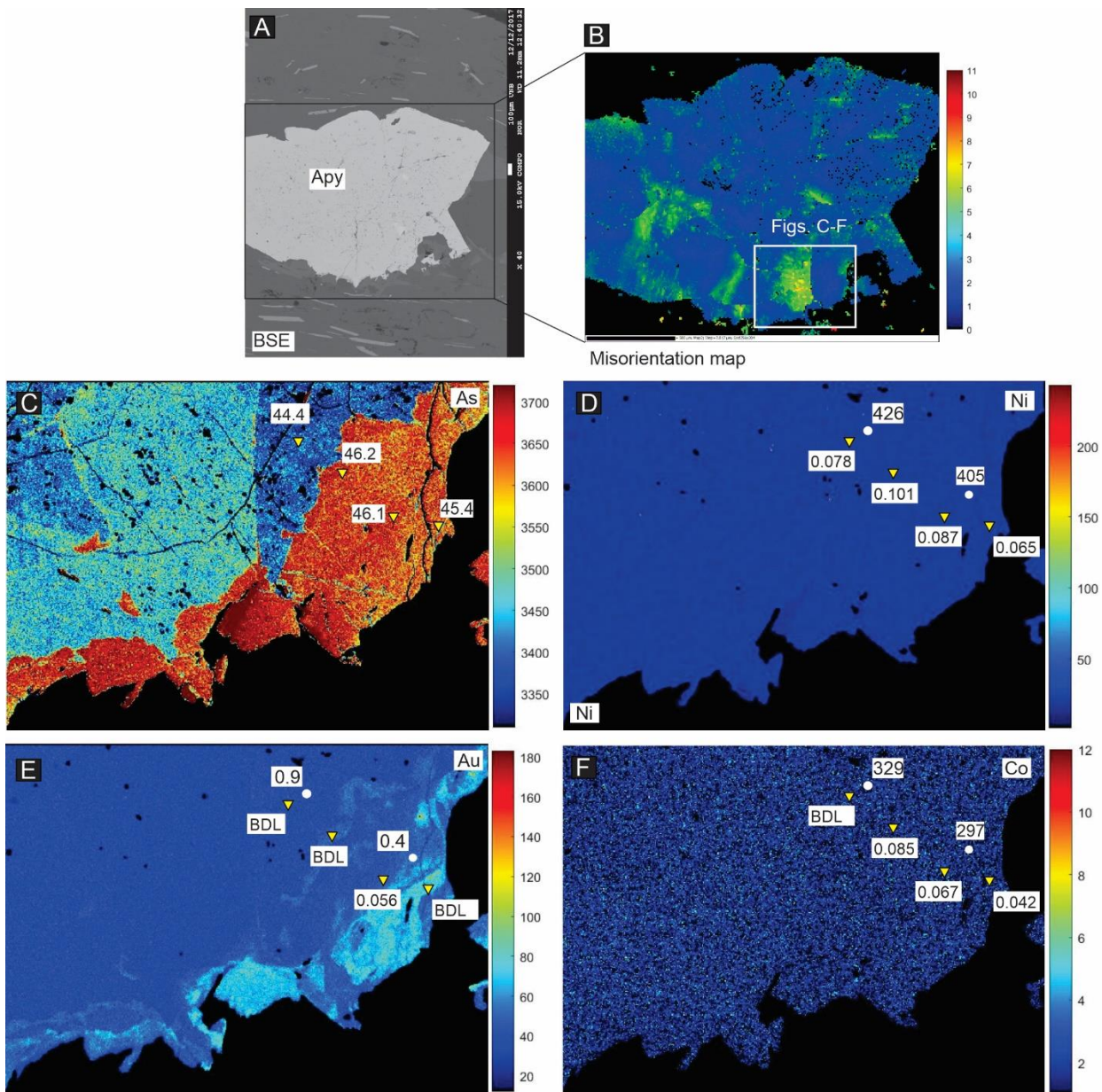


Fig. 5-3. Turmalina deposit. (A) BSE SEM image of coarse grained arsenopyrite from sulfide assemblage II (Apy₂). (B) Crystallographic misorientation angle in the range 0-11°. (C-F) Elemental As, Ni, Au, and Co X-ray maps from area represented as white box in B. Yellow triangle indicate the LA-ICP-MS spot analyses. The white circles show the EMP spot analyses.

5.5.3 Satinoco deposit

Two arsenopyrite types in the Satinoco deposit were defined (Fabricio-Silva et al., 2020). The first, Apy₁, occurs as disseminated, porous crystals oriented parallel to the main foliation and the bedding of the black shale. The Apy₁ occurs in equilibrium with pyrrhotite (Fig. 5-4) and is partially replaced by löllingite. Apy₂ consists of fine-grained, euhedral-subhedral grains (Fig. 5-5) intergrown with pyrrhotite and replacing earlier sulfide assemblage.

Based on the EMP data, the Apy₁ is enriched in As (~50 wt.%), Sb (average 0.32 wt.%; max 0.814 wt.%) and Pb (average 0.05 wt.%; max 0.23 wt.%), whereas Apy₂ contains high Co (1.09 wt.%; max 1.67 wt.%) and Ni (1.03 wt.%; max 0.23 wt.%) and Co (1.09 wt.%; max 1.67 wt.%).

Previous LA-ICP-MS by Fabricio-Silva et al. (2020) have shown that the Apy₁ are dominated by Ni (average 3803 ppm) and Mn (average 396 ppm), in addition to Co (average 148.72 ppm), Zn (average 58.04 ppm), and V (average 19.62 ppm). Apy₁ has lower concentrations of Se, Pb, Bi, and Ag. All analyzed Au in Apy₁ spots are BDL. Compared to Apy₁, the Apy₂ presents higher average contains of Sb (11,765 ppm), Co (365.77 ppm), Pb (93.99 ppm), Au (80.51 ppm), and Ag (1.33 ppm) but lower contents of Zn, Se, Bi, and Cu. One spot analysis in an intragrain microfracture within Apy₂ exposed high values of Au (21 wt.%), Sb (54 wt.%), and Ni (2.5 wt.%). Pyrite returned higher Cu (BDL-78.01 ppm), Se (9.77-36.81 ppm), Bi (0.04-33.51 ppm), Te (BDL- 7.04 ppm), and Ag contents (BDL-4.06 ppm) than Apy₁ and Apy₂.

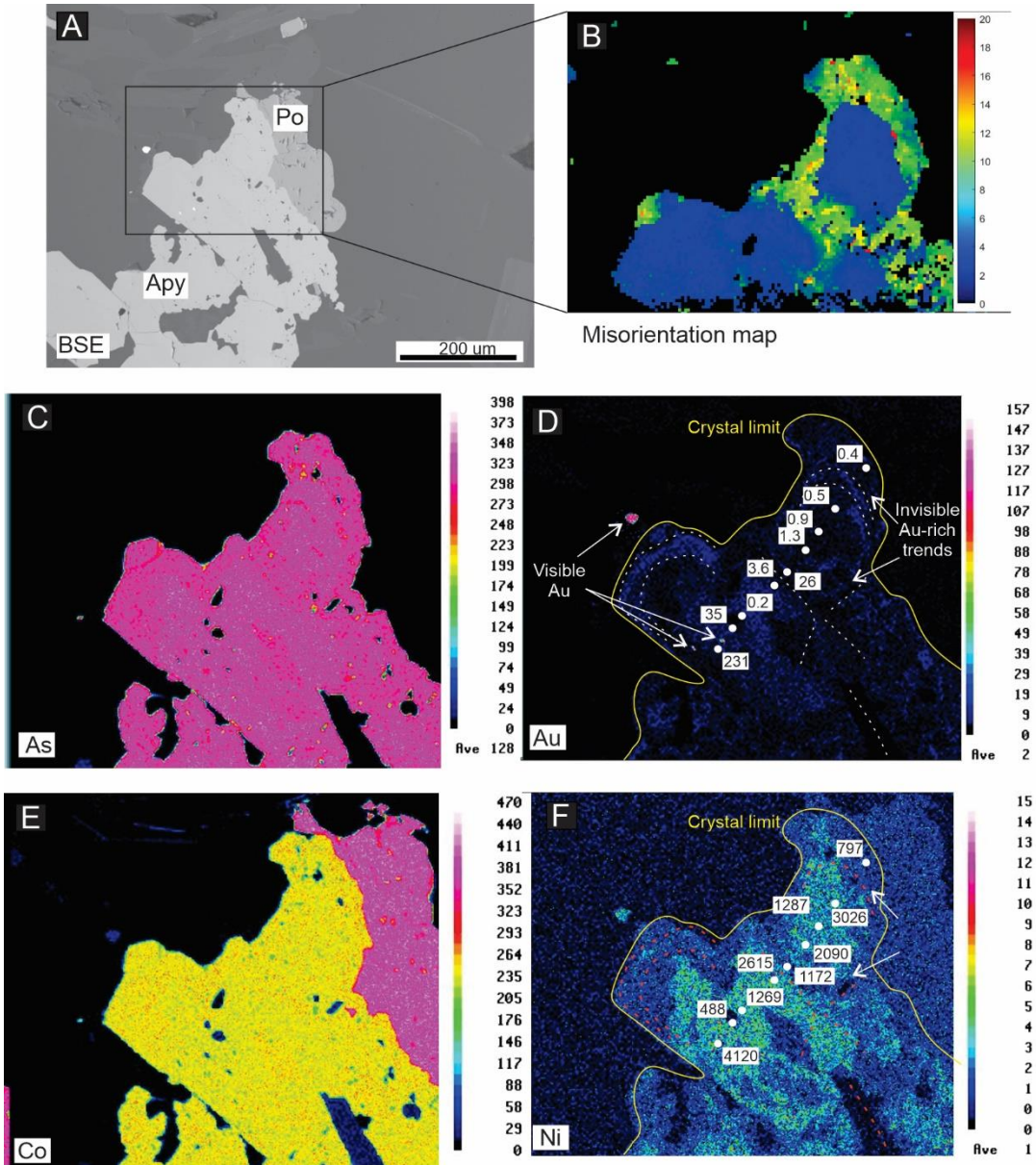


Fig. 5-4. Satinoco deposit. (A) BSE SEM image of course grained arsenopyrite from sulfide assemblage I (Apy_1). (B) Crystallographic misorientation angle in the range 0-20°. (C-F) Elemental As, Au, Co, and Ni X-ray maps from area represented as black box in A. Yellow triangle indicate the. The white circles show the LA-ICP-MS spot analyses. Note that the invisible gold forms Au-rich trends in the Apy-core.

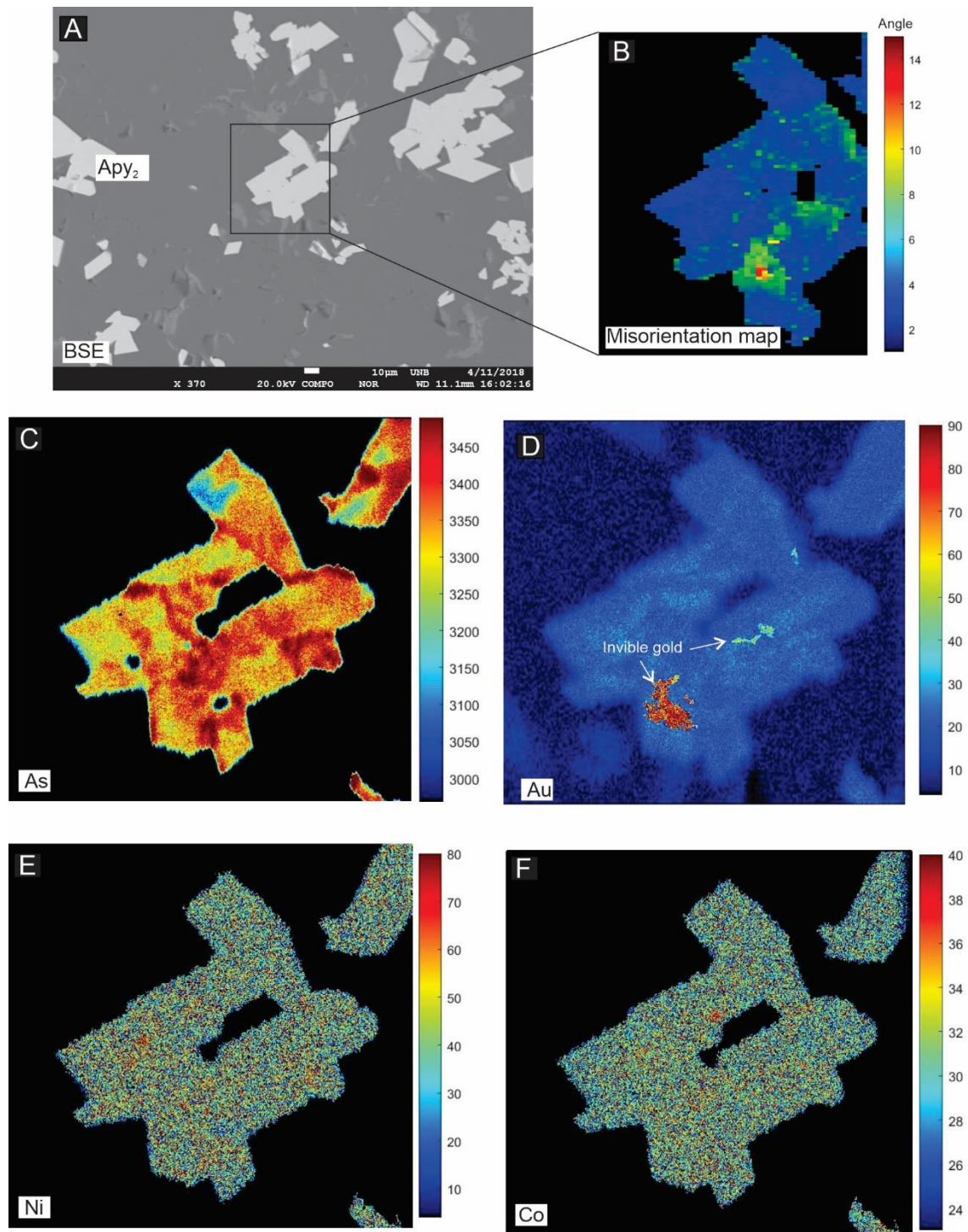


Fig. 5-5. Satinoco deposit. (A) BSE SEM image of fine grained arsenopyrite from sulfide assemblage II (Apy₂). (B) Crystallographic misorientation angle in the range 0-15°. (C-F) Elemental As, Au, Ni, and Co X-ray maps from area represented as black box in A.

Yellow triangle indicate the. The white circles show the LA-ICP-MS spot analyses. Note that the invible gold forms Au-rich zones in the Apy-core.

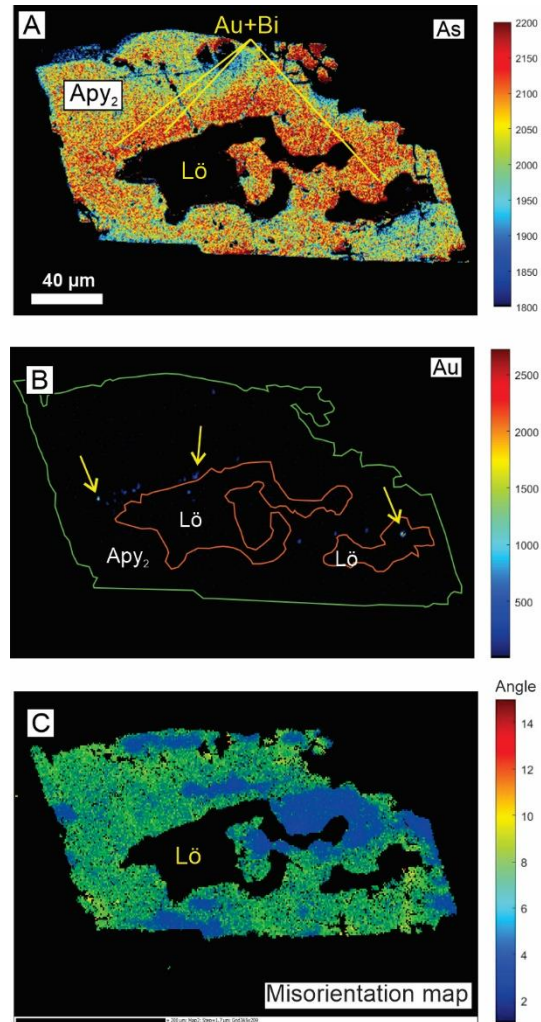


Fig. 5-6. Satinoco deposit. (A-B) Elemental X-ray mapping for As and Bi in a Apy₂ that rims Lö (after Fabricio-Silva et al., 2020). (C) Crystallographic misorientation angle in the range 0-15°.

5.5.4 Composition of pyrite compared to arsenopyrite

Pyrite occurs in the ore in all gold deposits studied. In short, hydrothermal pyrite occurs as subhedral-euhedral coarse-grained crystals that overgrowth earlier pyrrhotite-arsenopyrite based assemblages. A pre-metamorphic (syngenetic?) pyrite (Py0) was demonstrated by Fabricio-Silva et al. (2020) supported by cross-cut relationships and sulfur isotope ratios (Bosco-Santos et al.; 2020).

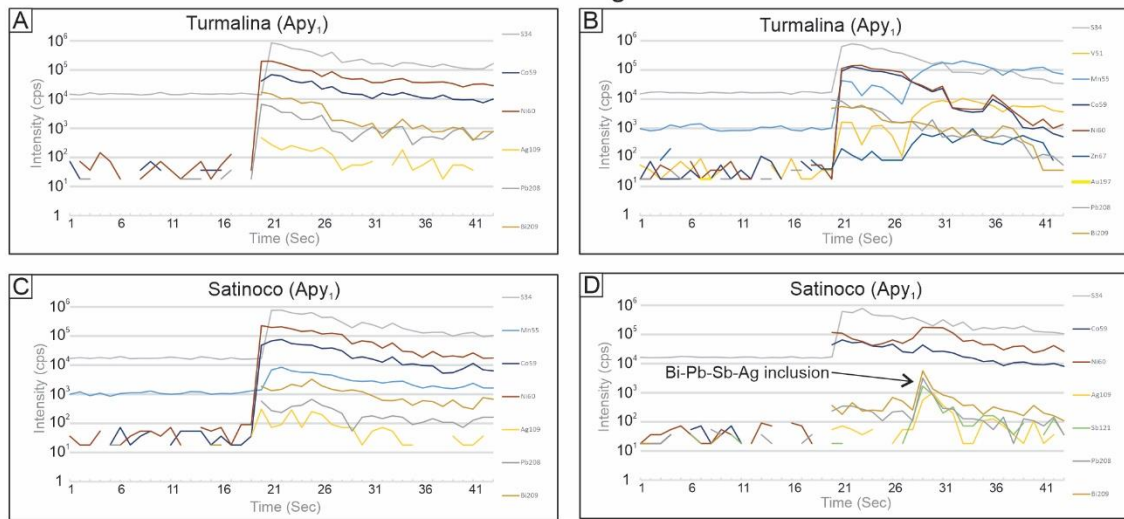
Based on EMP data, Py₃ from Satinoco deposit contains relatively higher concentration of Cu (average 0.07 wt.%; max 0.48 wt.%), Pb (average 0.2 wt.%; max 0.33 wt.%) and Bi (average 0.16 wt.%; max 1.28 wt.%) compared to its in equilibrium-arsenopyrite (Apy₂). Py₃ also contains high As (average 0.11 wt.%; max 0.45 wt.%). The pre-metamorphic pyrite from the distal orezone analysed show that the greater number of minor and trace elements, including As content, are close or below the detection limits.

Data from Brando Soares et al. (2018) and Fabricio-Silva et al. (2020) show that hydrothermal pyrite in São Sebastião and Satinoco have relatively higher values of trace elements compared to arsenopyrite crystals of older assemblages. However, in the youngest gold-bearing assemblage of the São Sebastião deposit, our analyzes show a greater enrichment of trace elements in Apy₃, compared to Py₃. Later Au-rich pyrite grains from Turmalina and Satinoco do not occur in equilibrium with arsenopyrite.

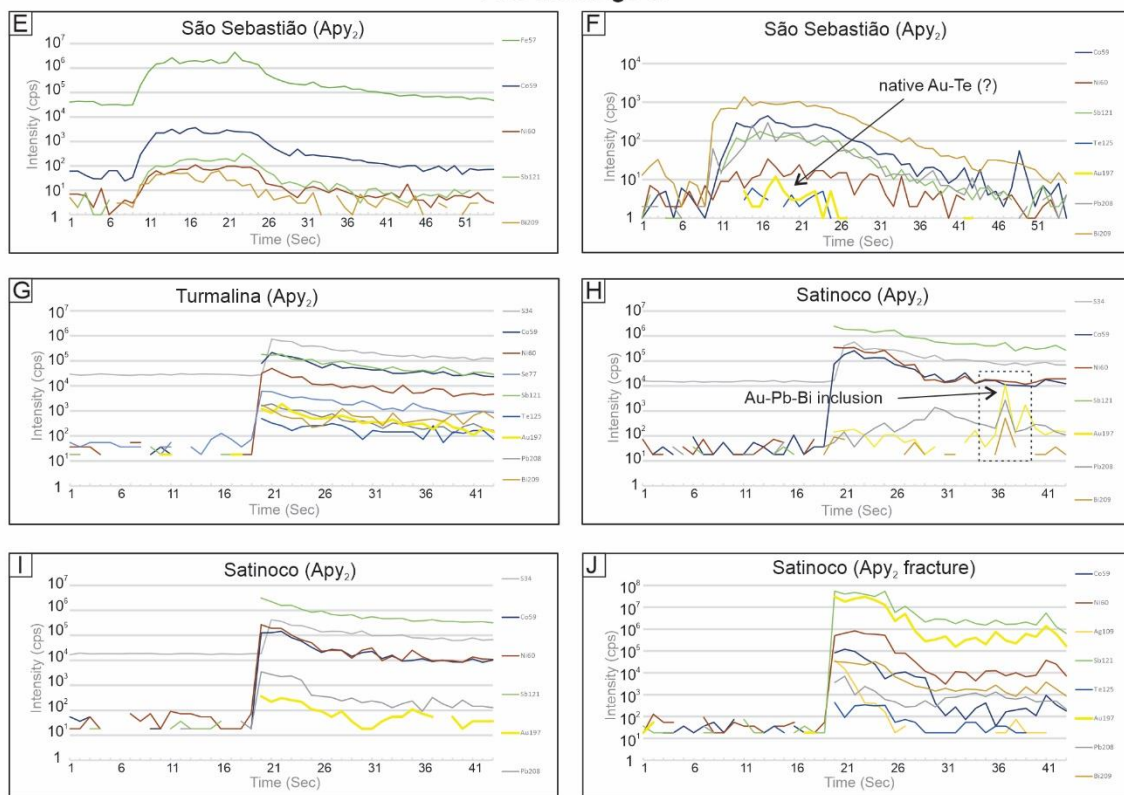
Table 5-3. Summary of minor and trace element contents in sulfide minerals performed by LA-ICP-MS (data in ppm)

Mineral	V	Mn	Co	Ni	Cu	Zn	Se	Mo	Ag	Sn	Sb	Te	Pb	Bi	Au															
Assemblage I																														
Apy₁ - Turmalina																														
Average (n = 5)	9.68	165.88	97.70	1754.77	2.56	BDL	47.77	BDL	BDL	BDL	56.94	0.19	1.09	2.74	BDL															
Reference	This study																													
Apy₁ - Satinoco																														
Average (n = 12)	19.62	396.38	148.72	3803.12	BDL	58.04	14.00	BDL	0.69	BDL	0.69	0.12	5.29	3.94	BDL															
Reference	Fabricio-Silva et al. (2020)																													
Assemblage II																														
Apy₂ - São Sebastião																														
Average (n = 10)	95.67			3.66	BDL	BDL	BDL			BDL	10.44	0.12			1.27															
Reference	Brando Soares et al. (2018)																													
Apy₂ fracture - São Sebastião																														
Average (n = 2)	27.70			2.64	BDL	BDL	BDL			BDL	18.73	2.77			52.59															
Reference	Brando Soares et al. (2018)																													
Apy₂ - Turmalina																														
Average (n = 8)	0.15	12.82	315.52	302.15	0.82	BDL	345.54	BDL	0.07	BDL	570.86	12.38	6.38	1.46	3.17															
Reference	This study																													
Apy₂ - Satinoco																														
Average (n = 25)	11.44	33.77	365.77	2618.78	0.74	8.06	BDL	BDL	1.33	0.28	11764.53	1.69	93.99	0.54	80.51															
Reference	Fabricio-Silva et al. (2020)																													
Apy₂ fracture - Satinoco																														
Result (n = 1)	BDL	26.88	455.86	25780.23	6.58	10.87	BDL	BDL	35.76	BDL	5.41E+05	30.00	16.77	107.93	2.14E+05															
Reference	Fabricio-Silva et al. (2020)																													
Assemblage III																														
Apy₃ - São Sebastião																														
Average (n = 4)	6.82	21.26	211.79	1075.69	1.77	23.56	0.00	0.15	2.02	0.57	36.12	0.72	268.09	19.79	27.23															
Reference	This study																													
Py₃ - São Sebastião																														
Average (n = 3)	13.23			115.48	1.37	BDL	2.34			BDL	0.95			11.70	3.74															
Reference	Brando Soares et al. (2018)																													
Py₃ - Satinoco																														
Average (n = 7)	0.07	17.54	191.40	844.74	23.88	BDL	20.64	0.22	1.36	0.12	22.55	2.87	26.90	13.71	0.33															
Reference	Fabricio-Silva et al. (2020)																													

Assemblage I



Assemblage II



Assemblage III

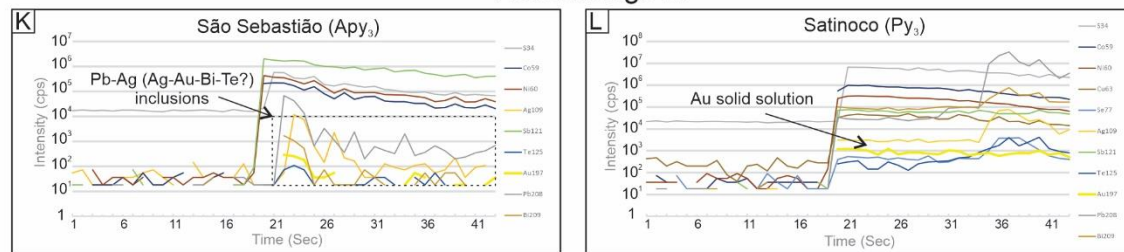


Fig. 5-7. Time-resolved LA-ICP-MS depth profiles for spot analyses of S, Fe, Co, Ni, Sb, Au, Pb and Bi of arsenopyrite and pyrite hosted in ores from Turmalina, Satinoco, and São Sebastião deposits from sulfide assemblages I (A-D), II (E-J), and III (K and L). Free gold particles are shown mainly in Apy₂ from Satinoco deposit and Apy₃ from São Sebastião deposit.

5.6 Discussion

Note: This discussion section is under development. Part of the data is interpreted as highlights and we expect to have the text completely written by the date of the presentation of this work.

5.6.1 Evolution of gold-bearing sulfides

The textural evidence, as well as Au distribution characteristics, indicate that gold mineralization in the PGB is commonly attributed to remobilization of invisible gold in preexisting pre- to syn-tectonic arsenopyrite (in Turmalina and Satinoco) or pyrite (in São Sebastião) during prograde metamorphism conditions. Considering that initial arsenopyrite grains are characterized by invisible gold distributions showing a systematic decrease in concentrations from the center of the grain to its rim, and that alteration rims are enriched with invisible gold (Fig. 5-2), it can be deduced that early invisible gold was exsolved and then remobilized to form at least part of the visible gold in sulfide assemblage I or the trend lines parallel to the grain boundary (Fig. 5-4 and 5-9). As Apy₁ grew syn-kinematically with regards to main foliation (and as inclusions in the cores of Grt₂; Fabricio-Silva et al., 2019), the sulfide assemblage I must pre-date the metamorphic peak.

Our petrographic observations of irregular contacts between löllingite and arsenopyrite and relicts of löllingite in arsenopyrite crystals (Fig. 5-6) are consistent for the formation of arsenopyrite at the expense of löllingite during retrograde metamorphism (cf. Tomkins and Mavrogenes, 2001). The destruction of löllingite during retrograde metamorphism would explain the presence of trace Co and Ni and their uneven distribution in Apy₂. Note that the löllingite was not described in São Sebastião, but the high temperature and the replacement of Po₁ by Apy₂ assemblage during the prograde metamorphism (Brando-Soares et al., 2018) requires the following reaction by (Barnicoat et al., 1991): $2\text{FeAsS} \rightarrow \text{FeAs}_2 + \text{FeS} + 0.5\text{S}_2$ (Barnicoat et al., 1991). During this stage, some of the arsenopyrite grains were replaced by löllingite and only the larger grains or those included in garnet survived as relicts. Garnet has not been observed in the BIF-hosted orebodies in São Sebastião.

During retrograde metamorphism, such löllingite is expected to be completely consumed to form arsenopyrite as experimentally demonstrated by Tomkins and Mavrogenes (2001) and observed at other localities (Deol et al., 2012; Saintilan et al., 2017) via the following reaction $\text{FeAs}_2 + (1/x) \text{FeS}_{(1+x)} \rightarrow 2\text{FeAsS} + ([1+x]/x)\text{FeS}$ (Neumayr et al., 1993).

The occurrence of visible gold in close association with the other late sulfide assemblage III minerals such as chalcopyrite, galena, sphalerite, ISS, and ullmannite raise the possibility of Au being additionally supplied with Ni, Pb, Cu, Zn, and Ag at the time of brittle fracture and hydrothermal fluid infiltration.

However, relatively stronger correlations occur among Au, Ag, Pb, Sb, and Bi (and Te?) in fractures, contrasting which the small concentrations of Cu, Zn, Sb may indicate that the additional influx of Au, as well as other precious and base metals, may have occurred during the remobilization stage after the brittle deformation.

Based on trace element composition and distribution in each sulfide assemblage, is possible to suggest that these elements incorporated into sulfide crystal lattice is likely to be mobile during the ore-evolution

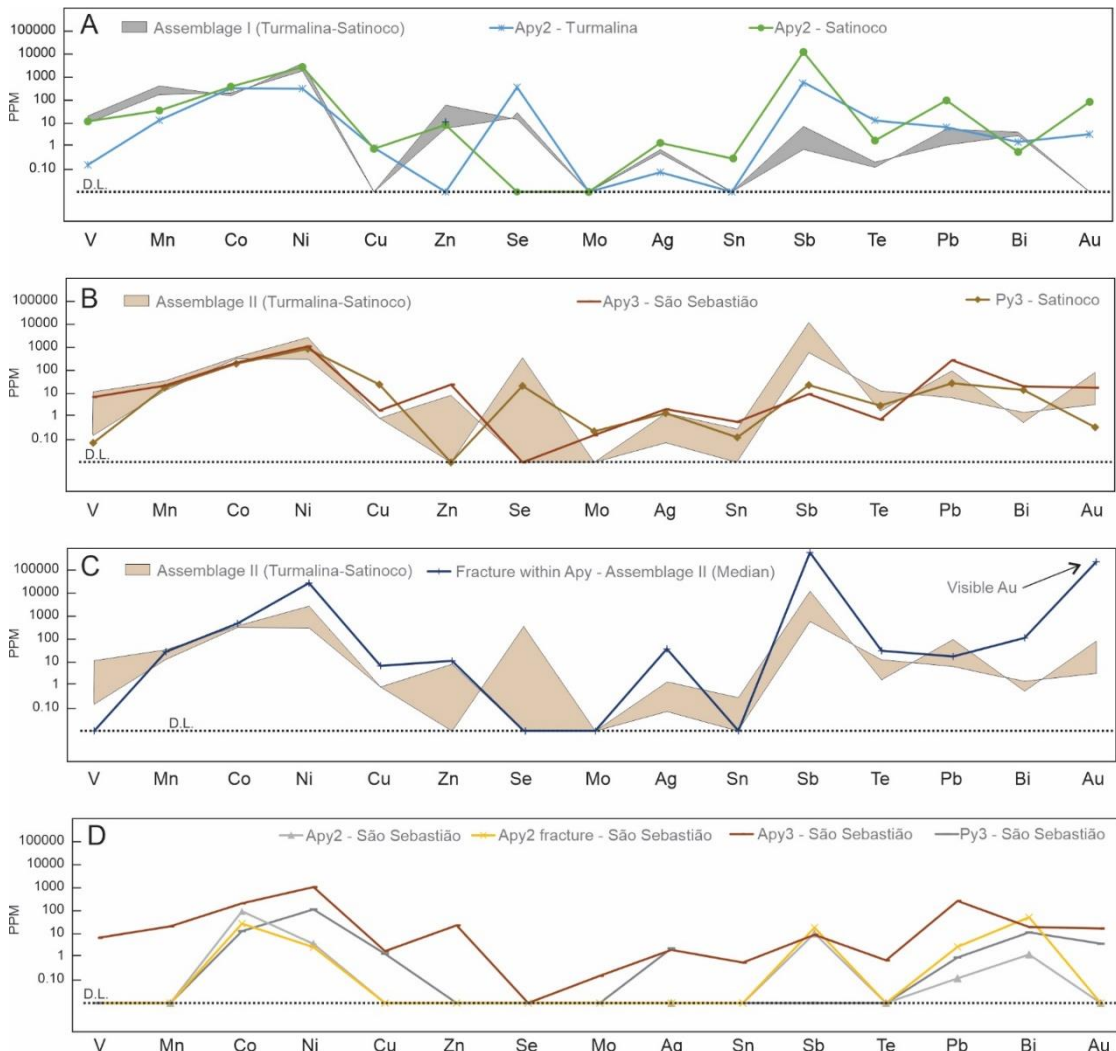


Fig. 5-8. Multi-element diagrams of arsenopyrite from Turmalina, Satinoco, and São Sebastião deposits showing median trace element values of the LA-ICP-MS analyses for specific sulfide assemblages. (A) Sulfide assemblage I (Apy_1) from the Turmalina and Satinoco deposits (grey region) showing similar trace element concentrations. In contrast, the sulfide assemblage II shows enrichment in Sb, Te, Pb, and Au, compared to assemblage I. (B) Relative similar patterns between assemblage II (beige region) from Turmalina and Satinoco and Apy_3 (São Sebastião) and Py_3 (Satinoco). Differences in Zn, Se, Mo, and Cu between assemblage II, considered to have formed in part from magmatic fluids, and the hydrothermal sulfide assemblage I. (C) Significant enrichment in Au, Sb, Te, Bi, and Ag in intragrain microfracture in Apy_2 , compared to non-fractured crystals. (D) Median values after Brando Soares et al. (2018) applied to the sulfide parageneses described here. Note

that, although only a few elements are above D.L. (detection limit), the later Py₃ and Apy₃ (this study) show enrichment in Au, Bi, Pb, and Sb, as observed in other studied deposits.

5.6.2 The Ni concentration from ore-forming fluids

The first sulfide assemblage I in Turmalina and Satinoco shows similar trace element content, except for a low variation in the contents of V and Mn (most present in Turmalina) and Sb (most common in Satinoco). However, the Ni concentrations are quite high in Satinoco (3803 ppm on average). It is also observed that the Ni concentrations in assemblages II and III in all deposits are much lower than the ratios in the sulfides of assemblage I (even in Turmalina; 1755 ppm on average).

It has been known that Ni, which is typically enriched in ultramafic and, lesser, mafic rocks, tends to be incorporated into the sulfide crystal lattice and is likely to be immobile during hydrothermal alteration (Huerta-Diaz and Morse, 1992; Morse and Luther, 1999; Large et al., 2009; Zhao et al., 2011). Therefore, considerably high Ni concentrations in Apy₁ from Satinoco deposit and amphibolitic wall rocks (876 ppm on average; nonpublished whole rock data, see Anexo VII) should indicate that a high proportion of mafic to ultramafic rock components was introduced in hydrothermal fluids responsible for the precipitation of arsenopyrite in sulfide assemblage I.

Nickel concentrations seem to be poorly correlated with Au concentrations in those sulfides, but they exhibit strong positive correlation in fractures and as enriched rims in assemblages II and III (Fig. 5-2). The assemblage II is Ni-depleted, in comparison with the earlier stage. Thus, it is likely that the ore-forming fluids from assemblage III (and final phase of assemblage II?) were introduced with brittle deformation and promoted the redistribution of Au under fluid-rock interaction. But the good correlation

with invisible Au and Ni in Apy₂-rim and those fractures suggest that the sulfide assemblage I may experienced partial melting releasing Ni into the new fluid.

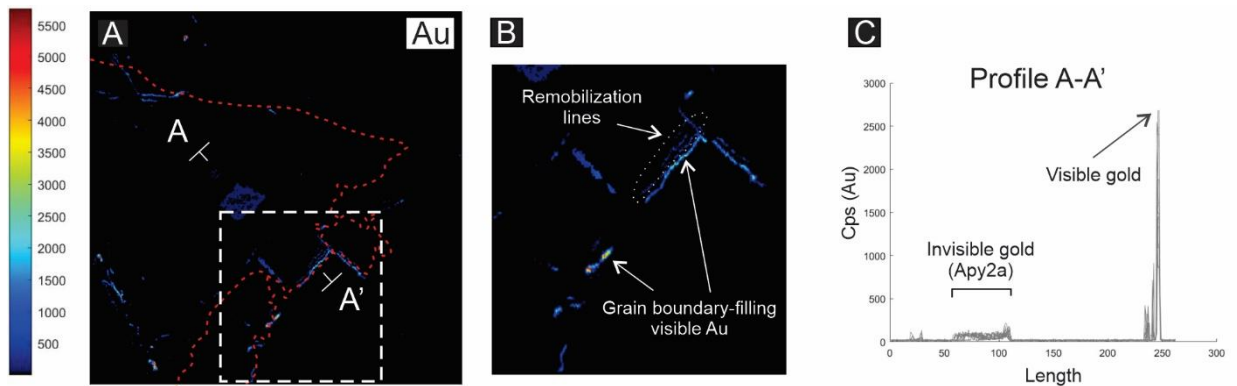


Fig. 5-9. The São Sebastião Apy₂ showing visible Au between the grain boundary (see Fig. 2D). The invisible gold occurs in Apy₂-core (Apy_{2a}) and as remobilization lines in the Apy_{2b}-rim.

5.6.3 Discriminating arsenopyrite and pyrite compositions

Our EMP and LA-ICP-MS data together with Brando Soares et al. (2018) and Fabricio-Silva et al. (2020) show that the geochemical signatures of trace elements in late-paragenesis of those deposits are similar. They show that the coarse-grained Py₃ is enriched in Co, Sb, Bi, and Pb which appears in the ore in all the gold deposits studied and occurs in equilibrium with pyrrhotite \pm arsenopyrite (Fig. 5.8). Based on texture and cross-cutting relationships, these pyrite grains show evidence to have formed as the expense of earlier arsenopyrite-pyrrhotite in a late to post-tectonic (as in Turmalina) or in a post-tectonic period (São Sebastião and Satinoco). In the Satinoco and Turmalina deposit, pyrite coexists with a significant number of base-metal sulfides, as galena, chalcopyrite, sphalerite, ullmannite, whereas in São Sebastião, the younger sulfide assemblage contains ISS, Bi-sulfides and Bi-Te minerals.

The potential influence of co-precipitation of arsenopyrite in the pyrite composition is highly observed (Mumin et al. 1994; Reich et al. 2005). In summary, only Sb shows a systematic enrichment in arsenopyrite relative to contemporaneous pyrite. Furthermore, there is no systematic depletion in Sb for pyrite associated with arsenopyrite relative to other pyrite types in the studied gold deposits. The other metals show variable behaviors (increasing, diminishing, and similar contents) in pyrite relative to arsenopyrite when both are co-precipitated. It appears that the co-precipitation of arsenopyrite has a very limited impact on the trace element content of pyrites.

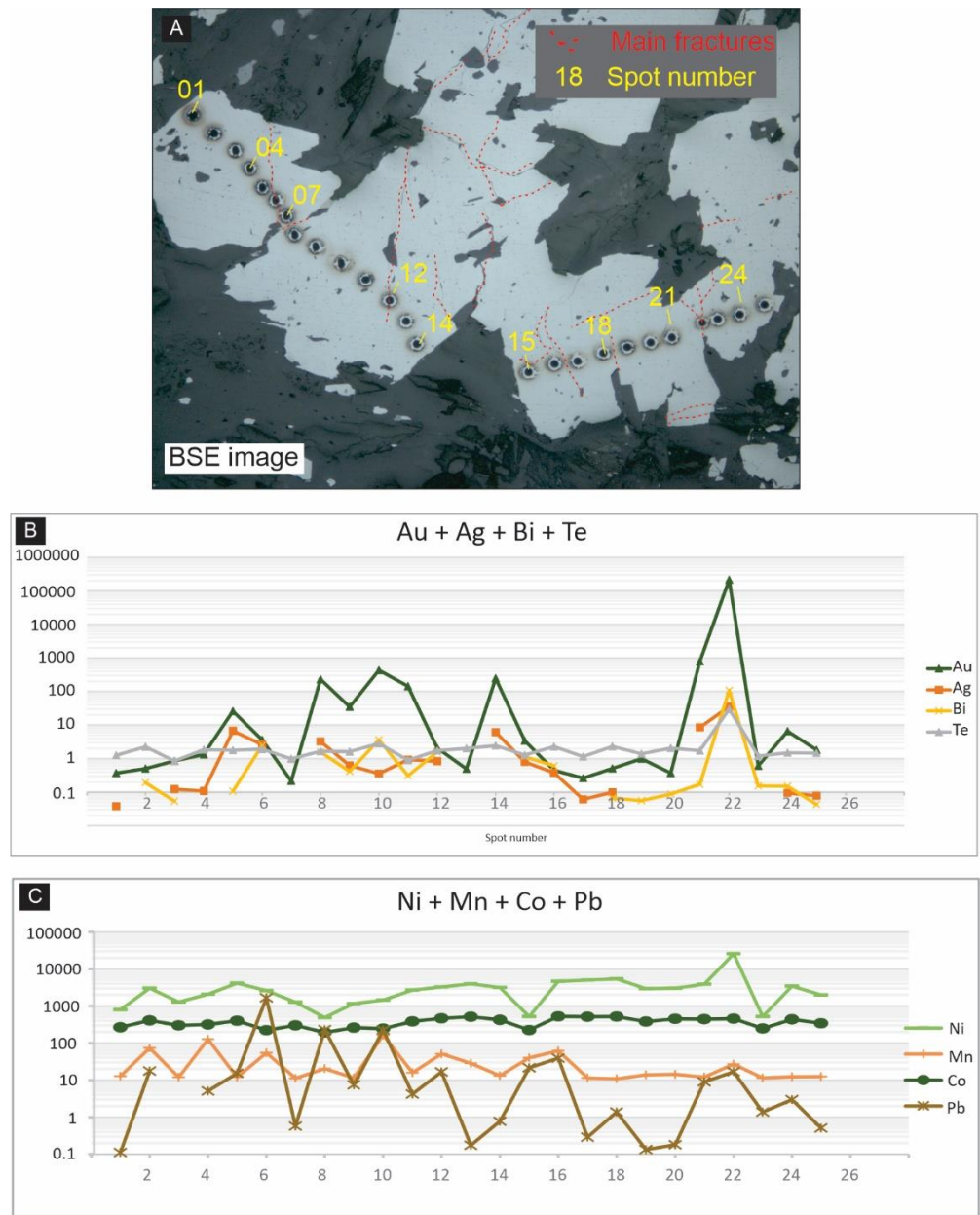


Fig. 5-10. Quantitative LA-ICP-MS elemental profiles (in ppm) acquired across an Apy_2 grain from Satinoco deposit. (A) BSE image of the analyzed arsenopyrite grain. The dashed red lines represent micro-fractures identified. (B-C) Concentration profiles for selected elements in each spot ablated along the profile shown in image A. The spot 22 is over a fracture-filling visible Au.

5.6.4 Au remobilization processes

Mineral-scale element and misorientation mapping, and spot analyses and depth profiles from LA-ICP-MS made it possible, in combination with previously published geochronological, S isotope and, fluid inclusion data, to draw the following interpretation on Au remobilization:

- It has been identified that Au was incorporated as part of new fluids at least twice, i.e., during the pre- to syn-tectonic and the late- to post (synchronously to granite magmatism) tectonic event. However, there is evidence of remobilization in all sulfide assemblages.
- The rare homogeneous distribution of Au in the cores of older arsenopyrite grains (Apy₂ in São Sebastião and Apy₁ in others), suggests that the gold contents were incorporated initially as invisible Au⁺, as observed in time-resolved spectra (Fig. 5-7). It is consistent with the EBSD maps in Apy₁ in Satinoco (Fig. 5-4), suggesting a deformation-driven intra-grain diffusion (by dislocation-impurity pair or high-diffusivity pathway diffusion (cf. Plümper et al., 2012 and Fougerouse et al., 2016).
- The occurrence of Au inclusions in Apy₂, Apy₃, and Py₃, as observed in LA-ICP-MS spectra suggests that the Au in these assemblages should have remobilized following the models of partial melting and/or fluid-mediated replacement.
- The phase boundaries of arsenopyrite in a line scan are demarcated clearly by a decrease in S and an increase in As. The line scan (Fig. 5-2) across Apy_{2a}-Apy_{2b} association shows that invisible Au is distinctly higher in Apy_{2a} than in

Apy_{2b}, and the pattern of the graph defines a plateau, suggesting incorporation of the noble metal in the structure of Apy_{2b}-rim. Contrastly, the fracture-filling Au are related to Apy_{2b} rims and several correlated spikes of Au, Bi, Te, Sb, and Pb in the time-resolved spectra are also noted. These features suggest that there are micro-inclusions of some Au-LMCE alloy in late Apy, whereas Au is present in structure in the early stages. A sharp rise in Au concentration is seen at the interface of arsenopyrite and löllingite, as well as in Bi values, suggesting that gold may be present as inclusions of Au-LCME or as Au-tellurides at the interface.

- During the remobilization process, Au and Ag were decoupled, which resulted in (i) a change in Au/Ag ratios of 0.5 to 5 in early arsenopyrite to ≈9 in the new native gold (900 Au fineness) and (ii) incorporation of Ag into cogenetic secondary mineral phases (e.g., chalcopyrite, sphalerite, ullmannite, and galena).
- The high concentration of LMCE in the late phases of sulfide in all deposits allowed the partial melting of the sulfides under greenschist facies (Frost et al., 2002; Tooth et al., 2011). However, the relatively absence of inclusions and zonation in some crystals of arsenopyrite from assemblage II, together with the provided new fluids during this period, allows interpreting the possibility of the fluid-mediated replacement by couple dissolution-reprecipitation.

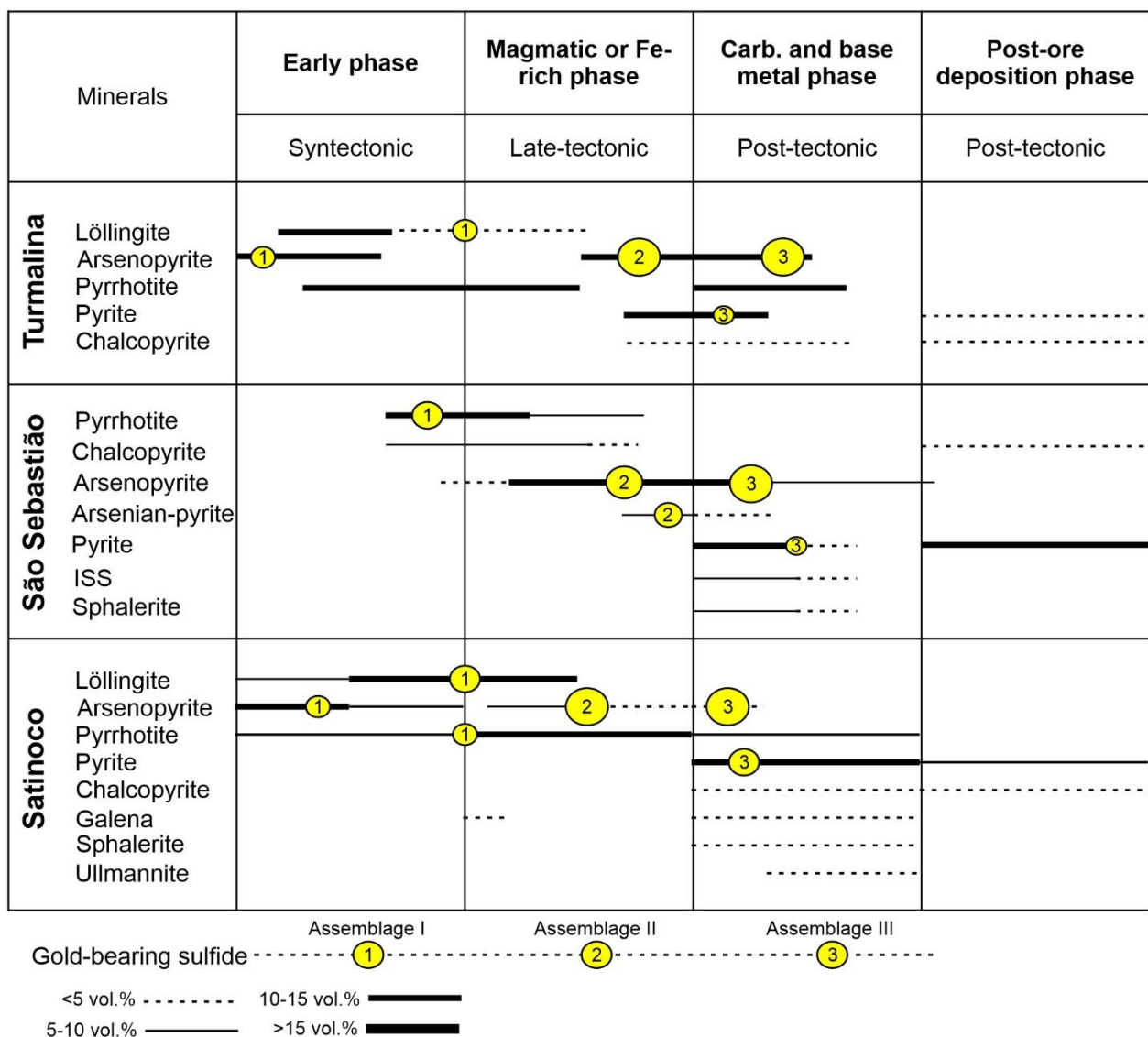


Fig. 5- 11. The paragenetic sequence of sulfides in the studied deposits. The yellow circles represent the relative proportion of gold (free or invisible) in the indicated sulfides.

5.6.5 Relative chronology between the sulfide parageneses and gold mobility

The relative sequence of mineralization stages established in this study, combined with several, partly very recent, publications on the geochronology of the study area, makes it possible to better constrain the chronology of gold mineralization in the PGB. Gold mineralization and associated hydrothermal minerals are spatially related with, and hosted within, shear zones. The first deformation event recorded in the basal komatiites in the Iron Quadrangle (Rio das Velhas and Pitangui greenstone belts) occurred in a collisional phase between 2780 and 2730 Ma (Baltazar and Zucchetti, 2007; Brando Soares et al., 2020). The tectonic collapse between the Belo Horizonte and Divinópolis TTG complexes started at c. 2730 to 2720 Ma (Brando Soares et al., 2020). Based on our data, the gold mineralization stage I must predate 2720 Ga. Inclusion bands show that the main foliation is older than the deformed quartz veins, which implies that the sulfide assemblage I predates the pinch-and-swell structures (Fabricio-Silva et al., 2020). Thus, the age of these veins and the shear zones can be confined between that of the main foliation and the granite intrusion.

As the mineralization stage II comprises recrystallized sulfide aggregates transposed within the crenulation cleavage foliation, the main gold-bearing event must have started in the final phase of the Archean tectonic event but before the Casquilho granite emplacement, i.e., between c. 2720 and 2695 Ma. This is further supported by some veins being cut by granite apophyses observed in Fabricio-Silva et al. (2019).

A temporal relationship between granite emplacement, especially late-magmatic apophyses, and the development of these veins can be inferred. Yet, as indicated by the somewhat lower temperatures obtained for Apy_2 in all deposits (Brando Soares et al., 2018; Fabricio-Silva et al., 2019; 2020) and the observed alteration assemblages, the mineralization stage II continued to lower temperatures as the granitic body

cooled, i.e., after 2695 Ma. However, stage II probably occurred before 2684 Ma, the maximum depositional age of non-mineralized upper units of the Pitangui Group.

The subsequent gold-bearing sulfide assemblages III formed during retrograde metamorphism. Considering the fracture-controlled texture of stage III, the final gold stage took place after the ductile to brittle deformation transition in the upper part of the Pitangui Group had been reached. This implies that the gold mineralization stage III occurred after the maximum depositional age (2684 Ma; Marinho et al., 2018) of the quartzite in the upper units of the Pitangui greenstone belt.

Fabricio-Silva et al. (2020), considering the age of the last felsic magmatism in the PGB as represented by the Caio Martins granodiorite (2593 ± 19 Ma; Romano, 1993), suggested the possibility that the sulfide assemblage III could be younger and might represent a short-lived, separate, event at around 2600 Ma.

The high concentration of LMCE in the late phases of sulfide in all deposits allowed the partial melting of the sulfides under greenschist facies (Frost et al., 2002; Tooth et al., 2011). In this case, the results of Re-Os geochronology for assemblage III in São Sebastião (Brando Soares et al. 2021), which returned values of c.a. 2.0 Ga are blunt with a reset of the Re-Os system in the Paleoproterozoic. Fabricio-Silva et al. (2020), considering the age of the last felsic magmatism in the PGB as represented by the Caio Martins granodiorite (2593 ± 19 Ma; Romano, 1993), suggested the probability that the sulfide assemblage III could be younger and might represent a short-lived, separate, event at around 2600 Ma.

Overall, regarding polystage hydrothermal fluids, the late sulfide stage in all deposits carry a great number of trace elements as a result of metal recycling while the early two stages act as a (re) concentrator process.

5.7 References

- Alkmim F.F., Marshak S. 1998. Transamazonian Orogeny in the Southern São Francisco Craton Region, Minas Gerais, Brazil: Evidence for Paleoproterozoic collision and collapse in the Quadrilátero Ferrífero. *Precambrian Research*, **70**:29–58.
- Almeida F.F.M. 1977. O Cráton do São Francisco. *Revista Brasileira de Geociências*, **7**:349–364.
- Bajwah Z.U., Seccombe P.K., Offler R. 1987. Trace element distribution, Co: Ni ratios and genesis of the Big Cadia iron-copper deposit, New South Wales, Australia. *Mineralium Deposita*, **22**:292–300.
- Baltazar O.F., Zucchetti M. 2007. Lithofacies associations and structural evolution of the Archean Rio das Velhas greenstone belt, Quadrilátero Ferrífero, Brazil: A review of the setting of gold deposits. *Ore Geology Reviews*, **32**:471–499.
- Barnicoat A.C., Fare R.J., Groves D.I., McNaughton N.J. 1991. Synmetamorphic lode-gold deposits in high-grade Archean settings. *Geology*, **19**:921–924.
- Barrie C.D., Boyle A.P., Cook N.J., Prior D.J. 2010. Pyrite deformation textures in the massive sulfide ore deposits of the Norwegian Caledonides. *Tectonophysics*, **483**:269–286.
- Becker U., Reich M., Utsunomiya S., Wang J., Kesler S., Wang L., Ewing R.C. 2007. Nanoparticle-host interactions in natural systems. AGU FM, **2007**:B31F-04.
- Berman R.G. 1991. Thermobarometry using multi-equilibrium calculations; a new technique, with petrological applications. *The Canadian Mineralogist*, **29**:833–855.
- Bierlein F.P., Reynolds N., Arne D., Bargmann C., McKeag S., Bullen W., Al-Athbah H., McKnight S., Maas R. 2016. Petrogenesis of a Neoproterozoic magmatic arc hosting porphyry Cu-Au mineralization at Jebel Ohier in the Gebeit Terrane, NE Sudan. *Ore Geology Reviews*, **79**:133–154.
- Bosco-Santos A., Gilhooly W.P., Fouskas F., Fabricio-Silva W., Oliveira E.P. 2020. Euxinia in the Neoarchean: The starting point for early oxygenation in a Brazilian Craton. *Precambrian Research*, **341**:105655.
- Brando Soares M., Corrêa Neto A.V., Zeh A., Cabral A.R., Pereira L.F., Prado M.G.B. do, Almeida A.M. de, Manduca L.G., Silva P.H.M. da, Mabub R.O. de A., Schlichta T.M. 2017. Geology of the Pitangui greenstone belt, Minas Gerais, Brazil: Stratigraphy, geochronology and BIF geochemistry. *Precambrian Research*, **291**:17–41.
- Brando Soares M., Corrêa Neto A.V., Bertolino L.C., Alves F.E.A., de Almeida A.M., Montenegro da Silva P.H., Mabub R.O. de A., Manduca L.G., Araújo I.M.C. de P. 2018. Multistage mineralization at the hypozonal São Sebastião gold deposit, Pitangui greenstone belt, Minas Gerais, Brazil. *Ore Geology Reviews*, **102**:618–

- Brando Soares M., Corrêa Neto A.V., Fabricio-Silva W. 2020. The development of a Meso- to Neoarchean rifting-convergence-collision-collapse cycle over an ancient thickened protocontinent in the south São Francisco craton, Brazil. *Gondwana Research*, **77**:40–66.
- Bühn B., Santos R. V., Dardenne M.A., de Oliveira C.G. 2012. Mass-dependent and mass-independent sulfur isotope fractionation (δ 34S and δ 33S) from Brazilian Archean and Proterozoic sulfide deposits by laser ablation multi-collector ICP-MS. *Chemical Geology*, **312–313**:163–176.
- Caddick M.J., Konopásek J., Thompson A.B. 2010. Preservation of Garnet Growth Zoning and the Duration of Prograde Metamorphism. *Journal of Petrology*, **51**:2327–2347.
- Carneiro M.A. 1992. O Complexo Metamórfico Bonfim Setentrional (Quadrilátero Ferrífero, MG): Litoestratigrafia e evolução geológica de um segmento de crosta continental do Arqueano: Universidade de São Paulo: 233 p.
- Chemale F., Rosière C.A., Endo I. 1994. The tectonic evolution of the Quadrilátero Ferrífero, Minas Gerais, Brazil. *Precambrian Research*, **65**:25–54.
- Ciobanu C.L., Cook N.J., Damian F., Damian G. 2006. Gold scavenged by bismuth melts: An example from Alpine shear-remobilizes in the Highiș Massif, Romania. *Mineralogy and Petrology*, **87**:351–384.
- Ciobanu C.L., Birch W.D., Cook N.J., Pring A., Grundler P. V 2010. Petrogenetic significance of Au–Bi–Te–S associations: the example of Maldon, Central Victorian gold province, Australia. *Lithos*, **116**:1–17.
- Ciobanu C.L., Cook N.J., Utsunomiya S., Kogagwa M., Green L., Gilbert S., Wade B. 2012. Gold-telluride nanoparticles revealed in arsenic-free pyrite. *American Mineralogist*, **97**:1515–1518.
- Cooke R.A., O'Brien P.J., Carswell D.A. 2000. Garnet zoning and the identification of equilibrium mineral compositions in high-pressure-temperature granulites from the Moldanubian Zone, Austria. *Journal of Metamorphic Geology*, **18**:551–569.
- Deditius A.P., Utsunomiya S., Reich M., Kesler S.E., Ewing R.C., Hough R., Walshe J. 2011. Trace metal nanoparticles in pyrite. *Ore Geology Reviews*, **42**:32–46.
- Deol S., Deb M., Large R.R., Gilbert S. 2012. LA-ICPMS and EPMA studies of pyrite, arsenopyrite and loellingite from the Bhukia-Jagpura gold prospect, southern Rajasthan, India: Implications for ore genesis and gold remobilization. *Chemical Geology*, **326–327**:72–87.
- Dorr J.V.N. 1969. Physiographic, stratigraphic, and structural development of the Quadrilatero Ferrifero, Minas Gerais, Brazil:, accessed at US Geological Survey - Professional Paper 614-A at <http://pubs.er.usgs.gov/publication/pp641A>.
- Dubosq R., Lawley C.J.M., Rogowitz A., Schneider D.A., Jackson S. 2018. Pyrite deformation and connections to gold mobility: Insight from micro-structural analysis and trace element mapping. *Lithos*, **310–311**:86–104.

- Dubosq R., Rogowitz A., Schweinar K., Gault B., Schneider D.A. 2019. A 2D and 3D nanostructural study of naturally deformed pyrite: assessing the links between trace element mobility and defect structures. Contributions to Mineralogy and Petrology, **174**:1–16.
- Fabricio-Silva W. 2016. Evolução tectono-metamórfica aplicada aos processos responsáveis pela mineralização no depósito de ouro Turmalina, Quadrilátero Ferrífero, Brasil: geologia, análise estrutural e isótopos de enxofre: Universidade Federal de Minas Gerais: 113 p.
- Fabricio-Silva W., Rosière C.A., Bühn B. 2019. The shear zone-related gold mineralization at the Turmalina deposit, Quadrilátero Ferrífero, Brazil: structural evolution and the two stages of mineralization. Mineralium Deposita, **54**:347–368.
- Fabricio-Silva W., Frimmel H.E., Shutesky M.E., Rosière C.A., Massucatto A.J. 2020. Temperature-controlled ore evolution in orogenic-gold systems related to synchronous granitic magmatism: An example from the Iron Quadrangle Province, Brazil. Economic Geology, .
- Fielding I.O.H., Johnson S.P., Meffre S., Zi J., Sheppard S., Large R.R., Rasmussen B. 2019. Linking gold mineralization to regional-scale drivers of mineral systems using in situ U–Pb geochronology and pyrite LA-ICP-MS element mapping. Geoscience Frontiers, **10**:89–105.
- Fougerouse D., Micklenthwaite S., Tomkins A.G., Mei Y., Kilburn M., Guagliardo P., Fisher L.A., Halfpenny A., Gee M., Paterson D., Howard D.L. 2016a. Gold remobilisation and formation of high grade ore shoots driven by dissolution-reprecipitation replacement and Ni substitution into auriferous arsenopyrite. Geochimica et Cosmochimica Acta, **178**:143–159.
- Fougerouse D., Reddy S.M., Saxey D.W., Rickard W.D.A., Van Riessen A., Micklenthwaite S. 2016b. Nanoscale gold clusters in arsenopyrite controlled by growth rate not concentration: Evidence from atom probe microscopy. American Mineralogist, **101**:1916–1919.
- Fougerouse D., Micklenthwaite S., Halfpenny A., Reddy S.M., Cliff J.B., Martin L.A.J., Kilburn M., Guagliardo P., Ulrich S. 2016c. The golden ark: Arsenopyrite crystal plasticity and the retention of gold through high strain and metamorphism. Terra Nova, **28**:181–187.
- Fougerouse D., Reddy S.M., Kirkland C.L., Saxey D.W., Rickard W.D., Hough R.M. 2019. Time-resolved, defect-hosted, trace element mobility in deformed Witwatersrand pyrite. Geoscience Frontiers, **10**:55–63.
- Fowler A., Prokoph A., Stern R., Dupuis C. 2002. Organization of oscillatory zoning in zircon: analysis, scaling, geochemistry, and model of a zircon from Kipawa, Quebec, Canada. Geochimica et Cosmochimica Acta, **66**:311–328.
- Frimmel H.E. 2008. Earth's continental crustal gold endowment. Earth and Planetary Science Letters, **267**:45–55.
- Frimmel H.E., Hennigh Q. 2015. First whiffs of atmospheric oxygen triggered onset of

- crustal gold cycle. *Mineralium Deposita*, **50**:5–23.
- Frizzo C., Takai V., Scarpelli W. 1991. Auriferous mineralization at Pitangui, Minas Gerais. *Brazil Gold '91 - Ladeira*, E. A. (ed), 579–583.
- Frost B.R., Mavrogenes J.A., Tomkins A.G. 2002. Partial melting of sulfide ore deposits during medium- and high-grade metamorphism. *The Canadian Mineralogist*, **40**:1–18.
- Gault B. 2016. A brief overview of atom probe tomography research. *Applied Microscopy*, **46**:117–126.
- Genkin A.D., Bortnikov N.S., Cabri L.J., Wagner F.E., Stanley C.J., Safonov Y.G., McMahon G., Friedl J., Kerzin A.L., Gamyanin G.N. 1998. A multidisciplinary study of invisible gold in arsenopyrite from four mesothermal gold deposits in Siberia, Russian Federation. *Economic Geology*, **93**:463–487.
- De Geuser F., Lefebvre W., Blavette D. 2006. 3D atom probe study of solute atoms clustering during natural ageing and pre-ageing of an Al-Mg-Si alloy. *Philosophical Magazine Letters*, **86**:227–234.
- Goldfarb R.J., Groves D.I. 2015. Orogenic gold: Common or evolving fluid and metal sources through time. *Lithos*, **233**:2–26.
- Gopon P., Douglas J.O., Auger M.A., Hansen L., Wade J., Cline J.S., Robb L.J., Moody M.P. 2019. A Nanoscale Investigation of Carlin-Type Gold Deposits: An Atom-Scale Elemental and Isotopic Perspective. *Economic Geology*, **114**:1123–1133.
- Gourcerol B., Kontak D.J., Thurston P.C., Petrus J.A. 2018. Results of LA-ICP-MS sulfide mapping from Algoma-type BIF gold systems with implications for the nature of mineralizing fluids, metal sources, and deposit models. *Mineralium Deposita*, **53**:871–894.
- Gourcerol B., Kontak D.J., Petrus J.A., Thurston P.C. 2020. Application of LA ICP-MS analysis of arsenopyrite to gold metallogeny of the Meguma Terrane, Nova Scotia, Canada. *Gondwana Research*, **81**:265–290.
- Groves D.I., Goldfarb R.J., Gebre-Mariam M., Hagemann S.G., Robert F. 1998. Orogenic gold deposits: a proposed classification in the context of their crustal distribution and relationship to other gold deposit types. *Ore Geology Reviews*, **13**:7–27.
- Groves D.I., Santosh M., Goldfarb R.J., Zhang L. 2018. Structural geometry of orogenic gold deposits: Implications for exploration of world-class and giant deposits. *Geoscience Frontiers*, **9**:1163–1177.
- Groves D.I., Santosh M., Deng J., Wang Q., Yang L., Zhang L. 2019. A holistic model for the origin of orogenic gold deposits and its implications for exploration. *Mineralium Deposita*, 1–18.
- Hagemann S.G., Brown P.E., Ridley J., Stern P., Fournelle J. 1998. Ore petrology, chemistry, and timing of electrum in the Archean hypozonal Transvaal lode gold deposit, Western Australia. *Economic Geology*, **93**:271–291.

- Harlov D.E., Wirth R., Hetherington C.J. 2011. Fluid-mediated partial alteration in monazite: the role of coupled dissolution–reprecipitation in element redistribution and mass transfer. *Contributions to Mineralogy and Petrology*, **162**:329–348.
- Hart C.J.R., McCoy D.T., Goldfarb R.J., Smith M., Roberts P., Hulstein R., Bakke A.A., Bundtzen T.K. 2002. Geology, exploration, and discovery in the Tintina Gold Province, Alaska and Yukon. Special Publication - Society of Economic Geologists, **9**:241–274.
- Hastie E.C.G., Kontak D.J., Lafrance B. 2020. Gold Remobilization: Insights from Gold Deposits in the Archean Swayze Greenstone Belt, Abitibi Subprovince, Canada. *Economic Geology*, **115**:241–277.
- Hazarika P., Mishra B., Lochan Pruseth K. 2017. Trace-element geochemistry of pyrite and arsenopyrite: ore genetic implications for late Archean orogenic gold deposits in southern India. *Mineralogical Magazine*, **81**:661–678.
- Herbig M., Choi P., Raabe D. 2015. Combining structural and chemical information at the nanometer scale by correlative transmission electron microscopy and atom probe tomography. *Ultramicroscopy*, **153**:32–39.
- Hofmann A.W. 1988. Chemical differentiation of the Earth: the relationship between mantle, continental crust, and oceanic crust. *Earth and Planetary Science Letters*, **90**:297–314.
- Hoppe P. 2006. NanoSIMS: A new tool in cosmochemistry. *Applied Surface Science*, **252**:7102–7106.
- Hoppe P., Cohen S., Meibom A. 2013. NanoSIMS: Technical Aspects and Applications in Cosmochemistry and Biological Geochemistry. *Geostandards and Geoanalytical Research*, **37**:111–154.
- Hough R.M., Noble R.R.P., Reich M. 2011. Natural gold nanoparticles. *Ore Geology Reviews*, **42**:55–61.
- Hu X., Gong Y., Zeng G., Zhang Z., Wang J., Yao S. 2018. Multistage pyrite in the Getang sediment-hosted disseminated gold deposit, southwestern Guizhou Province, China: Insights from textures and in situ chemical and sulfur isotopic analyses. *Ore Geology Reviews*, **99**:1–16.
- Jaguar Mining I. 2020. Technical report on the Turmalina mine Complex, Minas Gerais State, Brasil.:
- Kerr M.J., Hanley J.J., Kontak D.J., Morrison G.G., Petrus J., Fayek M., Zajacz Z. 2018. Evidence of upgrading of gold tenor in an orogenic quartz-carbonate vein system by late magmatic-hydrothermal fluids at the Madrid Deposit, Hope Bay Greenstone Belt, Nunavut, Canada. *Geochimica et Cosmochimica Acta*, **241**:180–218.
- Kretschmar U., Scott S.D. 1976. Phase relations involving arsenopyrite in the system Fe-As-S and their application. *The Canadian Mineralogist*, **14**:364–386.
- Lana C., Alkmim F.F., Armstrong R., Scholz R., Romano R., Nalini H.A. 2013. The ancestry and magmatic evolution of Archean TTG rocks of the Quadrilátero

- Ferrífero province, southeast Brazil. *Precambrian Research*, **231**:157–173.
- Lanari P., Vidal O., De Andrade V., Dubacq B., Lewin E., Grosch E.G., Schwartz S. 2014. XMapTools: A MATLAB®-based program for electron microprobe X-ray image processing and geothermobarometry. *Computers & Geosciences*, **62**:227–240.
- Large R.R., Danyushevsky L., Hollit C., Maslennikov V., Meffre S., Gilbert S., Bull S., Scott R., Emsbo P., Thomas H., Singh B., Foster J. 2009. Gold and Trace Element Zonation in Pyrite Using a Laser Imaging Technique: Implications for the Timing of Gold in Orogenic and Carlin-Style Sediment-Hosted Deposits. *Economic Geology*, **104**:635–668.
- Larocque A.C.L., Hodgson C.J., Cabri L.J., Jackman J.A. 1995. Ion-microprobe analysis of pyrite, chalcopyrite and pyrrhotite from the MoBrun VMS deposit in northwestern Quebec; evidence for metamorphic remobilization of gold. *The Canadian Mineralogist*, **33**:373–388.
- Lobato L.M., Ribeiro-Rodrigues L.C., Vieira F.W.R. 2001. Brazil's premier gold province. Part II: geology and genesis of gold deposits in the Archean Rio das Velhas greenstone belt, Quadrilátero Ferrífero. *Mineralium Deposita*, **36**:249–277.
- Machado N., Schrank A., Noce C.M., Gauthier G. 1996. Ages of detrital zircon from Archean-Paleoproterozoic sequences: Implications for Greenstone Belt setting and evolution of a Transamazonian foreland basin in Quadrilátero Ferrífero, southeast Brazil. *Earth and Planetary Science Letters*, **141**:259–276.
- Marinho M.S., Silva M.A., Lombello J.C., Di Salvio L.P., Silva R.N., Féboli W.L., Brito D.C. 2018. Projeto ARIM - Áreas de Relevante Interesse Mineral - Noroeste do Quadrilátero Ferrífero - Mapa Geológico Integrado do Sinclínorio Pitangui. 1 mapa colorido. Escala 1:75.000. 1.
- Marshall B., Gilligan L.B. 1987. An introduction to remobilization: information from ore-body geometry and experimental considerations. *Ore Geology Reviews*, **2**:87–131.
- Marshall B., Gilligan L.B. 1993. Structural Setting and Controls on Mineral Deposits Remobilization, syn-tectonic processes and massive sulphide deposits. *Ore Geology Reviews*, **8**:39–64.
- Masurel Q., Thébaud N., Miller J., Ulrich S., Hein K.A.A., Cameron G., Béziat D., Bruguier O., Davis J.A. 2017. Sadiola Hill: A world-class carbonate-hosted gold deposit in Mali, West Africa. *Economic Geology*, **112**:23–47.
- McQueen K.G. 2005. Ore deposit types and their primary expressions. *Regolith Expression of Australian Ore Systems*: ..., 1–14.
- Meinert L.D., Dipple G.M., Nicolescu S. 2005. World Skarn Deposits. *Economic Geology 100th Anniversary Volume*.
- de Melo-Silva P., da Silva Amaral W., Oliveira E.P. 2019. Geochronological evolution of the Pitangui greenstone belt, southern São Francisco Craton, Brazil:

Constraints from U-Pb zircon age, geochemistry and field relationships. *Journal of South American Earth Sciences*, .

de Melo-Silva P., Amaral W. da S., Oliveira E.P. 2020. Geochronological evolution of the Pitangui greenstone belt, southern São Francisco Craton, Brazil: Constraints from U-Pb zircon age, geochemistry and field relationships. *Journal of South American Earth Sciences*, **99**:

Mériaud N., Jébrak M. 2017. From intrusion-related to orogenic mineralization: The Wasamac deposit, Abitibi Greenstone Belt, Canada. *Ore Geology Reviews*, **84**:289–308.

Mikhlin Y.L., Romanchenko A.S., Asanov I.P. 2006. Oxidation of arsenopyrite and deposition of gold on the oxidized surfaces: A scanning probe microscopy, tunneling spectroscopy and XPS study. *Geochimica et Cosmochimica Acta*, **70**:4874–4888.

Mishra B., Pruseth K.L., Hazarika P., Chinnasamy S.S. 2018. Nature and source of the ore-forming fluids associated with orogenic gold deposits in the Dharwar Craton. *Geoscience Frontiers*, **9**:715–726.

Mo Y.-W., Savage D.E., Swartzentruber B.S., Lagally M.G. 1990. Kinetic pathway in Stranski-Krastanov growth of Ge on Si (001). *Physical Review Letters*, **65**:1020.

Morey A.A., Tomkins A.G., Bierlein F.P., Weinberg R.F., Davidson G.J. 2008. Bimodal distribution of gold in pyrite and arsenopyrite: Examples from the archean boorara and bardoc shear systems, Yilgarn Craton, Western Australia. *Economic Geology*, **103**:599–614.

Müller E.W. 1956. Resolution of the atomic structure of a metal surface by the field ion microscope. *Journal of Applied Physics*, **27**:474–476.

Mumin A.H., Fleet M.E., Chryssoulis S.L. 1994. Gold mineralization in As-rich mesothermal gold ores of the Bogosu-Prestea mining district of the Ashanti Gold Belt, Ghana: remobilization of “invisible” gold. *Mineralium Deposita*, **29**:445–460.

Neumayr P., Cabri L.J., Groves D.I., Mikucki E.J., Jackman J.A. 1993. The mineralogical distribution of gold and relative timing of gold mineralization in two Archean settings of high metamorphic grade in Australia. *The Canadian Mineralogist*, **31**:711–725.

Noce C.M., Tassinari C., Lobato L.M. 2007. Geochronological framework of the Quadrilátero Ferrífero, with emphasis on the age of gold mineralization hosted in Archean greenstone belts. *Ore Geology Reviews*, **32**:500–510.

Oliveira E.P., McNaughton N.J., Zincone S.A., Talavera C. 2020. Birthplace of the São Francisco Craton, Brazil: Evidence from 3.60 to 3.64 Ga Gneisses of the Mairi Gneiss Complex. *Terra Nova*, **32**:281–289.

Palenik C.S., Utsunomiya S., Reich M., Kesler S.E., Wang L., Ewing R.C. 2004. “Invisible” gold revealed: Direct imaging of gold nanoparticles in a Carlin-type deposit. *American Mineralogist*, **89**:1359–1366.

Palme H., Jones A. 2003. Solar system abundances of the elements. *TrGeo*, **1**:711.

- Pearce M.A., Godel B.M., Fisher L.A., Schoneveld L.E., Cleverley J.S., Oliver N.H.S., Nugus M. 2018. Microscale data to macroscale processes: A review of microcharacterization applied to mineral systems. Geological Society Special Publication, **453**:7–39.
- Petrakakis K. 1986. Metamorphism of high-grade gneisses from the Moldanubian zone, Austria, with particular reference to the garnets. Journal of Metamorphic Geology, **4**:323–344.
- Phillips G.N., Powell R. 2009. Formation of gold deposits: Review and evaluation of the continuum model. Earth-Science Reviews, **94**:1–21.
- Phillips G.N., Powell R. 2010. Formation of gold deposits: A metamorphic devolatilization model. Journal of Metamorphic Geology, **28**:689–718.
- Plümper O., King H.E., Vollmer C., Ramasse Q., Jung H., Austrheim H. 2012. The legacy of crystal-plastic deformation in olivine: high-diffusivity pathways during serpentinization. Contributions to Mineralogy and Petrology, **163**:701–724.
- Putnis A. 2009. Mineral replacement reactions. Reviews in mineralogy and geochemistry, **70**:87–124.
- Putnis A., Fernandez-Diaz L., Prieto M. 1992. Experimentally produced oscillatory zoning in the (Ba, Sr) SO₄ solid solution. Nature, **358**:743–745.
- Reddy S.M., Timms N.E., Pantleon W., Trimby P. 2007. Quantitative characterization of plastic deformation of zircon and geological implications. Contributions to Mineralogy and Petrology, **153**:625–645.
- Reich M., Kesler S.E., Utsunoyiya S., Palenik C.S., Chryssoulis S., Ewing R.C. 2005. Solubility of gold in arsenian pyrite: Geochemica et Cosmochimica Acta, vol. 69.
- Renger F.E., Noce C.M., Romano A.W., Machado N. 1994. Evolução Sedimentar Do Supergrupo Minas: 500 Ma. De Registro Geológico No Quadrilátero Ferrífero, Minas Gerais, Brasil. Geonomos, **2**:1–11.
- Ribeiro-Rodrigues L.C., de Oliveira C.G., Friedrich G. 2007. The Archean BIF-hosted Cuiabá Gold deposit, Quadrilátero Ferrífero, Minas Gerais, Brazil. Ore Geology Reviews, **32**:543–570.
- Rigutti L., Vella A., Vurpillot F., Gaillard A., Sevelin-Radiguet N., Houard J., Hideur A., Martel G., Jacopin G., Bugallo A.D.L. 2013. Coupling atom probe tomography and photoluminescence spectroscopy: Exploratory results and perspectives. Ultramicroscopy, **132**:75–80.
- Romano A.W. 1993. Parte, O Supergrupo Rio das Velhas da Faixa Mateus Leme-Pitangui - meridional do Cráton de São Francisco, MG - e seu sistema de alteração hidrotermal. Geonomos, **1**:16–32.
- Romano A.W. 2007. Programa Geologia do Brasil. Folha Pará de Minas, SE-23-Z-C-I. Escala 1:100.000 relatório final. UFMG-CPRM, Belo Horizonte. 74 p.
- Romano R., Lana C., Alkmim F.F., Stevens G., Armstrong R. 2013. Stabilization of the southern portion of the São Francisco craton, SE Brazil, through a long-lived

period of potassic magmatism. *Precambrian Research*, **224**:143–159.

- Saintilan N.J., Stephens M.B., Spikings R., Schneider J., Chiaradia M., Spangenberg J.E., Ulianov A., Fontboté L. 2017a. Polyphase vein mineralization in the Fennoscandian Shield at Åkerlandet, Järvsand, and Laisvall along the erosional front of the Caledonian orogen, Sweden. *Mineralium Deposita*, **52**:823–844.
- Saintilan N.J., Creaser R.A., Spry P.G., Hnatyshin D. 2017b. Re-Os Systematics of löllingite and arsenopyrite in granulite-facies garnet rocks: Insights into the metamorphic history and thermal evolution of the broken hill block during the early mesoproterozoic (New South Wales, Australia). *Canadian Mineralogist*, **55**:29–44.
- Saunders J.A. 1990. Colloidal transport of gold and silica in epithermal precious-metal systems: Evidence from the Sleeper deposit, Nevada. *Geology*, **18**:757–760.
- Sharp Z.D., Essene E.J., Kelly W.C. 1985. A re-examination of the arsenopyrite geothermometer: Pressure considerations and applications to natural assemblages. *The Canadian Mineralogist*, **23**:517–534.
- Shore M., Fowler A.D. 1996. Oscillatory zoning in minerals; a common phenomenon. *The Canadian Mineralogist*, **34**:1111–1126.
- Silva G.P.A., Carneiro M.A. 2009. The metatholeiitic suite of the Rio Manso metavolcanosedimentary sequence, Iron Quadrangle (MG). *Revista da Escola de Minas de Ouro Preto*, **62**:423–430.
- Spear F.S. 1991. Temperatures in Light of Garnet Diffusion During Cooling. *Journal of Metamorphic Geology*, **9**:379–388.
- Stromberg J.M., Barr E., Van Loon L.L., Gordon R.A., Banerjee N.R. 2019. Fingerprinting multiple gold mineralization events at the Dome mine in Timmins, Ontario, Canada: Trace element and gold content of pyrite. *Ore Geology Reviews*, **104**:603–619.
- Tassinari C.C.G., Mateus A.M., Velásquez M.E., Munhá J.M.U., Lobato L.M., Bello R.M., Chiquini A.P., Campos W.F. 2015. Geochronology and thermochronology of gold mineralization in the Turmalina deposit, NE of the Quadrilátero Ferrífero Region, Brazil. *Ore Geology Reviews*, **67**:368–381.
- Teixeira W., Ávila C.A., Dussin I.A., Corrêa Neto A. V., Bongiolo E.M., Santos J.O., Barbosa N.S. 2015. A juvenile accretion episode (2.35–2.32 Ga) in the Mineiro belt and its role to the Minas accretionary orogeny: Zircon U-Pb-Hf and geochemical evidences. *Precambrian Research*, **256**:148–169.
- Thorman C.H., DeWitt E., Maron M.A., Ladeira E.A. 2001. Major brazilian gold deposits - 1982 to 1999. *Mineralium Deposita*, **36**:218–227.
- Tomkins A.G. 2013. On the source of orogenic gold. *Geology*, **41**:1255–1256.
- Tomkins A.G., Mavrogenes J.A. 2001. Redistribution of gold within arsenopyrite and löllingite during pro- and retrograde metamorphism: Application to timing of mineralization. *Economic Geology*, **96**:525–534.

- Tomkins A.G., Pattison D.R.M., Zaleski E. 2004. The Hemlo Gold Deposit, Ontario: An Example of Melting and Mobilization of a Precious Metal-Sulfosalt Assemblage during Amphibolite Facies Metamorphism and Deformation. *Economic Geology*, **99**:1063–1084.
- Tomkins A.G., Pattison D.R.M., Frost B.R. 2007. On the initiation of metamorphic sulfide anatexis. *Journal of Petrology*, **48**:511–535.
- Tooth B., Ciobanu C.L., Green L., O'Neill B., Brugger J. 2011. Bi-melt formation and gold scavenging from hydrothermal fluids: An experimental study. *Geochimica et Cosmochimica Acta*, **75**:5423–5443.
- Tuccillo M.E., Essene E.J., van der Pluijm B.A. 1990. Growth and retrograde zoning in garnets from high-grade, metapelites: Implications for pressure-temperature paths. *Geology*, **18**:839–842.
- Valley J.W., Cavosie A.J., Ushikubo T., Reinhard D.A., Lawrence D.F., Larson D.J., Clifton P.H., Kelly T.F., Wilde S.A., Moser D.E. 2014. Hadean age for a post-magma-ocean zircon confirmed by atom-probe tomography. *Nature Geoscience*, **7**:219–223.
- Verma S.K., Oliveira E.P., Silva P.M., Moreno J.A., Amaral W.S. 2017. Geochemistry of komatiites and basalts from the Rio das Velhas and Pitangui greenstone belts, São Francisco Craton, Brazil: Implications for the origin, evolution, and tectonic setting. *Lithos*, **284–285**:560–577.
- Vial D.S., DeWitt E., Lobato L.M., Thorman C.H. 2007. The geology of the Morro Velho gold deposit in the Archean Rio das Velhas greenstone belt, Quadrilátero Ferrífero, Brazil. *Ore Geology Reviews*, **32**:511–542.
- Vigneresse J.L., Truche L., Richard A. 2019. How do metals escape from magmas to form porphyry-type ore deposits? *Ore Geology Reviews*, **105**:310–336.
- Vukmanovic Z., Reddy S.M., Godel B., Barnes S.J., Fiorentini M.L., Barnes S.-J., Kilburn M.R. 2014. Relationship between microstructures and grain-scale trace element distribution in komatiite-hosted magmatic sulphide ores. *Lithos*, **184**:42–61.
- Wagner T., Fusswinkel T., Wölle M., Heinrich C.A. 2016. Microanalysis of Fluid Inclusions in Crustal Hydrothermal Systems using Laser Ablation Methods. *Elements*, **12**:323–328.
- Widler A.M., Seward T.M. 2002. The adsorption of gold (I) hydrosulphide complexes by iron sulphide surfaces. *Geochimica et Cosmochimica Acta*, **66**:383–402.
- Williams-Jones A.E., Bowell R.J., Migdisov A.A. 2009. Gold in Solution. *Elements*, **5**:281–287.
- Williams D.B., Carter C.B. 1996. *Transmission Electron Microscopy: Spectrometry*. IV. Plenum Press.
- Wu Y.F., Fougerouse D., Evans K., Reddy S.M., Saxe D.W., Guagliardo P., Li J.W. 2019a. Gold, arsenic, and copper zoning in pyrite: A record of fluid chemistry and growth kinetics. *Geology*, **47**:641–644.

- Wu Y.F., Evans K., Li J.W., Fougerouse D., Large R.R., Guagliardo P. 2019b. Metal remobilization and ore-fluid perturbation during episodic replacement of auriferous pyrite from an epizonal orogenic gold deposit. *Geochimica et Cosmochimica Acta*, **245**:98–117.
- Xing Y., Brugger J., Tomkins A., Shvarov Y. 2019. Arsenic evolution as a tool for understanding formation of pyritic gold ores. *Geology*, **47**:335–338.
- Xue Y., Campbell I., Ireland T.R., Holden P., Armstrong R. 2013. No mass-independent sulfur isotope fractionation in auriferous fluids supports a magmatic origin for Archean gold deposits. *Geology*, **41**:791–794.
- Yan J., Hu R., Liu S., Lin Y., Zhang J., Fu S. 2018. NanoSIMS element mapping and sulfur isotope analysis of Au-bearing pyrite from Lannigou Carlin-type Au deposit in SW China: New insights into the origin and evolution of Au-bearing fluids. *Ore Geology Reviews*, **92**:29–41.

6. TEXTURA E ASSINATURA GEOQUÍMICA DE SULFETOS AURÍFEROS: CONJECTURAS SOBRE ALTERAÇÃO HIDROTERMAL, FONTE DOS METAIS E IDADE RELATIVA

Este capítulo está estruturado na forma de trabalhos apresentados e publicados em anais de congressos nacionais e internacionais (Tabela 6-1). Ele aborda a relação das paragêneses de sulfeto com a evolução termo-estrutural e hidrotermal em depósitos do greenstone belt Pitangui de uma maneira mais ampla e configurada na evolução dos conhecimentos. A disposição dos trabalhos acompanha a seguinte metodologia analítica: (i) análise de rocha total nos diferentes corpos de minério; (ii) descrição textural em microscópio petrográfico; (iii) microssonda eletrônica; (iv) isótopos de S por LA-ICP-MS; (v) mapeamento composicional intracristalino; (vi) elementos-traço po LA-ICP-MS; (vi) aplicações da nanogeoquímica e consequências em depósitos auríferos multifásicos.

Tabela 6-1. A evolução dos conhecimentos nos depósitos do Greenstone Belt Pitangui na forma de trabalhos publicados em anais de eventos científicos.

Título	Evento	Descrição
Evolução tectono-termal e sua relação com as fases de mineralização aurífera no depósito Turmalina, Quadrilátero Ferrífero, Minas Gerais	49º Congresso Brasileiro de Geologia. Rio de Janeiro	Mapeamento de galerias Análise estrutural Paragênese dos sulfetos
Tectonothermal Evolution and Multiphase Ore-Forming Processes at Turmalina Gold Deposit, Quadrilátero Ferrífero, Brazil	Goldschmidt 2018; Boston – USA	Paragênese dos sulfetos Alteração hidrotermal Geotermometria Isótopos de S
Multiple mineralization stages and relative timing of gold distribution in the Satinoco Deposit, NW of Quadrilátero Ferrífero, Brazil	Goldschmidt 2019; Barcelona – Spain	Paragênese de sulfetos Alteração hidrotermal Geotermometria Mapas composicionais
Depósitos de ouro orogênico e o papel do magmatismo granítico sincrônico: contribuição com fluido mineralizante ou apenas motor termodinâmico?	50º Congresso Brasileiro de Geologia. Brasília	Modelo metalogenético Fonte de fluidos Geocronologia EBSD Elementos-traço nos sulfetos
O paradigma “idade da mineralização”: porque precisamos revisitá-lo à luz da nanogeochímica?	50º Congresso Brasileiro de Geologia. Brasília	Aplicação da nanogeochímica Estudos de caso Reflexão sobre a idade de mineralização

6.1 Evolução tectono-termal e sua relação com as fases de mineralização aurífera no depósito Turmalina, Quadrilátero Ferrífero, Minas Gerais

Turmalina é um importante depósito de ouro-orogênico localizado na região NW do Quadrilátero Ferrífero. O depósito está hospedado no *greenstone belt* arqueano Pitangui (correlato ao Rio das Velhas) e é composto por orto-anfibolitos e pelitos com intercalações de tufo, metamorfizados na fácie anfibolito e intrudidos por um *stock* granítico. Os corpos mineralizados estão controlados por zonas de cisalhamento de direção WNW-ESE, associados com alteração hidrotermal.

Três eventos de deformação são reconhecidos no depósito Turmalina: D₁ e D₂ são o resultado de uma deformação arqueana progressiva entre 2749 ± 7 e 2664 ± 35 Ma e sob condições dúcteis; D₃ é caracterizado por um evento transpressional sob condições dúcteis-rúpteis com idade ainda incerta. As três gerações de granada observadas (Grt₁, Grt₂ e Grt₃) mostram que a blastose de Grt₁ é pré a sin-D₁ e que Grt₂ cresceu durante a fase tardia pós-tectônica relativa ao evento D₂. A temperatura inicial da deformação é de 548-600 °C, enquanto, no final do evento D₂, as temperaturas atingem 633 °C (pico metamórfico), provavelmente como resultado da intrusão granítica. A granada Grt₃ resultou de reequilíbrio sob condições retrógradas.

Ao menos três fases de alteração hidrotermal e dois estágios de mineralização foram identificados. A fase inicial de alteração hidrotermal, sincrônica com o estágio de mineralização I, é representada pela paragênese quartzo-sericita-sulfeto. Esta fase é caracterizada principalmente pela mineralização de ouro e pela intensa silicificação representada por veios de quartzo V₁₋₂ e brechas hidráulicas.

A sulfetação é composta por pirrotita-arsenopirita ± loellingita ± calcopirita (principal mineralização em ouro), foi precipitada abaixo da temperatura de pico metamórfico

de $598^{\circ} \pm 19^{\circ}$ C associada ao desenvolvimento da foliação S₁ (D₁). A fase inicial de alteração hidrotermal foi sobreimpressa pela segunda fase, composta pela associação quartzo-clorita-ankerita-sericita \pm sulfeto \pm turmalina. A sulfetação desta fase é representada por pirrotita-pirita-arsenopirita \pm calcopirita (estágio II), está localizada comumente ao longo dos veios de quartzo-carbonato V₃ e precipitou em condições de resfriamento de $510 \pm 30^{\circ}$ até $442 \pm 9^{\circ}$ C. A última fase de alteração hidrotermal reconhecida pós-data os dois estágios de mineralização e é caracterizada pela paragênese muscovita-calcita-clorita.

Usando estudos microestruturais, química mineral, geotermometria e valores isótopos de $\delta^{34}\text{S}$ (3.29 a 4.19‰ para os sulfetos do estágio I e 2.94 a 5.76‰ para os sulfetos do estágio II), propomos que o ouro derivou principalmente de fluidos metamórficos, mas que potencialmente se misturou com fluidos magmáticos causados pela ascensão do granito (2664 ± 35 Ma).

6.2 Tectonothermal Evolution and Multiphase Ore-Forming Processes at Turmalina Gold Deposit, Quadrilátero Ferrífero, Brazil

Turmalina is an important orogenic gold deposit hosted in an Archean greenstone belt, intruded by a granite stock, and located in the Quadrilátero Ferrífero, Brazil. The deformation events (D₁ to D₃) associated with the Au-bearing sulfide stages are reconstructed with the support of garnet porphyroblasts (Grt₁ to Grt₃). The Grt₁ have grown pre- to syn-D₁ and Grt₂ formed during the late to post-deformation stage of the D₂ event. The initial temperature was established as 548-600°C, reaching 633°C during late-D₂, likely as a result of granite intrusion. The Grt₃ resulted from re-equilibration under retrograde conditions. Two gold-bearing sulfide stages were identified using microstructural studies, mineral chemistry, geothermometry, and sulfur isotope analysis: po-apy \pm lös \pm ccp \pm gold stage I (the main stage) formed during

D₂ event and; po-py-ap_y±ccp±gold stage II precipitated below the metamorphic peak and continued towards lower than 450°C. We interpret that granite intrusion imposed magmatic fluids and increased metamorphism to promote gold mineralization.

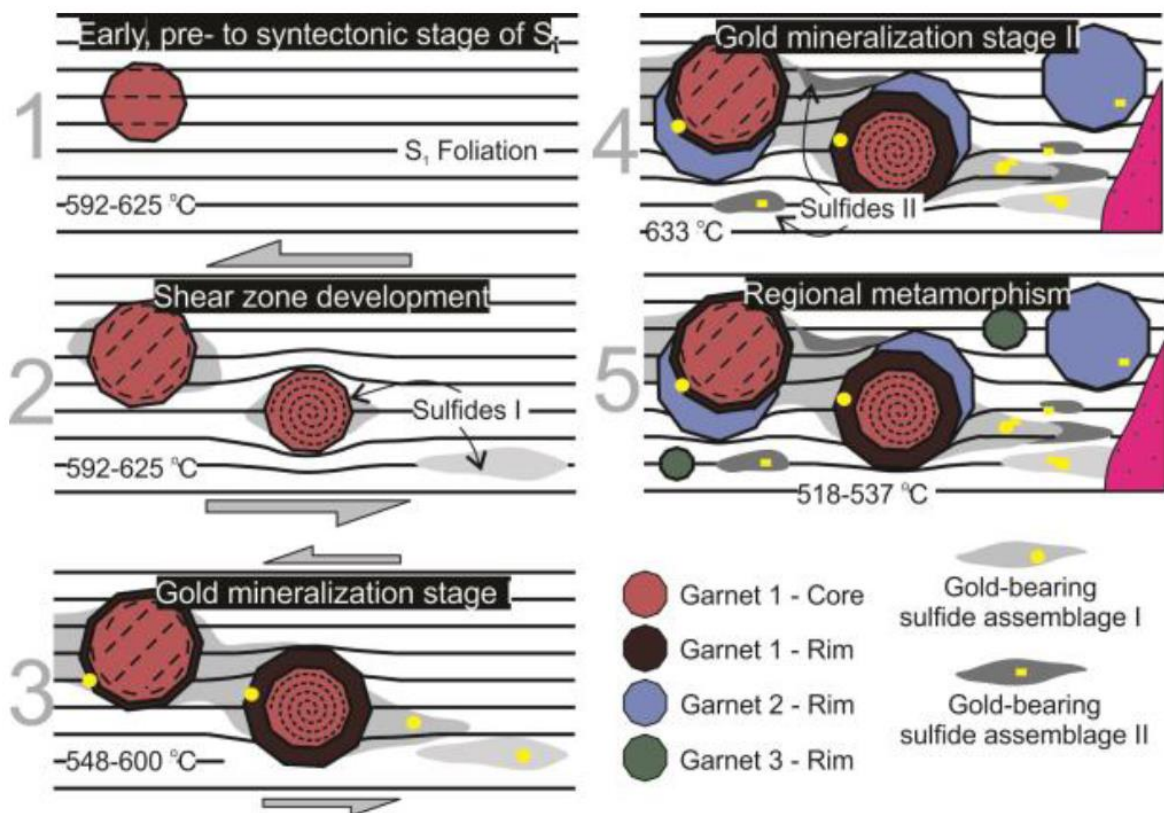


Fig. 6-1. Timing relationships of the garnet porphyroblasts related to deformation events, gold mineralization stages and sulfide assemblages.

6.3 Multiple mineralization stages and relative timing of gold distribution in the Satinoco Deposit, NW of Quadrilátero Ferrífero, Brazil

Satinoco is an Archean orogenic gold deposit located in a succession of metavolcanic mafic and ultramafic rocks that were intruded by granitic magma. Several Au-bearing sulfide mineralization stages were revealed by X-ray element maps acquired by electron microprobe, and reconstructed with the support of garnet porphyroblasts, whole rock geochemistry, geothermometry, and structural relationship of the granite apophyses. An early arsenopyrite-löllingite-pyrrhotite stage developed during prograde metamorphism (~468 to 650 °C), associated with progressive dehydration of the host rocks and induced by the emplacement of 2.66 Ga granite that likely also contributed some magmatic fluid. A subsequent Fe-rich hydrothermal stage generated a pyrrhotite-arsenopyrite assemblage upon cooling from c. 500 to 440 °C towards the end of granite emplacement. A further, base metal-rich, mineralization stage (Pb-Sb-Cu-Zn-Au) with pyrite-pyrrhotite-chalcopyrite-galena-ullmannite is ascribed to thermal re-equilibration during a post-tectonic event at upper greenschist-facies metamorphic conditions.

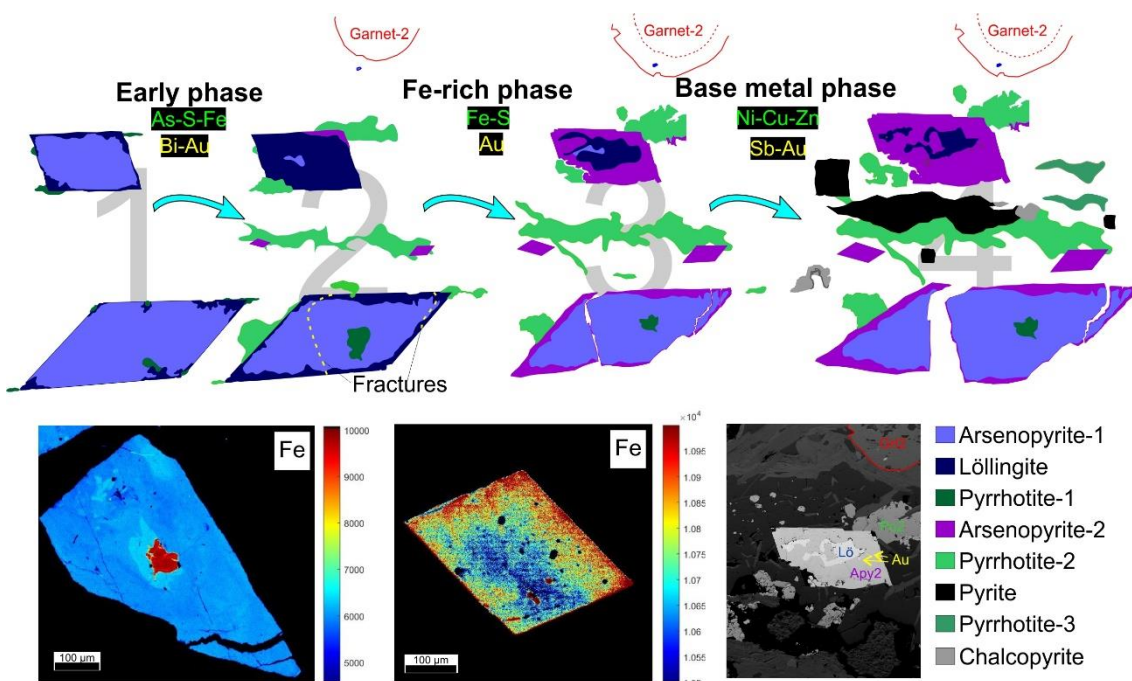


Fig. 6-2. Schematic geological evolution of the Satinoco deposit based on gold-bearing sulfide phases; also shown are EPMA element maps of Fe in arsenopyrites from first two au-bearing sulfide stages.

6.4 Depósitos de ouro orogênico e o papel do magmatismo granítico sincrônico: contribuição com fluido mineralizante ou apenas motor termodinâmico?

Embora não existam muitas dúvidas quanto à natureza hidrotermal dos depósitos de ouro do tipo orogênico, a fonte dos fluidos mineralizantes e a dos metais transportados por eles permanece enigmática. A visão predominante é de que as rochas metamórficas são a fonte dos fluidos auríferos, mas outros autores também sugerem que fluido rico em ouro pode ser de origem magmática.

Trabalhos recentes mostram que mesmo em depósitos onde fluidos magmatogênico-hidrotermais podem ter contribuído para a mineralização, a relação espacial, temporal e genética entre o magmatismo intrusivo e os corpos mineralizados permanece incerta. Assim, depósitos com uma clara conexão espacial entre corpos minerais e intrusões são os alvos ideais para testar a relação genética entre fluidos mineralizantes e magmatismo.

Um excelente exemplo desse objeto é o distrito de Pitangui, em Minas Gerais. Documentamos a evolução de um sistema de mineralização hospedado em zonas de cisalhamento e associado espacialmente a um stock e apófises do granito sin- a tardí-tectônico (2,69 Ga), no depósito Satinoco, *greenstone belt* Pitangui (Quadrilátero Ferrífero).

O mapeamento e análise petrográfica detalhada de galerias subterrâneas, mapeamento químico intragrão de sulfeto, Electron Backscatter Diffraction (EBSD) e aplicação de geotermometria revelaram uma história polifásica complexa, com pelo menos três estágios de sulfeto contendo ouro:

- (i) paragênese de arsenopirita-löllingita-pirrotita I, formada durante o condições metamórficas progradas (de 475 a > 700 °C). O magma granítico ascendente atuou nesse momento como um motor térmico e, juntamente com a desidratação das rochas hospedeiras máficas e ultramáficas, gerou essa paragênese;
- (ii) uma maior circulação de fluido durante o resfriamento do granito de 510 a 445 °C resultaram na paragênese pirrotita-arsenopirita ± galena II. Relações transversais de campo, juntamente com dados anteriores do isótopo S, indicam uma contribuição dos fluidos magmatogênicos graníticos para o sistema de mineralização nesta fase; e
- (iii) paragênese III de pirita-pirrotita-calcopirita-galena-ullmanita que se formou durante um evento posterior de deformação rúptil pós-tectônica, sob condições metamórficas da fácie de xisto verde.

Mapas de elementos de raios-X revelaram zoneamento oscilatório de As, Fe e Ni no arsenopirita da paragênese I. Uma correlação positiva de Au com Bi e As sugere facilitação da concentração de ouro no arsenopirita e seu precursor de pirita sedimentar. Grandes quantidades de pirrotita na paragênese II refletem o metassomatismo de Fe relacionado ao granito. A paragênese III envolveu a formação de veios com pirita e precipitação de ouro livre e sulfetos de Pb-Sb-Cu-Zn em microfraturas dessa pirita. Essa fase foi responsável pela remobilização de Ni, Cu e Zn.

Evidentemente, o ouro se formou durante os três estágios, seja como ouro "invisível" na arsenopirita ou como ouro livre, abrangendo um tempo de atividade metamórfica e magmática sin a pós-tectônica de 2,75 a 2,65 Ga. Concentração de ouro acima de 100 milhões anos ao longo de uma ampla faixa de temperaturas, conforme documentado aqui para o depósito de Satinoco, podem ter sido um componente essencial na formação de outros depósitos de ouro orogênicos em outras províncias metalogenéticas.

6.5 O paradigma “idade da mineralização”: porque precisamos revisitar este conceito à luz da nanogeоquímica?

O termo “Idade de Mineralização” é tema de diversos debates e produz um grande impacto em publicações em geologia econômica e prospecção mineral. Entretanto, este termo pode guardar inúmeras limitações, especialmente após novas descobertas relacionadas ao advento da nanogeоquímica.

Com o emprego de técnicas analíticas de altíssima resolução, como Nanoscale Secondary Ion Mass Spectrometry (NanoSIMS) e Atom Probe Tomography (APT), por vezes associadas ao Electron Backscatter Diffraction (EBSD), tem sido possível entender melhor os processos causadores de zonamento de elementos traço em sulfetos em nanoescala.

Aqui, fazemos uma análise panorâmica de pesquisas recentes que tratam dos diferentes mecanismos de cristalização ou remobilização de ouro em sulfetos e sugerimos que os processos orogênicos, hidrotermais e/ou metamórficos possuem trajetória suficientemente complexa para abordar a mineralização de forma simplista, como se desenvolvesse ao longo de um único evento, restrito no tempo geológico.

A composição química e as microestruturas constituem uma informação-chave para elucidar a evolução da mineralização relacionada às paragênese de sulfetos e o zonamento químico pode representar: *i*) processos primários e/ou *ii*) processos relacionados à remobilização.

Para processos primários, alguns trabalhos recentes mostram como o zonamento químico marca tanto a interação fluido-rocha quanto a cinética de crescimento dos sulfetos. Esses fenômenos possuem diversas consequências no zonamento oscilatório do ouro.

Já em termos de remobilização, outros autores demonstram e interpretam migrações intragrão de elementos traços na estrutura mineral dos sulfetos relacionados à diversos mecanismos e submecanismos.

Os variados modelos concebidos, e em diferentes tipos de depósito, sugerem que os processos de cristalização e posterior mobilidade desses elementos implicam em eventos geológicos complexos e muitas vezes separados por longos períodos durante eventos tectono-termais distintos. Estudos recentes com cinética de crescimento de pirita aurífera em depósitos de ouro-orogênicos australianos e chineses sugerem que a cristalização de sulfetos pode demorar centenas de milhares de anos. Outras pesquisas robustas com piritas de Witwatersrand utilizando APT indicam que parte do ouro invisível foi remobilizado do núcleo e concentrado como ouro livre no exterior do cristal quase 1 Ga após a cristalização deste sulfeto. Um evento hidrotermal e/ou tectônico mais recente, parece ter levado parte deste ouro, anteriormente preso na estrutura do sulfeto, a se recristalizar associado a outros minerais, trazendo um equívoco para dados geocronológicos isolados.

Nossos estudos nos depósitos de ouro da Subprovíncia NW-Quadrilátero Ferrífero sugerem que o fenômeno de concentração de minério teve componentes entre >2750 e ~1800 Ma. Esse processo amplo está registrado em mudanças na cinética de crescimento dos cristais, remobilização associada à deformação plástica, fusão parcial mediada por intrusão granítica, difusão intragrão e dissolução-reprecipitação com entrada de novos fluidos. Neste amplo intervalo de tempo, qual componente ou evento foi capaz de concentrar a maior parte do ouro e seria escolhido como “idade de mineralização”? Levamos, assim, o termo “idade de mineralização” ao campo dos paradigmas e sugerimos que ele seja usado com cautela ou evitado. O foco deve ser colocado em descrever os processos responsáveis pela concentração do ouro (e consequente formação do minério) ao longo de um tempo geológico definido.

7. CONCLUSÕES

O ouro se concentra em uma grande variedade de tipos de depósitos por meio de um espectro amplo de processos magmáticos, hidrotermais e físicos. Na grande maioria dos depósitos de ouro, os minerais-minério mais importantes são pirita e arsenopirita e a natureza refratária desses minerais traz um excelente potencial para preservar evidências da história da evolução dos corpos minerais, desde a precipitação primária, passando por deformação e metamorfismo. Em geral, depósitos de ouro são comumente associados a múltiplos eventos mineralizantes superimpostos e é frequentemente muito difícil estabelecer quais desses estágios representa a adição ou a remobilização de Au pré-existente.

Essa pesquisa integra a amostragem em corpos de minério em 9 depósitos de ouro brasileiros com diferentes histórias metalogenéticas e tectono-termais para estudar a assinatura geoquímica e a microtextura de sulfetos, notadamente arsenopirita. A reunião com as principais teorias para a distribuição e mobilidade de ouro e outros elementos-traço nesses sulfetos possibilitou subdividir os mecanismos de cristalização (processos primários) e remobilização, aplicando os conceitos nas amostras obtidas.

Processos primários ligados à cristalização produzem o zonamento químico por:

- (i) mecanismos extrínsecos, como mudanças de P e T, composição, fugacidade e interação fluido-rocha ou;
- (ii) mecanismos intrínsecos, como efeitos cinéticos, efeitos de estrutura da superfície do cristal, crescimento heteroepitaxial tipo SK ou auto-organização limitada por difusão.

Já nos processos de remobilização na escala de grão, os mecanismos estão geralmente ligados a fusão parcial de minério de sulfeto, difusão intra-grão, ou substituição mineral por fluido. Esses mecanismos ocorrem separadamente ou em conjunto. Dos diversos mecanismos capazes de gerar minérios de elevado teor (i.e., substituição mediada por fluido, fusão parcial e difusão intra-grão), destacamos um sub-mecanismo de remobilização por fluido que parece muito mais eficiente para o transporte de Au em grandes concentrações envolve o transporte como nanopartículas (ou coloides). Esse transporte ocorre como consequência de fluidos polimetálicos com presença dos elementos calcófilos de baixo ponto de fusão, que removem Au de mineralizações preexistentes pelo sub-mecanismo do par dissolução-reprecipitação.

Os depósitos Turmalina, Satinoco e São Sebastião (NW-Quadrilátero Ferrífero) exibem uma clara relação estrutural entre a mineralização e a intrusão de granitóides tardi a pós-tectônicos. Esses depósitos possuem rochas hospedeiras bastante diferentes, mas apresentam uma sequência de ao menos 3 paragêneses de minerais-minério correlacionáveis, ambos com sulfetos auríferos sin-, tardi- e pós-tectônicos (re) cristalizados.

Nossos estudos no depósito Satinoco possibilitaram extrair as seguintes conclusões:

- (i) A mineralização do ouro ocorreu ao longo de um período de c. 2720 a 2684 Ma, durante e após a colocação do magma granítico. Entre 2720 e 2695 Ma, as zonas de cisalhamento parecem ter sido um fator crítico no controle da mineralização durante o estágio de mineralização I, pré-granito, da entrada de fluido hidrotermal;
- (ii) Um segundo estágio de mineralização rico em Fe (estágio II) foi tardi- a pós-magmático em relação ao granito Casquilho, ou seja, entre c. 2695 e >2684 Ma, e envolve metassomatismo por fluidos ricos em Fe;

- (iii) A intrusão de magma granítico levou rochas hospedeiras à desidratação gerando uma mistura de fluidos metamórficos e magmáticos com um alta razão fluido/rocha, que foi essencial para a mineralização;
- (iv) Durante o posterior soerguimento tectônico pós-granito e/ou exumação e consequente diminuição da temperatura, um terceiro estágio levou à recristalização e remobilização de sulfetos e ouro. As duas hipóteses para a geocronologia deste evento são: Arqueano, em ~ 2600 Ma ou Paleoproterozoico, em ~2000 Ma.

Evidentemente, as associações de sulfetos nos depósitos do NW-Quadrilátero Ferrífero guardam diferentes evoluções químicas e são provenientes de fluidos metamórficos e magmáticos. Mapas compostionais intra-grão em arsenopirita e pirita associados a mapas de deformação plástica na estrutura cristalina demonstram zonamento composicional e sugerem remobilização de elementos-traço, incluindo Au e Pb da estrutura de cristais de arsenopirita da primeira geração. Esses cristais, por vezes, exibem sombras de pressão deformadas formadas por quartzo com extinção ondulante e pirita estirada.

O fenômeno de concentração de minério teve componentes entre >2750 e ~1800 Ma. Esse processo amplo parece estar registrado em mudanças na cinética de crescimento dos cristais, remobilização associada à deformação plástica, fusão parcial mediada por intrusão granítica, difusão intra-grão e dissolução-reprecipitação com entrada de novos fluidos. Interpretamos que o ouro foi sendo remobilizado da estrutura do sulfeto, transportado e depositado ao longo do tempo geológico.

Nos depósitos de Pilar de Goiás e Crixás, a arsenopirita exibe cristais grossos com sombras de pressão deformadas. Esses cristais comumente estão orientados com o eixo-c paralelo à foliação principal, mas alguns cristais estão rotacionados pelo evento de deformação D₂, contíguo à formação das sombras de pressão. Nossos resultados com mapeamento composicional, mapeamento de deformação plástica e

perfil de pontos com LA-ICP-MS levaram em conta a orientação dos cristais para a comparação com distribuição dos elementos-traço. Nesse quesito, foi possível observar que:

- (i) Os cristais de arsenopirita paralelos à foliação resistiram ligeiramente mais à deformação plástica. Essa conclusão corrobora com publicação recente onde a arsenopirita se mantém robusta quando o eixo de maior tensão faz altos ângulos com o eixo-c do cristal. Contrariamente, a tensão cisalhante permite maior deformação plástica (localizada);
- (ii) Mapas de deformação plástica obtidos com difração de elétrons retro espalhados mostram incipiente deformação associada à clivagem de crenulação na arsenopirita paralela à foliação principal;
- (iii) Mapas compostionais e análises pontuais com microssonda e LA-ICP-MS mostram que a distribuição de elementos-traço, como o Au, mostra clara relação direta com fraturas intracristalinas e bordas de grão;
- (iv) Na comparação entre os cristais paralelos e rotacionados na foliação, a distribuição de ouro indica leve empobrecimento nos cristais rotacionados, sugerindo uma contribuição da deformação plástica para a remobilização.

Os cristais de arsenopirita dos depósitos de Pilar de Goiás e Crixás apresentam ao menos dois mecanismos de remobilização, sendo a difusão intra-grão, possivelmente por HDPD ou por DIP e o par dissolução-reprecipitação. A ausência de inclusões e a relação direta entre as fraturas e o enriquecimento de ouro, além da baixa taxa de deformação plástica nos cristais, indicam que a dissolução-reprecipitação teve papel mais relevante na perda de ouro pela arsenopirita e consequente precipitação como nanopartículas nas bordas dos grãos.

Evidentemente, uma gama de processos ligados ao zonamento de ouro podem ocorrer em depósitos multiestágios. Esse trabalho demonstra a importância de se aplicar os conceitos ligados à cristalização e remobilização em sulfetos para entender melhor os processos metalogenéticos. Esses conceitos também têm se mostrado fundamentais para a determinação de fontes e idade relativa dos estágios

de mineralização. Para tanto, é necessário investir em técnicas analíticas modernas de altíssima resolução espacial, como o NanoSIMS e a microssonda atômica.

8. REFERÊNCIAS

Nota: As referências específicas correspondentes aos capítulos 2, 3, 4 e 5 encontram-se ao final de cada um deles.

- Alkmim F.F., Marshak S. 1998. Transamazonian Orogeny in the Southern São Francisco Craton Region, Minas Gerais, Brazil: Evidence for Paleoproterozoic collision and collapse in the Quadrilátero Ferrífero. *Precambrian Research*, **70**:29–58.
- Almeida F.F.M. 1977. O Cráton do São Francisco. *Revista Brasileira de Geociências*, **7**:349–364.
- Bajwah Z.U., Seccombe P.K., Offler R. 1987. Trace element distribution, Co: Ni ratios and genesis of the Big Cadia iron-copper deposit, New South Wales, Australia. *Mineralium Deposita*, **22**:292–300.
- Baltazar O.F., Zucchetti M. 2007. Lithofacies associations and structural evolution of the Archean Rio das Velhas greenstone belt, Quadrilátero Ferrífero, Brazil: A review of the setting of gold deposits. *Ore Geology Reviews*, **32**:471–499.
- Barnicoat A.C., Fare R.J., Groves D.I., McNaughton N.J. 1991. Synmetamorphic lode-gold deposits in high-grade Archean settings. *Geology*, **19**:921–924.
- Barrie C.D., Boyle A.P., Cook N.J., Prior D.J. 2010. Pyrite deformation textures in the massive sulfide ore deposits of the Norwegian Caledonides. *Tectonophysics*, **483**:269–286.
- Becker U., Reich M., Utsunomiya S., Wang J., Kesler S., Wang L., Ewing R.C. 2007. Nanoparticle-host interactions in natural systems. AGU FM, **2007**:B31F-04.
- Berman R.G. 1991. Thermobarometry using multi-equilibrium calculations; a new technique, with petrological applications. *The Canadian Mineralogist*, **29**:833–855.
- Bierlein F.P., Reynolds N., Arne D., Bargmann C., McKeag S., Bullen W., Al-Athbah

- H., McKnight S., Maas R. 2016. Petrogenesis of a Neoproterozoic magmatic arc hosting porphyry Cu-Au mineralization at Jebel Ohier in the Gebeit Terrane, NE Sudan. *Ore Geology Reviews*, **79**:133–154.
- Bosco-Santos A., Gilhooly W.P., Fouskas F., Fabricio-Silva W., Oliveira E.P. 2020. Euxinia in the Neoarchean: The starting point for early oxygenation in a Brazilian Craton. *Precambrian Research*, **341**:105655.
- Brando Soares M., Corrêa Neto A.V., Zeh A., Cabral A.R., Pereira L.F., Prado M.G.B. do, Almeida A.M. de, Manduca L.G., Silva P.H.M. da, Mabub R.O. de A., Schlichta T.M. 2017. Geology of the Pitangui greenstone belt, Minas Gerais, Brazil: Stratigraphy, geochronology and BIF geochemistry. *Precambrian Research*, **291**:17–41.
- Brando Soares M., Corrêa Neto A.V., Bertolino L.C., Alves F.E.A., de Almeida A.M., Montenegro da Silva P.H., Mabub R.O. de A., Manduca L.G., Araújo I.M.C. de P. 2018. Multistage mineralization at the hypozonal São Sebastião gold deposit, Pitangui greenstone belt, Minas Gerais, Brazil. *Ore Geology Reviews*, **102**:618–638.
- Brando Soares M., Corrêa Neto A.V., Fabricio-Silva W. 2020. The development of a Meso- to Neoarchean rifting-convergence-collision-collapse cycle over an ancient thickened protocontinent in the south São Francisco craton, Brazil. *Gondwana Research*, **77**:40–66.
- Bühn B., Santos R. V., Dardenne M.A., de Oliveira C.G. 2012. Mass-dependent and mass-independent sulfur isotope fractionation (δ 34S and δ 33S) from Brazilian Archean and Proterozoic sulfide deposits by laser ablation multi-collector ICP-MS. *Chemical Geology*, **312–313**:163–176.
- Caddick M.J., Konopásek J., Thompson A.B. 2010. Preservation of Garnet Growth Zoning and the Duration of Prograde Metamorphism. *Journal of Petrology*, **51**:2327–2347.
- Carneiro M.A. 1992. O Complexo Metamórfico Bonfim Setentrional (Quadrilátero Ferrífero, MG): Litoestratigrafia e evolução geológica de um segmento de crosta continental do Arqueano: Universidade de São Paulo: 233 p.

- Chemale F., Rosière C.A., Endo I. 1994. The tectonic evolution of the Quadrilátero Ferrífero, Minas Gerais, Brazil. *Precambrian Research*, **65**:25–54.
- Ciobanu C.L., Cook N.J., Damian F., Damian G. 2006. Gold scavenged by bismuth melts: An example from Alpine shear-remobilizes in the Highiș Massif, Romania. *Mineralogy and Petrology*, **87**:351–384.
- Ciobanu C.L., Birch W.D., Cook N.J., Pring A., Grundler P. V 2010. Petrogenetic significance of Au–Bi–Te–S associations: the example of Maldon, Central Victorian gold province, Australia. *Lithos*, **116**:1–17.
- Ciobanu C.L., Cook N.J., Utsunomiya S., Kogagwa M., Green L., Gilbert S., Wade B. 2012. Gold-telluride nanoparticles revealed in arsenic-free pyrite. *American Mineralogist*, **97**:1515–1518.
- Cooke R.A., O'Brien P.J., Carswell D.A. 2000. Garnet zoning and the identification of equilibrium mineral compositions in high-pressure-temperature granulites from the Moldanubian Zone, Austria. *Journal of Metamorphic Geology*, **18**:551–569.
- Deditius A.P., Utsunomiya S., Reich M., Kesler S.E., Ewing R.C., Hough R., Walshe J. 2011. Trace metal nanoparticles in pyrite. *Ore Geology Reviews*, **42**:32–46.
- Deol S., Deb M., Large R.R., Gilbert S. 2012. LA-ICPMS and EPMA studies of pyrite, arsenopyrite and loellingite from the Bhukia-Jagpura gold prospect, southern Rajasthan, India: Implications for ore genesis and gold remobilization. *Chemical Geology*, **326–327**:72–87.
- Dorr J.V.N. 1969. Physiographic, stratigraphic, and structural development of the Quadrilatero Ferrifero, Minas Gerais, Brazil:, accessed at US Geological Survey - Professional Paper 614-A at <http://pubs.er.usgs.gov/publication/pp641A>.
- Dubosq R., Lawley C.J.M., Rogowitz A., Schneider D.A., Jackson S. 2018. Pyrite deformation and connections to gold mobility: Insight from micro-structural analysis and trace element mapping. *Lithos*, **310–311**:86–104.
- Dubosq R., Rogowitz A., Schweinar K., Gault B., Schneider D.A. 2019. A 2D and 3D nanostructural study of naturally deformed pyrite: assessing the links between trace element mobility and defect structures. *Contributions to Mineralogy and Petrology*, **174**:1–16.

Fabricio-Silva W. 2016. Evolução tectono-metamórfica aplicada aos processos responsáveis pela mineralização no depósito de ouro Turmalina, Quadrilátero Ferrífero, Brasil: geologia, análise estrutural e isótopos de enxofre: Universidade Federal de Minas Gerais: 113 p.

Fabricio-Silva W., Rosière C.A., Bühn B. 2019. The shear zone-related gold mineralization at the Turmalina deposit, Quadrilátero Ferrífero, Brazil: structural evolution and the two stages of mineralization. *Mineralium Deposita*, **54**:347–368.

Fabricio-Silva W., Frimmel H.E., Shutesky M.E., Rosière C.A., Massucatto A.J. 2020. Temperature-controlled ore evolution in orogenic-gold systems related to synchronous granitic magmatism: An example from the Iron Quadrangle Province, Brazil. *Economic Geology*, .

Fielding I.O.H., Johnson S.P., Meffre S., Zi J., Sheppard S., Large R.R., Rasmussen B. 2019. Linking gold mineralization to regional-scale drivers of mineral systems using in situ U–Pb geochronology and pyrite LA-ICP-MS element mapping. *Geoscience Frontiers*, **10**:89–105.

Fougerouse D., Micklethwaite S., Tomkins A.G., Mei Y., Kilburn M., Guagliardo P., Fisher L.A., Halfpenny A., Gee M., Paterson D., Howard D.L. 2016a. Gold remobilisation and formation of high grade ore shoots driven by dissolution-reprecipitation replacement and Ni substitution into auriferous arsenopyrite. *Geochimica et Cosmochimica Acta*, **178**:143–159.

Fougerouse D., Reddy S.M., Saxey D.W., Rickard W.D.A., Van Riessen A., Micklethwaite S. 2016b. Nanoscale gold clusters in arsenopyrite controlled by growth rate not concentration: Evidence from atom probe microscopy. *American Mineralogist*, **101**:1916–1919.

Fougerouse D., Micklethwaite S., Halfpenny A., Reddy S.M., Cliff J.B., Martin L.A.J., Kilburn M., Guagliardo P., Ulrich S. 2016c. The golden ark: Arsenopyrite crystal plasticity and the retention of gold through high strain and metamorphism. *Terra Nova*, **28**:181–187.

Fougerouse D., Reddy S.M., Kirkland C.L., Saxey D.W., Rickard W.D., Hough R.M.

2019. Time-resolved, defect-hosted, trace element mobility in deformed Witwatersrand pyrite. *Geoscience Frontiers*, **10**:55–63.
- Fowler A., Prokoph A., Stern R., Dupuis C. 2002. Organization of oscillatory zoning in zircon: analysis, scaling, geochemistry, and model of a zircon from Kipawa, Quebec, Canada. *Geochimica et Cosmochimica Acta*, **66**:311–328.
- Frimmel H.E. 2008. Earth's continental crustal gold endowment. *Earth and Planetary Science Letters*, **267**:45–55.
- Frimmel H.E., Hennigh Q. 2015. First whiffs of atmospheric oxygen triggered onset of crustal gold cycle. *Mineralium Deposita*, **50**:5–23.
- Frizzo C., Takai V., Scarpelli W. 1991. Auriferous mineralization at Pitangui, Minas Gerais. Brazil Gold '91 - Ladeira, E. A. (ed), 579–583.
- Frost B.R., Mavrogenes J.A., Tomkins A.G. 2002. Partial melting of sulfide ore deposits during medium- and high-grade metamorphism. *The Canadian Mineralogist*, **40**:1–18.
- Gault B. 2016. A brief overview of atom probe tomography research. *Applied Microscopy*, **46**:117–126.
- Genkin A.D., Bortnikov N.S., Cabri L.J., Wagner F.E., Stanley C.J., Safonov Y.G., McMahon G., Friedl J., Kerzin A.L., Gamyanin G.N. 1998. A multidisciplinary study of invisible gold in arsenopyrite from four mesothermal gold deposits in Siberia, Russian Federation. *Economic Geology*, **93**:463–487.
- De Geuser F., Lefebvre W., Blavette D. 2006. 3D atom probe study of solute atoms clustering during natural ageing and pre-ageing of an Al-Mg-Si alloy. *Philosophical Magazine Letters*, **86**:227–234.
- Goldfarb R.J., Groves D.I. 2015. Orogenic gold: Common or evolving fluid and metal sources through time. *Lithos*, **233**:2–26.
- Gopon P., Douglas J.O., Auger M.A., Hansen L., Wade J., Cline J.S., Robb L.J., Moody M.P. 2019. A Nanoscale Investigation of Carlin-Type Gold Deposits: An Atom-Scale Elemental and Isotopic Perspective. *Economic Geology*, **114**:1123–1133.

- Gourcerol B., Kontak D.J., Thurston P.C., Petrus J.A. 2018. Results of LA-ICP-MS sulfide mapping from Algoma-type BIF gold systems with implications for the nature of mineralizing fluids, metal sources, and deposit models. *Mineralium Deposita*, **53**:871–894.
- Gourcerol B., Kontak D.J., Petrus J.A., Thurston P.C. 2020. Application of LA ICP-MS analysis of arsenopyrite to gold metallogeny of the Meguma Terrane, Nova Scotia, Canada. *Gondwana Research*, **81**:265–290.
- Groves D.I., Goldfarb R.J., Gebre-Mariam M., Hagemann S.G., Robert F. 1998. Orogenic gold deposits: a proposed classification in the context of their crustal distribution and relationship to other gold deposit types. *Ore Geology Reviews*, **13**:7–27.
- Groves D.I., Santosh M., Goldfarb R.J., Zhang L. 2018. Structural geometry of orogenic gold deposits: Implications for exploration of world-class and giant deposits. *Geoscience Frontiers*, **9**:1163–1177.
- Groves D.I., Santosh M., Deng J., Wang Q., Yang L., Zhang L. 2019. A holistic model for the origin of orogenic gold deposits and its implications for exploration. *Mineralium Deposita*, 1–18.
- Hagemann S.G., Brown P.E., Ridley J., Stern P., Fournelle J. 1998. Ore petrology, chemistry, and timing of electrum in the Archean hypozonal Transvaal lode gold deposit, Western Australia. *Economic Geology*, **93**:271–291.
- Harlov D.E., Wirth R., Hetherington C.J. 2011. Fluid-mediated partial alteration in monazite: the role of coupled dissolution–reprecipitation in element redistribution and mass transfer. *Contributions to Mineralogy and Petrology*, **162**:329–348.
- Hart C.J.R., McCoy D.T., Goldfarb R.J., Smith M., Roberts P., Hulstein R., Bakke A.A., Bundtzen T.K. 2002. Geology, exploration, and discovery in the Tintina Gold Province, Alaska and Yukon. Special Publication - Society of Economic Geologists, **9**:241–274.
- Hastie E.C.G., Kontak D.J., Lafrance B. 2020. Gold Remobilization: Insights from Gold Deposits in the Archean Swayze Greenstone Belt, Abitibi Subprovince, Canada. *Economic Geology*, **115**:241–277.

- Hazarika P., Mishra B., Lochan Pruseth K. 2017. Trace-element geochemistry of pyrite and arsenopyrite: ore genetic implications for late Archean orogenic gold deposits in southern India. *Mineralogical Magazine*, **81**:661–678.
- Herbig M., Choi P., Raabe D. 2015. Combining structural and chemical information at the nanometer scale by correlative transmission electron microscopy and atom probe tomography. *Ultramicroscopy*, **153**:32–39.
- Hofmann A.W. 1988. Chemical differentiation of the Earth: the relationship between mantle, continental crust, and oceanic crust. *Earth and Planetary Science Letters*, **90**:297–314.
- Hoppe P. 2006. NanoSIMS: A new tool in cosmochemistry. *Applied Surface Science*, **252**:7102–7106.
- Hoppe P., Cohen S., Meibom A. 2013. NanoSIMS: Technical Aspects and Applications in Cosmochemistry and Biological Geochemistry. *Geostandards and Geoanalytical Research*, **37**:111–154.
- Hough R.M., Noble R.R.P., Reich M. 2011. Natural gold nanoparticles. *Ore Geology Reviews*, **42**:55–61.
- Hu X., Gong Y., Zeng G., Zhang Z., Wang J., Yao S. 2018. Multistage pyrite in the Getang sediment-hosted disseminated gold deposit, southwestern Guizhou Province, China: Insights from textures and in situ chemical and sulfur isotopic analyses. *Ore Geology Reviews*, **99**:1–16.
- Jaguar Mining I. 2020. Technical report on the Turmalina mine Complex, Minas Gerais State, Brasil.:
- Kerr M.J., Hanley J.J., Kontak D.J., Morrison G.G., Petrus J., Fayek M., Zajacz Z. 2018. Evidence of upgrading of gold tenor in an orogenic quartz-carbonate vein system by late magmatic-hydrothermal fluids at the Madrid Deposit, Hope Bay Greenstone Belt, Nunavut, Canada. *Geochimica et Cosmochimica Acta*, **241**:180–218.
- Kretschmar U., Scott S.D. 1976. Phase relations involving arsenopyrite in the system Fe-As-S and their application. *The Canadian Mineralogist*, **14**:364–386.

- Lana C., Alkmim F.F., Armstrong R., Scholz R., Romano R., Nalini H.A. 2013. The ancestry and magmatic evolution of Archaean TTG rocks of the Quadrilátero Ferrífero province, southeast Brazil. *Precambrian Research*, **231**:157–173.
- Lanari P., Vidal O., De Andrade V., Dubacq B., Lewin E., Grosch E.G., Schwartz S. 2014. XMapTools: A MATLAB©-based program for electron microprobe X-ray image processing and geothermobarometry. *Computers & Geosciences*, **62**:227–240.
- Large R.R., Danyushevsky L., Hollit C., Maslennikov V., Meffre S., Gilbert S., Bull S., Scott R., Emsbo P., Thomas H., Singh B., Foster J. 2009. Gold and Trace Element Zonation in Pyrite Using a Laser Imaging Technique: Implications for the Timing of Gold in Orogenic and Carlin-Style Sediment-Hosted Deposits. *Economic Geology*, **104**:635–668.
- Larocque A.C.L., Hodgson C.J., Cabri L.J., Jackman J.A. 1995. Ion-microprobe analysis of pyrite, chalcopyrite and pyrrhotite from the Mobrun VMS deposit in northwestern Quebec; evidence for metamorphic remobilization of gold. *The Canadian Mineralogist*, **33**:373–388.
- Lobato L.M., Ribeiro-Rodrigues L.C., Vieira F.W.R. 2001. Brazil's premier gold province. Part II: geology and genesis of gold deposits in the Archean Rio das Velhas greenstone belt, Quadrilátero Ferrífero. *Mineralium Deposita*, **36**:249–277.
- Machado N., Schrank A., Noce C.M., Gauthier G. 1996. Ages of detrital zircon from Archean-Paleoproterozoic sequences: Implications for Greenstone Belt setting and evolution of a Transamazonian foreland basin in Quadrilátero Ferrífero, southeast Brazil. *Earth and Planetary Science Letters*, **141**:259–276.
- Marinho M.S., Silva M.A., Lombello J.C., Di Salvio L.P., Silva R.N., Féboli W.L., Brito D.C. 2018. Projeto ARIM - Áreas de Relevante Interesse Mineral - Noroeste do Quadrilátero Ferrífero - Mapa Geológico Integrado do Sinclínorio Pitangui. 1 mapa colorido. Escala 1:75.000. 1.
- Marshall B., Gilligan L.B. 1987. An introduction to remobilization: information from ore-body geometry and experimental considerations. *Ore Geology Reviews*,

2:87–131.

- Marshall B., Gilligan L.B. 1993. Structural Setting and Controls on Mineral Deposits Remobilization, syn-tectonic processes and massive sulphide deposits. *Ore Geology Reviews*, **8**:39–64.
- Masurel Q., Thébaud N., Miller J., Ulrich S., Hein K.A.A., Cameron G., Béziat D., Bruguier O., Davis J.A. 2017. Sadiola Hill: A world-class carbonate-hosted gold deposit in Mali, West Africa. *Economic Geology*, **112**:23–47.
- McQueen K.G. 2005. Ore deposit types and their primary expressions. *Regolith Expression of Australian Ore Systems*: ..., 1–14.
- Meinert L.D., Dipple G.M., Nicolescu S. 2005. World Skarn Deposits. *Economic Geology* 100th Anniversary Volume.
- de Melo-Silva P., da Silva Amaral W., Oliveira E.P. 2019. Geochronological evolution of the Pitangui greenstone belt, southern São Francisco Craton, Brazil: Constraints from U-Pb zircon age, geochemistry and field relationships. *Journal of South American Earth Sciences*, .
- de Melo-Silva P., Amaral W. da S., Oliveira E.P. 2020. Geochronological evolution of the Pitangui greenstone belt, southern São Francisco Craton, Brazil: Constraints from U-Pb zircon age, geochemistry and field relationships. *Journal of South American Earth Sciences*, **99**:
- Mériaud N., Jébrak M. 2017. From intrusion-related to orogenic mineralization: The Wasamac deposit, Abitibi Greenstone Belt, Canada. *Ore Geology Reviews*, **84**:289–308.
- Mikhlin Y.L., Romanchenko A.S., Asanov I.P. 2006. Oxidation of arsenopyrite and deposition of gold on the oxidized surfaces: A scanning probe microscopy, tunneling spectroscopy and XPS study. *Geochimica et Cosmochimica Acta*, **70**:4874–4888.
- Mishra B., Pruseth K.L., Hazarika P., Chinnasamy S.S. 2018. Nature and source of the ore-forming fluids associated with orogenic gold deposits in the Dharwar Craton. *Geoscience Frontiers*, **9**:715–726.

- Mo Y.-W., Savage D.E., Swartzentruber B.S., Lagally M.G. 1990. Kinetic pathway in Stranski-Krastanov growth of Ge on Si (001). *Physical Review Letters*, **65**:1020.
- Morey A.A., Tomkins A.G., Bierlein F.P., Weinberg R.F., Davidson G.J. 2008. Bimodal distribution of gold in pyrite and arsenopyrite: Examples from the archean boorara and bardoc shear systems, Yilgarn Craton, Western Australia. *Economic Geology*, **103**:599–614.
- Müller E.W. 1956. Resolution of the atomic structure of a metal surface by the field ion microscope. *Journal of Applied Physics*, **27**:474–476.
- Mumin A.H., Fleet M.E., Chryssoulis S.L. 1994. Gold mineralization in As-rich mesothermal gold ores of the Bogosu-Prestea mining district of the Ashanti Gold Belt, Ghana: remobilization of “invisible” gold. *Mineralium Deposita*, **29**:445–460.
- Neumayr P., Cabri L.J., Groves D.I., Mikucki E.J., Jackman J.A. 1993. The mineralogical distribution of gold and relative timing of gold mineralization in two Archean settings of high metamorphic grade in Australia. *The Canadian Mineralogist*, **31**:711–725.
- Noce C.M., Tassinari C., Lobato L.M. 2007. Geochronological framework of the Quadrilátero Ferrífero, with emphasis on the age of gold mineralization hosted in Archean greenstone belts. *Ore Geology Reviews*, **32**:500–510.
- Oliveira E.P., McNaughton N.J., Zincone S.A., Talavera C. 2020. Birthplace of the São Francisco Craton, Brazil: Evidence from 3.60 to 3.64 Ga Gneisses of the Mairi Gneiss Complex. *Terra Nova*, **32**:281–289.
- Palenik C.S., Utsunomiya S., Reich M., Kesler S.E., Wang L., Ewing R.C. 2004. “Invisible” gold revealed: Direct imaging of gold nanoparticles in a Carlin-type deposit. *American Mineralogist*, **89**:1359–1366.
- Palme H., Jones A. 2003. Solar system abundances of the elements. *TrGeo*, **1**:711.
- Pearce M.A., Godel B.M., Fisher L.A., Schoneveld L.E., Cleverley J.S., Oliver N.H.S., Nugus M. 2018. Microscale data to macroscale processes: A review of microcharacterization applied to mineral systems. *Geological Society Special Publication*, **453**:7–39.

- Petrakakis K. 1986. Metamorphism of high-grade gneisses from the Moldanubian zone, Austria, with particular reference to the garnets. *Journal of Metamorphic Geology*, **4**:323–344.
- Phillips G.N., Powell R. 2009. Formation of gold deposits: Review and evaluation of the continuum model. *Earth-Science Reviews*, **94**:1–21.
- Phillips G.N., Powell R. 2010. Formation of gold deposits: A metamorphic devolatilization model. *Journal of Metamorphic Geology*, **28**:689–718.
- Plümper O., King H.E., Vollmer C., Ramasse Q., Jung H., Austrheim H. 2012. The legacy of crystal-plastic deformation in olivine: high-diffusivity pathways during serpentinization. *Contributions to Mineralogy and Petrology*, **163**:701–724.
- Putnis A. 2009. Mineral replacement reactions. *Reviews in mineralogy and geochemistry*, **70**:87–124.
- Putnis A., Fernandez-Diaz L., Prieto M. 1992. Experimentally produced oscillatory zoning in the (Ba, Sr) SO₄ solid solution. *Nature*, **358**:743–745.
- Reddy S.M., Timms N.E., Pantleon W., Trimby P. 2007. Quantitative characterization of plastic deformation of zircon and geological implications. *Contributions to Mineralogy and Petrology*, **153**:625–645.
- Reich M., Kesler S.E., Utsunoyiya S., Palenik C.S., Chryssoulis S., Ewing R.C. 2005. Solubility of gold in arsenian pyrite: *Geochemica et Cosmochimica Acta*, vol. 69.
- Renger F.E., Noce C.M., Romano A.W., Machado N. 1994. Evolução Sedimentar Do Supergrupo Minas: 500 Ma. De Registro Geológico No Quadrilátero Ferrífero, Minas Gerais, Brasil. *Geonomos*, **2**:1–11.
- Ribeiro-Rodrigues L.C., de Oliveira C.G., Friedrich G. 2007. The Archean BIF-hosted Cuiabá Gold deposit, Quadrilátero Ferrífero, Minas Gerais, Brazil. *Ore Geology Reviews*, **32**:543–570.
- Rigutti L., Vella A., Vurpillot F., Gaillard A., Sevelin-Radiguet N., Houard J., Hideur A., Martel G., Jacopin G., Bugallo A.D.L. 2013. Coupling atom probe tomography and photoluminescence spectroscopy: Exploratory results and perspectives. *Ultramicroscopy*, **132**:75–80.

- Romano A.W. 1993. Parte, O Supergrupo Rio das Velhas da Faixa Mateus Leme-Pitangui - meridional do Cráton de São Francisco, MG - e seu sistema de alteração hidrotermal. *Geonomos*, **1**:16–32.
- Romano A.W. 2007. Programa Geologia do Brasil. Folha Pará de Minas, SE-23-Z-C-I. Escala 1:100.000 relatório final. UFMG-CPRM, Belo Horizonte. 74 p.
- Romano R., Lana C., Alkmim F.F., Stevens G., Armstrong R. 2013. Stabilization of the southern portion of the São Francisco craton, SE Brazil, through a long-lived period of potassic magmatism. *Precambrian Research*, **224**:143–159.
- Saintilan N.J., Stephens M.B., Spikings R., Schneider J., Chiaradia M., Spangenberg J.E., Ulianov A., Fontboté L. 2017a. Polyphase vein mineralization in the Fennoscandian Shield at Åkerlandet, Järvsand, and Laisvall along the erosional front of the Caledonian orogen, Sweden. *Mineralium Deposita*, **52**:823–844.
- Saintilan N.J., Creaser R.A., Spry P.G., Hnatyshin D. 2017b. Re-Os Systematics of löllingite and arsenopyrite in granulite-facies garnet rocks: Insights into the metamorphic history and thermal evolution of the broken hill block during the early mesoproterozoic (New South Wales, Australia). *Canadian Mineralogist*, **55**:29–44.
- Saunders J.A. 1990. Colloidal transport of gold and silica in epithermal precious-metal systems: Evidence from the Sleeper deposit, Nevada. *Geology*, **18**:757–760.
- Sharp Z.D., Essene E.J., Kelly W.C. 1985. A re-examination of the arsenopyrite geothermometer: Pressure considerations and applications to natural assemblages. *The Canadian Mineralogist*, **23**:517–534.
- Shore M., Fowler A.D. 1996. Oscillatory zoning in minerals; a common phenomenon. *The Canadian Mineralogist*, **34**:1111–1126.
- Silva G.P.A., Carneiro M.A. 2009. The metatholeiitic suite of the Rio Manso metavolcanosedimentary sequence, Iron Quadrangle (MG). *Revista da Escola de Minas de Ouro Preto*, **62**:423–430.
- Spear F.S. 1991. Temperatures in Light of Garnet Diffusion During Cooling. *Journal of Metamorphic Geology*, **9**:379–388.

- Stromberg J.M., Barr E., Van Loon L.L., Gordon R.A., Banerjee N.R. 2019. Fingerprinting multiple gold mineralization events at the Dome mine in Timmins, Ontario, Canada: Trace element and gold content of pyrite. *Ore Geology Reviews*, **104**:603–619.
- Tassinari C.C.G., Mateus A.M., Velásquez M.E., Munhá J.M.U., Lobato L.M., Bello R.M., Chiquini A.P., Campos W.F. 2015. Geochronology and thermochronology of gold mineralization in the Turmalina deposit, NE of the Quadrilátero Ferrífero Region, Brazil. *Ore Geology Reviews*, **67**:368–381.
- Teixeira W., Ávila C.A., Dussin I.A., Corrêa Neto A. V., Bongiolo E.M., Santos J.O., Barbosa N.S. 2015. A juvenile accretion episode (2.35-2.32Ga) in the Mineiro belt and its role to the Minas accretionary orogeny: Zircon U-Pb-Hf and geochemical evidences. *Precambrian Research*, **256**:148–169.
- Thorman C.H., DeWitt E., Maron M.A., Ladeira E.A. 2001. Major brazilian gold deposits - 1982 to 1999. *Mineralium Deposita*, **36**:218–227.
- Tomkins A.G. 2013. On the source of orogenic gold. *Geology*, **41**:1255–1256.
- Tomkins A.G., Mavrogenes J.A. 2001. Redistribution of gold within arsenopyrite and löllingite during pro- and retrograde metamorphism: Application to timing of mineralization. *Economic Geology*, **96**:525–534.
- Tomkins A.G., Pattison D.R.M., Zaleski E. 2004. The Hemlo Gold Deposit, Ontario: An Example of Melting and Mobilization of a Precious Metal-Sulfosalt Assemblage during Amphibolite Facies Metamorphism and Deformation. *Economic Geology*, **99**:1063–1084.
- Tomkins A.G., Pattison D.R.M., Frost B.R. 2007. On the initiation of metamorphic sulfide anatexis. *Journal of Petrology*, **48**:511–535.
- Tooth B., Ciobanu C.L., Green L., O'Neill B., Brugger J. 2011. Bi-melt formation and gold scavenging from hydrothermal fluids: An experimental study. *Geochimica et Cosmochimica Acta*, **75**:5423–5443.
- Tuccillo M.E., Essene E.J., van der Pluijm B.A. 1990. Growth and retrograde zoning in garnets from high-grade, metapelites: Implications for pressure-temperature paths. *Geology*, **18**:839–842.

- Valley J.W., Cavosie A.J., Ushikubo T., Reinhard D.A., Lawrence D.F., Larson D.J., Clifton P.H., Kelly T.F., Wilde S.A., Moser D.E. 2014. Hadean age for a post-magma-ocean zircon confirmed by atom-probe tomography. *Nature Geoscience*, **7**:219–223.
- Verma S.K., Oliveira E.P., Silva P.M., Moreno J.A., Amaral W.S. 2017. Geochemistry of komatiites and basalts from the Rio das Velhas and Pitangui greenstone belts, São Francisco Craton, Brazil: Implications for the origin, evolution, and tectonic setting. *Lithos*, **284–285**:560–577.
- Vial D.S., DeWitt E., Lobato L.M., Thorman C.H. 2007. The geology of the Morro Velho gold deposit in the Archean Rio das Velhas greenstone belt, Quadrilátero Ferrífero, Brazil. *Ore Geology Reviews*, **32**:511–542.
- Vigneresse J.L., Truche L., Richard A. 2019. How do metals escape from magmas to form porphyry-type ore deposits? *Ore Geology Reviews*, **105**:310–336.
- Vukmanovic Z., Reddy S.M., Godel B., Barnes S.J., Fiorentini M.L., Barnes S.-J., Kilburn M.R. 2014. Relationship between microstructures and grain-scale trace element distribution in komatiite-hosted magmatic sulphide ores. *Lithos*, **184**:42–61.
- Wagner T., Fusswinkel T., Wölle M., Heinrich C.A. 2016. Microanalysis of Fluid Inclusions in Crustal Hydrothermal Systems using Laser Ablation Methods. *Elements*, **12**:323–328.
- Widler A.M., Seward T.M. 2002. The adsorption of gold (I) hydrosulphide complexes by iron sulphide surfaces. *Geochimica et Cosmochimica Acta*, **66**:383–402.
- Williams-Jones A.E., Bowell R.J., Migdisov A.A. 2009. Gold in Solution. *Elements*, **5**:281–287.
- Williams D.B., Carter C.B. 1996. *Transmission Electron Microscopy: Spectrometry*. IV. Plenum Press.
- Wu Y.F., Fougerouse D., Evans K., Reddy S.M., Saxe D.W., Guagliardo P., Li J.W. 2019a. Gold, arsenic, and copper zoning in pyrite: A record of fluid chemistry and growth kinetics. *Geology*, **47**:641–644.

- Wu Y.F., Evans K., Li J.W., Fougerouse D., Large R.R., Guagliardo P. 2019b. Metal remobilization and ore-fluid perturbation during episodic replacement of auriferous pyrite from an epizonal orogenic gold deposit. *Geochimica et Cosmochimica Acta*, **245**:98–117.
- Xing Y., Brugger J., Tomkins A., Shvarov Y. 2019. Arsenic evolution as a tool for understanding formation of pyritic gold ores. *Geology*, **47**:335–338.
- Xue Y., Campbell I., Ireland T.R., Holden P., Armstrong R. 2013. No mass-independent sulfur isotope fractionation in auriferous fluids supports a magmatic origin for Archean gold deposits. *Geology*, **41**:791–794.
- Yan J., Hu R., Liu S., Lin Y., Zhang J., Fu S. 2018. NanoSIMS element mapping and sulfur isotope analysis of Au-bearing pyrite from Lannigou Carlin-type Au deposit in SW China: New insights into the origin and evolution of Au-bearing fluids. *Ore Geology Reviews*, **92**:29–41.

Anexo I: Mapas de EBSD e resultados de LA-ICP-MS para os depósitos de Pilar de Goiás e Crixás

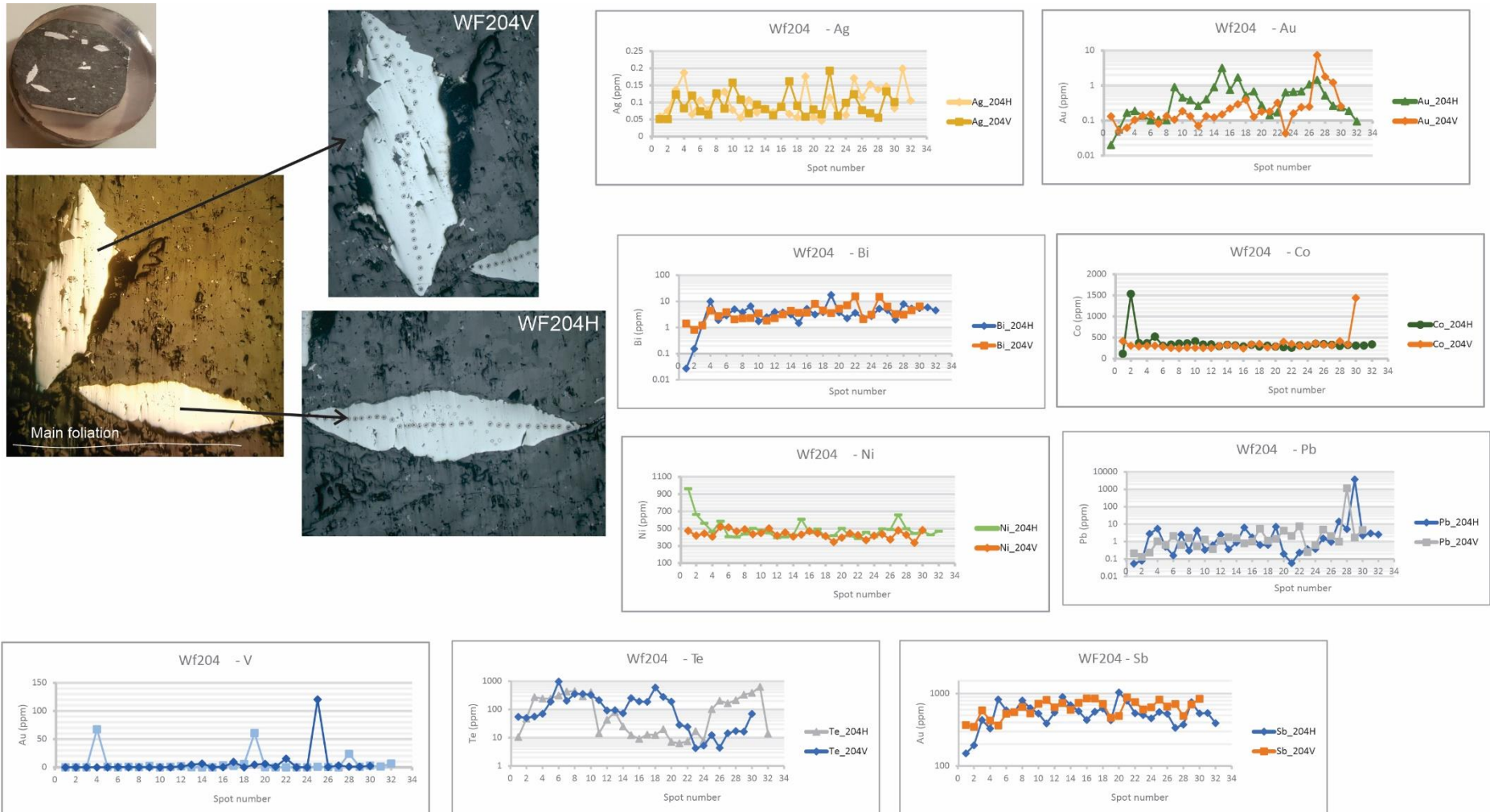
Os primeiros resultados de EBSD nativos de amostras dos depósitos de Pilar e Crixás sugerem existir uma relação entre deformação e distribuição de ouro nos cristais de arsenopirita, sobretudo quando comparados com os resultados de distribuição de elementos-traço obtidos por microssonda eletrônica.

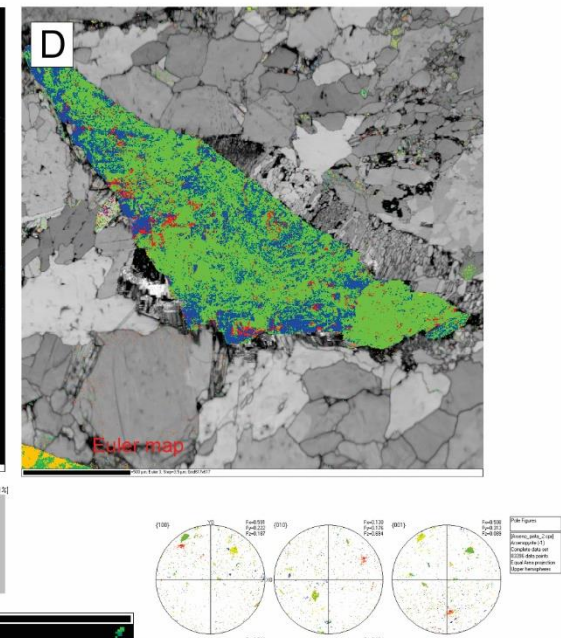
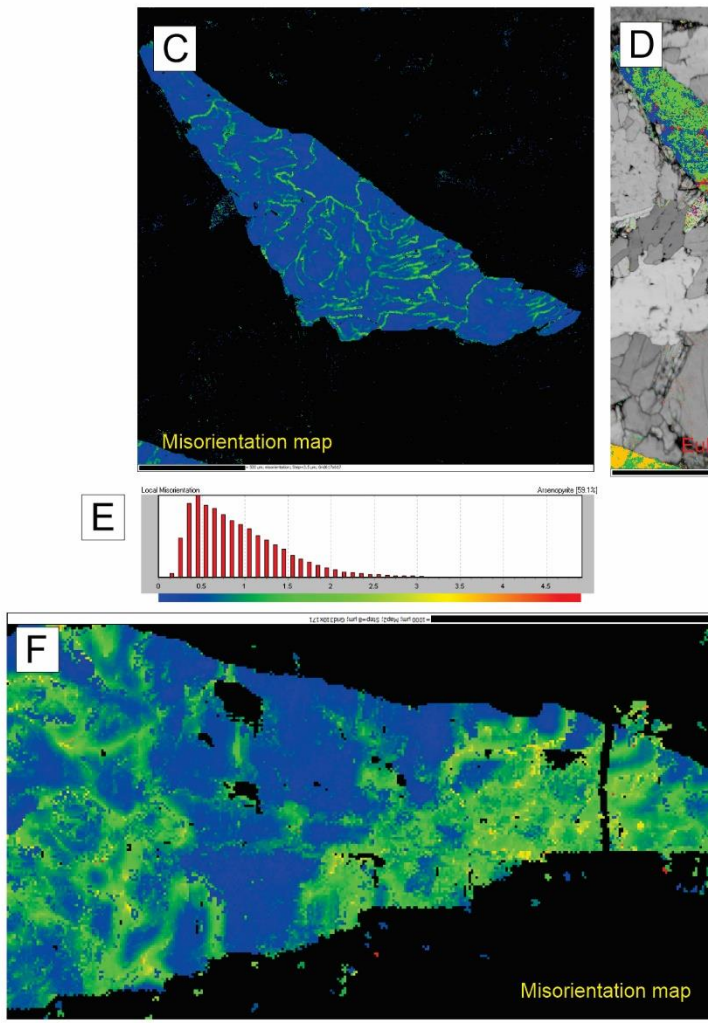
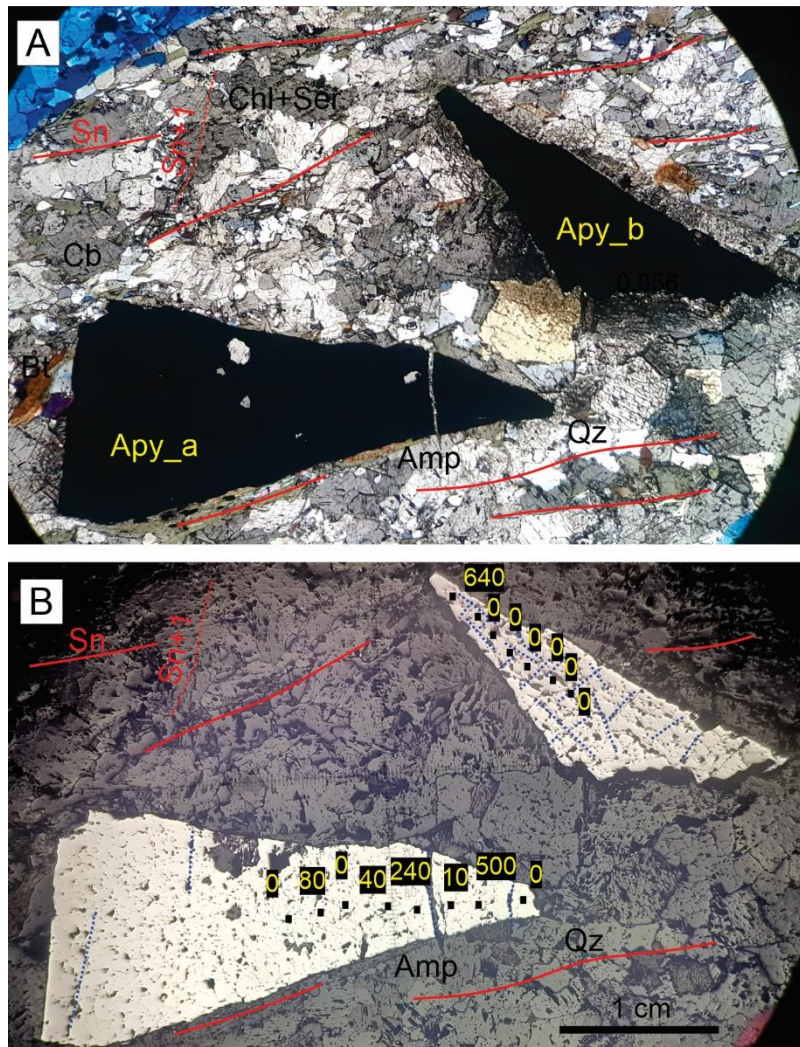
A amostra WF202 apresenta dois cristais de arsenopirita em diferentes orientações entre eixo cristalográfico e a foliação principal. Os mapas de desorientação evidenciam que a deformação plástica parece relacionada diretamente com os planos das fraturas. O fato de o grão Apy_b está consideravelmente mais fraturado sugere a possibilidade de deformação relacionada ao posicionamento do grão. Além disso, foi observada a diferença entre a distribuição dos teores de ouro (e outros traços, como Ni, Se e Sb) quando se analisa a borda e núcleo dos cristais.

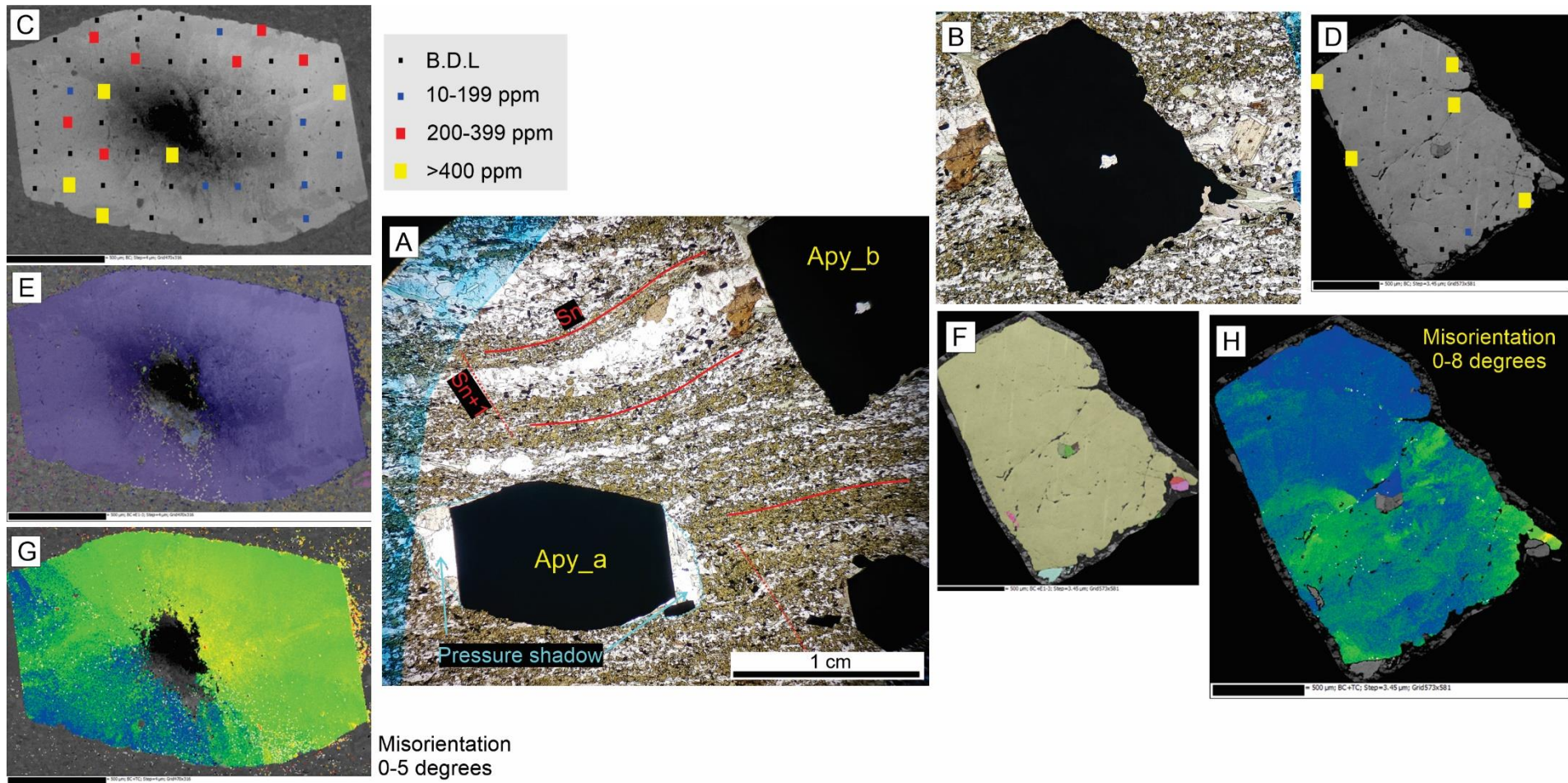
A amostra WF703 mostra dois cristais de arsenopirita em diferentes orientações, mas, diferentemente da amostra anterior, o padrão de deformação rúptil é o mesmo nos dois grãos. Tomando como referencial as sombras de pressão geradas, pode-se observar a ausência de deformação após a geração da foliação Sn+1. Neste caso, é possível verificar que existe uma clara diferença de distribuição de ouro nos dois grãos, em que o grão Apy_b mostra-se empobrecido em Au, com exceção em sua borda. Esta observação reforça que dificilmente os processos de substituição mineral por fluido e fusão parcial do sulfeto agiria diferentemente nestes dois grãos.

Caso que pode ser entendido como difusão intra-grão pelo mecanismo de difusão por caminhos de alta difusividade (Reddy et al. 2007; Plümper et al. 2012; Vukmanovic et al. 2014). De fato, é esperado que o mapa de desorientação evidencie a alta deformação plástica desses cristais (que são da primeira fase de

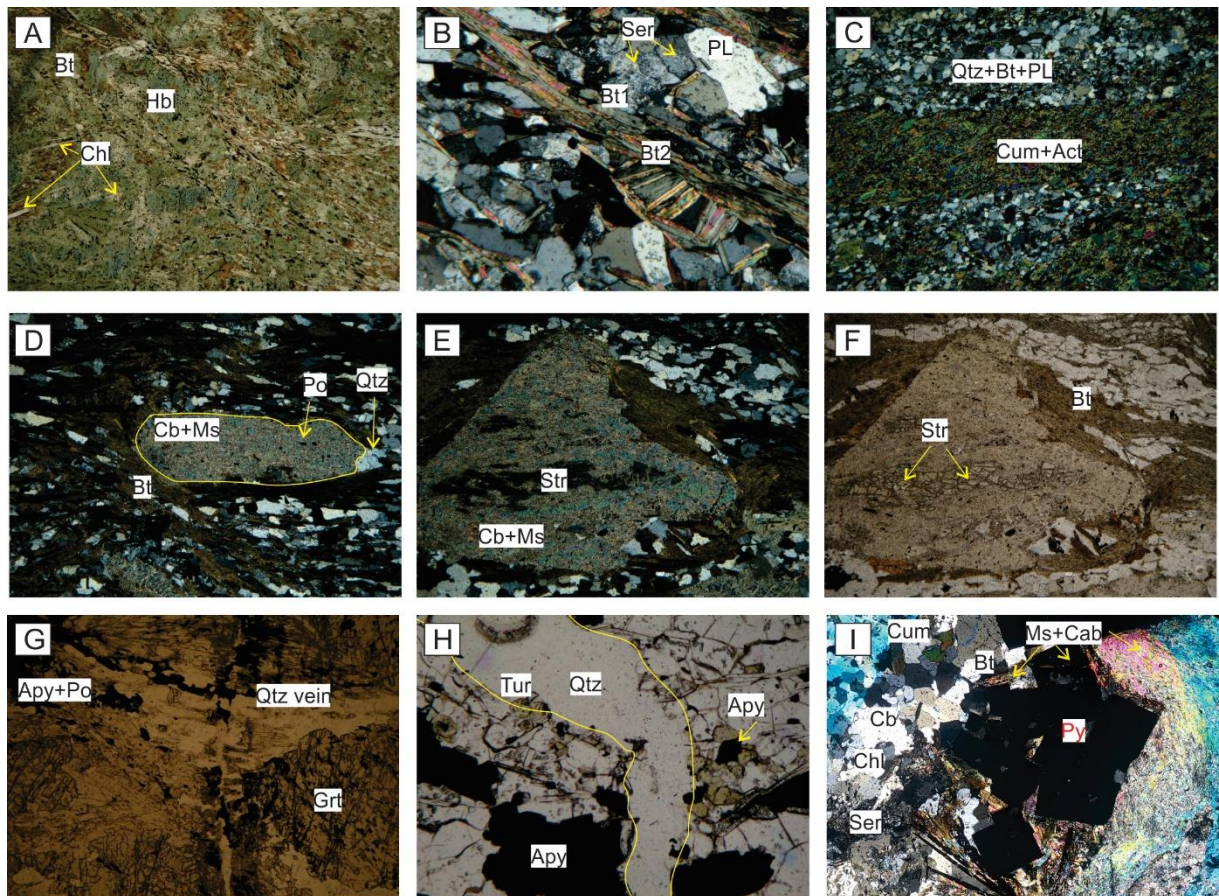
sulfetação), o que ajudaria a entender o papel dos mecanismos de deformação no processo de remobilização.







Anexo II: Feições petrográficas representativas dos depósitos Satinoco e Turmalina



A) Anfibolito apresentando textura nematoblástica de hornblenda e substituição de biotita por clorita. Nicóis paralelos. B) Biotita xisto apresentando a substituição de flogopita hidrotermal (Bt1) por siderofilita hidrotermal (Bt2) e plagioclásio por sericita. Nicóis cruzados. C) Substituição de hornblenda-plagioclásio ígnea ± quartzo ± biotita (?) por assembleia metamórfica (quartzo-cummingtonita-actinolita ± biotita). Nicóis cruzados. D) Porfiroblasto de estaurolita metamórfica completamente substituído por carbonato-mica microcristalina. A foliação S_1 defletida e a sombra de pressão composta por quartzo hidrotermal sugerem que o porfiroblasto representa a fase tardia da deformação D_2 . Observar o cristal de pirrotita ($Po_2?$) como inclusões na estaurolita pseudomórfica. Nicóis cruzados. E e F) Porfiroblasto de estaurolita metamórfica em estágio avançado de alteração para muscovita e carbonato. G) Porfiroblasto de granada substituído por clorita e interseccionado por veio de quartzo. Nicóis paralelos. H) Veio de quartzo (V_3) atravessando a associação

hidrotermal com sulfeto (principalmente Apy) e turmalina. I) Paragênese de muscovita-carbonato (metamórfico - metamorfismo regional) cortando pirita (associação de sulfeto III) e clorita-sericita hidrotermal.

Anexo III: Resultados de EPMA para granada de três gerações do Greenstone Belt Pitangui

Sample	102-A-2	112-B-1	112-B-2	112-B-4	112-B-6	112-B-7	112-B-9	112-B-11	112-B-12	112-B-15	112-B-16	120-B-1	120-B-3
Section	Grt2-Core	Grt2-Rim	Grt2-Rim	Grt1-Rim	Grt1-Core	Grt1-Core	Grt1-Core	Grt1-Core	Grt1-Rim	Grt2-Rim	Grt2-Rim	Grt2-Rim	Grt2-Rim
SiO ₂	36.90	36.56	36.66	36.80	36.39	36.82	36.94	36.22	36.93	36.72	36.75	36.67	36.56
Al ₂ O ₃	20.04	19.83	19.93	19.69	19.52	19.53	19.65	19.29	19.65	19.71	19.58	21.35	21.38
FeO	24.17	27.88	27.82	26.48	25.40	24.97	25.30	25.00	26.69	27.96	28.05	23.82	23.62
MnO	8.69	10.31	9.68	10.90	11.75	11.89	11.40	11.12	11.00	10.16	10.14	8.92	9.42
MgO	1.38	1.78	2.23	1.88	1.82	1.67	1.74	1.75	1.89	2.01	1.81	2.25	2.12
CaO	8.34	1.80	2.28	2.99	3.09	3.24	3.38	3.24	2.87	2.45	1.84	6.28	6.16
Total	99.88	98.21	98.73	98.86	98.16	98.50	98.49	96.88	99.30	99.22	98.37	99.37	99.50
Si	2.99	3.03	3.02	3.03	3.02	3.04	3.04	3.03	3.03	3.02	3.04	2.96	2.95
Al	1.91	1.94	1.93	1.91	1.91	1.90	1.91	1.91	1.90	1.91	1.91	2.03	2.03
Fe	1.64	1.93	1.91	1.82	1.76	1.72	1.74	1.75	1.83	1.92	1.94	1.61	1.59
Mn	0.60	0.72	0.67	0.76	0.83	0.83	0.80	0.79	0.76	0.71	0.71	0.61	0.64
Mg	0.17	0.22	0.27	0.23	0.22	0.21	0.21	0.22	0.23	0.25	0.22	0.27	0.25
Ca	0.72	0.16	0.20	0.26	0.27	0.29	0.30	0.29	0.25	0.22	0.16	0.54	0.53
Xalm	50.25	62.69	61.39	57.58	55.35	54.84	55.43	55.76	57.73	60.63	62.54	51.90	51.50
Xgrs	19.88	3.72	4.16	5.81	5.72	7.04	7.69	7.32	5.08	3.63	3.33	17.94	17.46
Xprp	5.58	7.43	9.19	7.80	7.58	7.02	7.28	7.44	7.82	8.29	7.63	9.13	8.62
Xsps	19.95	24.47	22.67	25.70	27.82	28.37	27.11	26.89	25.90	23.81	24.25	20.61	21.83
Sample	120-B-7	120-B-8	120-B-10	120-B-2	120-B-4	120-B-6	120-B-8	120-B-10	120-B-12	120-B-14	120-B-16	123B-A-1	123B-A-8
Section	Grt2-Core	Grt2-Core	Grt2-Core	Grt2-Rim	Grt2-Core	Grt2-Core	Grt2-Core	Grt2-Core	Grt2-Rim	Grt2-Rim	Grt2-Rim	Grt2-Rim	Grt2-Core
SiO ₂	36.30	36.10	36.32	36.73	36.48	36.23	35.72	35.56	35.91	36.72	37.49	38.17	38.12
Al ₂ O ₃	21.15	21.15	20.22	20.76	19.54	19.89	19.57	19.47	19.85	20.64	20.18	20.48	20.24
FeO	21.98	21.67	19.82	38.47	35.68	34.97	36.62	36.50	37.35	38.06	25.24	24.72	23.81
MnO	10.18	10.82	11.47	1.63	2.05	2.94	3.27	2.75	1.84	1.34	9.69	7.76	8.52
MgO	1.79	1.67	1.24	1.88	1.41	1.06	0.96	1.19	1.44	2.04	1.75	1.72	1.56
CaO	7.63	7.01	8.79	1.12	3.08	4.14	2.48	2.34	1.64	0.66	5.04	7.03	7.87
Total	99.28	98.85	98.04	100.77	98.61	99.60	99.00	98.02	98.21	99.59	99.76	99.89	100.44
Si	2.94	2.94	2.98	2.98	3.02	2.98	2.98	2.99	3.00	3.00	3.00	3.03	3.04
Al	2.02	2.03	1.96	1.99	1.91	1.93	1.92	1.93	1.95	1.99	1.92	1.93	1.91
Fe	1.49	1.47	1.36	2.61	2.47	2.41	2.55	2.57	2.61	2.60	1.71	1.66	1.59
Mn	0.70	0.75	0.80	0.11	0.14	0.21	0.23	0.20	0.13	0.09	0.66	0.53	0.58
Mg	0.22	0.20	0.15	0.23	0.17	0.13	0.12	0.15	0.18	0.25	0.21	0.20	0.19
Ca	0.66	0.61	0.77	0.10	0.27	0.37	0.22	0.21	0.15	0.06	0.44	0.60	0.67
Xalm	46.37	46.93	42.24	85.37	79.99	76.50	80.79	81.43	84.78	86.65	55.35	54.25	50.78
Xgrs	20.79	19.90	23.24	1.52	6.07	8.02	2.92	2.90	2.43	1.63	13.09	20.09	21.09
Xprp	7.36	6.89	5.11	7.62	5.91	4.37	4.02	4.98	5.98	8.32	7.19	7.03	6.37
Xsps	23.75	25.39	26.74	3.75	4.86	6.88	7.74	6.54	4.34	3.10	22.59	18.04	19.75
Sample	123B-A-12	125A-1	125A-4	125A-8	125A-11	125A-14	125A-17						
Section	Grt2-Core	Grt2-Rim	Grt2-Rim	Grt2-Rim	Grt2-Core	Grt2-Core	Grt2-Core						
SiO ₂	38.01	36.61	37.24	37.43	36.64	36.41	37.02						
Al ₂ O ₃	20.01	19.29	19.57	19.50	19.16	19.98	19.50						
FeO	24.61	27.87	27.45	27.65	21.71	23.17	25.81						
MnO	7.70	4.86	5.20	5.16	11.38	8.89	6.09						
MgO	1.80	1.36	0.91	0.91	0.48	0.53	1.55						
CaO	7.54	7.53	8.68	8.61	8.28	8.73	7.96						
Total	100.00	98.08	99.58	99.62	97.97	97.97	98.08						
Si	3.05	3.02	3.03	3.04	3.04	3.00	3.04						
Al	1.89	1.88	1.87	1.87	1.87	1.94	1.89						
Fe	1.65	1.92	1.87	1.88	1.50	1.60	1.77						
Mn	0.52	0.34	0.36	0.35	0.80	0.62	0.42						
Mg	0.22	0.17	0.11	0.11	0.06	0.07	0.19						
Ca	0.65	0.67	0.76	0.75	0.74	0.77	0.70						
Xalm	52.51	60.22	58.44	58.64	45.90	51.27	55.32						
Xgrs	19.41	17.99	21.12	20.89	20.32	23.15	20.13						
Xprp	7.38	5.68	3.74	3.76	1.99	2.18	6.45						
Xsps	17.92	11.53	12.16	12.08	27.13	20.75	14.41						

Anexo IV: Resultados de EPMA representativos de sulfetos nos depósitos de ouro selecionados

Depósito: Corrego do Sítio (Carvoaria Velha e Laranjeira)																	
Amostra	Mineral	As	Se	S	Pb	Bi	Cd	Te	Fe	Co	Cu	Ni	Mo	Au	Ag	Sb	Total
WF507	Apy	44.37	0.00	20.14	0.06	0.00	0.00	0.00	34.38	0.06	0.00	0.00	0.07	0.00	0.00	0.22	99.32
WF507	Apy	43.40	0.00	20.62	0.11	0.00	0.04	0.02	35.24	0.05	0.00	0.02	0.02	0.05	0.03	0.01	99.63
WF507	Apy	43.78	0.00	20.47	0.04	0.05	0.04	0.00	34.69	0.13	0.01	0.08	0.07	0.00	0.00	0.14	99.49
WF507	Apy	45.07	0.00	19.59	0.14	0.00	0.02	0.00	34.47	0.22	0.01	0.24	0.01	0.03	0.02	0.03	99.86
WF507	Apy	43.95	0.00	21.13	0.08	0.04	0.00	0.00	34.83	0.02	0.00	0.01	0.10	0.04	0.00	0.15	100.38
WF507	Apy	31.39	0.00	14.91	0.00	0.00	0.02	0.00	24.63	0.03	0.00	0.12	0.00	0.03	0.01	1.34	72.50
WF507	Apy	44.34	0.00	20.10	0.12	0.00	0.00	0.00	33.19	0.50	0.00	0.37	0.09	0.03	0.01	0.10	98.85
WF507	Apy	43.63	0.00	20.51	0.05	0.00	0.00	0.05	34.95	0.05	0.00	0.25	0.00	0.03	0.00	0.03	99.57
WF507	Apy	43.36	0.00	20.96	0.03	0.00	0.01	0.01	35.69	0.00	0.00	0.00	0.00	0.00	0.00	0.00	100.06
WF507	Apy	45.06	0.00	20.94	0.03	0.00	0.01	0.02	35.38	0.09	0.03	0.01	0.01	0.00	0.00	0.17	101.78
WF507	Ber	0.00	0.08	28.48	1.21	0.06	0.02	0.00	12.48	0.02	0.04	0.00	0.02	0.00	0.00	53.83	96.23
WF507	Ber	0.03	0.10	29.02	1.24	0.00	0.06	0.00	12.49	0.02	0.03	0.00	0.00	0.00	0.01	56.03	99.03
WF507	Ber	0.00	0.08	29.01	1.11	0.10	0.00	0.00	12.21	0.00	0.02	0.00	0.08	0.03	0.01	57.25	99.89
WF507	Ber	0.04	0.08	28.88	0.81	0.00	0.02	0.00	12.56	0.01	0.00	0.00	0.03	0.00	0.01	58.35	100.79
WF507	Pjs	0.00	0.18	20.58	36.30	0.00	0.15	0.00	2.65	0.00	0.00	0.01	0.54	0.02	0.00	36.05	96.48
WF507	Pjs	0.00	0.21	20.72	37.68	0.00	0.04	0.11	2.52	0.00	0.00	0.04	0.50	0.01	0.00	37.37	99.20
WF507	Po	0.00	0.02	36.65	0.25	0.00	0.00	0.00	57.93	0.11	0.02	0.00	0.06	0.00	0.01	0.00	95.08
WF507	Ull	0.00	0.12	14.39	0.09	0.01	0.00	0.08	0.42	1.66	0.00	25.93	0.00	0.00	0.00	57.14	99.86
WF507	SbFeNiS	0.01	0.04	3.72	0.04	0.00	0.01	0.00	27.29	0.51	0.00	6.08	0.03	0.00	0.00	17.05	54.86
WF507	Ull	0.16	0.14	14.02	0.06	0.01	0.02	0.15	3.07	1.77	0.00	25.11	0.01	0.00	0.04	53.76	98.33
WF507	Po	0.00	0.00	39.51	0.13	0.13	0.00	0.02	58.25	0.17	0.00	0.11	0.14	0.02	0.01	0.16	98.64
WF507	Po	0.00	0.10	38.57	0.17	0.08	0.00	0.00	58.20	0.13	0.00	0.03	0.05	0.00	0.00	0.00	97.35
WF507	SbNiFeS	0.00	0.19	10.78	0.14	0.00	0.00	0.04	9.64	2.84	0.00	19.12	0.00	0.00	0.02	43.99	86.76
WF507	Po	0.00	0.06	36.57	0.14	0.00	0.02	0.02	58.17	0.19	0.00	0.19	0.08	0.00	0.00	0.40	95.83
WF507	Ull	0.00	0.12	14.34	0.00	0.00	0.06	0.05	1.49	2.11	0.00	25.41	0.05	0.00	0.00	57.30	101.00
WF507	Ull	0.04	0.22	14.61	0.04	0.12	0.00	0.08	2.43	2.13	0.00	24.31	0.04	0.00	0.00	52.72	96.88
WF507	Po	0.00	0.02	38.83	0.05	0.00	0.03	0.00	57.80	0.15	0.01	0.00	0.12	0.00	0.02	0.00	97.06
WF507	Po	0.00	0.07	36.23	0.14	0.03	0.01	0.00	57.97	0.17	0.00	0.03	0.09	0.00	0.00	0.04	94.86
WF507	Po	0.00	0.08	38.20	0.17	0.00	0.00	0.01	57.14	0.13	0.00	0.00	0.03	0.00	0.00	0.02	95.88
WF507	Po	0.00	0.05	38.51	0.18	0.00	0.02	0.00	58.56	0.16	0.00	0.00	0.07	0.01	0.00	0.00	97.58
WF507	Po	0.00	0.03	34.21	0.12	0.02	0.00	0.00	56.98	0.17	0.00	0.01	0.05	0.03	0.00	0.00	91.60
WF507	Po	0.00	0.09	38.61	0.08	0.00	0.07	0.00	57.85	0.13	0.00	0.00	0.05	0.00	0.01	0.01	96.89

WF507	Po	0.00	0.01	38.93	0.24	0.00	0.02	0.02	58.85	0.11	0.05	0.00	0.08	0.00	0.02	0.03	98.39
WF507	Po	0.00	0.00	38.42	0.21	0.00	0.02	0.03	58.03	0.13	0.02	0.01	0.03	0.00	0.01	0.00	96.99
WF514	Po	0.00	0.04	38.69	0.14	0.00	0.02	0.01	58.55	0.10	0.01	0.02	0.09	0.00	0.00	0.02	97.67
WF504	Po	0.00	0.01	37.99	0.15	0.00	0.03	0.00	58.11	0.11	0.02	0.00	0.11	0.00	0.00	0.03	96.55
WF504	Po	0.00	0.05	38.34	0.17	0.00	0.00	0.00	58.05	0.13	0.00	0.02	0.05	0.00	0.02	0.00	96.82
WF504	Ber	0.04	0.07	29.00	1.19	0.03	0.02	0.00	12.36	0.05	0.05	0.00	0.15	0.00	0.00	56.40	99.35
WF504	Ber	0.05	0.03	28.98	1.46	0.00	0.02	0.00	12.49	0.04	0.01	0.01	0.05	0.00	0.02	56.01	99.16
WF504	Ber	0.00	0.07	28.56	1.12	0.00	0.01	0.00	12.10	0.01	0.00	0.00	0.06	0.00	0.02	56.21	98.15
WF504	Sb	0.03	0.08	0.00	0.00	0.07	0.00	0.00	0.01	0.00	0.00	0.03	0.00	0.00	0.00	98.63	98.89
WF504	Sb	0.02	0.07	0.03	0.08	0.04	0.02	0.00	0.02	0.00	0.01	0.02	0.06	0.00	0.00	99.61	100.01
WF504	Po	0.00	0.07	38.82	0.16	0.06	0.06	0.01	58.63	0.10	0.04	0.00	0.07	0.00	0.00	0.03	98.03
WF504	Ber	0.00	0.08	29.09	1.19	0.00	0.04	0.00	12.24	0.06	0.01	0.02	0.08	0.00	0.00	55.84	98.65
WF504	Ber	0.02	0.05	28.60	1.05	0.01	0.06	0.00	12.46	0.02	0.00	0.00	0.05	0.00	0.00	55.66	97.98
WF504	Ber	0.00	0.00	29.12	1.40	0.00	0.05	0.00	12.10	0.05	0.01	0.01	0.09	0.00	0.01	55.42	98.32
WF504	Ber	0.00	0.00	28.67	1.23	0.00	0.07	0.00	12.37	0.01	0.01	0.04	0.10	0.00	0.00	56.17	98.74
WF504	Py	0.42	0.01	51.08	0.28	0.00	0.00	0.03	46.18	0.07	0.04	0.00	0.16	0.00	0.00	0.00	98.30
WF504	Ber	0.00	0.06	28.63	1.20	0.00	0.00	0.00	12.26	0.02	0.00	0.00	0.07	0.00	0.00	56.03	98.35
WF504	Ber	0.00	0.01	28.87	1.32	0.00	0.00	0.00	12.45	0.03	0.00	0.02	0.06	0.00	0.04	55.99	98.85
WF504	Ber	0.02	0.12	28.80	1.15	0.00	0.04	0.00	12.37	0.04	0.00	0.03	0.06	0.00	0.00	56.01	98.64
WF504	Po	0.00	0.05	38.31	0.01	0.00	0.01	0.00	58.11	0.12	0.00	0.00	0.09	0.00	0.03	0.01	96.74
WF504	Po	0.00	0.05	39.18	0.23	0.00	0.02	0.03	56.81	0.13	0.04	0.00	0.14	0.00	0.01	0.00	96.70
WF504	Po	0.00	0.04	38.06	0.13	0.08	0.03	0.00	58.33	0.15	0.00	0.00	0.13	0.00	0.00	0.00	96.97
WF504	Po	0.00	0.06	39.29	0.09	0.00	0.02	0.00	58.29	0.15	0.00	0.02	0.05	0.00	0.00	0.01	97.98
WF504	Ull	0.00	0.13	14.28	0.02	0.11	0.01	0.07	1.77	0.10	0.00	26.75	0.00	0.00	0.02	55.88	99.15
WF504	Ull	0.00	0.26	15.02	0.09	0.00	0.00	0.02	2.22	2.36	0.00	24.28	0.00	0.00	0.05	55.20	99.54

Depósito: Crixás

Amostra	Mineral	As	Se	S	Pb	Bi	Cd	Te	Fe	Co	Cu	Ni	Mo	Au	Ag	Sb	Total
WF202B	Apy	47.09	0.00	16.10	0.04	0.00	0.00	0.00	33.93	0.12	0.00	0.09	0.08	0.00	0.00	97.49	
WF202B	Apy	44.74	0.00	17.47	0.01	0.06	0.03	0.07	34.60	0.07	0.00	0.03	0.07	0.01	0.02	97.19	
WF202B	Apy	44.28	0.00	17.83	0.04	0.00	0.00	0.05	34.78	0.08	0.05	0.08	0.08	0.00	0.02	97.30	
WF202B	Apy	42.90	0.00	18.73	0.15	0.00	0.03	0.07	34.38	0.10	0.00	0.09	0.08	0.00	0.01	96.63	
WF202B	Apy	42.73	0.00	18.63	0.04	0.00	0.00	0.03	34.60	0.10	0.00	0.08	0.08	0.02	0.01	96.36	
WF202B	Apy	42.94	0.00	18.68	0.06	0.00	0.00	0.00	35.04	0.06	0.00	0.12	0.09	0.00	0.00	97.06	
WF202B	Apy	43.85	0.00	17.76	0.10	0.00	0.01	0.04	34.33	0.04	0.01	0.05	0.08	0.05	0.00	96.32	
WF202B	Apy	45.06	0.00	17.54	0.15	0.01	0.03	0.01	34.62	0.09	0.00	0.05	0.07	0.00	0.00	97.68	
WF202B	Apy	45.14	0.00	17.55	0.01	0.00	0.01	0.00	34.67	0.09	0.00	0.06	0.00	0.06	0.00	97.69	
WF202B	Apy	44.65	0.00	18.25	0.12	0.00	0.00	0.05	34.90	0.09	0.00	0.04	0.04	0.00	0.00	98.19	
WF202B	Apy	43.82	0.00	17.99	0.10	0.00	0.03	0.04	34.95	0.10	0.00	0.07	0.04	0.00	0.00	97.14	

WF202B	Apy	43.66	0.00	18.25	0.09	0.07	0.00	0.00	34.99	0.11	0.06	0.05	0.00	0.00	0.00	97.28
WF202B	Apy	44.26	0.00	17.38	0.06	0.00	0.01	0.02	34.11	0.03	0.00	0.03	0.05	0.00	0.01	95.95
WF202B	Apy	47.06	0.00	15.93	0.21	0.00	0.00	0.03	33.70	0.12	0.00	0.03	0.06	0.00	0.00	97.14
WF202B	Apy	47.08	0.00	16.16	0.04	0.03	0.00	0.00	34.01	0.16	0.03	0.09	0.01	0.00	0.02	97.62
WF206	Apy	44.34	0.00	18.72	0.21	0.00	0.00	0.03	34.85	0.13	0.00	0.03	0.04	0.06	0.00	98.47
WF206	Apy	44.84	0.00	17.93	0.07	0.00	0.01	0.00	34.15	0.09	0.05	0.08	0.04	0.00	0.00	97.26
WF206	Apy	44.20	0.00	18.42	0.15	0.00	0.00	0.00	34.83	0.12	0.01	0.07	0.08	0.00	0.00	97.94
WF206	Apy	43.81	0.00	18.46	0.09	0.03	0.00	0.03	34.89	0.06	0.00	0.05	0.03	0.01	0.00	97.47
WF206	Apy	44.17	0.00	18.78	0.04	0.00	0.06	0.06	34.87	0.09	0.00	0.10	0.05	0.03	0.03	98.30
WF206	Apy	44.06	0.00	18.73	0.04	0.00	0.00	0.01	35.15	0.07	0.00	0.09	0.00	0.00	0.00	98.22
WF206	Apy	44.71	0.00	18.52	0.10	0.00	0.02	0.02	34.70	0.09	0.02	0.07	0.04	0.02	0.00	98.38
WF206	Apy	43.69	0.00	18.80	0.18	0.00	0.02	0.00	34.53	0.08	0.19	0.09	0.02	0.00	0.00	97.60
WF207	Apy	45.42	0.00	19.27	0.13	0.05	0.01	0.05	34.67	0.05	0.03	0.10	0.11	0.00	0.00	99.94
WF207	Apy	46.11	0.00	19.66	0.06	0.00	0.00	0.02	36.27	0.04	0.02	0.07	0.09	0.00	0.00	102.34
WF207	Apy	46.23	0.00	19.29	0.08	0.12	0.00	0.00	35.97	0.06	0.00	0.03	0.13	0.00	0.00	101.93
WF207	Apy	48.08	0.00	17.02	0.05	0.03	0.02	0.00	33.58	0.05	0.00	0.16	0.00	0.00	0.03	99.06
WF207	Apy	45.41	0.00	18.73	0.00	0.00	0.01	0.01	35.13	0.06	0.01	0.08	0.00	0.00	0.00	99.43
WF207	Apy	46.18	0.00	18.09	0.00	0.04	0.00	0.02	34.65	0.09	0.01	0.09	0.03	0.01	0.00	99.26
WF207	Apy	46.05	0.00	18.82	0.06	0.00	0.00	0.06	35.15	0.08	0.01	0.10	0.04	0.01	0.01	100.41
WF207	Apy	46.26	0.00	19.07	0.04	0.00	0.00	0.00	35.64	0.06	0.00	0.08	0.09	0.01	0.00	101.28
WF209	Apy	44.80	0.00	19.49	0.04	0.09	0.04	0.01	35.77	0.05	0.00	0.10	0.00	0.00	0.00	100.38
WF209	Apy	45.23	0.00	18.94	0.18	0.03	0.00	0.00	35.51	0.06	0.00	0.07	0.02	0.00	0.02	100.06
WF209	Apy	42.55	0.00	18.20	0.00	0.00	0.02	0.02	33.85	0.04	0.00	0.11	0.06	0.00	0.01	94.87
WF209	Apy	49.03	0.00	17.34	0.01	0.00	0.03	0.00	34.70	0.09	0.00	0.16	0.01	0.05	0.00	101.50
WF209	Apy	49.36	0.00	17.13	0.00	0.00	0.00	0.00	34.86	0.00	0.00	0.08	0.06	0.03	0.00	101.54
WF209	Apy	45.96	0.00	18.91	0.12	0.00	0.05	0.00	35.43	0.06	0.00	0.06	0.03	0.00	0.01	100.63
WF210	Apy	45.08	0.00	18.75	0.14	0.00	0.04	0.03	34.73	0.08	0.01	0.08	0.06	0.07	0.00	99.11
WF210	Apy	45.56	0.00	17.76	0.04	0.00	0.00	0.03	34.79	0.04	0.00	0.03	0.02	0.06	0.00	98.34
WF210	Apy	44.97	0.00	19.36	0.17	0.03	0.00	0.00	35.28	0.05	0.01	0.08	0.05	0.00	0.00	100.03
WF210	Apy	44.13	0.00	19.31	0.04	0.00	0.00	0.04	35.61	0.07	0.00	0.11	0.04	0.00	0.03	99.41
WF210	Apy	47.63	0.00	16.20	0.11	0.00	0.03	0.00	33.79	0.09	0.02	0.28	0.04	0.00	0.00	98.21
WF210	Apy	48.29	0.00	17.26	0.17	0.06	0.04	0.00	34.05	0.06	0.00	0.54	0.10	0.02	0.00	100.63
WF210	Apy	48.44	0.00	16.81	0.26	0.00	0.01	0.00	33.89	0.08	0.00	0.36	0.00	0.07	0.01	99.93
WF210	Apy	48.25	0.00	16.89	0.09	0.05	0.00	0.00	34.42	0.03	0.00	0.42	0.00	0.00	0.00	100.16
WF210	Py	0.06	0.02	31.80	0.24	0.00	0.03	0.00	52.78	0.06	0.00	0.51	0.08	0.00	0.00	85.64
WF210	Zn (?)	0.00	0.04	29.37	0.11	0.00	2.53	0.00	9.87	0.01	0.00	0.02	0.12	0.00	0.00	94.09
WF210	Po	0.00	0.00	35.11	0.21	0.00	0.00	0.00	57.49	0.05	0.00	0.61	0.10	0.00	0.00	93.61
WF210	Ccp	0.00	0.00	31.45	0.19	0.00	0.00	0.00	29.64	0.03	32.31	0.00	0.11	0.00	0.00	93.82
WF210	Po	0.09	0.01	36.03	0.13	0.04	0.00	0.00	57.91	0.04	0.00	0.26	0.11	0.00	0.00	94.61

WF210	Po	0.00	0.03	34.81	0.24	0.00	0.00	0.00	57.84	0.04	0.00	0.37	0.12	0.00	0.00	93.45
WF210	Po	0.00	0.01	36.49	0.19	0.00	0.03	0.00	57.62	0.04	0.00	0.43	0.08	0.00	0.01	94.89
WF210	Po	0.01	0.00	34.57	0.26	0.00	0.03	0.02	57.66	0.09	0.00	0.36	0.13	0.05	0.00	93.22

Depósito: Fazenda Nova

Amostra	Analise	Mineral	As	Se	S	Pb	Bi	Cd	Te	Fe	Co	Cu	Ni	Mo	Au	Ag	Sb	Total
WF301		Apy	42.29	0.00	22.79	0.00	0.01	0.03	0.00	35.53	0.05	0.00	0.01	0.07	0.00	0.00	0.05	100.83
WF301		Apy	41.37	0.00	18.11	0.13	0.00	0.00	0.02	33.60	0.01	0.00	0.02	0.06	0.61	0.02		94.00
WF301		Apy	43.46	0.00	18.19	0.14	0.00	0.01	0.00	34.66	0.04	0.02	0.01	0.03	0.25	0.02		96.83
WF301		Apy	43.16	0.00	22.55	0.10	0.00	0.05	0.00	35.22	0.02	0.01	0.02	0.08	0.04	0.02	0.02	101.28
WF301		Apy	43.78	0.00	21.59	0.08	0.00	0.00	0.02	34.81	0.00	0.00	0.00	0.06	0.08	0.01	0.04	100.49
WF301		Apy	43.59	0.00	19.06	0.22	0.00	0.01	0.00	35.72	0.04	0.00	0.00	0.00	0.07	0.00		98.77
WF301		Apy	42.78	0.00	17.74	0.00	0.00	0.01	0.00	34.22	0.04	0.00	0.00	0.05	0.00	0.00		94.84
WF301		Apy	43.93	0.00	21.53	0.08	0.00	0.00	0.00	35.01	0.02	0.05	0.01	0.07	0.02	0.02	0.05	100.79
WF301		Apy	42.35	0.00	19.16	0.18	0.05	0.02	0.00	35.30	0.06	0.00	0.02	0.01	0.08	0.00		97.33
WF301		Apy	47.39	0.00	19.69	0.04	0.00	0.00	0.00	34.33	0.01	0.01	0.00	0.00	0.03	0.00	0.08	101.57
WF301		Apy	42.43	0.00	19.24	0.05	0.00	0.00	0.00	35.10	0.02	0.00	0.00	0.06	0.00	0.00		96.92
WF301		Apy	45.37	0.00	17.31	0.10	0.11	0.01	0.02	34.32	0.04	0.00	0.03	0.02	0.04	0.00		97.38
WF301		Apy	43.42	0.00	22.06	0.06	0.06	0.00	0.06	35.31	0.04	0.00	0.01	0.06	0.00	0.00	0.14	101.21
WF301		Apy	48.20	0.00	19.49	0.17	0.00	0.00	0.01	34.61	0.02	0.02	0.01	0.00	0.03	0.02	0.00	102.61
WF301		Apy	42.91	0.00	22.60	0.01	0.00	0.03	0.00	35.16	0.04	0.00	0.00	0.01	0.12	0.00	0.02	100.92
WF301		Apy	45.03	0.00	21.29	0.09	0.09	0.00	0.00	35.09	0.07	0.00	0.00	0.00	0.00	0.00	0.00	101.65
WF301		Apy	42.80	0.00	19.40	0.05	0.00	0.00	0.03	35.33	0.04	0.00	0.00	0.08	0.01	0.02		97.79
WF301		Apy	42.45	0.00	19.74	0.05	0.02	0.02	0.00	35.49	0.02	0.03	0.03	0.04	0.04	0.00		97.93
WF301		Apy	44.22	0.00	18.97	0.21	0.04	0.01	0.03	36.45	0.08	0.06	0.02	0.04	0.02	0.00		100.16
WF301		Apy	43.74	0.00	18.69	0.18	0.03	0.02	0.00	35.78	0.02	0.00	0.00	0.09	0.08	0.00		98.72
WF301		Apy	43.89	0.00	19.01	0.21	0.02	0.01	0.00	35.72	0.02	0.00	0.00	0.11	0.00	0.00		99.04
WF301		Apy	42.81	0.00	19.59	0.17	0.07	0.00	0.02	35.53	0.03	0.02	0.02	0.07	0.04	0.00		98.36
WF301		Apy	28.70	0.00	17.96	0.18	0.00	0.00	0.00	32.20	0.01	0.00	0.00	0.00	0.00	0.00		79.06
WF301		Apy	43.06	0.00	19.76	0.01	0.04	0.00	0.00	36.05	0.03	0.01	0.00	0.04	0.08	0.00		99.08
WF301		Apy	43.83	0.00	19.26	0.20	0.08	0.00	0.00	35.60	0.04	0.02	0.00	0.02	0.09	0.00		99.19
WF301		Apy	42.85	0.00	19.73	0.13	0.07	0.00	0.00	36.44	0.03	0.00	0.02	0.02	0.04	0.00		99.32
WF301		Apy	42.76	0.00	19.24	0.13	0.00	0.00	0.00	36.20	0.08	0.00	0.03	0.06	0.00	0.00		98.52
WF301		Apy	43.62	0.00	18.86	0.00	0.01	0.00	0.00	35.25	0.09	0.00	0.00	0.06	0.01	0.01		97.90
WF301		Apy	44.64	0.00	18.67	0.10	0.00	0.03	0.00	35.10	0.04	0.00	0.00	0.00	0.00	0.00		98.61
WF301		Apy	43.46	0.00	22.14	0.21	0.00	0.00	0.00	36.00	0.02	0.00	0.02	0.07	0.05	0.00	0.04	102.00
WF301		Apy	43.68	0.00	21.88	0.03	0.00	0.00	0.02	35.22	0.03	0.00	0.01	0.02	0.00	0.00	0.00	100.94
WF301		Apy	44.66	0.00	21.61	0.02	0.10	0.00	0.00	35.40	0.03	0.01	0.01	0.00	0.00	0.03	0.00	101.88
WF301		Apy	43.14	0.00	22.45	0.11	0.00	0.06	0.05	35.51	0.07	0.02	0.03	0.13	0.00	0.02		101.60

WF301	Apy	44.26	0.00	21.52	0.06	0.00	0.02	0.02	35.52	0.04	0.02	0.00	0.08	0.00	0.00	0.00	101.58
WF301	Apy	44.57	0.00	18.37	0.13	0.09	0.00	0.04	32.17	0.23	0.02	0.02	0.00	0.00	0.02	1.20	96.92
WF301	Apy	43.82	0.00	21.98	0.07	0.00	0.01	0.00	35.86	0.11	0.01	0.02	0.00	0.00	0.00	0.00	101.91
WF301	Apy	44.26	0.00	21.31	0.11	0.00	0.03	0.00	35.23	0.07	0.05	0.01	0.01	0.05	0.01	0.00	101.18
WF301	Apy	44.73	0.00	20.81	0.07	0.05	0.00	0.02	35.25	0.03	0.00	0.02	0.00	0.00	0.01	0.01	100.99
WF301	Apy	42.07	0.00	22.51	0.17	0.00	0.00	0.00	35.33	0.04	0.03	0.00	0.00	0.00	0.00	0.00	100.15
WF301	Apy	34.63	0.00	15.29	0.00	0.03	0.01	0.00	27.04	0.16	0.00	0.02	0.00	0.00	0.00	0.35	77.53
WF301	Apy	44.97	0.00	20.57	0.09	0.00	0.01	0.03	34.72	0.05	0.00	0.05	0.00	0.02	0.00	0.24	100.76
WF301	Apy	40.32	0.00	21.92	0.02	0.00	0.00	0.00	34.08	0.07	0.03	0.01	0.01	0.00	0.01	0.21	96.68
WF301	Apy	43.83	0.00	19.74	0.01	0.04	0.00	0.00	33.43	0.45	0.04	0.03	0.02	0.03	0.01	0.09	97.73
WF302	Apy	43.86	0.00	17.96	0.17	0.00	0.01	0.00	35.15	0.02	0.00	0.00	0.09	0.00	0.00	0.00	97.40
WF302	Apy	43.67	0.00	18.53	0.30	0.00	0.02	0.00	35.57	0.03	0.00	0.01	0.04	0.00	0.00	0.00	98.23
WF302	Apy	43.91	0.00	18.01	0.05	0.00	0.02	0.02	34.69	0.01	0.00	0.00	0.09	0.02	0.00	0.00	96.81
WF302	Apy	44.59	0.00	17.72	0.00	0.00	0.05	0.00	34.41	0.01	0.00	0.04	0.02	0.00	0.00	0.00	96.86
WF302	Apy	42.31	0.00	18.71	0.22	0.00	0.04	0.00	34.60	0.02	0.00	0.00	0.05	0.00	0.01	0.00	95.98
WF302	Apy	41.18	0.00	18.91	0.04	0.00	0.05	0.00	35.02	0.02	0.00	0.03	0.03	0.00	0.00	0.00	95.28

Depósito: Pilar de Goiás

Amostra	Mineral	As	Se	S	Pb	Bi	Cd	Te	Fe	Co	Cu	Ni	Mo	Au	Ag	Sb	Total
RTB 010	Po	0.00	0.04	38.66	0.12	0.00	0.04	0.00	58.92	0.16	0.00	0.32	0.13	0.00	0.01	0.00	98.40
RTB 010	Po	0.00	0.08	38.77	0.01	0.00	0.02	0.00	58.93	0.15	0.00	0.28	0.14	0.04	0.02	0.00	98.43
RTB 010	Po	0.00	0.06	38.60	0.10	0.00	0.02	0.01	58.76	0.15	0.00	0.30	0.12	0.00	0.02	0.00	98.14
RTB 010	Po	0.00	0.01	38.88	0.22	0.00	0.00	0.00	58.23	0.15	0.00	0.18	0.05	0.00	0.01	0.00	97.76
RTB 010	Po	0.00	0.03	38.46	0.13	0.00	0.02	0.02	57.64	0.11	0.03	0.30	0.19	0.00	0.00	0.00	96.97
RTB 010	Po	0.00	0.00	39.09	0.08	0.00	0.00	0.00	58.04	0.11	0.32	0.30	0.14	0.00	0.01	0.02	98.11
RTB 010	Apy	45.98	0.00	18.98	0.08	0.00	0.01	0.01	31.48	2.80	0.00	1.01	0.00	0.03	0.00	0.00	100.45
RTB 010	Apy	47.37	0.00	18.34	0.05	0.00	0.02	0.00	32.81	1.93	0.00	0.33	0.05	0.00	0.02	0.00	100.92
RTB 010	Apy	47.64	0.00	18.25	0.00	0.00	0.00	0.01	32.17	2.19	0.00	0.47	0.02	0.00	0.00	0.00	100.82
WF701B	Apy	44.39	0.00	19.72	0.11	0.00	0.00	0.03	34.64	0.00	0.00	0.10	0.02	0.00	0.00	0.06	99.09
WF701B	Apy	44.20	0.00	19.69	0.07	0.00	0.06	0.01	34.60	0.12	0.00	0.16	0.03	0.00	0.00	0.11	99.07
WF701B	Apy	46.97	0.00	18.35	0.00	0.01	0.00	0.01	33.04	0.35	0.00	0.27	0.12	0.00	0.01	0.04	99.18
WF701B	Apy	45.01	0.00	19.51	0.01	0.02	0.02	0.02	34.33	0.07	0.03	0.13	0.04	0.00	0.02	0.00	99.27
WF701B	Apy	45.18	0.00	19.63	0.13	0.00	0.00	0.00	34.32	0.17	0.00	0.18	0.06	0.00	0.00	0.00	99.65
WF701B	Apy	44.90	0.00	19.82	0.13	0.10	0.04	0.00	34.49	0.11	0.02	0.17	0.00	0.06	0.00	0.01	99.85
WF701B	Apy	44.43	0.00	19.79	0.14	0.00	0.00	0.00	34.75	0.16	0.00	0.11	0.00	0.00	0.02	0.16	99.56
WF701B	Apy	44.92	0.00	19.99	0.20	0.03	0.00	0.00	34.76	0.12	0.00	0.15	0.06	0.00	0.00	0.00	100.25
WF701B	Apy	40.14	0.00	19.07	0.00	0.00	0.00	0.00	31.68	0.15	0.00	0.14	0.00	0.00	0.00	0.00	91.18
WF701B	Apy	45.31	0.00	19.42	0.04	0.04	0.00	0.06	34.22	0.06	0.00	0.14	0.00	0.03	0.00	0.00	99.32

WF701B	Apy	45.19	0.00	19.79	0.00	0.00	0.00	0.01	34.66	0.19	0.00	0.15	0.01	0.00	0.00	0.00	100.00
WF701B	Apy	45.97	0.00	18.85	0.03	0.00	0.00	0.02	34.09	0.06	0.06	0.14	0.01	0.00	0.02	0.02	99.32
WF701B	Apy	45.64	0.00	17.99	0.09	0.00	0.04	0.04	33.34	0.36	0.01	0.30	0.07	0.00	0.00	0.03	97.92
WF701B	Apy	44.97	0.00	19.05	0.11	0.00	0.00	0.00	34.02	0.16	0.03	0.10	0.03	0.00	0.00	0.07	98.55
WF701B	Apy	43.72	0.00	18.87	0.03	0.00	0.02	0.00	33.72	0.22	0.00	0.15	0.00	0.06	0.02	0.00	96.81
WF701B	Apy	45.29	0.00	19.33	0.00	0.00	0.01	0.00	34.05	0.17	0.00	0.11	0.01	0.00	0.00	0.02	98.99
WF701B	Apy	44.76	0.00	19.79	0.02	0.05	0.00	0.00	34.40	0.18	0.00	0.17	0.01	0.00	0.00	0.06	99.46
WF701B	Apy	44.68	0.00	19.48	0.15	0.10	0.00	0.00	34.19	0.12	0.05	0.12	0.01	0.00	0.00	0.05	98.94
WF701B	Apy	44.62	0.00	20.10	0.00	0.01	0.00	0.00	34.55	0.16	0.00	0.13	0.00	0.00	0.00	0.15	99.71
WF703	Apy	47.40	0.00	18.49	0.02	0.00	0.03	0.03	33.24	0.28	0.00	0.21	0.06	0.00	0.00	0.00	99.76
WF703	Apy	45.89	0.00	19.53	0.13	0.00	0.02	0.00	34.43	0.20	0.00	0.14	0.02	0.00	0.01	0.13	100.54
WF703	Apy	44.33	0.00	20.33	0.09	0.00	0.00	0.02	34.44	0.17	0.00	0.17	0.00	0.01	0.00	0.00	99.56
WF703	Apy	45.77	0.00	19.71	0.00	0.00	0.00	0.00	34.60	0.07	0.02	0.10	0.00	0.04	0.02	0.19	100.55
WF703	Apy	46.47	0.00	18.71	0.00	0.07	0.00	0.01	33.16	0.30	0.02	0.22	0.00	0.00	0.00	0.00	98.97
WF703	Apy	45.79	0.00	19.81	0.15	0.05	0.04	0.00	34.15	0.10	0.00	0.13	0.03	0.00	0.00	0.04	100.29
WF703	Apy	45.54	0.00	19.97	0.17	0.00	0.00	0.03	34.62	0.18	0.02	0.14	0.00	0.00	0.00	0.00	100.68
WF703	Apy	46.47	0.00	19.31	0.00	0.19	0.00	0.00	34.08	0.15	0.00	0.09	0.03	0.00	0.01	0.04	100.36
WF703	Apy	46.13	0.00	18.94	0.12	0.03	0.03	0.00	34.01	0.06	0.04	0.10	0.01	0.00	0.00	0.04	99.51
WF703	Apy	46.58	0.00	19.20	0.15	0.00	0.00	0.00	34.08	0.11	0.00	0.12	0.03	0.00	0.02	0.00	100.30
WF703	Apy	47.47	0.00	18.43	0.19	0.04	0.00	0.00	33.05	0.37	0.00	0.33	0.00	0.06	0.00	0.00	99.94
WF703	Apy	47.45	0.00	18.68	0.07	0.00	0.00	0.02	34.09	0.09	0.05	0.24	0.00	0.00	0.00	0.00	100.69
WF703	Apy	47.47	0.00	18.60	0.06	0.00	0.03	0.03	33.67	0.04	0.04	0.21	0.09	0.00	0.01	0.04	100.32
WF703	Apy	46.60	0.00	18.83	0.08	0.03	0.00	0.00	33.92	0.15	0.00	0.18	0.10	0.05	0.00	0.00	99.97
WF703	Apy	47.12	0.00	18.91	0.06	0.00	0.00	0.00	34.38	0.16	0.00	0.15	0.01	0.00	0.00	0.00	100.78
WF703	Apy	46.68	0.00	18.81	0.08	0.00	0.00	0.01	33.95	0.07	0.03	0.16	0.01	0.00	0.01	0.14	99.94
WF703	Apy	46.01	0.00	19.40	0.03	0.04	0.00	0.05	33.80	0.14	0.03	0.15	0.02	0.00	0.00	0.00	99.67
WF703	Apy	45.99	0.00	19.23	0.19	0.00	0.00	0.00	33.73	0.23	0.00	0.16	0.05	0.00	0.02	0.10	99.72
WF703	Apy	46.50	0.00	19.20	0.00	0.00	0.00	0.06	33.28	0.19	0.00	0.16	0.00	0.06	0.00	0.00	99.45
WF703	Apy	46.94	0.00	18.73	0.07	0.00	0.00	0.00	33.63	0.28	0.00	0.24	0.07	0.04	0.00	0.15	100.15
WF703	Apy	46.93	0.00	18.73	0.03	0.00	0.00	0.00	33.55	0.27	0.00	0.21	0.00	0.00	0.00	0.00	99.73
WF703	Apy	47.35	0.00	18.69	0.07	0.00	0.00	0.01	33.23	0.29	0.00	0.23	0.01	0.04	0.00	0.06	100.03
WF703	Apy	46.58	0.00	18.66	0.08	0.00	0.01	0.01	33.24	0.24	0.01	0.18	0.00	0.00	0.00	0.10	99.15
WF703	Apy	46.83	0.00	18.66	0.07	0.00	0.03	0.00	34.29	0.12	0.01	0.25	0.02	0.00	0.00	0.00	100.29
WF703	Apy	47.17	0.00	18.82	0.00	0.00	0.02	0.01	33.79	0.29	0.00	0.18	0.07	0.08	0.00	0.04	100.52
WF703	Apy	47.13	0.00	18.69	0.05	0.00	0.01	0.00	33.52	0.38	0.00	0.27	0.03	0.06	0.01	0.00	100.16
WF703	Apy	46.38	0.00	19.25	0.16	0.00	0.02	0.00	34.39	0.13	0.03	0.13	0.00	0.00	0.00	0.00	100.48
WF703	Apy	46.12	0.00	19.59	0.02	0.00	0.00	0.00	34.14	0.03	0.00	0.09	0.04	0.00	0.01	0.22	100.26
WF703	Apy	46.18	0.00	19.59	0.05	0.00	0.00	0.00	33.76	0.10	0.00	0.12	0.01	0.02	0.00	0.03	99.86
WF703	Apy	45.94	0.00	19.59	0.08	0.00	0.00	0.00	33.87	0.13	0.00	0.13	0.11	0.00	0.00	0.00	99.89

WF703	Apy	46.32	0.00	19.54	0.09	0.03	0.02	0.00	34.55	0.07	0.02	0.12	0.00	0.03	0.00	0.00	100.80
WF703	Apy	46.14	0.00	19.45	0.00	0.00	0.00	0.02	34.22	0.12	0.00	0.11	0.00	0.00	0.00	0.30	100.41
WF703	Apy	45.88	0.00	19.29	0.16	0.00	0.02	0.01	33.92	0.11	0.00	0.16	0.06	0.05	0.01	0.02	99.75
WF703	Apy	46.81	0.00	19.08	0.11	0.04	0.00	0.00	33.98	0.16	0.00	0.13	0.05	0.00	0.00	0.01	100.36
WF703	Apy	46.40	0.00	19.00	0.00	0.00	0.01	0.02	33.71	0.22	0.07	0.14	0.00	0.00	0.03	0.00	99.61
WF703	Apy	46.56	0.00	19.18	0.05	0.00	0.00	0.01	34.16	0.10	0.00	0.08	0.00	0.01	0.00	0.00	100.16
WF703	Apy	45.79	0.00	19.49	0.09	0.00	0.00	0.03	33.92	0.10	0.00	0.13	0.02	0.00	0.00	0.02	99.59
WF703	Apy	46.32	0.00	19.44	0.00	0.00	0.00	0.00	34.18	0.17	0.00	0.16	0.07	0.00	0.03	0.04	100.42
WF703	Apy	44.61	0.00	20.02	0.07	0.00	0.00	0.00	34.27	0.17	0.00	0.15	0.00	0.00	0.00	0.00	99.29
WF703	Apy	46.90	0.00	18.89	0.13	0.09	0.03	0.00	34.27	0.15	0.00	0.16	0.00	0.00	0.02	0.02	100.64
WF703	Apy	47.41	0.00	19.02	0.08	0.00	0.01	0.06	33.72	0.39	0.03	0.21	0.00	0.00	0.00	0.00	100.93
WF703	Apy	46.65	0.00	19.07	0.00	0.12	0.00	0.00	33.69	0.22	0.00	0.12	0.11	0.00	0.00	0.26	100.25
WF703	Apy	47.48	0.00	18.89	0.12	0.05	0.04	0.02	33.78	0.23	0.00	0.29	0.01	0.00	0.00	0.23	101.13
WF703	Apy	47.47	0.00	18.84	0.00	0.03	0.00	0.03	33.58	0.21	0.00	0.38	0.00	0.02	0.02	0.00	100.57
WF703	Apy	46.91	0.00	18.51	0.12	0.00	0.00	0.00	32.98	0.52	0.00	0.47	0.06	0.00	0.00	0.00	99.58
WF703	Apy	47.00	0.00	19.05	0.08	0.00	0.00	0.00	33.98	0.20	0.00	0.14	0.00	0.03	0.01	0.05	100.55
WF703	Apy	46.44	0.00	19.02	0.04	0.00	0.00	0.00	33.57	0.22	0.00	0.26	0.05	0.00	0.02	0.00	99.62
WF703	Apy	46.87	0.00	18.79	0.07	0.01	0.00	0.04	33.32	0.24	0.00	0.19	0.01	0.04	0.00	0.03	99.66
WF703	Apy	46.41	0.00	19.08	0.04	0.00	0.00	0.03	33.72	0.26	0.00	0.15	0.04	0.00	0.00	0.00	99.74
WF703	Apy	47.06	0.00	18.89	0.15	0.09	0.00	0.00	34.42	0.12	0.00	0.20	0.03	0.00	0.03	0.00	100.99
WF703	Apy	45.92	0.00	19.66	0.08	0.00	0.03	0.00	34.29	0.17	0.00	0.14	0.05	0.00	0.01	0.00	100.36
WF703	Apy	45.62	0.00	19.54	0.00	0.08	0.00	0.00	33.86	0.12	0.02	0.14	0.00	0.00	0.00	0.03	99.43
WF703	Apy	46.60	0.00	19.42	0.11	0.00	0.02	0.00	34.30	0.20	0.00	0.13	0.03	0.06	0.00	0.00	100.87
WF703	Apy	47.04	0.00	19.10	0.03	0.00	0.00	0.00	34.79	0.07	0.02	0.11	0.01	0.00	0.00	0.20	101.36
WF703	Apy	37.97	0.00	16.50	0.10	0.00	0.01	0.02	28.68	0.08	0.03	0.07	0.05	0.02	0.00	0.01	83.53
WF703	Apy	45.56	0.00	19.95	0.00	0.00	0.00	0.00	34.20	0.10	0.00	0.10	0.10	0.00	0.00	0.09	100.11
WF703	Apy	45.50	0.00	19.82	0.15	0.00	0.00	0.00	34.53	0.07	0.03	0.14	0.00	0.00	0.02	0.08	100.34
WF703	Apy	45.72	0.00	20.16	0.17	0.03	0.00	0.00	34.86	0.10	0.01	0.14	0.05	0.00	0.00	0.00	101.24
WF703	Apy	46.73	0.00	19.55	0.21	0.00	0.02	0.01	34.47	0.16	0.00	0.12	0.06	0.02	0.01	0.00	101.36
WF703	Apy	45.78	0.00	19.59	0.02	0.00	0.00	0.00	34.68	0.16	0.00	0.10	0.06	0.00	0.02	0.13	100.54
WF703	Apy	46.55	0.00	19.73	0.14	0.00	0.00	0.00	33.87	0.18	0.00	0.11	0.00	0.00	0.00	0.00	100.59
WF703	Apy	46.23	0.00	19.63	0.16	0.04	0.01	0.07	34.79	0.14	0.00	0.12	0.00	0.00	0.00	0.23	101.42
WF703	Apy	46.28	0.00	19.80	0.00	0.00	0.01	0.02	34.26	0.19	0.00	0.17	0.00	0.01	0.01	0.04	100.79
WF703	Apy	46.12	0.00	19.61	0.14	0.09	0.03	0.00	34.18	0.13	0.00	0.17	0.01	0.00	0.00	0.13	100.60
WF703	Apy	46.23	0.00	19.57	0.02	0.00	0.00	0.00	34.58	0.14	0.00	0.15	0.01	0.02	0.01	0.04	100.77
WF703	Apy	45.48	0.00	20.08	0.10	0.00	0.00	0.00	34.72	0.15	0.00	0.13	0.04	0.00	0.00	0.04	100.73
WF703	Apy	46.15	0.00	19.43	0.10	0.00	0.00	0.00	34.41	0.12	0.00	0.13	0.04	0.00	0.03	0.00	100.48
WF703	Apy	45.65	0.00	19.85	0.00	0.00	0.01	0.02	34.26	0.16	0.00	0.13	0.00	0.00	0.00	0.00	100.08
WF703	Apy	45.97	0.00	19.64	0.08	0.00	0.00	0.00	34.44	0.14	0.00	0.13	0.09	0.03	0.00	0.21	100.74

WF703	Apy	46.18	0.00	19.78	0.10	0.01	0.00	0.00	34.49	0.11	0.02	0.10	0.00	0.02	0.00	0.13	101.00
WF703	Apy	45.88	0.00	19.72	0.09	0.02	0.00	0.02	34.30	0.14	0.02	0.09	0.08	0.00	0.00	0.04	100.41
WF703	Apy	48.08	0.00	19.49	0.06	0.00	0.00	0.04	34.28	0.14	0.00	0.11	0.01	0.00	0.00	0.00	102.25
WF703	Apy	46.54	0.00	19.67	0.00	0.02	0.00	0.00	34.05	0.15	0.00	0.08	0.13	0.00	0.00	0.00	100.66
WF703	Apy	46.00	0.00	19.62	0.06	0.07	0.00	0.03	34.45	0.15	0.00	0.09	0.05	0.00	0.00	0.10	100.64
WF703	Apy	45.80	0.00	20.11	0.05	0.00	0.05	0.00	34.82	0.15	0.00	0.16	0.07	0.08	0.00	0.00	101.29
WF703	Apy	46.02	0.00	19.90	0.25	0.00	0.00	0.00	34.01	0.12	0.05	0.11	0.01	0.00	0.01	0.13	100.69
WF703	Apy	46.15	0.00	19.79	0.08	0.00	0.05	0.02	34.61	0.16	0.00	0.13	0.01	0.00	0.00	0.13	101.13
WF703	Apy	46.30	0.00	19.58	0.09	0.06	0.01	0.02	34.52	0.10	0.01	0.09	0.04	0.00	0.02	0.00	100.89
WF703	Apy	46.40	0.00	19.66	0.18	0.00	0.00	0.00	34.23	0.14	0.00	0.10	0.00	0.00	0.00	0.00	100.70
WF703	Apy	45.69	0.00	19.91	0.00	0.00	0.00	0.06	34.27	0.19	0.05	0.13	0.00	0.00	0.01	0.00	100.30
WF703	Apy	46.04	0.00	20.17	0.00	0.00	0.00	0.06	34.28	0.13	0.05	0.15	0.00	0.00	0.00	0.00	100.95
WF703	Apy	46.83	0.00	19.26	0.00	0.00	0.00	0.00	34.48	0.08	0.00	0.17	0.00	0.00	0.01	0.02	100.86
WF703	Apy	45.99	0.00	19.98	0.00	0.00	0.04	0.00	34.48	0.07	0.00	0.10	0.00	0.02	0.00	0.00	100.72
WF703	Apy	46.60	0.00	19.38	0.09	0.04	0.00	0.00	34.25	0.12	0.00	0.12	0.04	0.00	0.00	0.00	100.66
WF703	Apy	45.78	0.00	19.86	0.07	0.06	0.00	0.03	34.72	0.04	0.02	0.13	0.02	0.03	0.03	0.01	100.90
WF703	Apy	45.73	0.00	19.60	0.08	0.08	0.04	0.02	34.19	0.09	0.02	0.13	0.11	0.00	0.00	0.00	100.08
WF703	Apy	46.05	0.00	19.61	0.03	0.07	0.00	0.00	34.39	0.18	0.00	0.11	0.00	0.06	0.01	0.00	100.51
WF703	Apy	45.57	0.00	20.26	0.00	0.02	0.02	0.00	34.40	0.13	0.01	0.09	0.00	0.00	0.00	0.07	100.59
WF703	Apy	46.28	0.00	19.70	0.07	0.00	0.00	0.00	34.26	0.10	0.00	0.12	0.00	0.05	0.01	0.07	100.64
WF703	Apy	47.12	0.00	19.71	0.12	0.02	0.03	0.02	34.32	0.10	0.02	0.13	0.06	0.00	0.00	0.00	101.64
WF703	Apy	46.83	0.00	19.44	0.09	0.00	0.00	0.03	34.37	0.04	0.01	0.16	0.00	0.03	0.00	0.00	101.01
WF703	Apy	46.82	0.00	19.47	0.01	0.00	0.00	0.00	34.24	0.11	0.00	0.10	0.04	0.02	0.00	0.00	100.80
WF703	Apy	47.10	0.00	19.04	0.08	0.00	0.00	0.03	34.22	0.18	0.00	0.11	0.00	0.00	0.00	0.03	100.82
WF703	Apy	46.66	0.00	19.46	0.07	0.03	0.00	0.03	34.36	0.08	0.00	0.16	0.00	0.00	0.00	0.00	100.90
WF703	Apy	46.75	0.00	19.49	0.01	0.00	0.02	0.00	33.94	0.11	0.00	0.11	0.00	0.00	0.00	0.00	100.44
WF703	Apy	46.74	0.00	19.28	0.02	0.00	0.00	0.00	34.38	0.09	0.00	0.11	0.00	0.00	0.01	0.17	100.80
WF703	Apy	39.34	0.00	18.24	0.00	0.00	0.00	0.00	29.44	0.13	0.00	0.10	0.00	0.00	0.02	0.13	87.40
WF703	Apy	47.00	0.00	19.09	0.05	0.00	0.01	0.00	33.83	0.17	0.00	0.17	0.00	0.00	0.00	0.03	100.35
WF703	Apy	46.89	0.00	18.89	0.07	0.00	0.04	0.00	33.46	0.14	0.00	0.16	0.00	0.03	0.00	0.00	99.68
WF703	Apy	47.47	0.00	19.00	0.08	0.00	0.01	0.01	33.94	0.21	0.03	0.17	0.05	0.01	0.00	0.00	100.98
WF703	Apy	46.95	0.00	18.92	0.11	0.00	0.07	0.01	34.39	0.21	0.00	0.19	0.04	0.00	0.00	0.27	101.16
WF703	Apy	46.55	0.00	19.16	0.07	0.19	0.00	0.00	34.06	0.14	0.00	0.12	0.05	0.00	0.00	0.04	100.42
WF703	Apy	47.31	0.00	18.97	0.09	0.07	0.01	0.00	33.70	0.16	0.01	0.18	0.00	0.03	0.00	0.24	100.87
WF703	Apy	46.80	0.00	18.86	0.05	0.00	0.00	0.00	33.49	0.27	0.00	0.18	0.00	0.00	0.00	0.00	99.70
WF703	Apy	47.26	0.00	18.93	0.07	0.06	0.00	0.05	33.78	0.20	0.00	0.14	0.07	0.00	0.00	0.06	100.63
WF703	Apy	47.47	0.00	18.70	0.02	0.00	0.00	0.00	34.00	0.25	0.01	0.19	0.12	0.00	0.00	0.12	100.89
WF703	Apy	46.46	0.00	19.36	0.14	0.00	0.00	0.05	34.10	0.22	0.00	0.13	0.03	0.00	0.01	0.05	100.57
WF703	Apy	46.37	0.00	20.63	0.12	0.00	0.00	0.00	34.14	0.07	0.02	0.12	0.07	0.00	0.00	0.00	101.59

WF703	Apy	45.75	0.00	19.82	0.10	0.00	0.00	0.00	34.27	0.20	0.00	0.10	0.00	0.00	0.00	0.19	100.45
WF703	Apy	46.47	0.00	18.98	0.13	0.02	0.00	0.04	34.00	0.13	0.00	0.14	0.01	0.00	0.01	0.00	99.94
WF703	Apy	47.81	0.00	18.68	0.11	0.00	0.00	0.00	33.79	0.26	0.00	0.26	0.01	0.00	0.01	0.13	101.06
WF703	Apy	46.17	0.00	19.48	0.03	0.00	0.00	0.00	34.08	0.20	0.00	0.12	0.04	0.00	0.02	0.00	100.13
WF703	Apy	45.73	0.00	19.68	0.16	0.00	0.04	0.00	34.31	0.18	0.00	0.09	0.00	0.00	0.01	0.00	100.20
WF703	Apy	45.62	0.00	19.64	0.09	0.17	0.02	0.04	34.29	0.16	0.00	0.15	0.00	0.00	0.00	0.11	100.28
WF703	Apy	47.72	0.00	18.43	0.07	0.00	0.00	0.04	34.14	0.32	0.00	0.31	0.07	0.00	0.01	0.04	101.14
WF703	Apy	47.22	0.00	18.89	0.13	0.14	0.00	0.00	34.36	0.12	0.00	0.15	0.06	0.00	0.00	0.05	101.12
WF703	Apy	47.31	0.00	18.77	0.06	0.08	0.00	0.00	34.14	0.30	0.00	0.18	0.00	0.00	0.00	0.13	101.01
WF703	Apy	47.23	0.00	19.02	0.08	0.08	0.03	0.00	34.32	0.19	0.00	0.12	0.05	0.01	0.00	0.00	101.12
WF703	Apy	46.72	0.00	19.38	0.08	0.00	0.00	0.00	34.28	0.11	0.00	0.12	0.00	0.00	0.00	0.00	100.68
WF703	Apy	46.36	0.00	19.83	0.14	0.13	0.07	0.02	34.38	0.10	0.00	0.12	0.00	0.00	0.00	0.01	101.15
WF703	Apy	46.77	0.00	19.20	0.08	0.06	0.00	0.00	33.99	0.18	0.00	0.14	0.04	0.00	0.00	0.10	100.60
WF703	Apy	46.53	0.00	19.00	0.08	0.00	0.00	0.02	34.14	0.15	0.00	0.11	0.06	0.00	0.00	0.26	100.35
WF703	Apy	47.16	0.00	18.97	0.18	0.00	0.00	0.00	33.95	0.10	0.00	0.17	0.03	0.05	0.00	0.03	100.66
WF703	Apy	47.92	0.00	18.53	0.06	0.13	0.00	0.00	33.25	0.35	0.00	0.27	0.01	0.00	0.00	0.00	100.51
WF703	Apy	45.63	0.00	20.07	0.07	0.07	0.00	0.04	34.57	0.18	0.00	0.13	0.06	0.00	0.00	0.00	100.87
WF703	Apy	46.26	0.00	19.46	0.10	0.00	0.02	0.00	34.42	0.15	0.02	0.16	0.00	0.03	0.00	0.06	100.71
WF703	Apy	45.84	0.00	19.98	0.18	0.00	0.00	0.07	34.35	0.17	0.01	0.11	0.10	0.00	0.02	0.00	100.83
WF703	Apy	46.52	0.00	19.64	0.10	0.14	0.00	0.04	34.43	0.14	0.00	0.15	0.12	0.00	0.00	0.00	101.29
WF703	Apy	46.27	0.00	19.14	0.00	0.00	0.02	0.00	34.34	0.15	0.00	0.12	0.02	0.00	0.00	0.01	100.11
WF703	Apy	45.54	0.00	19.10	0.00	0.03	0.02	0.01	33.78	0.16	0.04	0.11	0.00	0.00	0.00	0.00	98.78
WF703	Apy	45.99	0.00	19.74	0.05	0.00	0.01	0.00	34.41	0.17	0.00	0.08	0.00	0.00	0.03	0.11	100.57
WF703	Apy	45.16	0.00	19.89	0.07	0.00	0.00	0.07	34.54	0.15	0.00	0.15	0.04	0.00	0.02	0.00	100.09
WF703	Apy	46.96	0.00	18.79	0.07	0.00	0.02	0.02	34.33	0.29	0.01	0.14	0.00	0.00	0.00	0.00	100.64
WF703	Apy	47.39	0.00	18.57	0.00	0.00	0.04	0.00	33.56	0.25	0.00	0.17	0.00	0.00	0.02	0.01	100.04
WF703	Apy	45.92	0.00	19.53	0.13	0.00	0.02	0.00	33.62	0.19	0.03	0.12	0.00	0.00	0.03	0.00	99.58
WF703	Apy	46.36	0.00	19.37	0.03	0.00	0.02	0.00	34.16	0.18	0.00	0.14	0.00	0.00	0.01	0.02	100.29
WF703	Apy	45.89	0.00	19.94	0.17	0.00	0.00	0.00	34.39	0.18	0.01	0.16	0.01	0.00	0.00	0.09	100.83
WF703	Apy	47.42	0.00	18.82	0.06	0.03	0.00	0.01	33.94	0.17	0.03	0.20	0.03	0.00	0.04	0.00	100.75
WF703	Apy	46.97	0.00	18.93	0.20	0.00	0.02	0.03	34.08	0.24	0.00	0.15	0.03	0.08	0.00	0.02	100.75
WF703	Apy	46.32	0.00	19.55	0.12	0.00	0.00	0.00	34.20	0.15	0.00	0.10	0.06	0.05	0.00	0.00	100.64
WF703	Apy	46.26	0.00	19.58	0.01	0.05	0.01	0.00	34.52	0.06	0.04	0.06	0.06	0.00	0.00	0.00	100.64
WF703	Apy	45.93	0.00	19.49	0.11	0.00	0.03	0.00	34.23	0.15	0.00	0.15	0.00	0.06	0.00	0.00	100.14
WF703	Apy	47.35	0.00	18.81	0.15	0.00	0.00	0.00	33.89	0.17	0.00	0.22	0.07	0.00	0.09	0.09	100.78

Depósito: Poconé

Amostra	Mineral	As	Se	S	Pb	Bi	Cd	Te	Fe	Co	Cu	Ni	Mo	Au	Ag	Sb	Total
WF603	Py	0.00	0.08	51.00	0.10	0.00	0.00	0.02	45.43	0.08	0.01	0.02	0.12	0.00	0.02	0.00	96.95

WF603	Py	0.00	0.08	50.27	0.09	0.01	0.04	0.00	44.32	0.10	0.01	0.01	0.10	0.03	0.00	0.01	0.01	95.08
WF603	Py	0.00	0.12	51.49	0.15	0.00	0.00	0.00	45.67	0.09	0.00	0.00	0.13	0.00	0.01	0.00	0.00	97.71
WF603	Py	0.00	0.01	54.02	0.23	0.00	0.03	0.00	47.00	0.08	0.02	0.05	0.11	0.00	0.00	0.01	0.01	101.56

Depósito: Satinoco

Amostra	Mineral	As	Se	S	Pb	Bi	Cd	Te	Fe	Co	Cu	Ni	Mo	Au	Ag	Sb	Total
WF102	Po	0.00	0.02	38.28	0.14	0.00	0.05	0.00	56.42	0.06	0.00	0.20	0.11	0.00	0.01	0.00	95.33
WF102	Po	0.00	0.00	38.08	0.21	0.00	0.00	0.02	57.59	0.08	0.00	0.24	0.09	0.00	0.00	0.01	96.34
WF106	Py	0.19	0.02	52.96	0.27	0.00	0.02	0.00	45.45	0.06	0.01	0.00	0.06	0.00	0.00	0.00	99.02
WF106	Gn	0.00	0.16	12.88	70.90	0.00	0.10	0.07	0.22	0.01	0.28	0.17	0.88	0.00	0.00	0.00	85.68
WF106	Ccp	0.00	0.00	33.83	0.20	0.00	0.00	0.00	29.18	0.03	32.66	0.03	0.03	0.01	0.00	0.03	96.04
WF106	Ull	0.64	0.07	14.42	0.06	0.04	0.00	0.11	1.36	0.10	0.05	26.42	0.00	0.00	0.02	57.45	100.75
WF107	Po	0.00	0.00	38.63	0.19	0.00	0.01	0.00	56.32	0.10	0.00	0.15	0.13	0.00	0.01	0.00	95.53
WF107	Py	0.00	0.02	51.76	0.21	0.00	0.00	0.00	45.40	0.07	0.00	0.04	0.13	0.00	0.00	0.00	97.67
WF107	Po	0.00	0.00	37.67	0.21	0.00	0.02	0.00	57.46	0.07	0.01	0.21	0.08	0.00	0.00	0.00	95.74
WF107	Po	0.00	0.02	38.79	0.30	0.00	0.00	0.00	55.91	0.05	0.00	0.27	0.15	0.01	0.00	0.00	95.50
WF107	Po	0.00	0.01	37.96	0.15	0.00	0.05	0.01	57.69	0.07	0.01	0.05	0.13	0.00	0.02	0.00	96.14
WF107	Py	0.00	0.00	50.65	0.20	0.00	0.08	0.01	44.83	0.05	0.00	0.17	0.09	0.00	0.00	0.01	96.10
WF107	Ccp	0.00	0.02	35.02	0.04	0.00	0.00	0.02	29.43	0.03	33.72	0.00	0.08	0.00	0.01	0.00	98.37
WF109	Po	0.00	0.04	38.18	0.23	0.08	0.00	0.00	56.40	0.04	0.00	0.29	0.12	0.00	0.02	0.00	95.39
WF109	Po	0.00	0.02	38.48	0.06	0.00	0.00	0.00	57.37	0.07	0.01	0.42	0.08	0.00	0.01	0.00	96.51
WF111	Po	0.00	0.03	39.40	0.09	0.00	0.02	0.00	58.82	0.14	0.00	0.02	0.13	0.00	0.00	0.00	98.64
WF111	Po	0.00	0.02	39.52	0.07	0.00	0.03	0.00	58.55	0.15	0.00	0.09	0.05	0.00	0.01	0.00	98.52
WF111	Po	0.00	0.03	39.45	0.09	0.01	0.02	0.00	57.58	0.10	0.01	0.16	0.08	0.00	0.02	0.00	97.55
WF111	Po	0.00	0.11	39.13	0.19	0.00	0.00	0.00	57.90	0.14	0.00	0.10	0.14	0.00	0.03	0.00	97.81
WF111	Ccp	0.00	0.00	29.83	0.11	0.00	0.00	0.03	27.80	0.04	31.12	0.00	0.05	0.00	0.02	0.00	89.04
WF111	Ccp	0.00	0.06	33.83	0.13	0.00	0.00	0.00	28.97	0.03	31.33	0.00	0.06	0.00	0.03	0.00	94.44
WF111	Po	0.00	0.00	30.79	0.13	0.02	0.00	0.04	53.69	0.13	0.00	0.19	0.06	0.00	0.00	0.00	85.04
WF111	Po	0.00	0.03	38.83	0.07	0.02	0.01	0.00	58.66	0.12	0.00	0.18	0.12	0.00	0.00	0.00	98.08
WF111	Po	0.00	0.04	39.00	0.09	0.00	0.00	0.01	58.41	0.15	0.00	0.25	0.15	0.00	0.00	0.02	98.14
WF112	Po	0.00	0.09	39.05	0.18	0.00	0.09	0.03	58.69	0.10	0.00	0.79	0.08	0.00	0.00	0.00	99.13
WF112	Po	0.04	0.03	38.38	0.17	0.11	0.03	0.03	58.65	0.10	0.01	0.58	0.09	0.01	0.00	0.00	98.28
WF113	Po	0.03	0.06	36.67	0.22	0.00	0.00	0.00	56.78	0.04	0.00	0.11	0.10	0.00	0.00	0.04	94.06
WF113	Po	0.00	0.04	36.43	0.08	0.00	0.03	0.07	55.96	0.00	0.00	0.06	0.00	0.00	0.00	0.10	92.86
WF113	Po	0.00	0.05	36.63	0.20	0.03	0.04	0.02	57.12	0.00	0.00	0.08	0.00	0.00	0.02	0.14	94.31
WF115	Po	0.01	0.02	39.27	0.13	0.00	0.00	0.06	58.26	0.12	0.01	0.17	0.10	0.00	0.00	0.00	98.16
WF115	Po	0.00	0.07	39.23	0.12	0.03	0.00	0.00	58.22	0.12	0.00	0.19	0.12	0.00	0.01	0.00	98.16
WF120	Po	0.00	0.08	38.11	0.16	0.00	0.01	0.00	54.35	0.10	0.00	0.05	0.10	0.00	0.00	0.01	92.99
WF121	Po	0.00	0.02	38.41	0.19	0.04	0.06	0.03	58.60	0.06	0.00	0.24	0.07	0.00	0.00	0.01	97.76

WF121	Po	0.00	0.10	38.85	0.20	0.04	0.02	0.00	57.64	0.08	0.02	0.12	0.05	0.01	0.00	0.07	97.18
WF123	PbSFe	0.00	0.33	21.42	55.43	0.16	0.09	0.07	13.33	0.03	0.05	0.03	0.16	0.07	0.04	0.00	91.26
WF123	Py	0.00	0.07	53.46	0.04	0.00	0.00	0.00	46.28	0.07	0.01	0.03	0.14	0.00	0.03	0.00	100.14
WF123	Py	0.00	0.00	53.30	0.11	0.00	0.00	0.00	46.16	0.05	0.02	0.00	0.11	0.01	0.00	0.00	99.79
WF123	Py	0.00	0.03	53.05	0.19	0.00	0.05	0.04	45.45	0.06	0.33	0.00	0.13	0.00	0.00	0.00	99.36
WF123	Py	0.00	0.01	53.31	0.22	0.00	0.00	0.00	45.93	0.05	0.06	0.07	0.13	0.00	0.00	0.00	99.78
WF123	Sph	0.06	0.12	49.36	0.22	0.06	0.04	0.00	40.63	0.18	0.05	0.09	0.14	0.00	0.02	0.00	99.89
WF123	Py	0.00	0.01	53.20	0.33	0.00	0.02	0.00	45.81	0.04	0.48	0.03	0.19	0.00	0.02	0.00	100.14
WF123	Py	0.00	0.01	53.13	0.19	0.00	0.04	0.00	46.01	0.07	0.01	0.09	0.15	0.00	0.01	0.04	99.75
WF123	Py	0.00	0.01	53.35	0.15	0.00	0.02	0.02	45.75	0.05	0.01	0.00	0.11	0.00	0.00	0.05	99.52
WF123	Py	0.00	0.07	51.23	0.11	0.00	0.00	0.02	41.93	0.06	0.04	0.00	0.17	0.00	0.00	0.07	93.69
WF123	Py	0.00	0.00	50.94	0.12	0.00	0.00	0.00	41.46	0.06	0.00	0.00	0.00	0.00	0.01	0.15	92.80
WF123	Py	0.45	0.07	50.92	0.17	0.00	0.00	0.00	42.02	0.07	0.03	0.22	0.27	0.00	0.00	0.16	94.42
WF123	PbSFe	0.00	0.16	30.48	30.35	0.00	0.04	0.02	29.40	0.33	0.03	0.25	0.00	0.00	0.00	0.22	91.29
WF123B	Po	0.00	0.00	38.52	0.16	0.00	0.00	0.00	58.39	0.13	0.00	0.09	0.12	0.04	0.00	0.00	97.45
WF123B	Po	0.00	0.04	39.09	0.14	0.00	0.00	0.00	58.64	0.14	0.00	0.09	0.08	0.00	0.00	0.00	98.22
WF123B	Po	0.01	0.02	38.67	0.20	0.00	0.01	0.02	58.23	0.15	0.00	0.18	0.06	0.00	0.00	0.00	97.55
WF123B	Py	0.07	0.03	51.61	0.29	0.00	0.02	0.00	46.58	0.09	0.00	0.00	0.06	0.00	0.00	0.00	98.79
WF123B	Po	0.01	0.07	40.25	0.18	0.00	0.05	0.00	55.90	0.16	0.02	0.29	0.13	0.00	0.00	0.00	97.03
WF123B	Po	0.00	0.01	40.73	0.09	0.00	0.00	0.02	57.04	0.16	0.00	0.37	0.07	0.00	0.00	0.00	98.50
WF123B	Py	0.00	0.06	51.72	0.14	0.00	0.00	0.00	45.96	0.08	0.00	0.00	0.14	0.00	0.00	0.00	98.09
WF123B	Py	0.00	0.09	52.37	0.19	0.00	0.00	0.00	46.58	0.07	0.00	0.00	0.14	0.00	0.03	0.00	99.47
WF123B	Py	0.00	0.00	52.45	0.22	0.02	0.05	0.01	45.84	0.09	0.02	0.00	0.14	0.00	0.00	0.00	98.86
WF123B	Po	0.00	0.03	38.42	0.16	0.00	0.04	0.03	58.02	0.14	0.03	0.10	0.11	0.00	0.01	0.01	97.09
WF123B	Po	0.00	0.00	38.49	0.22	0.00	0.03	0.00	58.34	0.15	0.00	0.07	0.09	0.00	0.00	0.02	97.42
WF123B	Po	0.00	0.10	40.17	0.08	0.06	0.04	0.00	58.90	0.16	0.04	0.18	0.11	0.00	0.00	0.02	99.91
WF123B	Po	0.00	0.00	38.50	0.21	0.00	0.02	0.02	58.29	0.13	0.00	0.11	0.10	0.00	0.00	0.02	97.44
WF112	Apy	48.55	0.00	17.34	0.09	0.00	0.00	0.00	32.35	0.98	0.00	1.06	0.00	0.00	0.01	0.19	100.56
WF112	Apy	48.55	0.00	17.39	0.04	0.00	0.00	0.05	32.96	0.97	0.00	1.03	0.00	0.09	0.02	0.00	101.14
WF112	Apy	49.98	0.00	16.19	0.09	0.09	0.00	0.05	31.59	1.13	0.00	1.79	0.00	0.00	0.00	0.00	100.90
WF112	Apy	50.14	0.00	16.84	0.00	0.06	0.01	0.02	31.93	1.11	0.00	1.55	0.00	0.00	0.00	0.00	101.71
WF112	Apy	50.05	0.00	16.40	0.06	0.00	0.02	0.00	32.17	1.11	0.00	1.72	0.00	0.00	0.01	0.00	101.54
WF112	Apy	49.31	0.00	16.83	0.06	0.00	0.04	0.00	31.74	1.05	0.00	1.36	0.11	0.00	0.01	0.00	100.55
WF112	Apy	49.32	0.00	16.76	0.00	0.02	0.02	0.01	32.44	1.05	0.00	1.25	0.05	0.09	0.00	0.04	101.04
WF112	Apy	49.55	0.00	16.94	0.02	0.00	0.00	0.02	32.16	1.09	0.00	1.44	0.02	0.06	0.00	0.00	101.30
WF112	Apy	49.88	0.00	17.01	0.02	0.00	0.01	0.00	32.31	1.03	0.00	1.37	0.01	0.03	0.00	0.00	101.65
WF112	Apy	49.55	0.00	16.96	0.00	0.00	0.01	0.01	32.72	1.02	0.00	1.35	0.03	0.00	0.00	0.05	101.69
WF112	Apy	49.87	0.00	16.85	0.03	0.00	0.01	0.00	31.88	1.05	0.00	1.46	0.00	0.00	0.00	0.08	101.24
WF112	Apy	48.79	0.00	17.15	0.02	0.05	0.01	0.03	32.20	1.00	0.00	1.08	0.00	0.06	0.00	0.10	100.51

WF112	Apy	49.38	0.00	17.18	0.09	0.04	0.00	0.03	32.18	1.03	0.00	1.23	0.02	0.07	0.00	0.06	101.32
WF112	Apy	48.99	0.00	17.07	0.10	0.00	0.01	0.00	32.32	1.00	0.00	1.27	0.01	0.00	0.02	0.13	100.91
WF112	Apy	50.23	0.00	17.54	1.55	0.06	0.00	0.08	32.01	0.95	0.00	0.94	0.00	0.00	0.00	0.08	103.45
WF112	Apy	48.66	0.00	16.49	0.14	0.00	0.01	0.01	31.93	1.06	0.00	1.40	0.07	0.00	0.00	0.09	99.85
WF112	Apy	48.38	0.00	17.27	0.00	0.00	0.00	0.05	32.79	0.98	0.00	1.11	0.03	0.00	0.00	0.08	100.74
WF112	Apy	48.89	0.00	17.24	0.05	0.00	0.00	0.00	32.76	1.01	0.00	1.16	0.07	0.02	0.01	0.00	101.24
WF112	Apy	46.36	0.00	18.81	0.09	0.05	0.01	0.00	34.49	0.67	0.02	0.30	0.03	0.00	0.00	0.14	100.98
WF112	Apy	49.02	0.00	17.13	0.15	0.02	0.01	0.00	32.71	1.01	0.00	1.21	0.00	0.00	0.00	0.01	101.31
WF112	Apy	48.36	0.00	17.05	0.00	0.01	0.02	0.00	32.92	0.71	0.00	0.69	0.01	0.00	0.02	0.02	99.81
WF112	Apy	47.47	0.00	16.03	0.04	0.00	0.02	0.00	32.44	0.80	0.00	1.07	0.11	0.00	0.00	0.06	98.06
WF112	Apy	49.12	0.00	17.13	0.00	0.00	0.02	0.01	32.71	0.76	0.00	0.78	0.00	0.00	0.00	0.05	100.61
WF115	Apy	48.78	0.00	17.14	0.12	0.00	0.00	0.00	32.90	1.41	0.00	0.42	0.04	0.02	0.00	0.49	101.37
WF115	Apy	49.08	0.00	16.94	0.01	0.05	0.04	0.00	32.92	1.35	0.00	0.46	0.12	0.00	0.00	0.30	101.27
WF115	Apy	48.79	0.00	16.94	0.03	0.11	0.00	0.00	32.63	1.33	0.00	0.48	0.00	0.00	0.02	0.43	100.76
WF115	Apy	49.73	0.00	16.39	0.00	0.03	0.03	0.00	31.93	1.30	0.00	0.56	0.05	0.00	0.00	0.54	100.54
WF115	Apy	47.21	0.00	16.00	0.09	0.00	0.00	0.01	32.51	1.36	0.00	0.58	0.00	0.00	0.01	0.35	98.12
WF121	Apy	48.90	0.00	16.88	0.07	0.00	0.00	0.00	31.81	1.67	0.00	0.33	0.06	0.00	0.00	0.74	100.47
WF121	Apy	50.16	0.00	17.18	0.05	0.01	0.00	0.00	32.00	1.66	0.00	0.38	0.01	0.00	0.00	0.83	102.27
WF121	Apy	51.28	0.00	16.59	0.02	0.00	0.01	0.00	30.28	2.34	0.00	0.55	0.10	0.07	0.00	1.18	102.41
WF121	Apy	52.06	0.00	15.91	0.00	0.14	0.02	0.04	29.51	2.66	0.00	0.74	0.08	0.11	0.03	1.52	102.82
WF121	Apy	51.31	0.00	17.85	0.00	0.00	0.00	0.01	31.70	1.56	0.00	0.31	0.03	0.02	0.01	0.55	103.40
WF121	Apy	51.68	0.00	16.39	0.07	0.00	0.00	0.04	30.25	2.09	0.00	0.60	0.03	0.00	0.00	0.95	102.09
WF121	Apy	51.11	0.00	16.96	0.01	0.03	0.04	0.00	31.43	2.02	0.00	0.40	0.02	0.04	0.01	0.83	102.86
WF121	Apy	50.00	0.00	17.39	0.10	0.00	0.03	0.00	31.51	1.60	0.00	0.36	0.00	0.00	0.00	0.53	101.51

Depósito: Turmalina

Amostra	Mineral	As	Se	S	Pb	Bi	Cd	Te	Fe	Co	Cu	Ni	Mo	Au	Ag	Sb	Total
WF001	Lö	75.80	0.00	1.65	0.00	0.15	0.00	0.00	25.78	0.29	0.00	2.31	0.00	0.05	0.00	0.00	106.03
WF001	Lö	74.55	0.00	1.52	0.23	0.00	0.00	0.01	26.16	0.37	0.00	2.30	0.01	0.00	0.00	0.00	105.15
WF001	Lö	75.39	0.00	1.67	0.08	0.00	0.00	0.04	25.77	0.35	0.00	2.31	0.00	0.04	0.00	0.00	105.67
WF001	Po	0.00	0.01	38.15	0.23	0.00	0.02	0.01	59.28	0.04	0.00	0.03	0.07	0.00	0.01	0.00	97.87
WF001	Lö	73.69	0.00	2.13	0.08	0.00	0.00	0.00	26.24	0.36	0.00	2.10	0.00	0.12	0.00	0.03	104.74
WF001	Po	0.00	0.00	38.08	0.08	0.00	0.00	0.01	59.20	0.06	0.02	0.06	0.11	0.00	0.02	0.05	97.67
WF001	Lö	73.84	0.00	1.82	0.11	0.00	0.04	0.00	25.58	0.33	0.00	2.24	0.02	0.00	0.00	0.07	104.05
WF001	Po	0.00	0.02	37.69	0.08	0.00	0.05	0.02	59.32	0.05	0.00	0.03	0.10	0.00	0.01	0.09	97.47
WF001	Lö	74.68	0.00	1.57	0.07	0.03	0.00	0.04	25.73	0.38	0.00	2.45	0.00	0.07	0.00	0.11	105.13
WF010	Po	0.00	0.05	36.89	0.21	0.00	0.05	0.05	57.03	0.04	0.00	0.11	0.18	0.02	0.00	0.00	94.62
WF010	Po	0.00	0.06	37.45	0.18	0.00	0.01	0.05	57.74	0.06	0.01	0.10	0.06	0.00	0.00	0.03	95.74
WF010	Po	0.00	0.04	37.52	0.18	0.00	0.02	0.04	57.85	0.05	0.00	0.14	0.10	0.00	0.00	0.05	95.99

WF010	Po	0.00	0.03	37.26	0.12	0.00	0.01	0.00	57.31	0.07	0.01	0.16	0.06	0.02	0.02	0.08	95.14
WF001	Apy	48.79	0.00	18.76	0.08	0.00	0.02	0.00	33.51	0.12	0.00	0.13	0.00	0.00	0.00	0.09	101.56
WF001	Apy	50.32	0.00	17.81	0.09	0.00	0.00	0.05	33.89	0.17	0.00	0.23	0.00	0.00	0.00	0.10	102.65
WF001	Apy	50.65	0.00	17.51	0.11	0.05	0.00	0.00	33.71	0.21	0.00	0.30	0.00	0.00	0.01	0.12	102.67
WF001	Apy	49.24	0.00	17.56	0.11	0.00	0.00	0.00	33.71	0.20	0.02	0.14	0.03	0.00	0.00	0.14	101.16
WF001	Apy	51.19	0.00	17.24	0.04	0.04	0.00	0.00	33.53	0.16	0.00	0.25	0.00	0.00	0.00	0.03	102.49
WF001	Apy	51.08	0.00	17.42	0.02	0.06	0.00	0.04	33.63	0.18	0.01	0.28	0.00	0.07	0.00	0.00	102.80
WF001	Apy	51.28	0.00	17.28	0.03	0.05	0.03	0.00	33.54	0.21	0.00	0.28	0.09	0.00	0.00	0.07	102.91
WF001	Apy	50.83	0.00	17.75	0.13	0.00	0.01	0.01	33.49	0.24	0.00	0.23	0.00	0.01	0.01	0.12	102.83
WF001	Apy	50.30	0.00	17.61	0.03	0.02	0.04	0.00	33.54	0.22	0.00	0.17	0.00	0.00	0.00	0.07	102.00
WF001	Apy	50.96	0.00	17.54	0.13	0.00	0.04	0.00	33.46	0.18	0.00	0.11	0.00	0.00	0.00	0.06	102.50
WF001	Apy	47.96	0.00	17.18	0.09	0.00	0.00	0.04	32.86	0.17	0.03	0.22	0.00	0.00	0.01	0.24	98.79
WF001	Apy	50.17	0.00	17.77	0.00	0.00	0.05	0.00	34.17	0.15	0.00	0.18	0.00	0.00	0.00	0.04	102.55
WF001	Apy	48.42	0.00	17.77	0.11	0.04	0.02	0.00	34.73	0.16	0.02	0.16	0.03	0.01	0.02	0.05	101.55
WF001	Apy	48.91	0.00	17.87	0.00	0.00	0.00	0.01	34.27	0.21	0.00	0.13	0.07	0.00	0.00	0.08	101.56
WF001	Apy	50.22	0.00	17.67	0.07	0.00	0.00	0.00	34.24	0.18	0.00	0.18	0.03	0.00	0.00	0.16	102.74
WF001	Apy	49.19	0.00	17.83	0.04	0.00	0.00	0.02	34.51	0.24	0.03	0.14	0.00	0.00	0.01	0.02	102.04
WF001	Apy	50.29	0.00	17.74	0.04	0.00	0.00	0.00	33.83	0.23	0.01	0.17	0.04	0.00	0.03	0.08	102.49
WF001	Apy	48.95	0.00	17.24	0.10	0.00	0.01	0.01	33.87	0.21	0.00	0.21	0.06	0.00	0.00	0.03	100.71
WF001	Apy	50.11	0.00	17.71	0.00	0.07	0.06	0.01	33.92	0.22	0.01	0.16	0.00	0.00	0.01	0.05	102.30
WF001	Apy	49.57	0.00	17.37	0.19	0.03	0.00	0.00	33.91	0.25	0.00	0.23	0.02	0.00	0.00	0.09	101.65
WF001	Apy	50.22	0.00	17.62	0.05	0.02	0.05	0.00	33.86	0.14	0.00	0.20	0.00	0.00	0.00	0.15	102.31
WF001	Apy	50.19	0.00	17.43	0.15	0.00	0.01	0.00	34.11	0.17	0.00	0.25	0.01	0.00	0.02	0.03	102.37
WF001	Apy	51.03	0.00	17.73	0.03	0.00	0.00	0.00	34.21	0.20	0.02	0.24	0.00	0.00	0.01	0.16	103.65
WF001	Apy	50.23	0.00	17.47	0.08	0.00	0.02	0.00	33.65	0.25	0.00	0.27	0.01	0.00	0.00	0.00	101.98
WF001	Apy	50.16	0.00	18.08	0.15	0.00	0.03	0.00	33.93	0.25	0.00	0.19	0.00	0.00	0.00	0.07	102.86
WF001	Apy	49.78	0.00	17.70	0.21	0.00	0.01	0.00	34.10	0.17	0.00	0.26	0.06	0.00	0.00	0.19	102.54
WF001	Apy	51.02	0.00	18.25	0.04	0.00	0.03	0.01	33.71	0.20	0.01	0.14	0.00	0.01	0.01	0.06	103.52
WF001	Apy	50.27	0.00	17.30	0.06	0.05	0.00	0.04	33.58	0.13	0.01	0.29	0.03	0.00	0.02	0.16	101.94
WF001	Apy	50.04	0.00	17.27	0.11	0.00	0.00	0.01	33.64	0.17	0.00	0.32	0.06	0.00	0.00	0.24	101.89
WF001	Apy	44.54	0.00	15.05	0.17	0.00	0.01	0.00	32.66	0.18	0.01	0.21	0.01	0.00	0.00	0.18	93.02
WF001	Apy	50.74	0.00	18.15	0.20	0.00	0.00	0.00	34.24	0.13	0.00	0.24	0.00	0.01	0.00	0.12	103.86
WF001	Apy	50.18	0.00	17.58	0.00	0.00	0.05	0.00	34.25	0.16	0.00	0.14	0.00	0.00	0.02	0.18	102.54
WF001	Apy	49.88	0.00	18.09	0.05	0.00	0.00	0.01	34.46	0.17	0.00	0.24	0.03	0.02	0.00	0.04	103.02
WF001	Apy	49.61	0.00	17.76	0.00	0.01	0.00	0.05	34.07	0.21	0.00	0.15	0.00	0.00	0.00	0.06	101.96
WF001	Apy	50.78	0.00	17.69	0.05	0.00	0.02	0.04	34.13	0.22	0.00	0.20	0.04	0.05	0.01	0.02	103.25
WF010	Apy	47.69	0.00	18.41	0.14	0.00	0.00	0.00	33.36	0.04	0.00	0.00	0.00	0.00	0.02	0.30	99.97
WF010	Apy	50.55	0.00	17.09	0.01	0.07	0.05	0.00	32.93	0.12	0.00	0.50	0.01	0.03	0.00	0.33	101.69
WF010	Apy	48.44	0.00	18.19	0.02	0.02	0.01	0.01	33.49	0.07	0.00	0.13	0.08	0.00	0.00	0.44	100.89

WF010	Apy	48.14	0.00	18.31	0.18	0.00	0.00	0.00	33.81	0.00	0.00	0.05	0.03	0.00	0.00	0.03	100.56
WF010	Apy	49.46	0.00	17.11	0.02	0.00	0.01	0.00	32.06	0.07	0.00	0.58	0.13	0.02	0.01	0.53	100.01
WF010	Apy	48.11	0.00	17.98	0.00	0.00	0.02	0.01	33.45	0.02	0.00	0.07	0.03	0.10	0.01	0.63	100.43
WF010	Apy	47.72	0.00	18.52	0.15	0.00	0.00	0.02	33.26	0.02	0.02	0.06	0.00	0.00	0.02	0.14	99.92
WF010	Apy	48.29	0.00	17.80	0.15	0.00	0.03	0.01	33.55	0.07	0.00	0.09	0.00	0.05	0.02	0.41	100.47
WF010	Apy	50.32	0.00	16.87	0.16	0.00	0.00	0.03	32.95	0.08	0.00	0.65	0.04	0.00	0.03	0.34	101.48
WF010	Apy	49.95	0.00	16.69	0.10	0.00	0.00	0.04	32.18	0.05	0.00	0.58	0.00	0.00	0.00	0.61	100.23
WF010	Apy	48.22	0.00	17.88	0.00	0.00	0.05	0.00	33.36	0.05	0.00	0.12	0.00	0.00	0.00	0.43	100.18
WF010	Apy	49.96	0.00	16.73	0.03	0.00	0.00	0.04	32.15	0.09	0.02	0.70	0.01	0.00	0.00	0.69	100.41
WF010	Apy	50.28	0.00	16.53	0.11	0.06	0.02	0.00	32.59	0.09	0.00	0.76	0.00	0.00	0.00	0.14	100.59
WF010	Apy	50.35	0.00	16.68	0.14	0.00	0.00	0.01	32.57	0.08	0.00	0.64	0.07	0.01	0.00	0.73	101.28
WF010	Apy	50.37	0.00	16.76	0.15	0.00	0.01	0.02	32.62	0.08	0.00	0.70	0.04	0.00	0.00	0.39	101.15
WF010	Apy	49.98	0.00	17.00	0.07	0.00	0.00	0.03	32.99	0.09	0.00	0.48	0.00	0.00	0.01	0.25	100.95
WF010	Apy	48.60	0.00	18.41	0.16	0.00	0.00	0.04	33.27	0.07	0.00	0.06	0.00	0.00	0.01	0.25	100.86
WF010	Apy	49.51	0.00	18.08	0.18	0.00	0.00	0.02	33.26	0.01	0.00	0.10	0.02	0.00	0.00	0.58	101.76
WF010	Apy	49.69	0.00	17.39	0.11	0.00	0.00	0.00	32.90	0.04	0.00	0.36	0.06	0.02	0.00	0.05	100.64
WF010	Apy	50.05	0.00	17.39	0.07	0.00	0.00	0.00	32.88	0.12	0.00	0.42	0.04	0.06	0.02	0.15	101.20
WF010	Apy	50.79	0.00	17.21	0.01	0.00	0.03	0.00	32.84	0.07	0.00	0.46	0.04	0.00	0.00	0.12	101.62
WF010	Apy	49.71	0.00	17.69	0.04	0.00	0.00	0.00	33.12	0.08	0.00	0.31	0.00	0.00	0.02	0.27	101.26
WF082	Apy	47.70	0.00	18.25	0.18	0.00	0.01	0.00	34.66	0.07	0.03	0.03	0.00	0.01	0.00	1.19	102.16
WF082	Apy	48.20	0.00	18.64	0.00	0.00	0.04	0.04	34.61	0.06	0.00	0.05	0.05	0.05	0.00	0.17	101.93
WF082	Apy	47.93	0.00	18.79	0.00	0.00	0.02	0.00	35.15	0.04	0.01	0.02	0.00	0.00	0.01	0.61	102.61
WF082	Apy	47.93	0.00	18.47	0.09	0.00	0.00	0.03	34.89	0.07	0.00	0.05	0.01	0.06	0.01	0.81	102.43
WF082	Apy	48.21	0.00	18.36	0.11	0.00	0.00	0.00	34.64	0.06	0.00	0.06	0.00	0.05	0.00	1.06	102.55
WF082	Apy	47.96	0.00	18.00	0.11	0.00	0.00	0.01	34.35	0.03	0.00	0.08	0.02	0.00	0.01	1.38	101.97
WF082	Apy	48.15	0.00	17.88	0.00	0.00	0.00	0.05	34.31	0.07	0.00	0.16	0.02	0.00	0.00	1.35	101.99
WF082	Apy	48.50	0.00	17.90	0.23	0.00	0.04	0.00	34.63	0.03	0.00	0.13	0.01	0.07	0.00	1.41	102.96
WF082	Apy	48.12	0.00	17.96	0.05	0.00	0.00	0.00	34.48	0.08	0.05	0.10	0.12	0.07	0.00	0.81	101.82
WF082	Apy	48.33	0.00	18.30	0.00	0.00	0.00	0.00	34.73	0.08	0.01	0.08	0.06	0.00	0.03	0.63	102.25
WF082	Apy	47.70	0.00	18.71	0.13	0.06	0.04	0.01	34.70	0.06	0.00	0.06	0.05	0.00	0.00	0.83	102.34
WF082	Apy	48.79	0.00	18.02	0.10	0.04	0.00	0.00	34.60	0.05	0.00	0.11	0.05	0.00	0.00	0.50	102.28
WF082	Apy	46.85	0.00	18.51	0.10	0.00	0.00	0.00	34.20	0.07	0.00	0.01	0.00	0.00	0.01	0.83	100.58
WF082	Apy	49.43	0.00	17.43	0.10	0.01	0.00	0.00	33.79	0.07	0.01	0.28	0.03	0.00	0.00	0.65	101.81
WF082	Apy	48.51	0.00	18.08	0.03	0.00	0.00	0.03	34.34	0.06	0.00	0.08	0.03	0.00	0.00	0.56	101.72

Legenda

Apy	Arsenopirita	Gold	Ouro livre	Py	Pirita
Ber	Berthierita	Lö	Löllingita	Sb	Antimônio native
Ccp	Calcopirita	Pjs	Parajamesonita	Sph	Esfalerita

Anexo V: Resultados de LA-ICP-MS com conteúdos de elementos menores e traços em sulfetos dos depósitos Turmalina, Satinoco e São Sebastião

Mineral	V	Mn	Co	Ni	Cu	Zn	Se	Mo	Ag	Sn	Sb	Te	Pb	Bi	Au	Co:Ni	
Apy1 (9)	83.7	1700.	196.	3298.0	238.	12.2	0.9	1.9	0	0.50	0.68	8.80	8.43	BDL	0.06		
	4	53	39	0	BDL	77	6	8	1.67	0	0.50	0.68	8.80	8.43	BDL	0.06	
	52.0	1131.	173.	3040.4	134.	16.3	BD	BD									
	6	82	58	2	BDL	88	8	L	0.61	L	0.80	BDL	5.83	3.48	BDL	0.06	
		151.2	209.	3475.7	25.2	11.5	0.2			0.5							
	8.84	8	06	0	BDL	0	9	6	0.70	3	1.08	BDL	10.69	3.63	BDL	0.06	
		102.7	175.	2688.8	18.8	15.1	BD	BD									
	5.41	9	26	6	BDL	9	7	L	0.39	L	0.97	BDL	6.45	2.62	BDL	0.07	
	26.5	444.5	176.	3281.0	101.	13.7	BD	0.6									
	1	6	50	0	BDL	25	4	L	0.85	2	0.74	BDL	7.65	4.25	BDL	0.05	
		101.	4901.0			11.5	BD	BD									
Mean	0.00	9.25	50	7	BDL	0.00	8	L	0.35	L	0.07	0.36	0.74	2.26	BDL	0.02	
		101.	4455.1			15.4	0.2	BD	BD								
	0.00	8.73	70	6	BDL	0.00	2	7	0.36	L	0.71	BDL	0.93	0.73	BDL	0.02	
		107.	4646.4			15.6	BD	BD									
	0.00	9.31	93	0	BDL	0.00	7	L	0.71	L	1.17	BDL	1.15	1.30	BDL	0.02	
		96.5	4441.5			14.1	0.2	BD	BD								
	0.00	9.17	7	0	BDL	3.39	9	1	0.54	L	0.20	BDL	5.35	8.78	BDL	0.02	
Maximum	19.6	396.3	148.	3803.1	58.0	14.0	BD	BD									
	2	8	72	2	BDL	4	0	L	0.69	L	0.69	0.12	5.29	3.94	BDL	0.04	
	83.7	1700.	209.	4901.0	238.	16.3	0.9			1.9							
	4	53	06	7	BDL	77	8	8	1.67	0	1.17	0.68	10.69	8.78	BDL	0.07	
Minimum Standard deviation	0.00	8.73	7	6	BDL	BDL	8	L	0.35	L	0.07	BDL	0.74	0.73	BDL	0.02	
	29.7	611.3	45.8			83.7											
Apy2 (25)		267.	02	797.43	BDL	BDL	2.92	0.5	BD	16110.6							
	0.10	12.78	408.	3025.7		13.2	BD	1.4									
	17.2	73.96	00	5	BDL	0	BDL	L	BDL	1	9995.99	2.26	17.52	0.19	0.50	0.13	
	5	299.	1287.3				0.6	BD									
		BDL	11.92	42	7	BDL	BDL	6	0.12	L	8659.49	0.85	BDL	0.05	0.85	0.23	
		127.9	315.	2090.3		60.6	0.7	BD	BD	11578.5							
	6.70	7	58	3	1.36	8	BDL	6	0.11	L	4	1.84	5.05	BDL	1.33	0.15	
		401.	4120.2				BD	BD	BD	11732.3							
		BDL	12.01	78	6	BDL	BDL	L	6.77	L	7	1.77	15.23	0.11	25.90	0.10	
		221.	2615.4				BD	BD	BD	BD							
	1.21	54.80	76	2	2.93	BDL	BDL	L	2.60	L	9035.03	1.92	35	2.48	3.61	0.08	
		301.	1269.3				0.0	BDL	9	9	0.99	0.57	BDL	0.21	0.24		
	0.44	11.15	10	4	1.25	BDL	5.55	8	BDL	BD	11441.0		229.0				
		194.	488.00	2.66	BDL	BDL	L	3.27	L	0	1.66	0	1.59	231.00	0.40		
	0.40	20.40	00				BD	BD	BD	13670.0							
		261.	1172.0				BD	BD	BD	BD							
		BDL	11.40	00	0	1.11	BDL	BDL	L	0.62	L	0	1.62	7.38	0.42	34.90	0.22
	214.	164.8	244.	1448.4		112.	BD	2.4	BDL	10547.1			225.3				
	76	2	54	4	BDL	44	BDL	L	0.36	6	1	2.83	9	3.64	431.00	0.17	
		383.	2702.1				BD	BD	BD	BD							
	0.53	15.78	21	6	1.34	BDL	BDL	L	0.93	L	9518.56	0.90	4.18	0.31	144.00	0.14	
		463.	3281.7				BD	BD	BD	10702.9							
	9.16	51.49	59	2	2.43	BDL	BDL	L	0.84	L	6	1.75	16.67	1.59	2.08	0.14	
		511.	3951.2				BD	BD	BD	10899.1							
	1.28	28.47	74	8	1.28	BDL	BDL	L	BDL	L	0	2.01	0.17	BDL	0.50	0.13	
		423.	3174.3				0.5	BD	11027.7								
	2.80	13.14	95	1	1.19	BDL	BDL	3	6.13	L	3	2.44	0.77	BDL	247.00	0.13	
		223.	517.62	1.10	BDL	BDL	L	0.80	BD	14784.8							
	6.34	40.02	524.	4651.6			BD	BD	BD	10254.8							
		8.54	61.58	20	6	1.12	BDL	BDL	L	0.38	L	5	2.28	39.11	0.60	0.45	0.11
		514.	5009.3				0.5	BD	12409.4								
	0.18	11.41	94	7	BDL	BDL	BDL	4	0.06	L	7	1.15	0.29	BDL	0.26	0.10	
		518.	5413.7				BD	BD	BD	11908.8							
	4.34	10.83	91	2	BDL	BDL	BDL	L	0.10	1	8	2.31	1.37	0.07	0.51	0.10	
		381.	2948.6				BD	BD	BD	12545.1							
	0.24	13.90	03	1	BDL	BDL	BDL	L	BDL	L	6	1.40	0.13	0.06	1.00	0.13	
		451.	3045.4				0.3	BD	14828.9								
		BDL	14.26	67	8	BDL	BDL	7.13	5	BDL	L	8	2.06	0.18	0.09	0.37	0.15
		441.	3874.1				BD	BD	BD	9425.00	1.20	1.38	0.15	0.61	0.48		
		BDL	12.06	99	1	BDL	BDL	BDL	8.53	L	9526.08	1.72	8.94	0.17	794.00	0.11	
		455.	25780.				BD	35.7	BD	541413.	30.0	107.	213803.				
		BDL	26.88	86	23	6.58	7	BDL	L	63	0	16.77	93	00	0.02		
		248.	441.	3874.1			BD	BD	BD	9425.00	1.20	1.38	0.15	0.61	0.48		
		BDL	11.50	14	517.40	BDL	BDL	L	BDL	L							

		437.	3444.4			BD		BD	10442.6								
	0.29	12.39	28	8	BDL	BDL	BDL	L	0.10	L	6	1.49	2.98	0.15	6.56	0.13	
		339.	2004.4			0.2		BD	10466.0								
	<u>BDL</u>	12.47	92	4	BDL	7.04	5.80	2	0.08	L	2	1.46	0.51	0.04	1.82	0.17	
Mean	11.4		365.	2618.7			BD		0.2	11764.5							
	4	33.77	77	8	0.74	8.06	BDL	L	1.33	8	3	1.69	93.99	0.54	80.51	0.18	
Maximum	214.	164.8	524.	5413.7		112.		0.7		2.4		20838.0		1657.			
	76	2	20	2	2.93	44	7.13	6	8.53	6	9	2.83	35	3.64	794.00	0.48	
Minimum	BDL	10.83	00	488.00	BDL	BDL	BDL	L	BDL	L	8659.49	0.85	BDL	BDL	0.21	0.02	
Standard	43.5		106.	1467.9		25.5		0.2		0.6		338.8					
deviation	1	39.71	01	1	0.94	3	2.13	5	2.42	7	2717.98	0.52	6	0.92	186.23	0.11	
Apy2 fracture (1)	BDL	26.88	455.	25780.	10.8	BDL	35.7	BD	541413.	30.0	107.	213803.	00	0.02			
			18.9			29.5	0.3	BD									
	0.07	16.73	7	260.63	6.66	BDL	7	8	0.21	L	8.20	2.04	52.32	2.24	0.16	0.07	
		402.	1164.4	27.4		11.0	0.1		0.3				33.5				
	0.08	22.17	46	8	5	BDL	5	6	4.06	9	12.36	6.52	80.63	1	0.35	0.35	
		508.	1805.8	48.0		0.2		0.2		0.2			30.8				
	0.09	17.85	02	1	6	0.94	9.77	4	2.47	4	67.74	3.12	15.50	8	0.74	0.28	
Py (7)	0.06	15.93	0.42	9.03	BDL	BDL	3	6	BDL	L	0.17	0.15	1.53	0.09	0.02	0.05	
		97.8				10.4	0.1	BD									
	0.08	16.48	2	950.22	6.80	BDL	5	5	0.04	L	2.18	BDL	0.54	0.03	0.01	0.10	
		44.3				36.8	0.2	BD									
	0.06	14.82	5	130.40	0.17	BDL	1	0	0.01	L	0.49	7.04	3.64	0.51	0.38	0.34	
		267.	1592.5	78.0		29.2	0.2		0.2				28.6				
	0.05	18.83	77	8	1	BDL	0	7	2.74	1	66.68	1.23	34.17	8	0.67	0.17	
Mean	0.07	17.54	40	844.74	8	BDL	4	2	1.36	2	22.55	2.87	26.90	1	0.33	0.19	
		508.	1805.8	78.0		36.8	0.3		0.3				33.5				
Maximum	0.09	22.17	02	1	1	0.94	1	8	4.06	9	67.74	7.04	80.63	1	0.74	0.35	
Minimum	0.05	14.82	0.42	9.03	BDL	BDL	9.77	5	BDL	L	0.17	BDL	0.54	0.03	0.01	0.05	
Standard	0.02	2.41	98	724.13	8	-	9	8	1.69	-	30.83	2.88	30.54	8	0.29	0.13	

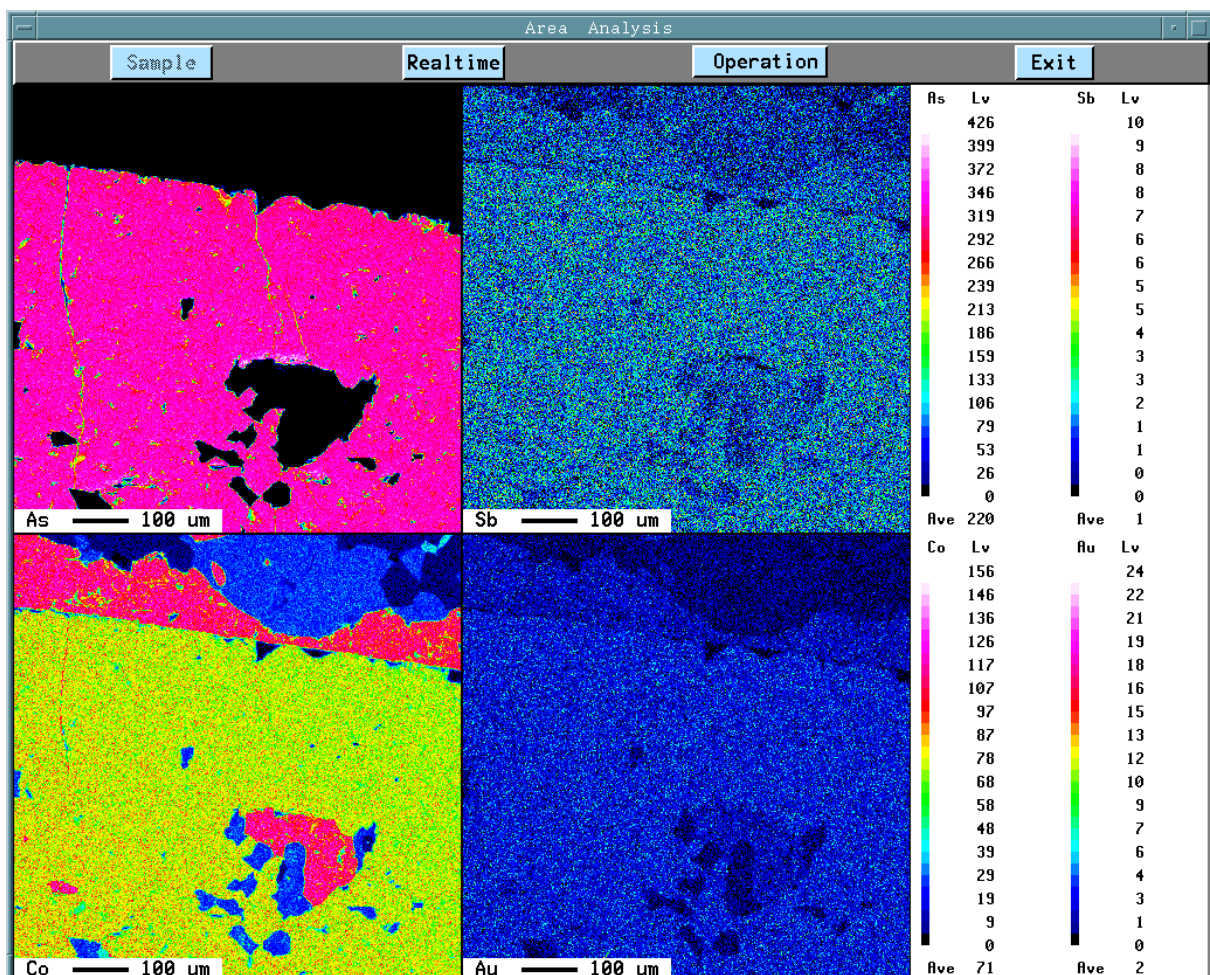
BDL: below detection limit.

Zero values were used for statistical calculations of samples with values below detection limit

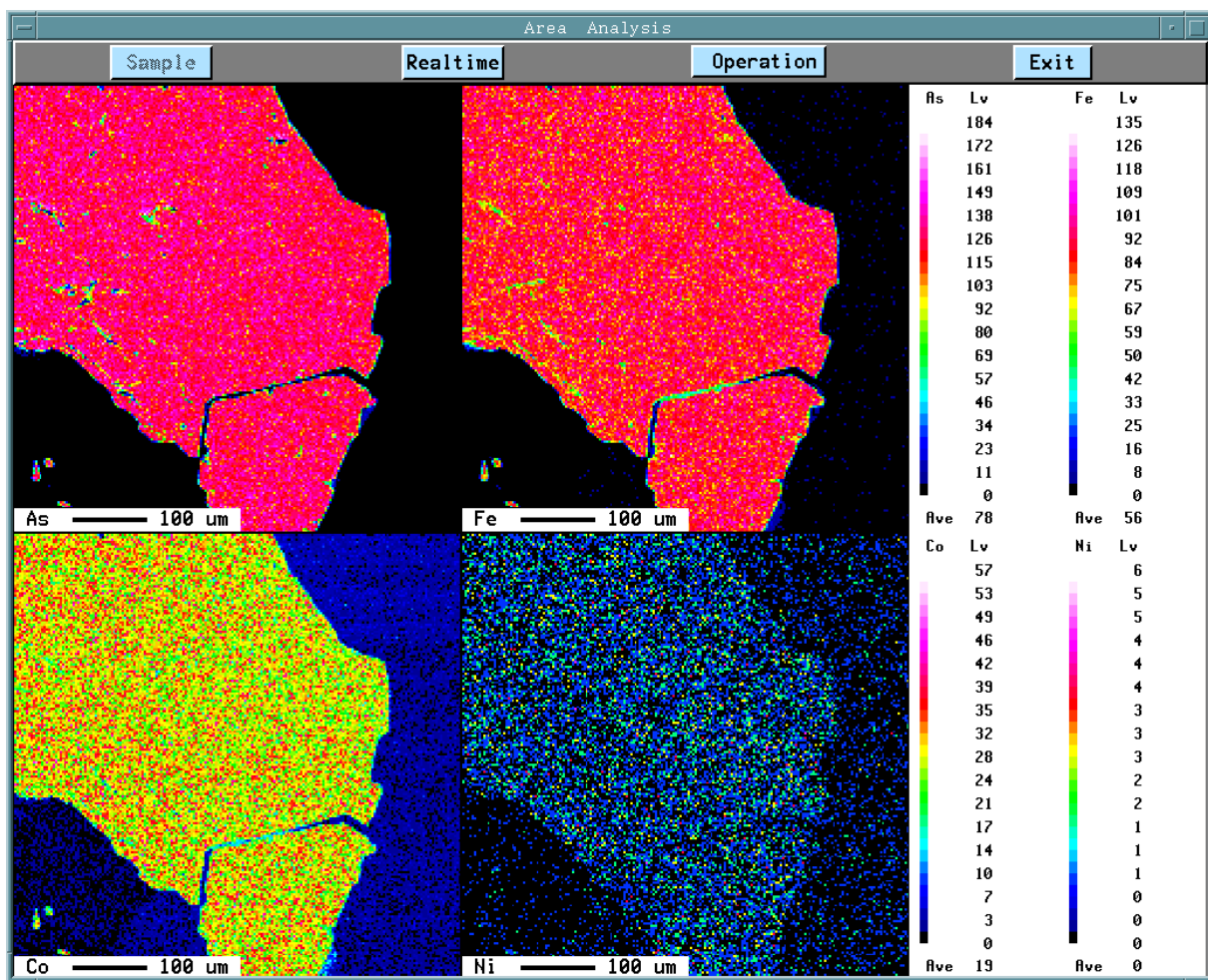
Numbers in parentheses refer to number of analyses

'-' refer to meaningless standard deviation, due to insufficient data exceeding detection limit

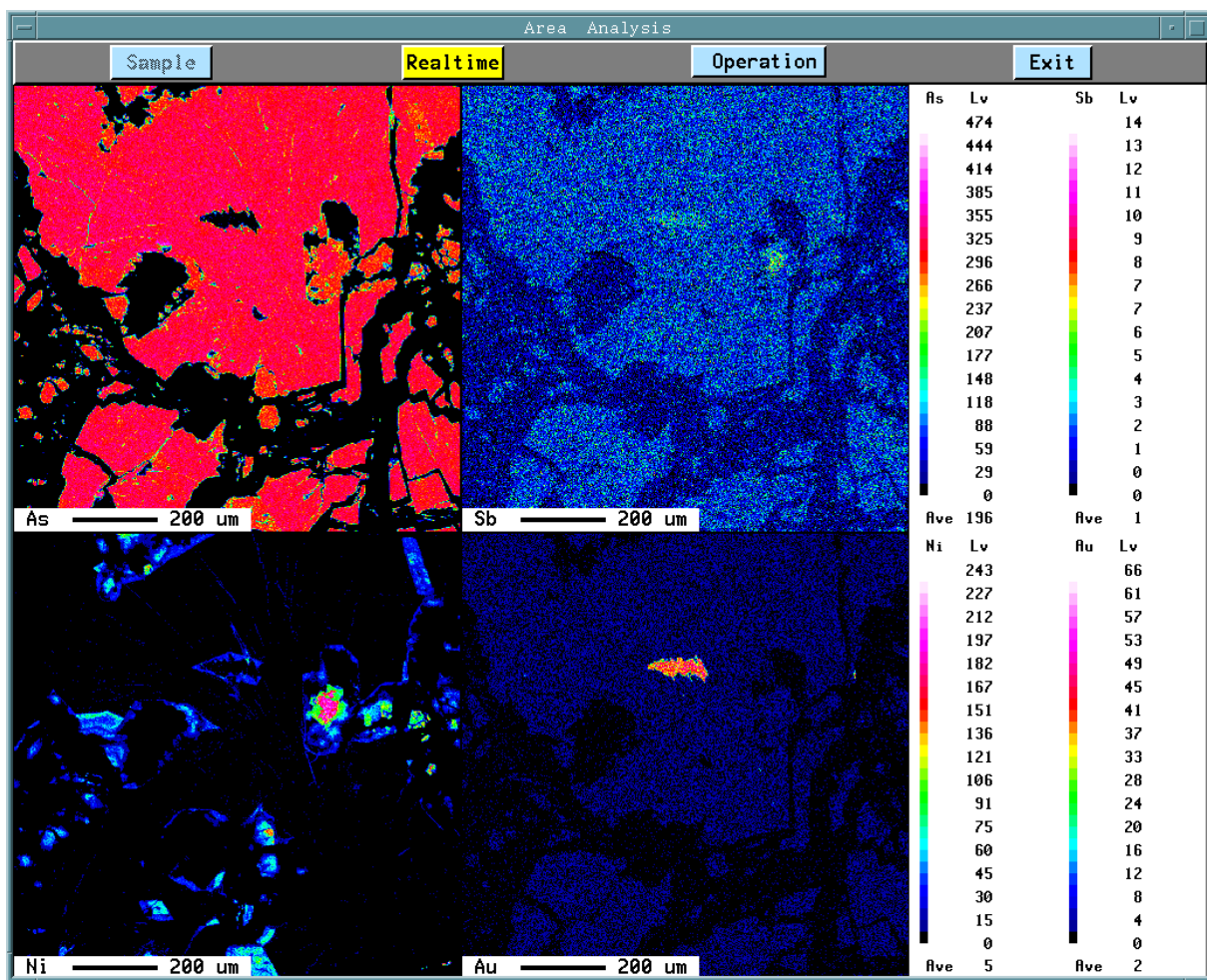
Anexo VI: Mapas compositionais intracristalinos suplementares dos depósitos estudados



Mapa compositionais de raio-X de arsenopirita Apy3 do depósito São Sebastião.



Mapa composicional de raio-X de arsenopirita Neoproterozóica do depósito do tipo Intrusion-Related Fazenda Nova, mostrando pouca variação na distribuição dos elementos-traço.



Mapa composicional de raio-X de arsenopirita do depósito Carvoaria Velha. Mostra ouro livre no núcleo do cristal, relacionado ao fraturamento radial com indução por fluido tardio à cristalização da arsenopirita.

Anexo VII: Geoquímica de rocha total em Satinoco e Turmalina: resultados e discussões

Segue abaixo a descrição da amostragem, resultados e interpretação da campanha de Geoquímica de Rocha Total para os depósitos Satinoco e Turmalina.

Os objetivos dessa amostragem e dos resultados foram:

- Identificar se as apófises de granitóides encontrados nas minas Satinoco e Turmalina possuem a mesma assinatura do Batólito de Granito aflorante na “Pedreira Casquilho”;
- Identificar os protólitos (ou rochas não alteradas hidrotermalmente) das rochas encaixantes dos depósitos Satinoco e Turmalina;
- Entender qual a natureza química das alterações hidrotermais e confrontar com os resultados de química mineral das fases de sulfetação identificadas.

Relação das amostras

Furo FTS-1562: Corpo Satinoco SE, composto por um pacote de anfibolito (encaixante), com níveis hidrotermalizados em zonas de alteração. A composição rocha encaixante vulcânica está enriquecida em matéria orgânica em alguns níveis. Em termos da alteração hidrotermal, as zonas de alteração proximais estão enriquecidas em sílica, sulfetos, clorita e carbonato.

Furo FTS-1406: Corpo Satinoco Central, composto de pacote de anfibolito (encaixante) com níveis hidrotermalizados em zonas de alteração. As zonas de alteração exibem uma rocha xistosa com diferentes quantidades de quartzo hidrotermal, enriquecido na zona proximal (corpo de minério). Os termos

metamórficos das rochas são: (i) anfibolito bandado, na zona distal; (ii) anfibólito-quartzo-clorita xisto e (iii) biotita-clorita quartzo xisto, na zona proximal.

Cabe destacar que, tanto no furo FTS-1562 quanto no furo FTS-1406, existe um notável enriquecimento em Fe nos sulfetos, anfibólitos, biotita e clorita, levantados nas análises de química mineral em microssonda eletrônica. Contudo, a composição do Fe nas análises de rocha total fica mascarada pela maior concentração de ferro primário nas rochas das zonas de alteração distais (ou fora das zonas de alteração?), cujo protólito se mostra representado por basaltos.

Furo FTS-1607: Corpo A. Trata-se de apenas duas amostras, nas profundidades 19-20m e 31.9-32.9m, onde buscou-se investigar o possível protólito ultramáfico, o que foi confirmado por uma das amostras.

Furo FTS-1442: Corpo B. Três amostras foram coletadas no final do furo, que interceptou o stock do granito. O objetivo foi o de comparar a química do granito no furo, com uma amostra-de-mão do granito na rampa do B e outras três amostras-de-mão de possíveis apófises nos níveis 10.1 e 11.1 e 11.2 da mina.

Interpretações e discussões

Sobre as possíveis rochas ultramáficas no greenstone belt Pitangui

Foram coletadas duas amostras no furo FTS-1607 com o objetivo de verificar os protólitos dessas amostras. Embora essas rochas apareçam com algum grau de alteração hidrotermal por silicificação, alguns resultados denotam se tratar de rocha ultramáfica (ao menos na amostra WF-146). Em comparativos com as amostras de komatiítos do trabalho Verma et al. (2017), para o GBRV, esta amostra apresenta química bastante semelhante. Originalmente, as rochas encaixantes do corpo A e B do depósito de Turmalina são descritas como predominante vulcanoclásticas com

horizontes de detritos pelíticos (Fabricio-Silva et al, 2018). Contudo, os presentes resultados químicos das amostras do furo FTS-1607 (e também uma possível tendência das rochas vulcânicas da zona distal no depósito Satinoco) mostram que horizontes finos com komatiítos também devem fazer parte do conjunto petrogenético dentro do depósito Turmalina. Salienta-se que a composição mais magnesiana também pode representar acumulação de sedimentos vulcanoclásticos com origem nas rochas ultramáficas.

Rochas encaixantes não hidrotermalizadas no depósito Satinoco

No diagrama TAS para rochas vulcânicas, observa-se que as amostras menos hidrotermalizadas ficam posicionadas no campo dos basaltos andesíticos a basaltos, denotando que os protólitos devem se tratar de basaltos. A amostra WF146 cai no diagrama como foidito. Destaca-se que a amostragem foi feita ao longo das zonas hidrotermais (incluindo zona mineralizada), deslocando as amostras no campo da maior concentração de sílica. Portanto, os campos dos andesitos e dos dacitos não indicam a composição do protólitos.

Os diagramas de variação de MgO Vs. SiO₂, Cr, Al₂O₃ e TiO₂ (Fig. 3) foram comparados com trabalhos clássicos para rochas vulcânicas (cf. Pearce, 2006) e o trabalho de Verma et al. (2017) e as amostras (fora da zona alteração ou na zona de alteração distal) estão no campo dos basaltos, com exceção da amostra WF142, que apresenta grande similaridade com os komatiítos (tanto os clássicos quanto os observados no leste do Quadrilátero Ferrífero). Outra ferramenta importante é usar os elementos terras raras, que são bem menos móveis para alterações pós-magmatismo. Novamente, foi comparado com os resultados de Verma et al. (2017) e os padrões são bastante parecidos com os basaltos do greenstone belt Pitangui.

O diagrama de MgO e Cr mostra uma correlação positiva entre esses compostos, sendo que a amostra WF146 indica uma grande concentração de Cr (5200 ppm), até

mesmo se comparado a dados de rochas ultramáficas do QF, onde os valores oscilam entre 2500 e 4200 ppm.

Implicações para prospecção mineral

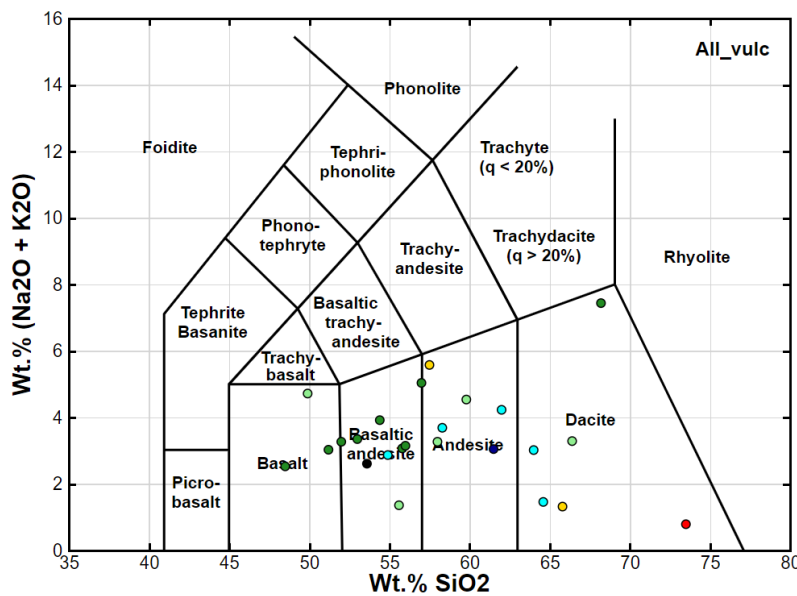
Levando em conta a amostragem sistemática ao longo dos furos FTS-1562 e FTS-1406, foram estudados previamente a distribuição de alguns elementos, tentando-se atribuir a variação deles com relação aos corpos mineralizados. Algumas observações importantes se seguem abaixo.

Os maiores teores de As não estão restritos aos locais de ocorrência de ouro. Muito embora os teores de As são altos nas zonas mineralizadas, existem também teores altos nos locais com sulfetos onde se descrevem arsenopirita. Contudo, os teores de Bi e Te crescem exponencialmente na zona proximal e nos corpos mineralizados, sendo um bom indicativo de teor de ouro em Satinoco.

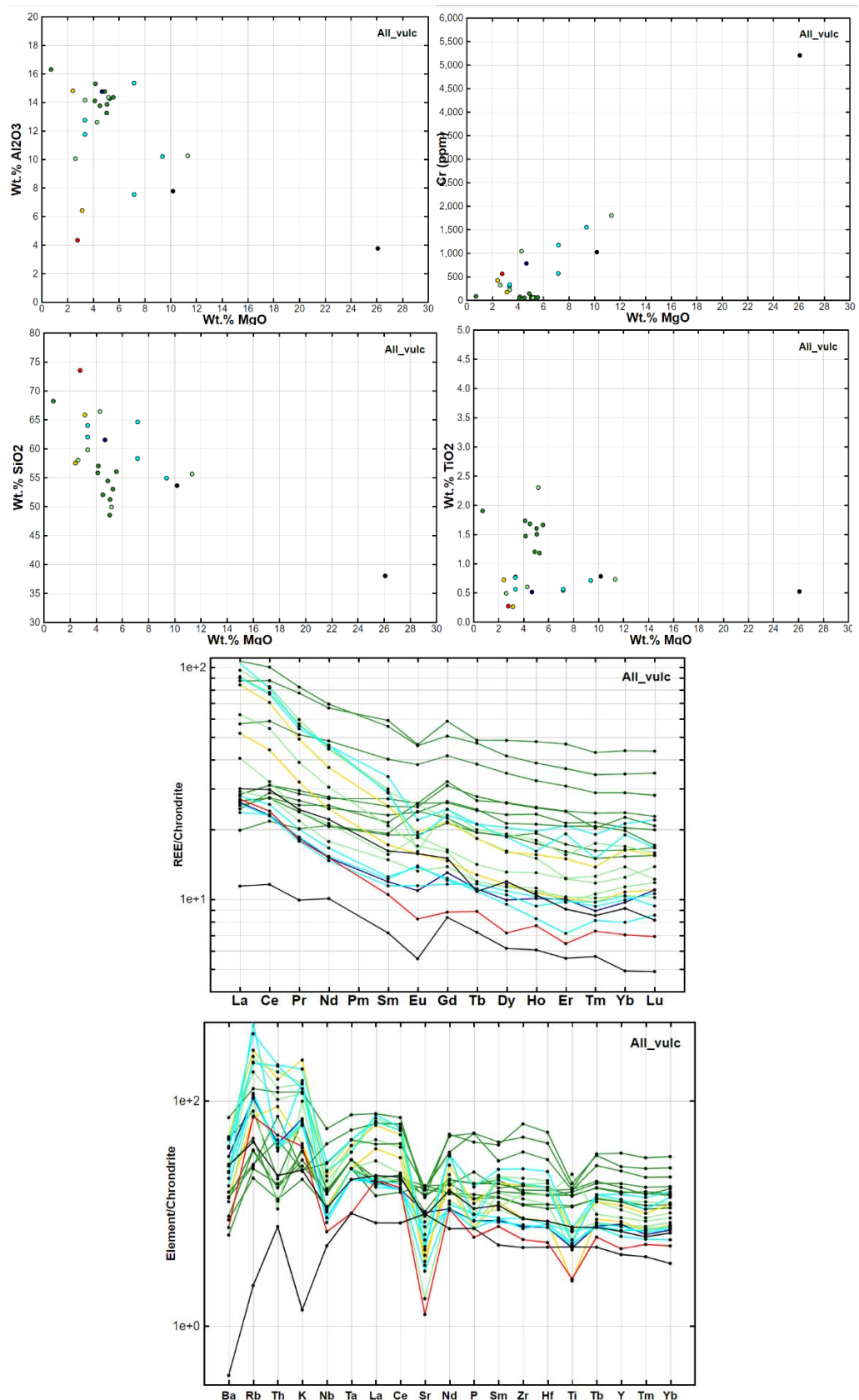
Em princípio, o forte enriquecimento de Bi e Te foi identificado nas análises com microssonda nos sulfetos da segunda fase de sulfatação e não da primeira (maior responsável pela mineralização em Au), o que gera alguma inconsistência. Uma alternativa seria a possível lixiviação desses elementos na primeira fase.

química do furo FTS-1562 mostra que existem duas regiões de enriquecimento de metais (Au, Ag, Pb, Cu, Ni e Cr), uma primeira na altura das amostras WF135 a WF137 e outra entre as amostras WF140 e WF141, sendo esta segunda com os maiores teores. Confrontando com o posicionamento dos horizontes mais enriquecidos de matéria carbonosa, cabe observar que esses folhelhos impuros se apresentam como barreiras físicas para o avanço dos fluidos hidrotermais no sentido da estratigrafia, como observado pela equipe de campo da empresa e visto em outros diversos depósitos de ouro orogênico. Contudo, cabe destacar que a

distribuição e concentração dos metais relativos à estas camadas sugere que a fonte dos fluidos vem de sul (ou sudeste ou sudoeste) para norte. Isso deve ser observado, pois os corpos mineralizados devem estar mais enriquecidos na base da primeira camada (a sul) mais enriquecida em matéria orgânica ou na primeira zona de cisalhamento. Uma fonte de fluidos (ou apenas fonte térmica) atribuída ao granito, traria os maiores teores para o corpo Satinoco SE.



Rochas dos furos FTS-1406, FTS-1562 e FTS-1607. As composições não refletem os protólitos das rochas, uma vez que as amostras foram coletadas ao longo da zona de alteração hidrotermal (refletindo falsas composições de Andesito e Dacito).

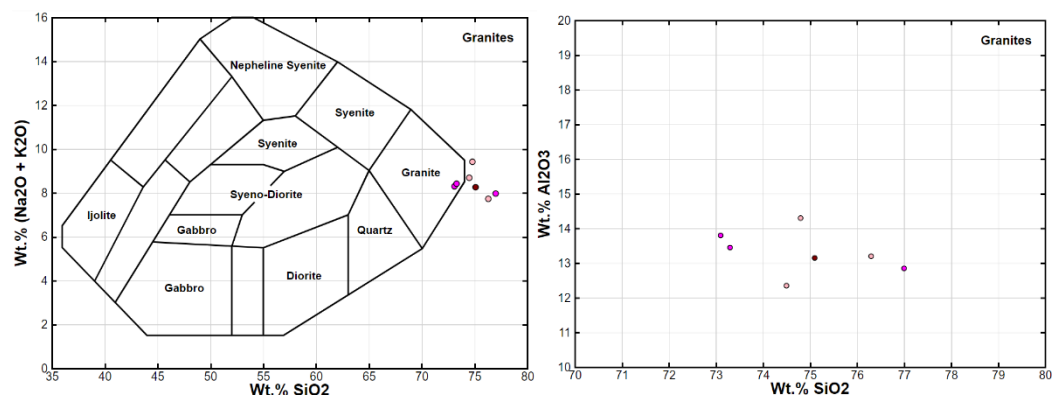


(Superiores) Diagramas de variação de MgO com Al₂O₃ e Cr, mostrando a composição predominantemente basáltica das amostras com correlação negativa do MgO com o Al₂O₃ (excluindo-se as amostras das zonas proximais) e positiva do MgO com o Cr. (Inferiores) Diagramas de variação de MgO com SiO₂ e TiO₂, mostrando que as amostras com baixos índices de hidrotermalismo representam basaltos e komatititos. Verde escuro: Anfibolitos com pouca alteração hidrotermal (FTS-1562); Verde médio: anfibolitos bandados (zonas de alteração proximal a intermediária – FTS-1562); Azul escuro: anfibolitos bandados (zonas de alteração proximal a intermediária – FTS-1406); Azul cyan: anfibolitos bandados (zonas de alteração proximal – FTS-1406); Vermelho e amarelo: zonas mineralizadas dos furos FTS-1406 e FTS-1562, respectivamente.

Implicações sobre a química dos granitos e apófises

O primeiro objetivo a se destacar é o comparativo dos resultados das amostras de granito (no furo FTS- 1442 e a amostra da rampa do B0) com as três possíveis apófises amostradas. Existia uma dúvida sobre se as possíveis apófises eram do corpo granítico ou eram veios de quartzo.

Todas as amostras supracitadas apresentam uma química bastante parecida, indicando que se trata da mesma rocha, no caso um granito (Fig. 4A) de afinidade cálcio-alcalina (Fig. 4B). Contudo, é importante salientar que, muito embora existam essas apófises de granito, algumas estruturas discordantes nos corpos minerais (principalmente no corpo A-SE) são veios de quartzo B ou D (B e V4-type veins).



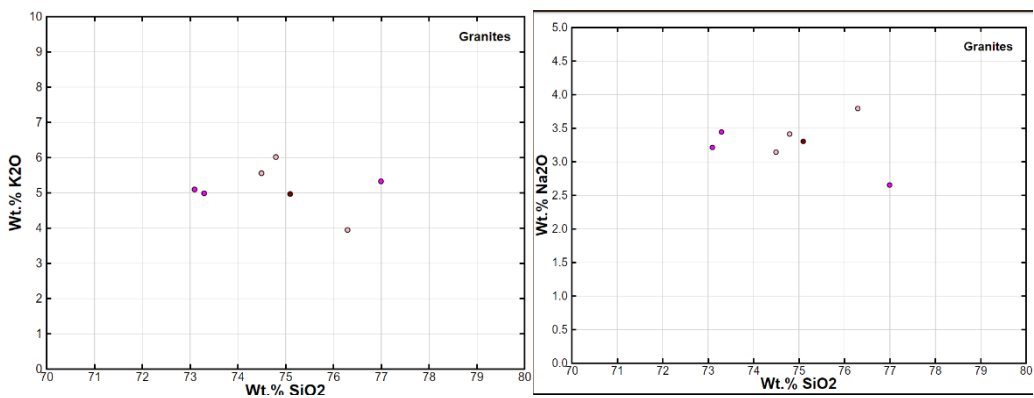


Diagrama TAS de rochas plutônicas. Em rosa escuro: granitos do furo FTS-1442; Em rosa claro: Apófises dos níveis 10 e 11; Em vermelho: granito na rampa B0. Os diagramas de variação mostram a distribuição homogênea das amostras de granitos (stock) e apófises. O diagrama de SiO₂ Vs. Al₂O₃ indica a natureza cálcio-alcalina da rocha. Em rosa escuro: granitos do furo FTS-1442; Em rosa claro: Apófises dos níveis 10 e 11; Em vermelho: granito na rampa B0.

